JERZY BAŁDYGA, MAGDALENA JASIŃSKA[*]

FLOW STRUCTURE, DROP DEFORMATION AND MASS TRANSFER IN DENSE EMULSIONS

STRUKTURA PRZEPŁYWU, DEFORMACJA KROPEL I TRANSPORT MASY W GĘSTYCH EMULSJACH

Abstract

This paper presents applications of a new model of the rheological behaviour of dense oil-in-water emulsions of non-colloidal droplets to describe the flow structure, the effects of the flow of dense emulsion on drop deformation and the related increase of the interfacial area and the mass transfer rate.

Keywords: dense emulsions, rheology, mass transfer

Streszczenie

W artykule przedstawiono metodę wykorzystania modelu reologii gęstych emulsji olej/woda do opisu struktury przepływu, deformacji kropel, rozwinięcia powierzchni międzyfazowej oraz współczynników wymiany masy. Przedyskutowano możliwość wykorzystania podobnych metod do opisu układów micelarnych.

Słowa kluczowe: gęste emulsje, reologia, wymiana masy

[*] Prof. PhD. DSc. Eng. Jerzy Bałdyga, PhD. DSc. Eng. Magdalena Jasińska, Department of Engineering and Chemical Reactors Dynamic, Faculty of Chemical and Process Engineering, Warsaw University of Technology.

1. Introduction

Dense emulsions form many useful products including food products (homogenised milk, sauces, dressings, beverages, butter), as well as pharmaceutical and cosmetic products such as creams and balms. Emulsions are used as personal hygiene products, fire-fighting agents, agricultural industry products, paints and inks. In the manufacturing and applying of emulsions, it is often necessary to predict or control the emulsion viscosity and the flow pattern. The mass transfer between the continuous and dispersed phase can also affect this process.

Emulsion viscosity η depends on the continuous phase viscosity η_c, the volume fraction of the dispersed phase ϕ and its viscosity η_d, the interfacial tension σ, the shear rate $\dot{\gamma}$, the emulsifying agent (if present) and of course, on temperatures that obviously affect the physicochemical properties. The development of strict theoretical models is possible for infinitely dilute emulsions of spherical uncharged droplets.

The equation for the relative viscosity η_r under the limiting conditions listed below, when the hydrodynamic viscous stress is negligible compared to the interfacial stress, was proposed by Taylor [1]:

$$\eta_r = \frac{\eta}{\eta_c} = 1 + \left[\frac{5 \cdot K + 2}{2 \cdot (K+1)} \right] \cdot \phi \tag{1}$$

where $K = \eta_d/\eta_c$ is the ratio of the dispersed-phase viscosity η_d to the continuous-phase viscosity η_c and ϕ is the volume fraction of droplets. Equation (1) is valid for $\phi \to 0$, $N_{Ca} \to 0$ and $Pe \to \infty$, where N_{Ca} is the capillary number,

$$N_{Ca} = \eta_c \cdot \dot{\gamma} \cdot R / \sigma \tag{2}$$

being the ratio of the hydrodynamic stress that tends to stretch the droplet and increase its surface energy, to the interfacial tensile stress resulting from interfacial tension, σ. The tensile stress tends to decrease the surface energy by maintaining the spherical shape of the droplet. Pe is the Péclet number defined by

$$Pe = \frac{\dot{\gamma} \cdot R^2}{D_B^\infty} \tag{3}$$

where D_B^∞ is the coefficient of Brownian diffusion for a particle separated from other particles, R is the drop radius, and $Pe \gg 1$ is equivalent to the condition that the drops are much larger than the distance travelled due to Brownian motions.

Most of models on the rheology of emulsions are based on the extension of this early model proposed by Taylor. Recently, a new method was proposed for including the effect of the droplet size distribution on the rheological behaviour of dense oil-in-water emulsions of non-colloidal droplets [2]. The method is based on an extension of the advanced model [3] for the relative viscosity of the concentrated monodisperse emulsion to account for polydispersity effects.

Model [3] is constituted by Equation (4) with three parameters M, N and P defined by Equations (5), (6) and (7) and dependent upon the capillary number $N_{Ca} = \eta_c \cdot \dot{\gamma} \cdot R / \sigma$ and the viscosity ratio K.

$$\eta_r \cdot \left[\frac{M - P + 32 \cdot \eta_r}{M - P + 32} \right]^{N-1.25} \cdot \left[\frac{M + P - 32}{M + P - 32 \cdot \eta_r} \right]^{N+1.25} = \left(1 - \frac{\phi}{\phi_m} \right)^{-2.5 \cdot \phi_m} \tag{4}$$

$$M = \sqrt{\left(64 / N_{Ca}^2 \right) + 1225 \cdot K^2 + 1232 \cdot \left(K / N_{Ca} \right)} \tag{5}$$

$$P = 8 / N_{Ca} - 3 \cdot K \tag{6}$$

$$N = \frac{\left(22 / N_{Ca} \right) + 43.75 \cdot K}{\sqrt{\left(64 / N_{Ca}^2 \right) + 1225 \cdot K^2 + 1232 \cdot \left(K / N_{Ca} \right)}} \tag{7}$$

The model expressed by Equations (4) to (7) was validated using much experimental data starting from the paper by Pal [3]; however, effects resulting from the drop size distribution were explained in [2].
To include the polydispersity of emulsion [2] one needs to calculate the equivalent radius R of the polydisperse system using the drop volume distribution $f_V(R_i)$, such that $f_V(R_i) dR_i$ means a volume fraction of drops from the range R_i to $R_i + dR_i$.

$$I(R) = \int_0^\infty f_V(R_i) \cdot I(R_i) dR_i \tag{8}$$

with $I(R_i)$ given by

$$I(R_i) = \frac{\left(4 / N_{Ca,i} \right) \cdot \left(2 + 5 \cdot K \right) + \left(K - 1 \right) \cdot \left(16 + 19 \cdot K \right)}{\left(40 / N_{Ca,i} \right) \cdot \left(1 + K \right) + \left(2 \cdot K + 3 \right) \cdot \left(16 + 19 \cdot K \right)} \tag{9}$$

where $N_{Ca,i} = \eta_c \cdot \dot{\gamma} \cdot R_i / \sigma$.

Figure 1 shows the relative viscosity calculated using bimodal distribution; the viscosity is plotted against the capillary number based on the equivalent radius R that is defined by Equations (8) and (9). There are three more curves on the figure that are constructed using the capillary number based on the mean sizes R_{10}, R_{32} and R_{30} that characterise the considered population for the same relative viscosity, η_r. The difference between the curves $\eta_r = f(N_{Ca})$ is significant.

Figure 1 shows that neither of the mean sizes traditionally used to characterise population, i.e. R_{10}, R_{32} and R_{43} is able to represent the population as the characteristic size in the model for the emulsion viscosity in the case of the bimodal distribution. However, as shown in Figure 2, in the case of the bell-shaped, unimodal distribution, the curve for the capillary number defined using R_{32} represents the distribution quite well – the difference in

the predicted viscosity is less than 10% in such a case. This problem is discussed in detail in Ref. [2].
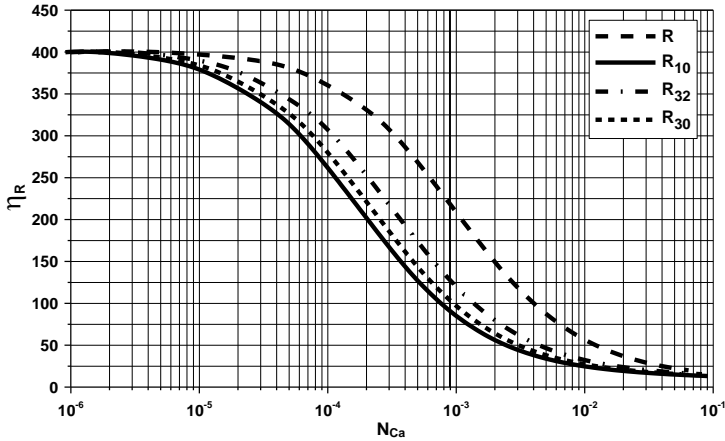
Fig. 1. Effect of the capillary number on the relative viscosity for $\phi_m = 0.8$, volume fractions of dispersed phase $\phi = 0.795$, $\eta_c = 0.91$ mPas, $\eta_d = 9.4$ mPas; bimodal distribution
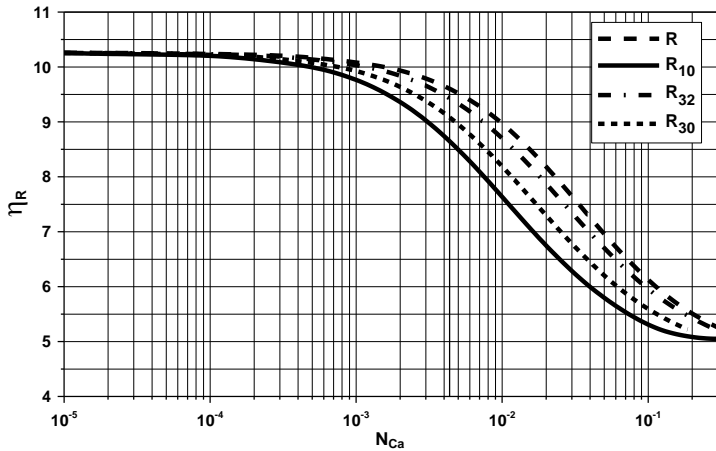
Fig. 2. Effect of the capillary number on the relative viscosity for $\phi_m = 0.8$, volume fractions of dispersed phase $\phi = 0.60$, $\eta_c = 0.91$ mPas, $\eta_d = 9.4$ mPas; unimodal distribution

As shown in Ref. [2], the model has a universal character and can be combined with the population balance equation and CFD. Examples of modelling are presented in [2] for laminar and turbulent flows of dense emulsions. In the case of laminar flow, the Couette flow and the Taylor-Couette flow were considered. In the case of turbulent flow, it has been shown how dispersion of droplets in the high-shear, rotor-stator mixer affects the flow pattern and rheology of the emulsion product.

2. Simulation of turbulent dispersion of drops in dense emulsion

To perform computations, it has been assumed that dense emulsions can be treated as the shear thinning pseudo-homogeneous fluids of the constant volume fraction of the dispersed phase of viscosity expressed by Equations (4) to (9). The local values of the drop size distribution are calculated using the moment transformation of population balance and QMOM to solve the moment balances using the breakage kernel based on the multifractal theory of turbulence as presented by Bałdyga and Podgórska [4]. The assumption of pseudo-homogeneity is supported by the observation of Ovarlez et al. [5], that no migration of droplets takes place in dense emulsions during the Couette flow. According to Ovarlez et al. [5], a reason for keeping homogeneity could be the deformability of droplets resulting from shear.

Following the results presented in [2], we consider here the dispersion of droplets present in dense emulsion in the in-line Silverson 150/250 MS high-shear, rotor-stator mixer and observe the modification of the rheological properties of the emulsion.

A performance of the Silverson double-screen mixer 150/250/MS, the same as that applied in [2] and [6], is investigated to simulate drop dispersion. The mixer is equipped with twin rotors that rotate with the same frequency within close-fitting screens. The inner rotor has an inner diameter of $2.62 \cdot 10^{-2}$ m, the outer diameter is $3.81 \cdot 10^{-2}$ m, and is equipped with four blades. The outer rotor diameters are $4.99 \cdot 10^{-2}$ m (internal) and $6.35 \cdot 10^{-2}$ m (external) and this rotor is equipped with eight blades.
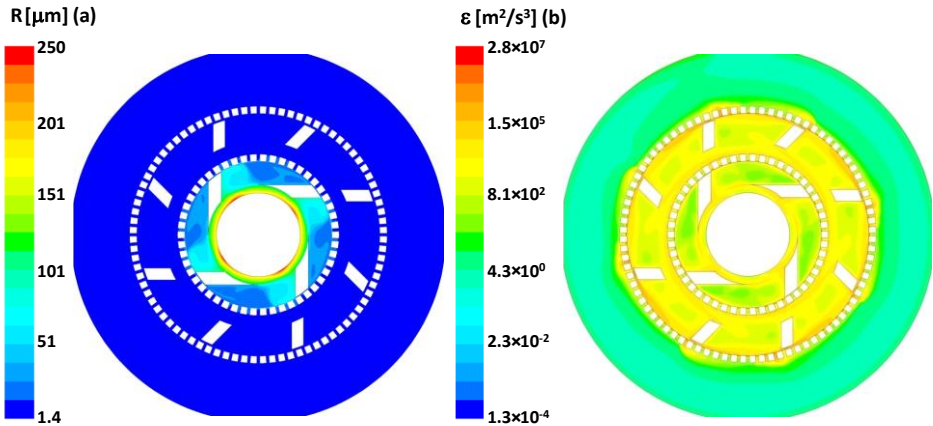
Fig. 3. Distribution of the equivalent radius (a) and the rate of energy dissipation (b) for $\phi_m = 0.8$, $\phi = 0.75$, $\eta_c = 0.91$ mPas, $\eta_d = 9.4$ mPas, $Q = 600$ kg/h, $N = 11000$ rpm

The inner stator screen has six rows of fifty circular holes each with a diameter of $1.59 \cdot 10^{-3}$ m. The inner stator screen of diameter 42.4 mm has six rows of fifty circular holes each with a diameter of $1.59 \cdot 10^{-3}$ m, (1/16 inch) on a 0.100 inch tri pitch. The outer screen, with a diameter of 67.6 mm, has seven rows of eighty circular holes each with a diameter of

$1.59 \cdot 10^{-3}$ m on a 0.100 inch tri pitch. The rotor-stator gap is 0.24 mm. In all calculations the interfacial tension was equal to 10.6 mN/m.

Figures 3 (a) and (b) show that the region of drop breakage is localised in the rotor swept region where the rate of energy dissipation is the highest. Figure 4 shows distribution of the relative viscosity in the mixer. The shear thinning properties of emulsion are very well observed. As presented in Ref. [2], the flow curves characterising the rheology of the emulsion after processing in the rotor-stator mixer under different process conditions depend on the resulting drop size distributions.
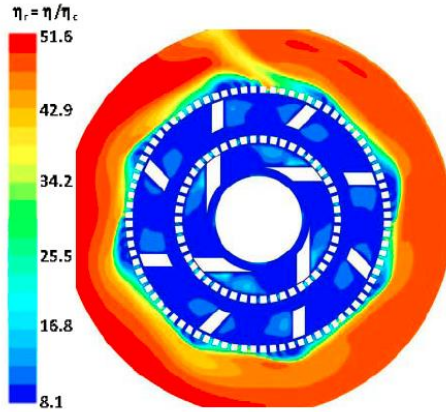
Fig. 4. Distribution of the relative, effective viscosity for $\phi_m = 0.8$, $\phi = 0.75$, $\eta_c = 0.91$ mPas, $\eta_d = 9.4$ mPas, Q = 600 kg/h, N = 3000 rpm

3. Drop deformation and mass transfer in dense emulsion

In the case of shear flow or extensional flow when the external viscous force is smaller than the surface tension force ($N_{Ca} < 10$), the droplets are slightly deformed. According to an analytical solution by Taylor [7], the drop is represented by an elongated sphere that can be approximated by a prolate ellipsoid, as shown schematically in Figure 5. The drop shape is then determined by Equation (10)

$$D_T = \frac{L - B}{L + B} = \frac{19 + 19 \cdot K}{16 \cdot (1 + K)} \cdot N_{Ca} \tag{10}$$

where D_T represents the Taylor shape deformation parameter, whereas L and B are the major and minor axes of the deformed drop, respectively.
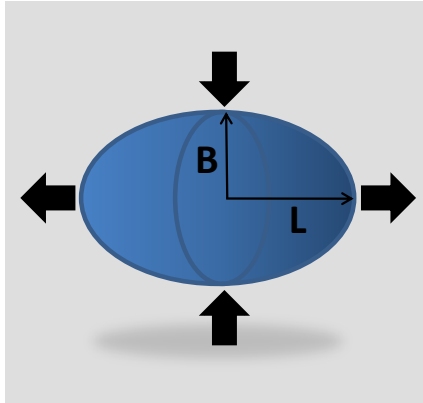
Fig. 5. Schematic of a slightly deformed drop

Combining eq. (10) with two expressions for the drop volume

$$V = \frac{4}{3} \cdot \pi \cdot B^2 \cdot L \qquad (11)$$

$$V = \frac{4}{3} \cdot \pi \cdot R^3 \qquad (12)$$

where R denotes the equivalent radius, one can calculate L and B, and the resulting surface area of the drop. Under the process conditions applied in this work, the drops are only slightly deformed; it can be seen in Figures 6 and 7 that increase of the specific interfacial area due to shear effect is rather small, when compared to spherical particles of the same volume.
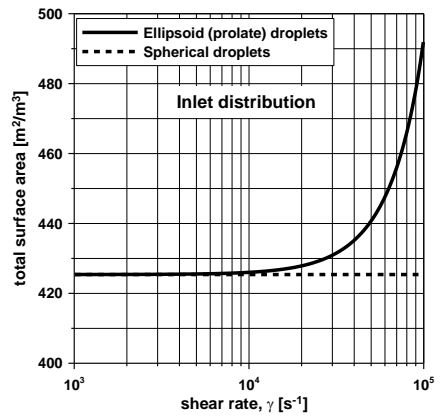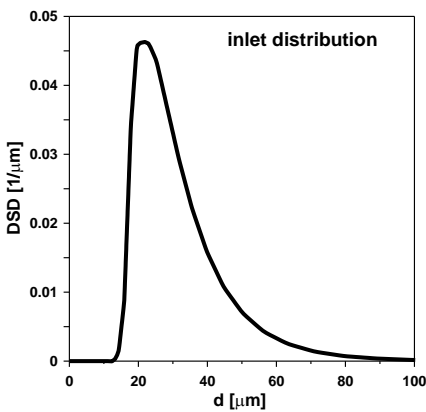
Fig. 6. The drop size distribution (DSD) at the inlet to the mixer (left) and the specific interfacial area of the feed emulsion (right)
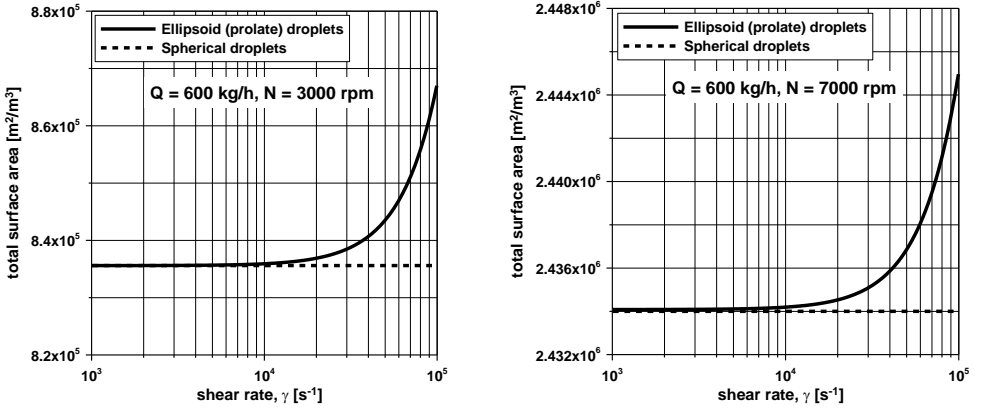
Fig. 7. The specific interfacial area after processing emulsion for $\phi_m = 0.8$, $\phi = 0.75$, $\eta_c = 0.91$ mPas, $\eta_d = 9.4$ mPas, $Q = 600$ kg/h, $N = 3000$ rpm and 7000 rpm, respectively

The effect of drop elongation is also observed during emulsion processing. This is presented in Figure 8.
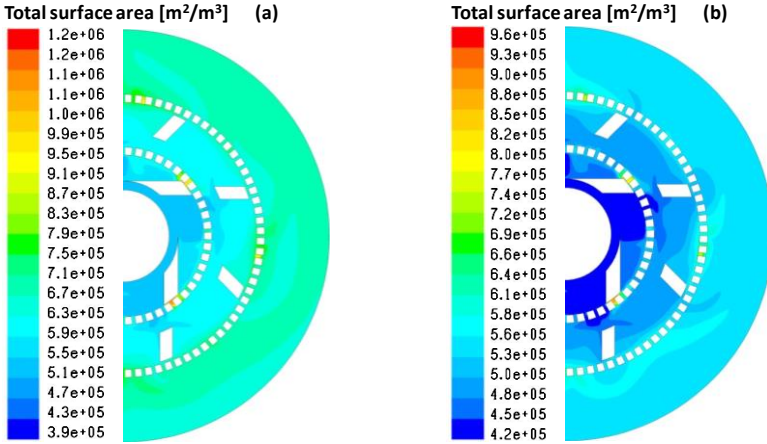
Fig. 8. The specific interfacial area during the process of creating emulsion for $\phi_m = 0.8$, $\phi = 0.75$, $\eta_c = 0.91$ mPas, $\eta_d = 9.4$ mPas, $Q = 600$ kg/h, $N = 1000$ rpm. (a) elongated droplets, (b) neglecting drop deformation

The model for predicting external mass transfer coefficient to or from prolate, ellipsoid drops submerged in an extensional flow was recently proposed by Favelukis and Lavrenteva [8].

$$k_L a_{drop} = 4 \cdot \pi \cdot R \cdot D_i \cdot \sqrt{\frac{3}{2 \cdot \pi \cdot (1+K)}} \cdot \left[1 - \frac{4 \cdot (4 + 31 \cdot K) \cdot Y}{315 \cdot (1+K)} \cdot N_{Ca} \right] \cdot Pe^{1/2} \qquad (13)$$

where $Y = (19 \cdot K + 16)/(16 \cdot K + 16)$ and in this equation, $Pe = \dot{\gamma} \cdot R^2 / D_i$. Equation (13) is valid at steady state, for $t \gg \dot{\gamma}^{-1}$. Hence, Equation (13) represents the asymptotic solution. For $t \to 0$, one has $k_L a_{drop} = 4 \cdot R^2 \cdot \sqrt{\pi \cdot D_i / t}$. For $N_{Ca} = 0$, Equation (13) describes mass transfer to or from spherical drops.

The population of droplets was identified using population balance, and it was possible to recalculate the specific interfacial area, a, from the surface of deformed droplet a_{drop} and calculate the volumetric mass transfer coefficient $k_L a$ in this manner.
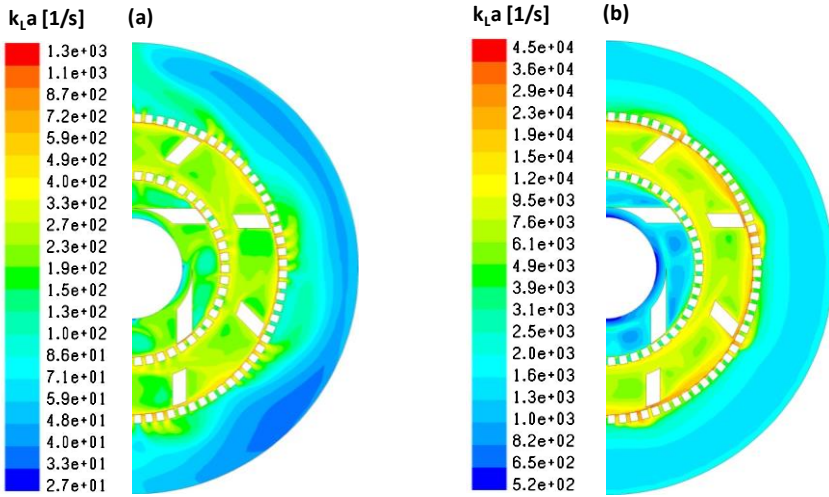
Fig. 9. The volumetric mass transfer coefficient in dense emulsion
for $\phi_m = 0.8$, $\phi = 0.75$, $\eta_c = 0.91$ mPas, $\eta_d = 9.4$ mPas, $Q = 600$ kg/h,
for for $N = 1000$ rpm, (b) for $N = 11000$ rpm

Figure 9 shows that there is very large difference in the mass transfer rate between different regions of the rotor-stator mixer. The presented example shows that the new rheological model can be useful for describing interfacial mass transfer as well as the flow of dense emulsion.

4. Possibility of application of rheological model to micelle dispersion

Bouchoux et al. [9] presented measurements of the rheological properties of casein micelle dispersions. They considered three concentration regimes; in the present paper we are interested in the first of these, where the steady shear viscosities were measured with casein micelle dispersions "that flow, i.e., dispersions that do not behave as solids" [9]. For the interpretation of measured viscosity they applied the Krieger and Dougherty model with characteristic stress calculated from

$$\tau_c = \frac{k_B \cdot T}{b \cdot R \cdot T} \tag{14}$$

where k_B is the Boltzmann constant and the average micelle radius R is equal to 100 nm. Parameter b is used for fitting and takes values of between 1 and 3.5. The rate of shear $\dot\gamma$ from a range 0.1s^{-1} to 1000s^{-1} was used in the experiments. The volume fraction of casein micelles was between 0.044 and 0.739. The application of Equation (14) is based on the assumption that the shear is induced by particle thermal fluctuations. Hence, we start by checking if all experiments are in this regime. To this end, we apply the Péclet number defined as follows:

$$Pe = \frac{\dot\gamma \cdot R^2}{D_B(\phi)} \tag{15}$$

where $D_B(\phi)$ is the coefficient of Brownian diffusion in suspension of volume fraction ϕ.
If Pe exceeds unity, the Brownian motion does not contribute much to viscosity. To calculate Pe, the method of Buyevich and Kabpsov [10] is applied.

$$D_B(\phi) = \frac{D_B^\infty}{\chi(\phi)} \tag{16}$$

$$\varphi(\phi) = \chi cs(\phi) + 1.08 \cdot \frac{(\phi / \phi_m)}{1 - \phi / \phi_m} \tag{17}$$

$$\chi cs(\phi) = \frac{1 - 0.5 \cdot \phi}{(1 - \phi)^3} \tag{18}$$

Figure 10 shows the effects of the shear rate and micelle volume fraction on Pe.
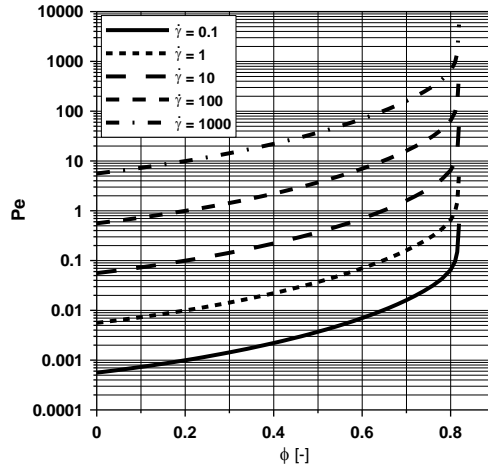
Fig. 10. Effect of micelle volume fraction on Pe, $\phi_m = 0.82$

When Equation (4) is presented in the form

$$F(\phi,\dot{\gamma}) = \frac{\eta_r(\phi,\dot{\gamma})}{\left(1 - \dfrac{\phi}{\phi_m}\right)^{-2.5 \cdot \phi_m}} \tag{19}$$

one can check if there is any non-Brownian regime where the $F(\phi,\dot{\gamma})$ curves collapse. Figure 11 shows that this is the case.
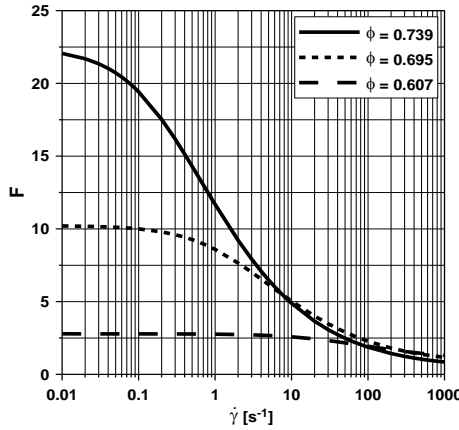
Fig. 11. Effect of shear rate on $F(\phi,\dot{\gamma})$, $\phi_m = 0.82$

Figure 11 shows that both the Brownian and non-Brownian mechanisms should be combined and applied to interpret experimental data properly. This can be done in future by combining the model presented in this work with the model valid for the Brownian regime.

5. Conclusions

In this paper, several new possible applications of the model developed initially to describe rheology of dense emulsions have been presented. These new applications include modelling of the specific interfacial area and the volumetric mass transfer coefficient during the process of emulsion formation and afterwards, during emulsion flow. Another potential application is related to modelling the viscosity of micelle suspensions; the combining of Brownian and non-Brownian mechanisms is proposed for future research.

14

R e f e r e n c e s

[1] Taylor G. I., *The viscosity of a fluid containing small drops of another liquid*. Proc. R. Soc. London, Ser. A, vol. 138, 1932, 41-48.

[2] Bałdyga, J., Jasińska M., Kowalski A. J., *Effect of rheology of dense emulsions on the flow structure in agitated systems.* Chem. Eng. Res. Des. 2015, http://dx.doi.org/10.1016/j.cherd.2015.11.026

[3] Pal R., *Viscous behavior of concentrated emulsions of two immiscible Newtonian fluids with interfacial tension*, Journal of Colloid and Interface Science, vol. 263, 2003, 296-305.

[4] Bałdyga J. and W. Podgórska, *Drop break-up in intermittent turbulence. Maximum stable and transient sizes of drops*, Can. J. Chem. Eng., vol. 76, 1988, 456-470.

[5] Ovarlez G., Rodts, S., Ragouilliaux A., Coussot P., Goyon J., A. Colin A., *Wide-gap Couette flows of dense emulsions: Local concentration measurements, and comparison between macroscopic and local constitutive law measurements through magnetic resonance imaging*. Physical Review E, vol. 78, 2008, 036307

[6] Jasińska, M., Bałdyga, J., Hall, S., Pacek, A.W., *Dispersion of oil droplets in rotor-stator mixers: Experimental investigations and modeling*, Chemical Engineering and Processing, vol. 84, 2014, 45-53.

[7] Taylor, T. D. and A. Acrivos, *On the deformation and drag of a falling viscous drop at low Reynolds number*, J. Fluid Mech. vol. 18, 1964, 466–476.

[8] Favelukis M. and Lavrenteva O. M., *Mass transfer around prolate spheroidal drops in an extensional flow.* The Canadian Journal of Chemical Engineering, vol. 91, 2013, 1190-1199.

[9] Bouchoux A., Debbou B., Gésan-Guiziou G., Famelart M.-H., Doublier J.-L., Cabane B., *Rheology and phase behavior of dense casein micelle dispersions* The Journal of Chemical Physics, vol. 131, 2009, 65106.

[10] Buyevich Yu.A., Kabpsov S.K., *Segregation of fine suspension in channel flow*, J. Non-Newtonian Fluid Mech., vol. 86, 1999, 157-184.

DOMINIKA BOROŃ, JAKUB SZYMAN[*]

A COMPARISON OF HYDRODYNAMIC MODELS OF DIFFERENT HYBRID, FLUIDISED-BED BIOREACTORS

PORÓWNANIE MODELI HYDRODYNAMICZNYCH HYBRYDOWYCH BIOREAKTORÓW FLUIDYZACYJNYCHTY

A b s t r a c t

This is a preliminary study of hybrid fluidised-bed bioreactors considered the hydrodynamic models and their comparison. In this type of bioreactor, there are two characteristic components which determine their work mode. One part of the bioreactor works as a two-phase, gas-liquid, air-lift bioreactor. The second part is a two-phase, liquid-solid, fluidised-bed bioreactor. This type of construction provides high biomass concentration and low shear forces which influence biofilm. Two different types of construction of hybrid fluidised-bed bioreactors were proposed: with external or internal draft tube. Two different mathematical models are needed to design and analyse the operation of these devices.

Keywords: fluidised bed, air lift, hydrodynamics, mathematical modelling

S t r e s z c z e n i e

W artykule przeprowadzono wstępne badania fluidyzacyjnych bioreaktorów hybrydowych. Przedstawiono modele hydrodynamiki hybrydowych bioreaktorów fluidyzacyjnych i porównano je. W takich aparatach występują dwie strefy decydujące o ich warunkach pracy. Jedna z nich pracuje, jako dwufazowy bioreaktor airlift, natomiast druga to dwufazowy bioreaktor fluidyzacyjny ciało stałe - ciecz. Zastosowanie takiego bioreaktora hybrydowego umożliwia osiągnięcie większego stężenia biomasy oraz małych sił ścinających. W literaturze występują dwa typy analizowanych bioreaktorów- z zewnętrzną lub wewnętrzną recyrkulacją cieczy. Do projektowania i analizy warunków pracy obu konstrukcji niezbędne jest stworzenie dwóch oddzielnych modeli matematycznych.

Słowa kluczowe: złoże fluidalne, reaktor air lift, hydrodynamika, modelowanie matematyczne

[*] MSc. Eng. Dominika Boroń, MSc. Eng. Jakub Szyman, Chair of Chemical and Process Engineering, Faculty of Chemical Engineering and Technology, Cracow University of Technology.

1. Introduction

Experimental and theoretic studies about fluidisation have been conducted for years [1-4]. Nevertheless, chemical engineering scientists around the world [5-9] are strongly engaged in the topic. Most of works focuses on the intensification of mass and heat transfer.

Fluidised beds are used also in the engineering of biochemical reactors. Tang and Fan [10], Godia and Sola [11], and Summerfelt [6] presented the advantages of fluidised beds, the main advantages being:

- significantly higher average biomass concentrations can be reached in fluidised beds than in tank reactors;
- average residence time of biomass immobilised as a biofilm, apart from slurry reactors, is not related with the average residence time of a liquid phase;
- intensification of mass transfer between the liquid phase and the biofilm.

Two types of fluidised-bed bioreactors are used: two-phase, liquid-solid and three-phase gas-liquid-solid apparatus. The optimal oxygen level is achieved by oxygen mass transfer from gas bubbles to a liquid phase inside the bioreactor. The oxidation of liquid stream can be also realized by an external oxygenate apparatus. Usage of two-phase, fluidised-bed bioreactors is limited by the amount of oxygen dissolved in the liquid phase. On the other hand, in three-phase fluidised bed bioreactors shear forces affecting the biofilm may damage microorganisms' cells. The point is to construct a piece of apparatus that provides a high level of oxidation in a two-phase, fluidised-bed bioreactor.
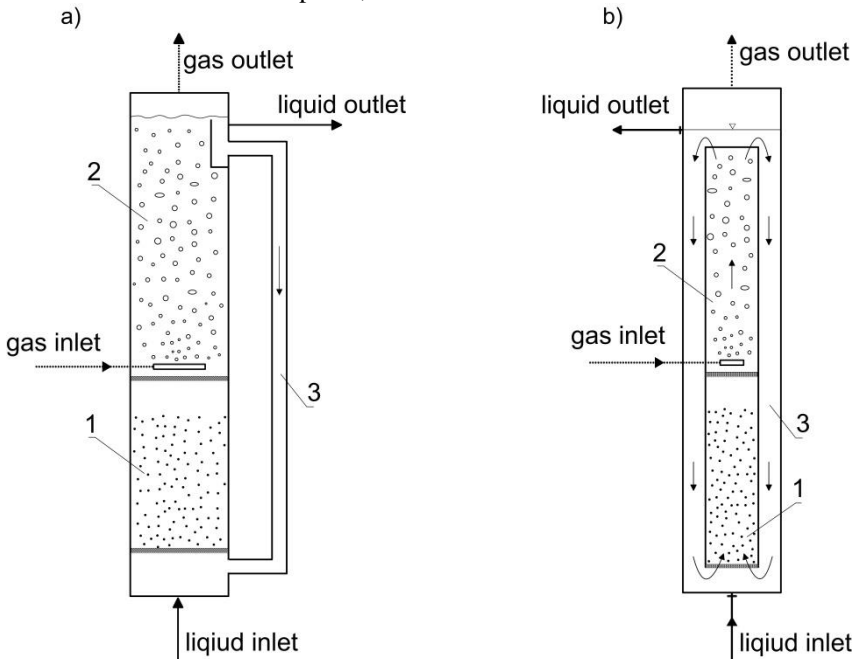
Fig. 1. Scheme of hybrid, fluidised-bed bioreactor: a) with external liquid recirculation, b) with internal liquid recirculation

2. Characteristics of hybrid, fluidised-bed bioreactors

Guo et al. [12] proposed the construction of apparatus in which a two-phase, fluidised-bed bioreactor and an air-lift bioreactor (gas-liquid apparatus) were combined. Such solution is presented in Fig. 1a and is alternatively proposed by Olivieri et al. [13] in Fig. 1b. These pieces of apparatus differ from each other by the method in which recirculation of liquid could be realized.

There are two zones in the main part of the apparatus – a zone with a two-phase, fluidised bed marked as '1' and a zone of barbotage apparatus marked as '2' in which the oxidation of the liquid phase is realised. Due to differences of densities between riser '1' and downcomer zone '3', the liquid circulates in the apparatus in the same manner as in the air-lift bioreactor.

Hybrid, fluidised-bed bioreactors provide an aerobic bioprocess in a two-phase, fluidised-bed bioreactor where drug forces affecting the biofilm are lower than shear forces in three-phase, fluidised-bed bioreactors. Another advantage of hybrid, fluidised-bed bioreactors is higher level of biomass concentration then in two-phase airlift bioreactors. Moreover, in this case energy is not consumed by liquid circulation pump.

3. Mathematical model of hydrodynamics

The mathematical modelling of innovative and not widely used reactor may qualify it to use in industry. The numerical calculations are needed to determine proper geometrical parameters of apparatus and process parameters characteristics. The comparison of mathematical model of hybrid, fluidised-bed bioreactor with internal and external circulation of liquid is important to choose the better construction, when we consider only the hydrodynamics of those bioreactors.

Optimal geometrical dimensions of apparatus may be obtained by mathematical modelling, simulating its operation. The work of the hybrid, fluidised-bed bioreactor can be characterised by the following values:
- velocity of liquid (u_{0ci}) and gas (u_{gi}) in each zone of the apparatus
- gas hold-up in each zone of the apparatus (ε_i)
- dynamic height of the fluidised-bed (H_f).

In order to estimate these parameters, the model of hydrodynamics has to be defined. Balancing of pressure drops during media flow through the bioreactor can be used to do it. The driving force of liquid circulation corresponds to density differences of the binary phase mixture between air-lift zone '2' and downcomer zone '3' and it can be obtained by:

$$\Delta p = H_r \cdot \varepsilon_2 \cdot \rho_c \cdot g \tag{1}$$

where

H_r – height of barbotage zone in meters;
ε_2 – gas hold-up in barbotage zone '2';
ρ_c – liquid density, kg·m^{-3};
g – gravitational acceleration, m·s^{-2}.

3.1. The mathematical model of hybrid, fluidised-bed bioreactor hydrodynamics with an internal pipe

Formation of the mathematical model for such device (Fig. 1b) may be realised by balancing the driving force with following pressure drops:

a) hydrodynamic resistances in zones '1', '2' and '3'

$$\Delta p_1 = 0,5 \cdot \lambda_1 \cdot \frac{H - H_r}{d_1} \cdot u_{c1}^2 \cdot \rho_c \qquad (2)$$

$$\Delta p_2 = 0,5 \cdot \lambda_2 \cdot \frac{H_r}{d_2} \cdot u_{c2}^2 \cdot \rho_c \qquad (3)$$

$$\Delta p_3 = 0,5 \cdot \lambda_3 \cdot \frac{H}{d_h} \cdot u_{c3}^2 \cdot \rho_c \qquad d_h = d_3 - d_2 \qquad (4)$$

where
   λ_i – coefficient of axial hydrodynamic resistances for zone i, $i = 1, 2, 3$;
   H – overall bioreactor height in meters;
   d_i – the zone i diameter, $i = 1, 2, 3$ in meters;
   u_{ci} – liquid velocity in zone i, $i = 1, 2, 3$ m·s^{-1}.

b) pressure drop on a fluidised bed:

$$\Delta p_f = H_{mf} \cdot (\rho_s - \rho_c) \cdot (1 - \varepsilon_{mf}) \cdot g \qquad (5)$$

where
   H_{mf} – height of fluidised bed refers to minimum fluidisation conditions in meters;
   ε_{mf} – fluidised-bed porosity refers to minimum fluidisation conditions;
   ρ_s – density of fluidised material, kg·m^{-3}.

c) pressure drop in the surroundings of the lower edge of the draft tube:

$$\Delta p_b = 0,5 \cdot \zeta_b \cdot u_{c3}^2 \cdot \rho_c \qquad (6)$$

where
   ζ_b – hydrodynamic resistance coefficient in the surroundings of the lower edge of the draft tube.

d) pressure drop onto two supporting nets,

$$\Delta p_s = \zeta_s \cdot u_{c1}^2 \cdot \rho_c \qquad (7)$$

where

ζ_s – hydraulic resistance coefficient of the net.

The pressure-drop balance from equations (1-7) may be presented as:

$$\Delta p = \sum_{i=1}^{3} \Delta p_i + \Delta p_f + \Delta p_b + \Delta p_s \tag{8}$$

Obtaining these quantities is possible when to equation (8) mass balances of gas and liquid will be added:

$$S_2 \cdot \varepsilon_2 \cdot (u_{c2} + \upsilon) = S_2 \cdot u_{0g} \tag{9}$$

$$S_2 \cdot (1 - \varepsilon_2) \cdot u_{c2} = S_3 \cdot u_{c3} + S_2 \cdot u_{0c} \tag{10}$$

where

S_i – vertical superficial of zone i, $i = 1, 2, 3$ m^2;

υ – slip velocity of gas bubbles, m·s^{-1};

u_{0g} – velocity of gas referring to the cross-sectional area of zone '1', m·s^{-1}.

In a steady state, velocities of liquid in zones '1' and '2' are tied up by continuity equation:

$$S_1 \cdot u_{0c1} = S_2 \cdot u_{c2} \cdot (1 - \varepsilon_2) \tag{11}$$

where

u_{0ci} – liquid velocity referring to cross sectional area of zone i, $i = 1, 2, 3$ m·s^{-1}.

After fusion of equations (8-11) a model is stated as a function of two variables: gas hold-up in zone '2' and liquid velocity in zone '2':

$$\varepsilon_2 \cdot u_{g2} - u_{0g} = f_1(\varepsilon_2, u_{c2}) = 0 \tag{12a}$$

$$\Delta p - \sum_{i=1}^{3} \Delta p_i + \Delta p_f + \Delta p_b + \Delta p_s = f_2(\varepsilon_2, u_{c2}) = 0 \tag{12b}$$

To solve the system of equations (12a and 12b), the Newton method may be applied. In the literature exists the other approach to calculation of pressure drop balance [13]; the same results from presented here mathematical models in a different way were obtained by Olivieri et al. [13].

3.2. Mathematical model of hydrodynamics of hybrid, fluidised-bed bioreactor with external recirculation pipe

In the case shown in Fig. 1a, the driving force is defined in the same way as in hybrid, fluidised-bed bioreactors with an internal draft tube (1). The model in such an example is obtained by balancing the following pressure drops:

a) hydrodynamic resistances in all zones of bioreactor:

$$\Delta p_1 = 0.5 \cdot \lambda_1 \cdot \frac{H - H_r}{d_1} \cdot u_{c1}^2 \cdot \rho_c \tag{13}$$

$$\Delta p_2 = 0.5 \cdot \lambda_2 \cdot \frac{H_r}{d_2} \cdot u_{c2}^2 \cdot \rho_c \tag{14}$$

$$\Delta p_3 = 0.5 \cdot \lambda_3 \cdot \frac{H}{d_3} \cdot u_{c3}^2 \cdot \rho_c \tag{15}$$

b) the pressure drop on the fluidised bed:

$$\Delta p_f = H_{mf} \cdot (\rho_s - \rho_c) \cdot (1 - \varepsilon_{mf}) \cdot g \tag{16}$$

c) the pressure drop on the bottom and upper nets in the fluidisation zone:

$$\Delta p_s = \zeta_s \cdot u_{c1}^2 \cdot \rho_c \tag{17}$$

d) the pressure drop in the inlet of the external draft tube:

$$\Delta p_{m1} = 0{,}5 \cdot \xi_1 \cdot u_{c3}^2 \cdot \rho_c \tag{18}$$

where
ξ_1 – local friction coefficient in the inlet of the external draft tube.

e) the pressure drop in the outlet of the external pipe:

$$\Delta p_{m2} = 0.5 \cdot \xi_2 \cdot u_{c3}^2 \cdot \rho_c \tag{19}$$

where
ξ_2 – local friction coefficient in the outlet of the external draft tube.
f) the pressure drops on two nodes of the external draft tube

$$\Delta p_{m3} = \xi_3 \cdot u_{c3}^2 \cdot \rho_c \tag{20}$$

where
ξ_3 – local friction coefficient on the node of the external pipe.
The balance of the pressure drops is given by:

$$\Delta p = \sum_{i=1}^{3} \Delta p_i + \Delta p_f + \Delta p_s + \sum_{i=1}^{3} \Delta p_{mi} \tag{21}$$

Equation (21) differs with equation (8) because of different friction coefficients and the pressure drop in zone '3'. Equations (9-11), which are also valid for this case were matched with the model (21). Obtained in that way model is presented in eq. (22).

$$\varepsilon_2 \cdot u_{g2} - u_{0g} = f_1(\varepsilon_2, u_{c2}) = 0 \tag{22a}$$

$$\Delta p - \sum_{i=1}^{3} \Delta p_i + \Delta p_f + \Delta p_b + \Delta p_s + \sum_{i=1}^{3} \Delta p_{mi} = f_2(\varepsilon_2, u_{c2}) = 0 \tag{22b}$$

To solve model (22), Newton's method may be applied.

4. Hydrodynamic restrictions

The operation characterization of hybrid bioreactors is schematically presented in Fig.1. depends on behavior of granular biomass medium in zone "1". There are three kinds of fluidised bed behaviour depending upon the liquid velocity in the given zone – a stationary bed lies on the bottom site (if the velocity of liquid is lower than minimum fluidization velocity u_{mf}) ; immobilised on the top of the zone bed (if the velocity of the liquid is at least equal to terminal velocity u_t), and a fluidised bed (if the velocity is between the presented values). When fluidisation occurs, the dynamic height of the fluidised bed increases with increases in velocity and it corresponds to the functioning of the bioreactor. It can be noted that in both cases, two boundary velocities have to be obtained and that the work area of apparatus could be described.

The porosity of the fluidised bed also changes when the velocity of liquid increases and of course, the dynamic height of the fluidised bed in zone '1' is limited by the geometric height of the zone so that additionally, the velocity of fluidisation can comply with the following relationship:

$$u_{0c1} : H_f < H - H_r \tag{23}$$

The above relationship means that the fluidised bed may only expand at the moment when all of zone '1' is completely filled by the fluidised grains. After crossing presented in equation (23) limitation, the fluidised material will be assembling under the top site of fluidization zone. In that case the liquid flow through the porosity stationary bed and it can lead to overgrowth the bed by biomass.
Inequality (24) prevents the chance of gas bubbles being present in the fluidization zone. Limitation (24) may prevent it.

$$u_{c3} = u_{0c3} < \upsilon \tag{24}$$

When the bioreactor is equipped with the external recirculating pipe, this situation cannot occur, so restriction (24) is not needed.

Characterisation of operation regimes of hybrid fluidised bed bioreactors indicate, that liquid and gas flow in the apparatus have to be limited for both gas and liquid to provide its correct operation. These restrictions are related with specificity of fluidisation process.

5. Hydrodynamic characterisation of hybrid, fluidised-bed bioreactors

In this part of the paper, solutions of model will be presented. Calculations were performed for both hybrid, fluidised bed bioreactors with internal and external draft tubes. Technical specifications of the apparatus is presented in Table 1. The values of the other parameters were the same in all analyzed cases. The grain diameters are equal to $7 \cdot 10^{-4}$ m, the density of solid $\rho_s = 1800$ kg·m^{-3}, the fluidised-bed porosity refers to minimum fluidisation conditions $\varepsilon_{mf} = 0.5$, the density of liquid $\rho_c = 1000$ kg·m^{-3} and the viscosity of liquid $\eta_c = 0.001$ kg·m^{-1}·s^{-1}.

Table 1

Technical specifications of hybrid, fluidised-bed bioreactors with external and internal draft tubes (all measurements are in meters)

	Bioreactor with external draft tube	Bioreactor with internal draft tube
Overall height of apparatus	3	3
Height of barbotage zone '2'	1.5	1.5
Zone '1' diameter	0.3	0.3
Zone '2' diameter	0.3	0.3
Zone '3' diameter	0.4	0.05
Diameter of grains of fluidised material	$1.5 \cdot 10^{-3}$	$1.5 \cdot 10^{-3}$
Height of stationary bed of grains	0.03	0.03

Aerobic microbiological processes may occur in these items of apparatus. As has been noticed before, it is important to provide optimal oxygen concentration in the reacting medium. The change of gas velocity has an influence upon the hydrodynamic parameters in all bioreactor zones – for that reason, this value should be studied.
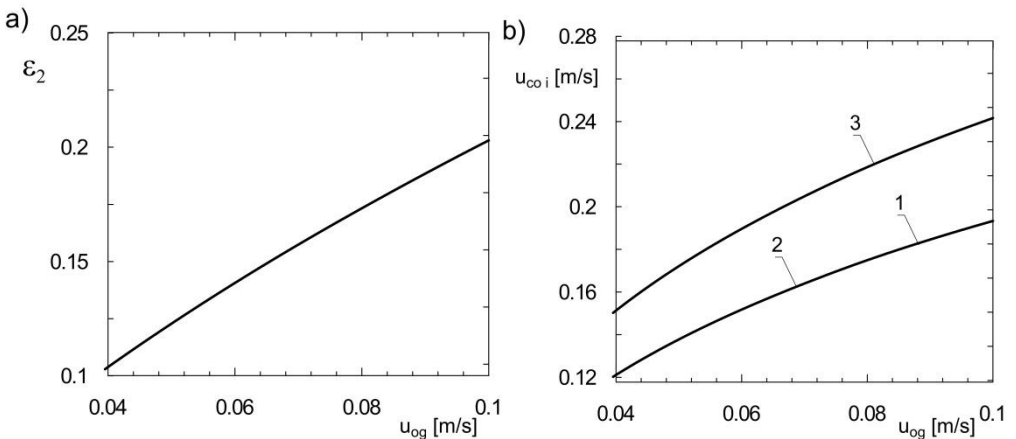
Fig. 2. Relationships of a) gas hold-up in zone '2' and b) apparent liquid velocities in all zones of bioreactor from the velocity of gas delivered to hybrid, fluidised-bed bioreactor with internal draft tube

In Fig. 2, the relationship between gas hold-up in barbotage zone '2' and the apparent liquid velocity in all zones was presented. These results let to account operation parameters for hybrid fluidised-bed bioreactor with internal draft tube instead of velocity of delivered gas. From Fig. 2a, it could be interpreted that increases of gas velocity cause gas hold-up increase in zone '2'. Due to a larger gas phase, oxygen transfer from gas to liquid phase is intensified and, as a consequence, the oxygenation of the microbiological environment increases. Moreover, increasing the gas hold-up causes a change of driving force, as is signified in Equation (1). Increased velocities of the liquid phase in all zones of the bioreactor can be observed (Fig. 2b). Due to the diameters of zones '1' and '2' being the apparent velocities of liquid in these zones also have the same values. Change of liquid velocity in the fluidisation zone increases the expansion of the fluidised bed. In case of significant gas distribution increase in the hybrid fluidized bed bioreactor, may it causes fluidized material assemblage under the upper site and additionally bubbles can flow to that zone. For that reason, hydrodynamic parameters should still be under control, using conditions (23, 24).

The simulation results for the hybrid, fluidised-bed bioreactor with external recirculation pipe are presented in Fig. 3. Due to the analyses, it can be observed that there is a strong similarity of hydrodynamic process parameters in both devices. In this case, a higher rate of gas flow can be achieved due to no possibility of gas bubbles flowing to zone '3'. It effects in increasing the oxidation level without significant change of work conditions.
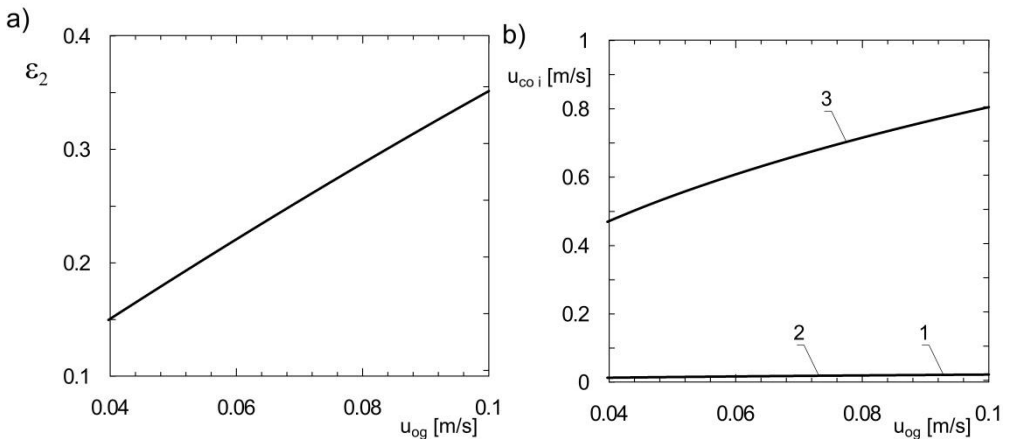
Fig. 3. Relation a) gas hold-up in zone "2" and b) apparent liquid velocities in all zones of apparatus with velocity of delivered gas for hybrid fluidized bed bioreactor with external draft tube

6. Summary

In this paper, mathematical models of two cases of hydrodynamic, hybrid, fluidised-bed bioreactors were presented. The rules of modelling such devices are similar. For each device, the mathematical model is stated by a system of two nonlinear equations. These two

equations have to be completed by correspond system of hydrodynamic conditions. The difference between models is realised within condition, presented in equation (23). In the bioreactor with an external recirculation pipe, there is no risk of bubbles transferring into the fluidisation zone and that is the main advantage of such a solution.

Obtained models can be used to numerical simulation of hydrodynamics of analysed reactors. As is shown, hydrodynamics parameters of different items of apparatus are qualitatively the same – differences between results are caused by the geometric dimensions of devices.

R e f e r e n c e s

[1] Kunii D., Levenspiel O., *Fluidization Engineering,* Boston-Wellington, Butterworh-Heinemann 1991.
[2] Chiba S., Chiba T., Nienow A.W., Kobayashi H., *The minimum fluidisation velocity, bed expansion and pressure-drop profile of binary particle mixtures*, Powder Technology, vol. 22, 1979, 255-269.
[3] Pinchbeck P.H., Popper F*., Critical and terminal velocities in fluidization,* Chemical Engineering Science, vol. 6, 1956, 57-64.
[4] De Jong J.A.H., Nomden J.F., *Homogeneous gas-solid fluidization*, Powder Technology, vol. 9, 1974, 91-97.
[5] Schügerl K., *Three-phase-biofluidization-Application of three-phase fluidization in the biotechnology-A review,* Chemical Engineering Science, vol. 52, 1997, 3661-3668.
[6] Summerfelt S.T., *Design and management of conventional fluidized-sand biofilters,* Aquacultural Engineering, vol. 34, 2006, 275-302.
[7] Onysko K.A., Robinson C.W., Budman H.M., *Improved modelling of the unsteady-state behaviour of an immobilized-cell, fluidized-bed bioreactor for phenol biodegradation,* The Canadian Journal of Chemical Engineering, vol. 80, 2002, 239-252.
[8] Englart S., Kmieć A., Ludwińska A., *Teoria i technika fluidyzacji*, Oficyna Wydaw. Politech. Wrocławskiej, Wrocław 2007.
[9] Kmieć A., *Zastosowanie i modelowanie procesów i aparatów ze złożem fluidalnym*, Oficyna Wydaw. Politech. Wrocławskiej, Wrocław 2012.
[10] Tang W.-T., Fan L.-S., *Steady state phenol degradation in a draft-tube, gas-liquid-solid fluidized-bed bioreactor*, AIChE Journal, vol. 33, 1987, 239-249.
[11] Gòdia F., Solà C., *Fluidized-Bed Bioreactors,* Biotechnology Progress, vol. 11, 1995, 479-497.
[12] Guo Y.X., Rathor M.N., Ti H.C., *Hydrodynamics and mass transfer studies in a novel external-loop airlift reactor*, Chemical Engineering Journal, vol. 67, 1997, 205-214.
[13] Olivieri G., Marzocchella A., Salatino P., *A novel three-phase airlift reactor without circulation of solids*, The Canadian Journal of Chemical Engineering, vol. 88, 2010, 574-578.

LUTZ BÖHM, MARKUS KOLANO, MATTHIAS KRAUME[*]

SIMULATION OF THE SINGLE BUBBLE ASCENT WITH OPENFOAM

SYMULACJA WZNOSZENIA POJEDYNCZEGO PĘCHERZA ZA POMOCĄ PROGRAMU OPENFOAM

A b s t r a c t

This project is motivated by the challenge of cleaning flat sheet membrane surfaces with the help of aeration. On the basis of earlier experiments and CFD simulations, a decision was made to use the CFD-tool OpenFOAM in contrast to earlier simulations which were performed with Ansys Fluent. In the new simulations, the advancing computing power allowed the simulation of a bubble ascent in the full channel which is of special interest in cases where the bubble size is smaller than the channel depths. Besides saving the licensing cost, OpenFOAM allows access to the source code and, therefore, easier implementation of sub-models if necessary.

Keywords: computational fluid dynamics, OpenFOAM, bubble

S t r e s z c z e n i e

W pracy podjęto próbę poprawy możliwości czyszczenia płaskich powierzchni membrany za pomocą napowietrzania. Na podstawie wcześniejszych eksperymentów (z wykorzystaniem ANSYS Fluent) podjęto decyzję wykorzystania programu OpenFOAM – jednego z narzędzi CFD. W nowych symulacjach wzrost mocy obliczeniowej umożliwił symulację wznoszenia pęcherzyka w pełnym kanale. Oprócz oszczędności kosztów licencji, OpenFOAM umożliwia dostęp do kodów źródłowych, a więc łatwiejsze wdrażanie modeli podrzędnych.

Słowa kluczowe: CFD, OpenFOAM, pęcherz

[*] DSc. Eng. Lutz Böhm, MSc. Eng. Markus Kolano, Prof. PhD. DSc. Eng. Matthias Kraume, Chair of Chemical and Process Engineering, Faculty of Process Sciences, Technical University of Berlin.

1. Introduction

The investigation of the ascent of a bubble in a quiescent liquid is a common topic in literature. It has been extensively discussed for Newtonian [1] and non-Newtonian liquids [2] as the continuous phase. In the frame of this project, the focus was specifically on cases motivated by the process of membrane filtration in flat-sheet membrane modules. In this case, narrow channels between the flat-sheet membranes with a rectangular cross-section (width >> depth; here: width: 160 mm and depth: 3÷7 mm; height: 1500 mm) which are filled with activated sludge (if used for waste water treatment) can be found. Due to the filtration process, a layer of deposits develops over time on the surface of the membrane. The thickness of the layer of deposits, which is proportional to the resistance of the filtration, can be controlled by inducing flows in the channel. One common method to induce this flow is aeration. Therefore, breaking it down to the basics, a bubbly flow in a channel with a rectangular cross-section with a non-Newtonian, co-current flowing continuous phase (activated sludge) is apparent in this process.

The aeration which controls the growth of the layer of deposits is doing so by inducing shear on the membrane surface through the liquid. No model is yet known that more or less accurately correlates the aeration rate and the induced shear or reduction of the layer of deposits This is also partly due to the fact that the even more simple system of one bubble rising in a narrow channel with a rectangular cross-section has not yet been sufficiently investigated. Based on this lack of knowledge, in the recent past, this project experiment-tally investigated this basic system [3]. The following parameters were varied: channel depth (d_c, 3÷7 mm); bubble size (d_B, 3÷9 mm equivalent bubble diameter); superimposed liquid velocity (v_L, 0÷0.2 m/s); rheology of the continuous phase (Newtonian, non-Newtonian). High speed camera imaging, particle image velocimetry and electro-diffusion methods were applied as measurement techniques. This allows the analysis of the bubble behaviour [4, 5], the effect of the bubble on the surrounding liquid [6], and the local wall shear stress resulting from the liquid flow induced by the bubble ascent [7]. The last mentioned property, the local wall shear stress, is of especially high interest. Unfortunately, it is very demanding to actually measure this property. Only a few wall shear stress measurement techniques are available, but all of them have their shortcomings. Therefore, a CFD approach was chosen here to get a deeper insight into the influence of the ascent of a bubble on the resulting local wall shear stress. As is partially discussed in Prieske et al. [8], the idea of a numerical approach for this specific system is something that has already been realised by using Ansys Fluent. Mainly due to simulation capacity limitations, whilst this model was a good first approach, it also had its shortcomings. The most significant drawback was that only half of the channel depth was implemented in the grid used for the simulation. The measure to halve the cell number and, therefore, reducing the calculation time was chosen as no enhanced movement of the bubble was expected. Here, it has to be kept in mind that in most of the investigated cases, the bubble was squeezed into the channel as its equivalent bubble diameter was equal to or larger than the channel depth. Especially for cases with a bubble size smaller than the channel depth, this did not apply and, therefore, bubble movement normal to walls would be possible but is suppressed by the model.

These simulations were all performed in water. Basically, it would be possible to calculate a non-Newtonian case, as well. This would have increased the calculation demand

significantly. Additionally, in the case of this commercial CFD tool, the implementation of this model is, up to a degree, a black box.

Based on the evolution of this project and increasing computational power in general, a new approach has been formulated which, at this point, has a large experimental database in the background for the purposes of validation and is able to overcome the shortcomings of prior simulations, including simulations from other groups in this field. The requirements for the new simulations were:

- transient, full 3D model to resolve the complex three-dimensional deformation and movement of the bubble during its ascent;
- sufficient resolution of the rising event, especially near the wall, as the wall shear stress induced by the bubble is of particular interest;
- adequate rising length/duration to reach the steady or stable periodic movement (from experience: more than one second of rising time)
- implementation of suitable non-Newtonian characteristic describing the behaviour of activated sludge after validation of the case with a Newtonian continuous phase.

In this project, OpenFOAM was used for the CFD simulations. As a free, open source program, it allows access to and, if necessary, adjustments to the source code. There are basically, no limitations to cell numbers or multithreading as often the case for commercial programs in the past.

2. Materials and Methods

OpenFOAM 2.0 was used for the simulation of the single bubble ascent. As the surface of the bubble was supposed to be resolved, a volume of fluid method was used as the multiphase model, implemented here with the help of interFoam. Due to the fact that in most cases of interest, the bubble ascent is a stable periodic movement (here: bubble size $d_B = 3$, 5 and 7 mm), a transient calculation had to be conducted. The grid used for the calculation (according to the experimental setup described, for example, in [5]), was 200 by 160 and 3 mm, 5 mm or 7 mm in height, width and depth (only the results for $d_c = 3$ mm are shown here) with a total number of approx. 500,000 cells. As is known from experience, it takes roughly one second from the beginning of the ascent until periodic movement of the bubble, 200 mm would not be sufficient as potential rising path. To minimise the calculation time, another approach was chosen here. The bubble was initialised 40 mm from the top of the grid.

Once the bubble moved one cell layer upwards, the lowest cell layer of the grid was deleted and a new cell layer was added at the top of the grid. Hence, the bubble was again in the same position as it was initially, relative to the top of the grid.

The OpenFOAM results shown here were, consequently, found for one channel depth of $d_c = 3$ mm and three bubble sizes $d_B = 3$ mm, 5 mm and 7 mm calculated in water without superimposed liquid velocity. The post-processing was performed with a Matlab code extracting all data of interest, e.g. the centroid of the bubble. In all cases, a rising duration of two seconds was simulated. As mentioned earlier, it takes roughly one second to gain a stable movement – this part was ignored for the analysis. The OpenFOAM data is mainly

compared to results published in [5] for the same bubble sizes but a channel depth of $d_c = 5$ mm and 7 mm as comparable experiments were not performed in smaller channels.
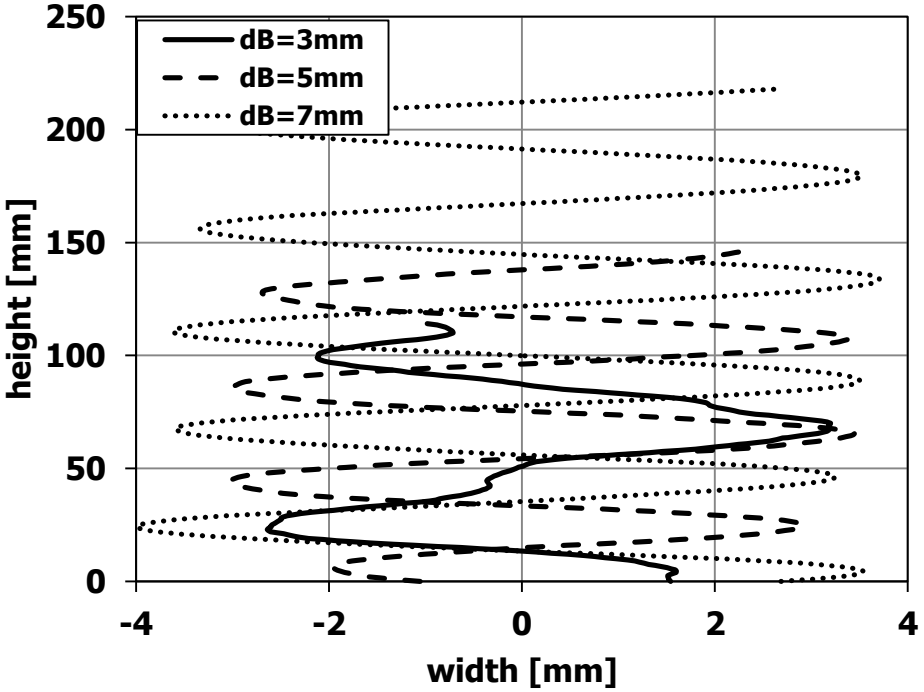
Fig. 1. Rising paths of three differently sized bubbles for a rising duration of 1 second each in a channel with a depth of $d_c = 3$ mm (from OpenFOAM simulation)

3. Results and Discussions

Figure 1 shows the rising path found with OpenFOAM for the three different bubble sizes. Illustrated is the position of the centroid with regard to both width and height. This illustration leads to three different ending points with regard to height for the three bubble sizes as all three of them have a different velocity.

While the movement of the smallest bubble seems slightly irregular, the other two bubble sizes show very smooth rising behaviour. Based on experience in confined geometries and, for example, Clift et al. [1] for free rising bubbles, a bubble with an equivalent diameter of $d_B = 3$ mm can perform several types of movements during its ascent, such as a straight, zigzag or helical movement. Due to the geometry, helical rising behaviour is not possible here. In the given case, this restriction leads to the zigzag

movement. Qualitatively, the movements of all the bubble sizes look pretty comparable when it comes to, for example, the amplitude of the oscillation during its ascent. Based on experience with a larger channel depth [5], this is rather surprising.
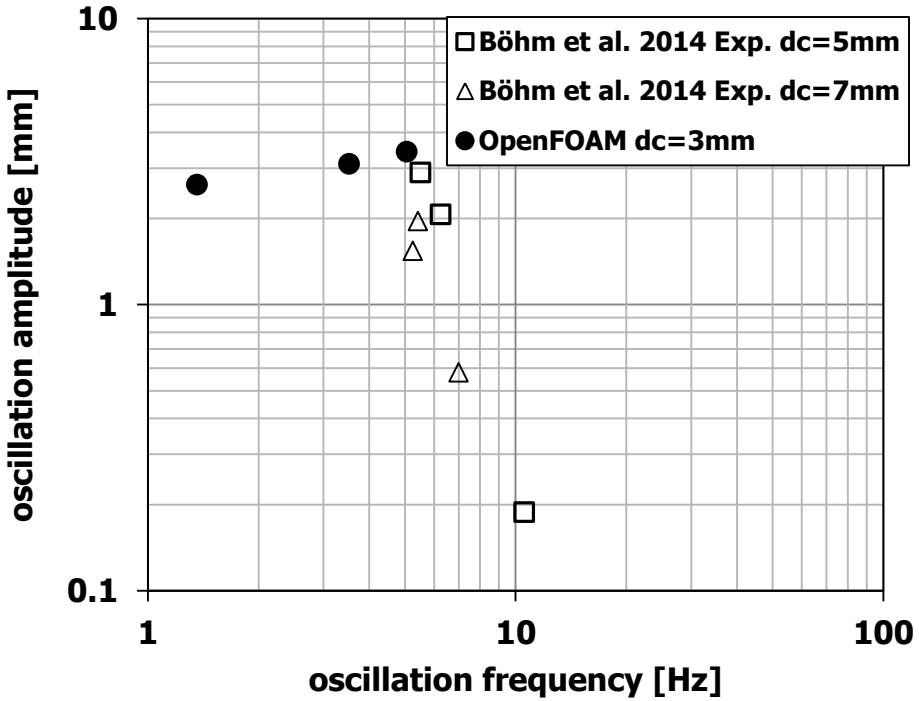
Fig. 2. Oscillation amplitude over oscillation frequency in a confining rectangular geometry with channel depths of d_c =5 mm and 7 mm (experimental data, [5]) and for a channel depth of d_c = 3 mm (OpenFOAM)

Figure 2 shows both, the quantitative results of the oscillation frequency and amplitude from the earlier experiments as well as the according results from the OpenFOAM simulation. The results found in the experiments in the larger channels tend to have a lower fluctuation in frequency and a broader range with regard to amplitude (with higher frequencies and lower amplitudes for smaller bubbles and vice versa for larger bubbles). On the other hand, in the simulation with the smaller channel depth, the results are contrary to those obtained with larger channels. The amplitudes are almost independent of the bubble size, but the frequency of the oscillation increases with the bubble size.

At this point, it is not clear if this differing behaviour is an effect of the channel depth or the simulation. One explanation could be that it is a result of the enhanced confinement in the 3 mm channel which leads to a stronger deformation of the bubble, which is the case for the smallest bubble size in particular. Figure 3 shows the ratio of the vertical and horizontal dimension of the bubble. Generally, the simulation and experimental results follow the

trend that the ratio decreases with increasing bubble size, simply due to the enhanced confinement. Still, in case of the 3 mm bubble, the deformation is most enhanced for the smallest channel depth with a ratio below 0.8. This kind of deformation has an unavoidable effect on the bubble rising behaviour. Regarding the experimental data of the 3 mm bubble, it is worth mentioning, that due to experimental circumstances, the analysed high frequencies and low amplitudes mean that there is almost no oscillation at all. As mentioned earlier, in unconfined geometries, the 3 mm bubble is known to potentially behave in several ways. In the performed experiments, obviously straight movement appeared predominantly; however, from observations it can be stated that in some cases, the zigzag movement started in the analysed field of view or even earlier. This stochastic characteristic cannot be simulated properly, as the term 'stochastic' actually means in this case 'under unknown conditions'. This means that there might be the possibility to set an initial condition for a simulation that leads to a straight movement of the bubble.
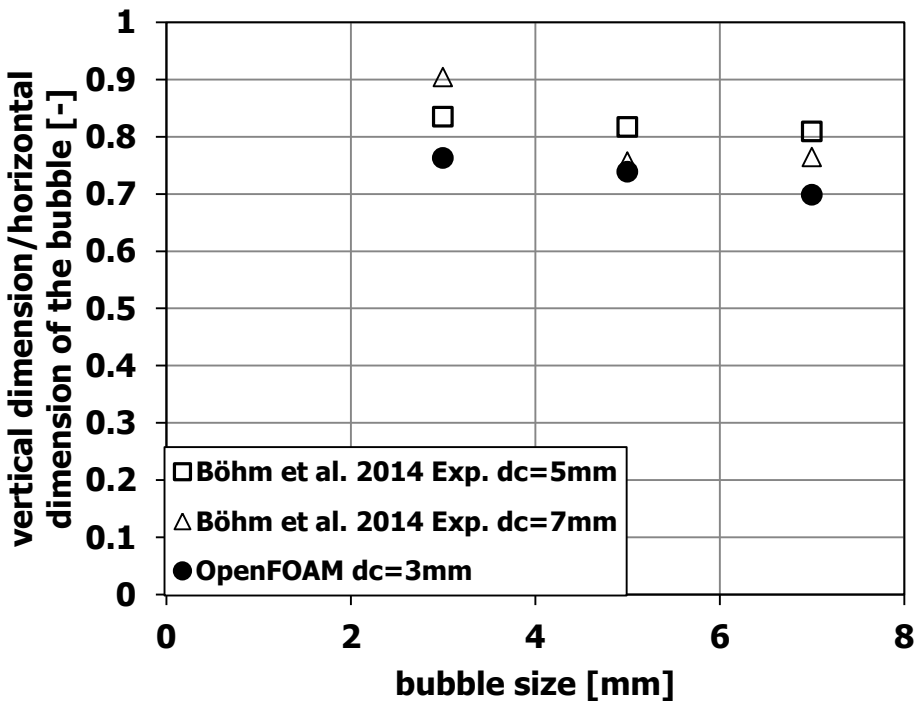
Fig. 3. Ratio of the horizontal and vertical dimension of the bubble over the bubble size in a confining rectangular geometry with channel depths of d_c = 5 mm and 7 mm (experimental data, [5]) and for a channel depth of d_c = 3 mm (OpenFOAM)
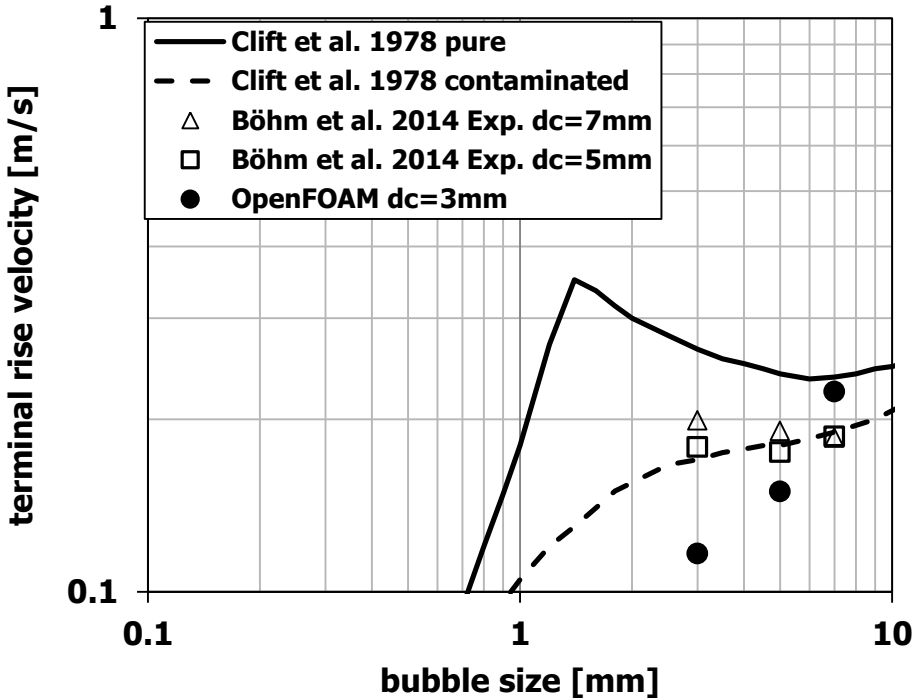
Fig. 4. Terminal rise velocity for free rising bubbles in pure and contaminated water (experimental data, [1]), in a confining rectangular geometry with channel depths of d_c = 5 mm and 7 mm (experimental data, [5]) and for a channel depth of d_c = 3 mm (OpenFOAM)

The effect of the deformation is also strongly visible in the trend of the terminal rise velocity of the bubble (Fig. 4). The experimental results are in agreement with the data found for free rising bubbles in contaminated water. Contamination results in a non-moving bubble surface which leads to a movement equal to that of a solid particle. Hence, although the experiments in [5] were performed in pure water, the confinement leads to a deceleration of the bubble. This behaviour is basically the same in the simulation results in the 3 mm channel while the deceleration is much more enhanced for the smaller bubbles. It is clear that a 3 mm bubble is much stronger influenced by the confining walls in a 3 mm channel than in a 5 mm or 7 mm channel. For the 3 mm and the 5 mm bubble, it is visible that the larger the channel depth, the higher the terminal rise velocity. Only in case of the 7mm bubble is the simulation value higher than in the experiments.

4. Conclusions

A simulation of the single bubble ascent in a confining rectangular geometry was performed with OpenFOAM. The developed model proved to be able to reproduce the

oscillating movement during the bubble ascent, as it was also found in earlier experiments. The results shown here were simulated in a first channel depth that was not extensively tested in the experimental test phase. The several discussed effects on the oscillation parameters, the deformation and the terminal rise velocity cannot finally be attributed to be an effect of the enhanced confinement in the 3 mm channel (although potential explanations are given). These might also be an impulse for further model improvements. However, the developed model allows an extension to test cases with superimposed liquid velocities as well as cases with a non-Newtonian rheology of the continuous phase.

R e f e r e n c e s

[1] Clift R.J., Grace J.M., Weber M., *Bubbles, drops and particles*, Academic Press New York 1978.

[2] Chhabra R., *Bubbles, drops, and particles in non-Newtonian fluids*, CRC Boca Raton 2006.

[3] Böhm L., *Comparison of single bubble and bubble swarm behavior in narrow gaps inside flat sheet membrane modules*, Technische Universität Berlin 2015.

[4] Böhm L. Kraume M., *Hydrodynamic investigation of single bubbles*, Czasopismo Techniczne Mechanika, vol. 109(5), 2012, 21-29.

[5] Böhm L.T. Kurita T. Kimura K., Kraume, M., *Rising behaviour of single bubbles in narrow rectangular channels in Newtonian and non-Newtonian liquids*, Int. J. Multiphase Flow, vol. 65, 2014, 11-23.

[6] Böhm L., Brehmer M., Kraume M., *Comparison of the Single Bubble Ascent in a Newtonian and a Non-Newtonian Liquid: A Phenomenological PIV Study*, Chem. Ing. Tech., vol. 88(1-2), 2016, 93-106.

[7] Böhm L., Drews A., Kraume M., *Bubble induced shear stress in flat sheet membrane systems – Serial examination of single bubble experiments with the electrodiffusion method*, J. Membr. Sci., vol. 437, 2013, 131-140.

[8] Prieske H., Böhm L., Drews A., Kraume, M., *Optimised hydrodynamics for membrane bioreactors with immersed flat sheet membrane modules*, Desalin. Water Treat., vol. 8(1-3), 2010, 270-276.

MANUEL BREHMER, MATTHIAS KRAUME[*]

EXPERIMENTAL STUDY
TO DEVELOP A CONTROL SYSTEM
FOR SUBMERSIBLE MIXERS IN BIOGAS PLANTS

BADANIA DOŚWIADCZALNE
NAD ROZWOJEM SYSTEMU STEROWANIA MIESZADEŁ
W INSTALACJACH BIOGAZU

A b s t r a c t

For developing a control system for these agitators, the analysis focused on the rheological characteristics of digestates, the open jet in non-Newtonian fluids and the flow conditions in a biogas reactor. In addition to a clearly visible shear-thinning effect, the viscoelastic proportion of these substrates was also determined. Depending on the stirrer speed and the rheology, the angle of spread varies and a reverse flow can occur directly at the stirrer. Therefore, not only can the position of the stirrer be used to optimise the flow field. The conical spreading of the liquid jet also enhance the mixing process. By using thrust measurements, their suitability as controlled process variables could be demonstrated.

Keywords: biogas, viscoelastic behaviour, open jet, thrust

S t r e s z c z e n i e

W pracy przedstawiono możliwość sterowania mieszadłami w oparciu o analizę charak-terystyki reologicznej odpadów pofermentacyjnych, przepływu w płynach nienewtonowskich oraz warunków przepływu w reaktorach biogazu. W zależności od szybkości mieszania i reologii zmienia się kąt rozprzestrzeniania i możliwy jest przepływ wsteczny bezpośrednio przy mieszadle – oprócz położenia mieszadła również stożkowe rozprowadzanie strumienia cieczy może wzmacniać proces mieszania. Potwierdzono przydatność pomiarów tensomet-rycznych do kontroli zmiennych procesowych.

Słowa kluczowe: biogaz, własności lepkosprężyste, napór

[*] MSc. Eng. Manuel Brehmer, Prof. PhD. DSc. Eng. Matthias Kraume, Chair of Chemical & Process Engineering, Faculty of Process Sciences, Technical University of Berlin.

1. Introduction

The mixing of large storage tanks was studied in a thorough and comprehensive manner between 1960 and 1985. At that time, the focus was on homogenising mineral oils of different densities [1, 2, 3]. Fermenters with a similar geometry are used in biogas plants and the submersible mixers also resemble those used for the stirring technique in the petrochemical industry. By installing them inside the tank, their height, the azimuth direction angle and their pitch angle can be adjusted; therefore, it is possible to respond to changes in the substrate mixture and therefore, the flow behaviour. However, the positioning of stirrers is usually done only at the first commissioning process. The plant operator has often no information about the rheology and the flow field.

The published results of research from the mixing of large storage tanks cannot be transferred to the biogas process as the structure of the digestates is much more complex than the crude oil. The stirred medium in the fermenter is fibrous and has a large number of coarse components. This leads to a more complicated rheology and support the formation of floating and sinking layers. During the operation of the stirrers, the distinctive shear thinning and viscoelastic behaviour of the substrates must be considered; therefore, knowledge about the rheology, the open jet and the impact from the stirrer position on the fluid flow in the biogas reactors is necessary for developing a control system.

The simultaneous deployment of up to four stirrers in one fermenter offers a wide range of variables.

2. Setup

Investigations on the flow fields, the effects of scale and the development of a process control system for the submersible mixers were performed by using two pilot plants with a diameter of 635 mm and 1,300 mm (Fig. 1 and 2); these are geometrically similar to large-scale biogas digesters. The thrust is determined in accordance with ISO 21630 [4] by using strain gauges. For the description of the open jet by using particle image velocimetry (PIV), a rectangular tank was employed (Fig. 3). The design was set up in a way that no interaction between the open jet and the wall could occur. According to the specifications of biogas plants, the stirrer is in a horizontal position.

Solutions of carboxymethylcellulose and xanthan gum in distilled water were used as model substance systems. The rheology of these could be adapted to the flow curves of the digestate by varying their concentrations [5].
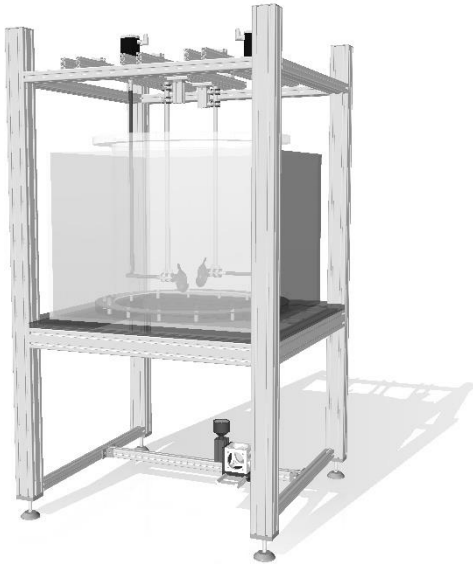
Fig. 1. The pilot plants with a diameter of 635 mm for studying the flow field by using PIV
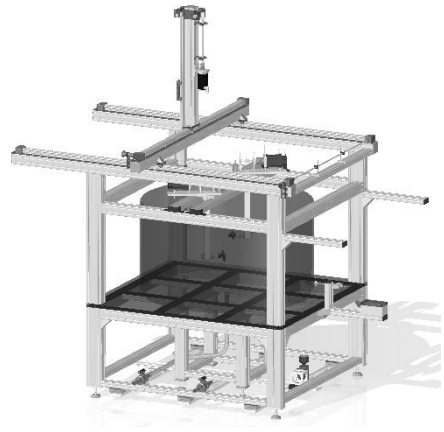
Fig. 2. The pilot plants with a diameter of 1,300 mm for studying the flow field and measuring the thrust
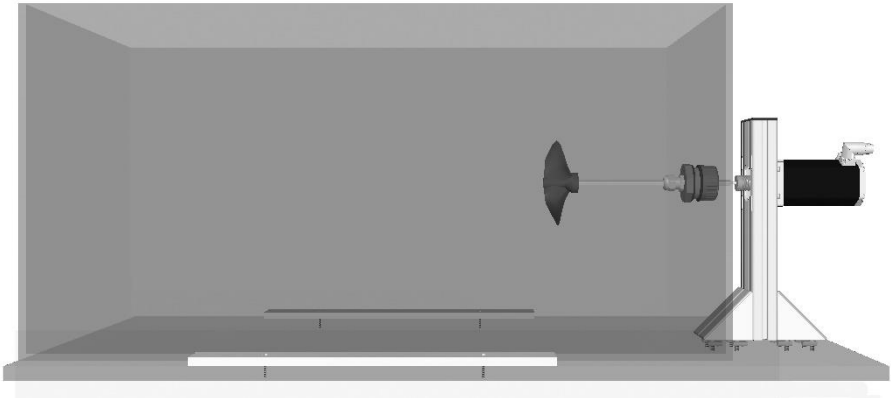
Fig. 3. The pilot plants for studying the open jet in viscoelastic fluids

3. Results

3.1. Rheological characterisation

The rheology of digestate either cannot be determined or can only be insufficiently determined with standardised rheometers [6]. Therefore, to characterise the substrate, the Metzner-Otto method [7] as well as a tube viscosimeter was used. The description is based on the Ostwald and de Waele equation

$$\mu_{eff} = K \cdot (\partial u_x / \partial y)^{n-1} \tag{1}$$

where

μ_{eff}	–	apparent or effective viscosity,
K	–	Ostwald coefficient,
n	–	shear rate exponent,
y	–	y-coordinate,
u_x	–	velocity in x-direction.

In Figure 4, the parameters of the power law equation are presented. Taking the example of corn silage, significant fluctuations can be observed during the year. The shear rate exponent lies in the range of 0.06 and 0.18 and the Ostwald factor from 6 to 44. In contrast, there are only low fluctuations in the dry matter.
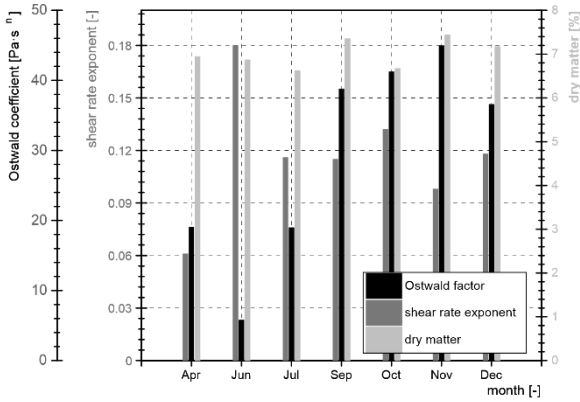
Fig. 4. Rheological parameter for corn silage during the year
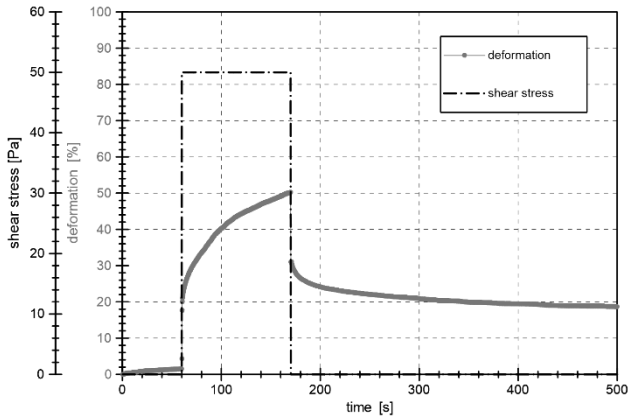
Fig. 5. Determining the viscoelastic part of corn silage

In addition to the shear thinning character, a viscoelastic portion of this substrate could also be detected in creep tests. The deformation was measured during stress- and relaxation periods (Fig. 5) by using a blade stirrer. Here, the viscoelastic portion was 65% and is in the same range as xanthan gum with a concentration above 3 g/kg.

Due to the fact that the range and characteristics of the open jet is essential for the positioning of the stirrers, the viscoelastic effects of the fluid must be considered while stirring a biogas reactor.

3.2. Open jet

The angle of spread at the stirrer was characterised for various non-Newtonian media and different stirrer speeds in a rectangular tank. Figures 6 to 11 show the open jet of a stirrer in different model substance systems. Solutions with Carboxymethylcellulose (CMC) in a concentration of 2 g/kg_{H2O} and 5 g/kg_{H2O} as well as xanthan gum of 1g/kg_{H2O} were used. The description of the flow curves can be carried out according to Equation 1 as follows:

Xanthan gum of 1 g/kg: $\qquad \mu_{eff} = 0.26 \cdot (\partial u_x / \partial y)^{0.4-1}$ (2)

CMC of 2 g/kg: $\qquad \mu_{eff} = 0.06 \cdot (\partial u_x / \partial y)^{0.74-1}$ (3)

CMC of 5 g/kg: $\qquad \mu_{eff} = 0.67 \cdot (\partial u_x / \partial y)^{0.56-1}$ (4)

The angle of spread of the liquid jet clearly depends on the rotation speed. In the case of an angle greater than zero the flow direction along the rotation axis turns around, as also known for viscoelastic fluids [8]. However, an explicit viscoelastic behaviour of the CMC or xanthan gum solution with 1 g/kg could not been detected, neither with an air bearing oscillating rheometer nor with the Giesekus experiment [9]. The range of the open jet is substantially reduced by the reverse flow – this affects the correspondence of the stirrers in the biogas plant and therefore, the flow field.
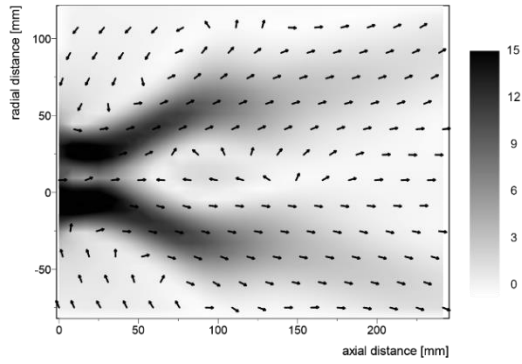
Fig. 6. Open jet of a propeller in a carboxymethylcellulose solution of 2 g/kg
(stirrer speed: 300 rpm)
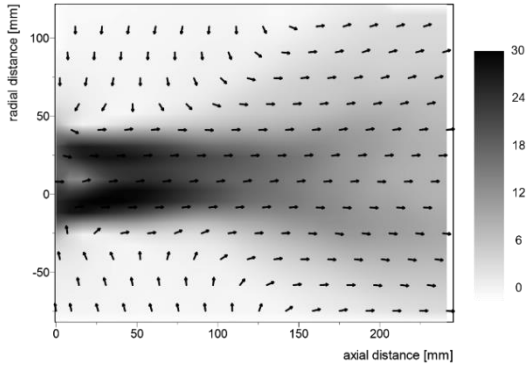
Fig. 7. Open jet of a propeller in a carboxymethylcellulose solution of 2 g/kg
(stirrer speed: 1000 rpm)
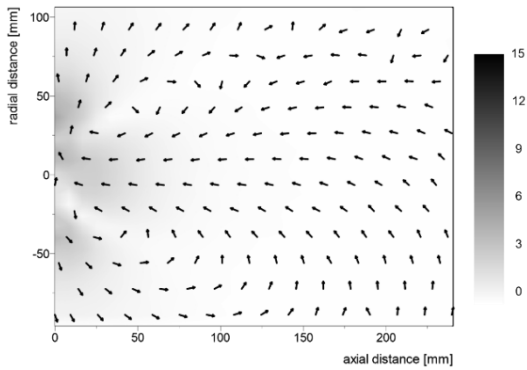
Fig. 8. Open jet of a propeller in a carboxymethylcellulose solution of 5 g/kg
(stirrer speed: 300 rpm)
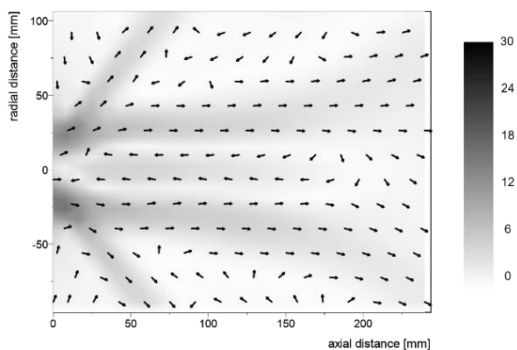
Fig. 9. Open jet of a propeller in a carboxymethylcellulose solution of 5 g/kg
(stirrer speed: 1000 rpm)
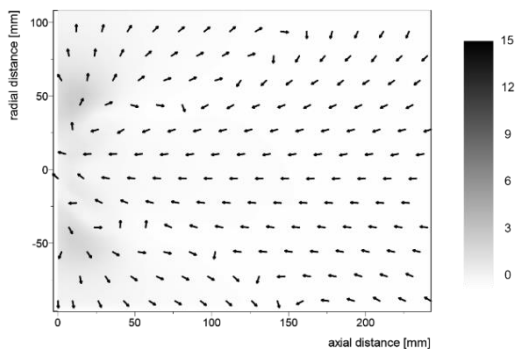
Fig. 10. Open jet of a propeller in a xanthan gum solution of 1 g/kg
(stirrer speed: 300 rpm)
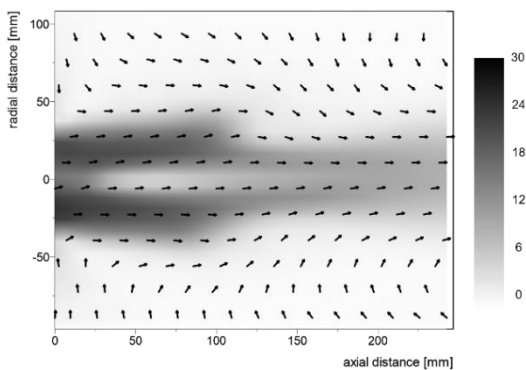
Fig. 11. Open jet of a propeller in a xanthan gum solution of 1 g/kg
(stirrer speed: 1000 rpm)

3.3. Flow conditions in a fermenter

By using a tracer, the flow field in the pilot plant can be visualised and the mixing time determined. As shown in Figures 12 and 13, there is a clear dependence on the viscosity, the azimuth angle and the stirrer speed. However, a higher viscosity does not always lead to lower-mixed volumes. Due to the spreading of the liquid jet, it is possible that the fluid flow reach the centre of the reactor. The classic stagnation zone in the centre reduces or completely disappears.

As expected, interactive stirrers also decrease the thrust; therefore, by measuring the thrust, conclusions about the interaction of the stirrers and the flow field can be drawn.

Fig. 12. Flow field at a xanthan gum of 2 g/kg (stirrer speed: 3000 rpm; azimuth angle: 65°)
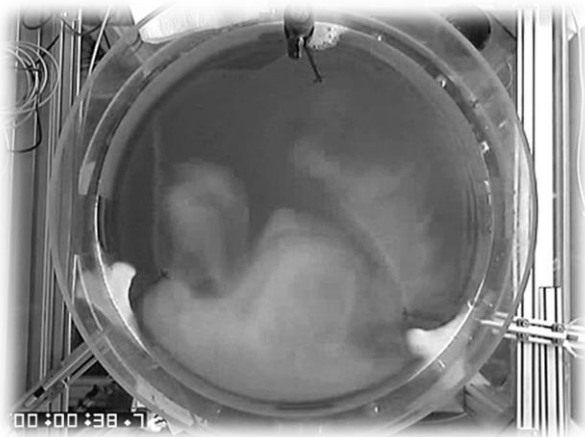
Fig. 13. Flow field at a xanthan gum of 3 g/kg (stirrer speed: 3000 rpm; azimuth angle: 65°)

4. Conclusion

According to rheological studies, the digestates show a distinctive pseudoplastic behaviour. Due to the varying feeding of the fermenter, these viscosity values fluctuate considerably during the year. Furthermore, viscoelastic effects must be considered for the positioning and operation of the agitators. Based on measurements of the open jet by using particle image velocimetry, there are huge dependencies of the stirrer speed, the rheology and the propeller geometry on the open jet (especially the angle of spread) the range and the field of return flows. These results provide the basis for determining the optimal positioning of the stirrers in the fermenter. The ideal operation could be quantified by measuring the mixing time and visualising the flow field. Classical stagnation zones are avoided in the reactor centre, or at least reduced. However, for all adjustments, the interaction of the agitators was important to achieve an adequate flow field. This interaction could be detected by measuring the thrust. In addition to the viscosity, the thrust is a second parameter for a control system for submersible mixers in biogas plants.

R e f e r e n c e s

[1] Vusse V., *Vergleichende Rührversuche zum Mischen löslicher Flüssigkeiten in einem 12000m³ Behälter*, Chemie-Ing.-Techn., vol. 31(9), 1959, 583-587.

[2] Wesselingh J. A., *Mixing of Liquids in cylindrical storage tanks with side-entering propellers*, Chem. Eng. Science, vol. 30, 1975, 973-981.

[3] Kipke K., *Suspension by Side Entering Agitators*, Chem. Eng. Process., vol. 18, 1984, 233-238.

[4] ISO 21630, *Pumps – Testing – Submersible mixers for wastewater and similar applications*, ISO copyright office, Switzerland 2007.

[5] Brehmer M., Eppinger T. and Kraume M., *Einfluss der Rheologie auf das Strömungsregime in gerührten großtechnischen Biogasreaktoren*, Chemie-Ing.-Techn., vol. 84(11), 2012, 2048-2056.

[6] Brehmer M., Kraume M., *Rheological properties of substrates for the biogas production from renewable resources*, Progress in Biogas II, conference transcript, FNBB 2011.

[7] Metzner A.B., Otto R.E., *Agitation of Non-Newtonian Fluids*, AIChE J., vol. 3, 1957, 3-10.

[8] Pahl M., *Mischen und Rühren: Grundlagen und moderne Verfahren*, Hrsg. Matthias Kraume, WILEY-VCH Verlag GmbH & Co KGaA, Weinheim 2003.

[9] Giesekus H., *Sekundärströmungen in viskoelastischen Flüssigkeiten bei stationärer und periodischer Bewegung*, Rheologica Acta, vol. 4(2), 1965, 85-101.

GEORG BRÖSIGKE, JENS-UWE REPKE[*], ALEXANDER HERTER,
MATTHIAS RÄDLE[**]

ANALYSIS OF THE INFLUENCE OF TURBULENCE ON THE HEAT TRANSFER BETWEEN SPHERICAL PARTICLES AND PLANAR SURFACES

ANALIZA WPŁYWU TURBULENCJI NA TRANSFER CIEPŁA POMIĘDZY CZĄSTKAMI KULISTYMI A PŁASKIMI POWIERZCHNIAMI

A b s t r a c t

The heat transfer between particles and walls plays an important role in several industrial processes. Since established models often deal with simplifications for the surrounding gaseous phase, this work aims to acquire a fundamental understanding of the occurring transport phenomena. In this work, a high-resolved finite-volume method is applied carrying out direct numerical simulation of fluid dynamics and heat transfer simultaneously. The influence of turbulence on the heat transfer is discussed in this paper.

Keywords: heat transfer, particles, direct numerical simulation, turbulence

S t r e s z c z e n i e

Przekazywanie ciepła pomiędzy cząstkami i ścianami odgrywa ważną rolę w wielu procesach przemysłowych. W uznanych modelach często wprowadzane są uproszczenia – celem tej pracy był opis fundamentalnych zjawisk transportu. Zastosowano metodę objętości skończonych do przeprowadzenie bezpośredniej symulacji numerycznej ruchu płynu i wymiany ciepła jednocześnie z uwzględnieniem wpływu turbulencji na transfer ciepła.

Słowa kluczowe: przenikanie ciepła, cząstki, symulacja numeryczna bezpośrednia, turbulencja

[*] MSc. Eng. Georg Brösigke, Prof. PhD. DSc. Eng. Jens-Uwe Repke, Process Dynamics and Operations Group, Faculty Of Process Sciences, Technical University of Berlin.
[**] MSc. Alexander Herter, Prof. PhD. DSc. Matthias Rädle, Hochschule Mannheim.

1. Introduction

The heat transfer between spherical particles and walls on the one hand, and solely between particles on the other hand is relevant in several pieces of industrial apparatus – amongst others, these include fixed-bed reactors, fluidised beds, tube dryers and rotary kilns. The occurring mechanisms are not yet fully understood or rather, their different degrees of contribution have not yet been quantified satisfactorily. For the purposive development and efficient design of the mentioned pieces of apparatus, a fundamental understanding of the occurring mechanisms is crucial.

In previous work [1], the heat conduction through the gaseous gap between a single spherical particle and a planar surface was identified as the dominating mechanism for the laminar regime. The investigation was carried out with CFD simulations and the results were validated against both experimental data and a correlation from literature for a static sphere on a planar surface [2].

For calculating the heat transfer, simplified approaches via Nusselt correlations are often chosen. These correlations frequently neglect transport resistances in the solid phase and the actual fluid dynamics in the surrounding fluid (i.e. gas or liquid) phase.

In order to identify the basic transport mechanisms, the generic system is transformed to a system of basic geometries, i.e. sphere and plate.

2. Methods

Since the particles are small (< 1 mm) an experimental approach would require enormous effort, if it was possible at all; therefore, a 3D finite volume approach was chosen for the simulations in order to resolve both temperature and velocity boundary layers in all involved phases.

2.1. Solver-development

The open source toolbox OpenFOAM® developed on the basis of [3] and [4] was used to carry out the simulations. The toolbox offers a variety of preassembled standard solvers, which can be customised in order to meet specific requirements. For the fundamental investigations of heat transfer between a rolling sphere and plate, the solver has to fulfil several requirements that no standard solver incorporates, i.e. different regions for solids and fluids (gas or liquid), topological mesh movement, temperature dependent physical properties and arbitrary composition of the fluid phase. The postulated requirements can be met by modification of the standard solver *chtMultiRegionFoam* with:

- the *dynamicFvMesh* library for the topological mesh movement;
- a modified *thermophysicalModels* library for the temperature dependent properties;
- a link between energy and momentum balance, which describes the momentum dissipation.

The simulation domain is built with three different meshes, each representing a region with different physical properties, i.e. sphere, plate and surrounding gas phase. Fig. 1 shows the assembly.
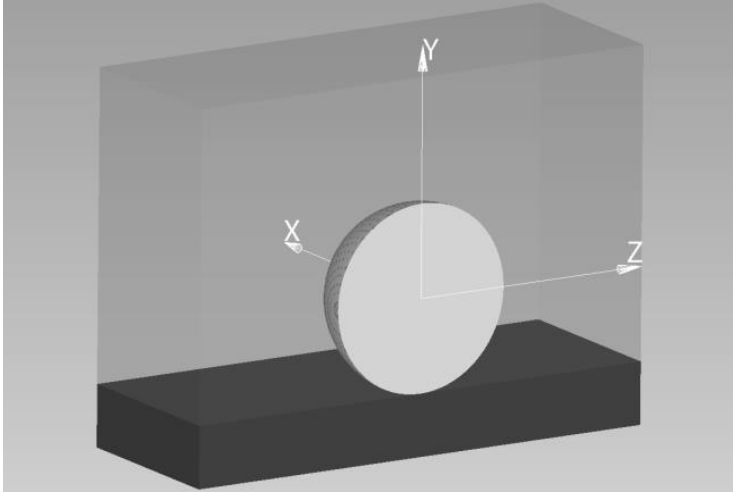
Fig. 1. CFD Domain with different regions: mid-grey – gas phase; dark grey – plate; light grey – sphere

2.2. Simulation conditions

For the fluid phase, the compressible Navier-Stokes equations

$$\frac{\partial \rho \hat{v}}{\partial t} + \nabla(\rho \hat{v} \hat{v}) = \nabla(\eta \nabla \hat{v}) - \nabla p + \rho g \tag{1}$$

are applied, although the Mach Number is small. The reason is to be able to implicitly link density and temperature with the perfect gas equation

$$pV = nRT. \tag{2}$$

The heat transfer is described with the energy equation

$$\frac{\partial \rho e + \frac{1}{2}\rho|\hat{v}|^2}{\partial t} + \nabla\left(\rho e + \frac{1}{2}\rho|\hat{v}|^2\right)\hat{v} = \nabla\left(\frac{\lambda}{c_p}\nabla e\right) - \nabla p\hat{v} + \rho g\hat{v} + \nabla\tau\hat{v} \tag{3}$$

incorporating convective and diffusive heat transfer terms as well as the dissipation term.

For the solid phase, the movement is described by a moving mesh approach and the diffusive heat transport is calculated with the equation for transient heat conduction

$$\frac{\partial \rho e}{\partial t} = \nabla\left(\frac{\lambda}{c_p}\nabla e\right). \tag{4}$$

The simulation is set up in a way, which implies the observer to be moving with the coordinate system at the same absolute velocity as the sphere does. This way the sphere's mesh only has to perform an according rotational movement within the surrounding gas

phase, whereas the translational movement is simulated by an approaching flow with according velocity. The plate is represented by a mesh adjacent to the bottom of the gas phase. Due to the prescribed view of a moving observer the plate has to perform a linear movement with the sphere's velocity. The plate's movement is represented by treating the plate as an inviscid fluid with the physical properties of a solid, so that the plate's mesh does not have to be moved. The mesh regions are coupled via a Cauchy boundary condition for the temperature and the temperature gradient respectively

$$T_{sphere,surface} = T_{fluid,surface} \tag{5}$$

$$\dot{q}_{sphere} = \dot{q}_{fluid} \tag{6}$$

By using the arbitrary mesh interface (AMI) mapping function, which works with an algorithm using Galerkin projection [5], the faces at the boundaries do not need to conform with adjacent faces.

During the evaluation of the equation system, different arithmetical operations have to be carried out including surface and volume integrals as well as time integration. In order to do this numerically, the operations have to be carried out in a discretised form. There are a variety of discretisation schemes available which have different influences on the solution of the equation system. The upwind differencing scheme increases solution stability due to numerically dissipative behaviour. This is a first-order scheme which means the interpolation error decreases linearly with an increasing discretisation resolution. On the other hand, higher order schemes, like central differencing schemes, behave in the opposite way. In Table 1, the applied discretisation schemes are listed for the gas region and the plate region. The significant difference lies in the scheme for the divergence discretisation. For the gas region, a scheme of high order, which is not diffusive, is applied in order to use the truncation error for turbulence creation. In contrast, a first order scheme, which is very diffusive, is applied for the plate region in order to supress any turbulence, since this region actually describes a solid.

Table 1

Spatial and temporal discretisation schemes for gas and plate region

region	temporal	gradient	divergence	Laplace
gas	Crank-Nicolson, 2nd order	least squares, 2nd order	central differencing, 4th order	central differencing, 2nd order
plate	Crank-Nicolson, 2nd order	central differencing, 2nd order	upwind, 1st order	central differencing, 2nd order

2.3. Meshing

As mentioned in section 2.1, the three different regions (i.e. sphere, gas and plate) are each treated with their own mesh. The meshes for the sphere and plate are physically describing solids where only the heat flux is investigated in this work. The resolution is

rather coarse compared to the gas region, so that the mesh generation is not described in detail. In the latter region, fluid dynamics is of high interest; therefore, the mesh generation is crucial. The mesh for direct numerical simulation in this region has to fulfil certain conditions. The spatial resolution has to be high in order to resolve all vortices down to where the energy is dissipated, the so-called *Kolmogorov* scale [6], which is basically determined by the viscosity.

$$\eta = \left(\frac{v^3}{\varepsilon}\right)^{1/4} \tag{7}$$

The mesh is built on the basis of a structured hexahedral mesh which is advantageous for parallelisation during the actual calculation. The sphere is inserted via the OpenFOAM® meshing tool *snappyHexMesh*. The grid is simultaneously refined in this step. Fig. 2 depicts the refined mesh assembly for all regions. The overall domain includes a very highly resolved region of interest, which was gained by previous turbulence modelling simulations. The point distance in each coordinate direction is maximal 25 µm wide. The surface of the sphere and the gap are resolved even with a smaller point distance. Employing the results from the DNS to equation (7) gives a *Kolmogorov* scale of about 50µm for this case, so that the condition is satisfied.

The contact point between the sphere and plate cannot be represented in a finite volume method. In the literature, several approaches can be found that introduce solutions for this task. The particle is flattened near to the contact point to leave a gap between two solid surfaces in the 'caps' approach by Eppinger et al. [7]. Dixon et al. [8], alternatively, give an overview of possible solutions; in particular, shrinking, overlap, bridge connection and an approach similar to the 'caps' approach.

Since this work is a fundamental investigation of heat transfer mechanisms, the characteristic geometry of the sphere should be conserved. The contact point is therefore replaced by a gap of 1µm width which is resolved with at least four finite volume cells.
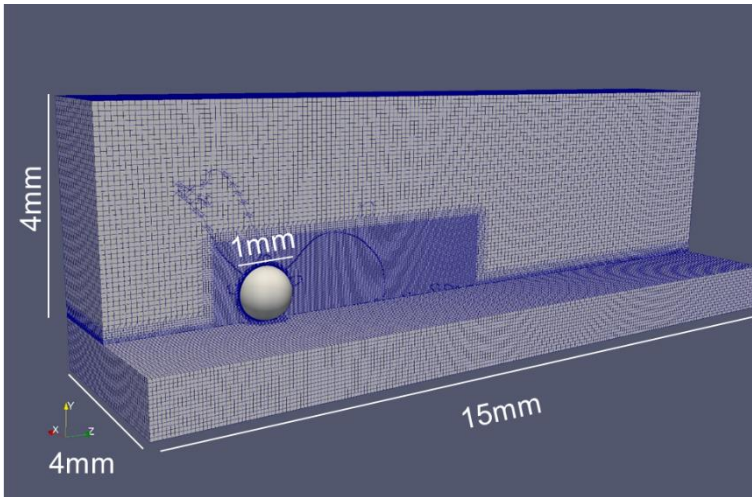
Fig. 2. Refined mesh assembly

2.4. Boundary conditions

The flow fields of the gas and plate are velocity driven since the pressure does not significantly change in this case. Constant values for velocity (5 m/s) and temperature (430 K) are applied at the inlet. At the outlet and the top of the gas phase region, a mixed boundary condition is applied – this changes between the Dirichlet and Neumann condition depending on the direction of the flux. Hereby, backflow into the domain, which might occur, can be handled. At the boundaries between gas and solid regions, the velocity is also fixed in order to represent the no slip condition for the mentioned moving observer. As mentioned in section 2.2, a Cauchy boundary condition for the temperature at the contact surfaces of the gas with the solid is implemented.

The velocity and pressure field results from the turbulence modelling simulations mentioned in section 2.3 were used as starting values for the direct numerical simulations in order to improve convergence. The initial values for the temperature were 550 K for the sphere and 430 K for the gas and plate region.

3. Results

Simulations with Reynolds Averaged Navier Stokes turbulence were carried out for the generation of starting values for the actual direct numerical simulation. In these steady state simulations, only the fluid dynamics in the gas phase was solved, neglecting the transient heat transfer. The OpenFOAM® standard solver *simpleFOAM* was used and both standard k-ε- and k-ω-SST-models were applied in a low-Reynolds approach with the absence of wall functions. Since the standard k-ε-model showed better stability in the convergence behaviour, the DNS was initialised with its results for velocity and pressure field.

The velocity magnitude field for both DNS and the standard k-ε-model are depicted in Fig. 3. One has to keep in mind that for an observer, who moves with the same velocity as the sphere does, the relative velocity is depicted. The domain's symmetry plane in rolling direction is shown, so that the sphere moves from right to left. For the transient DNS, a time-averaged velocity field is generated for comparison with the stationary RANS model. The simulations show qualitatively similar results with a slight difference in the description of the flow detachment. The direct numerical simulation predicts a more distinct vortex in the flow detachment area behind the sphere and a slightly different shape of the area near the wall.

In Fig. 4, the energy dissipation rate is shown for the same cases shown before. Both results show a qualitatively strong agreement. The highest values for the dissipation rate are predicted around the surface of the sphere and near to the plate in the sphere's wake. As can be seen in Fig. 3, there is a very sharp gradient near to the surface of the sphere due to its no slip condition. The displacement of fluid caused by the sphere enforces this effect by accelerating the fluid. Referring once more to the observer, who moves with the sphere's velocity, it can be seen, that downstream of the touching point of sphere and plate large gradients occur as well. The velocity gradients 'feed' eddies in which the energy is finally dissipated.
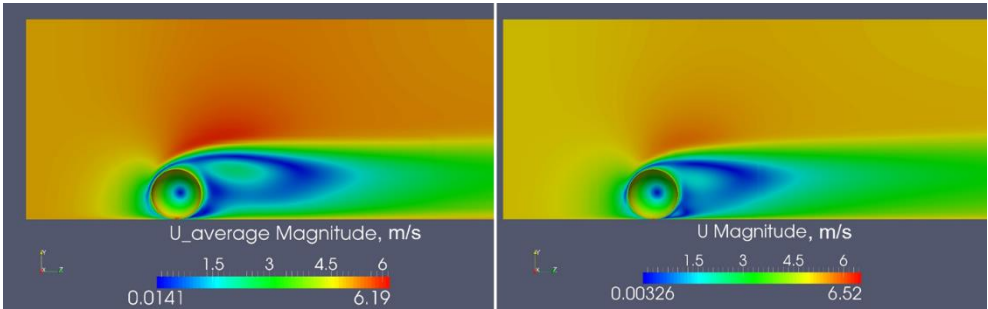
Fig. 3. Velocity magnitude fields: left – DNS; right – standard k-ε-model

Conversely, the quantity of the dissipated energy differs significantly. The DNS delivers much higher dissipation rates compared to the standard k-ε-model.
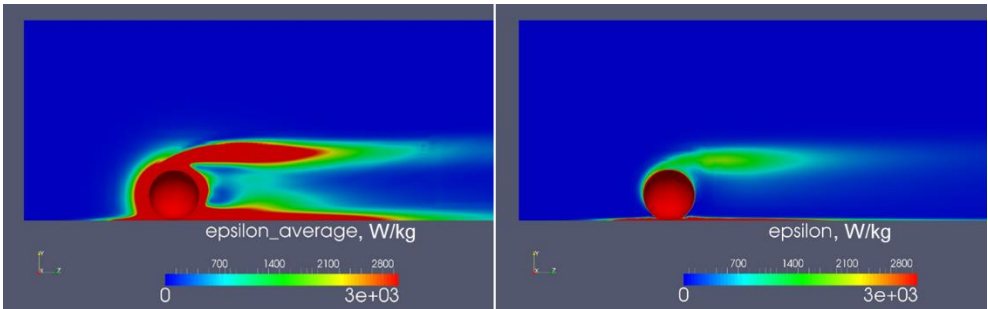
Fig. 4. Dissipation rate of turbulent kinetic energy: left – DNS; right – standard k-ε-model

In order to determine the influence of turbulence on the heat transfer, both convective and diffusive heat flux are calculated and shown in Fig. 5 for turbulent conditions (DNS, 5 m/s) on the left-hand side, and for a simulation under laminar conditions (0.1 m/s) on the right-hand side. In each picture, the convective heat flux is on the sphere's left-hand side and the diffusive heat flux on its right-hand side. The sphere rolls towards the observer, so that the fluid flow is in accord with the convective heat flux (Z-direction). Both vector fields are scaled in size with the absolute amount of heat flux. The heat flux component in the Y-direction (i.e. normal to the plate) is represented in colour. Due to the no slip condition on the sphere's surface, heat is convectively transported to the plate on the sphere's front side and transported away on the rear side. On the other side, heat is diffusively transported by conduction in normal direction to the plate. In the turbulent case, both mechanisms take place at the same order of magnitude, whereas in the laminar case, the diffusive transport clearly dominates. In Table 2, the overall heat transfer coefficients for the wall-heat transfer

$$k_{sphere/wall} = \frac{\dot{Q}_{projection}}{A_{projection}(\bar{T}_{projection} - \bar{T}_{lower\;hemisphere})} \qquad (8)$$

and the heat transfer towards the surrounding fluid

$$k_{sphere/gas} = \frac{\dot{Q}_{sphere}}{A_{sphere}(\bar{T}_{sphere} - \bar{T}_{gas})} \qquad (9)$$

are listed. For $k_{sphere/wall}$, the overall heat flux into the plate is integrated over the sphere's projection area and area averaged values are applied for the temperature difference. For $k_{sphere/gas}$, the heat overall flux into the gas phase is integrated over the surface of the sphere and again area averaged values are applied for the temperature difference.

The wall-heat transfer is not significantly affected by the occurrence of turbulence, whereas the heat transfer towards the surrounding fluid increases.
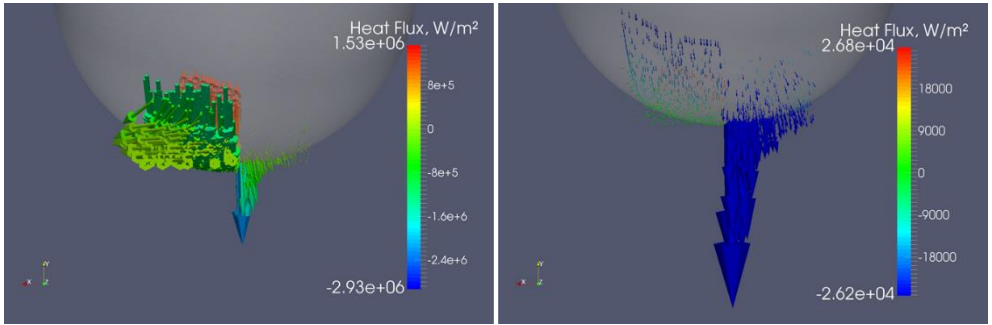
Fig. 5. Convective and diffusive heat flux: left – DNS; right – laminar

T a b l e 2

Overall heat transfer coefficients

regime	$k_{sphere/wall}$, W/m²K	$k_{sphere/gas}$, W/m²K
turbulent	790	437
laminar	807	317

4. Summary & Conclusion

In this paper, a first direct numerical simulation of a rolling sphere on a flat plate incorporating heat transfer is shown. The fluid dynamics is compared against a stationary RANS simulation with the standard k-ε-model. It is shown that the turbulence model underestimates the dissipation of turbulent kinetic energy in comparison to the solution of the DNS.

In the second step, the result for the heat transfer is compared against a simulation of the heat transfer under laminar conditions. Although the convective heat flux is shown to have

increased with the presence of turbulence, the overall wall-heat transfer coefficient does not change significantly from the laminar to the turbulent regime. Nevertheless, the heat transfer from the sphere to the surrounding gas phase increases with rolling speed and occurring turbulence as expected due to the decreased thickness of the boundary layer.

5. Outlook

The thesis that the presence of turbulence seems to have negligible influence on the heat transfer between a rolling sphere and a plate has to be verified by a wider range of parameter variation (e.g. velocity, diameter). To this aim, further simulations with turbulence models are planned. It has to be established if the standard k-ε-model's parameters can be calibrated with the result from the DNS in order to represent the correct velocity field and amount of dissipated energy.

R e f e r e n c e s

[1] Brösigke G., Herter A., Rädle M., Repke J.-U., *Investigations of Heat Transfer Mechanisms between a Moving Sphere and a Static Plate with Computational Fluid Dynamics*, 17th Conference on Process Integration, Modelling and Optimisation for Energy Saving and Pollution Reduction, Prague 24.-27.8.2014.

[2] Schlünder E.-U., Chem. Eng. Process., vol. 18, 1984, 31-53.

[3] Weller H.G., Tabor G., Jasak H., Fureby C., *A tensorial approach to computational continuum mechanics using object-oriented techniques*, Computers In Physics, vol. 12(6) 1998, DOI: 10.1063/1.168744.

[4] Jasak H., *Error analysis and estimation for the finite volume method with applications to fluid flows*, PhD Imperial College London (University of London) 1996.

[5] Farrell P.E; Maddison J.R, *Conservative interpolation between volume meshes by local Galerkin projection*, Computer Methods In Applied Mechanics And Engineering vol. 200(1-4), 2011, 89-100, DOI: 10.1016/j.cma.2010.07.015.

[6] Ferziger J.H., Perić M., *Computational Methods for Fluid Dynamics*, Springer, Berlin, Heidelberg 2002.

[7] Eppinger T.; Seidler K.; Kraume M., *DEM-CFD simulations of fixed bed reactors with small tube to particle diameter ratios*, Chemical Engineering Journal, vol. 166(1), 2011, 324-331, DOI: 10.1016/j.cej.2010.10.053.

[8] Dixon A.G.; Nijemeisland M., Stitt E.H., *Systematic mesh development for 3D CFD simulation of fixed beds: Contact points study*, Computers & Chemical Engineering vol. 48, 2013, 135-153, DOI: 10.1016/j.compchemeng.2012.08.011.

THOMAS BUDIARTO, ERIK ESCHE, JENS-UWE REPKE[*]

DYNAMIC MODELLING AND OPERATION OF THE CHLOR-ALKALI PROCESS

MODELOWANIE I STEROWANIE PROCESEM ELEKTROLIZY CHLORKU SODU

A b s t r a c t

Chlorine it is commonly produced through the Chlor-alkali process, which is an electrochemical process – the process energy consumption dominates the production cost. Therefore, optimization of the process has become a major issue to achieve energy conservation and cost effective production. This study aims at investigating the transient and steady-state behavior of the chlorine production system through process modeling and simulation. Material balance and energy balance of the Chlor-alkali membrane process (electrolysis), brine pre-treatment, and chlorine handling are modelled and investigated using rigorous models. MOSAIC and MATLAB, are used to model and to simulate the process response when receiving dynamic input. For validation, the simulation result is compared to experimental data.

Keywords: chlor-alkali membrane process, dynamic model, electrochemical cell

Streszczenie

Chlor wytwarzany jest powszechnie w procesie elektrolizy chlorków metali alkalicznych – energochłonność procesu dominuje koszt produkcji. Dlatego optymalizacja procesu stała się poważnym problemem. Celem pracy było zbadanie i modelowanie procesu produkcji chloru w stadiach stacjonarnych i przejściowych. Bilanse materiałowy i energetyczny procesu membranowego (elektroliza), wstępna obróbka solanki i magazynowanie chloru zostały przetestowane przy użyciu rygorystycznych modeli. MOSAIC i MATLAB były wykorzystywane do modelowania i symulacji procesów odpowiedzi układu na dynamiczne wymuszenie. Dla weryfikacji wyniki symulacji porównano z danymi doświadczalnymi.

Słowa kluczowe: proces membranowy, przemysł chloro-alkaiczny, model dynamiczny, ogniwo elektrochemiczne

[*] MSc. Thomas Budiarto, DSc. Eng. Erik Esche, Prof. PhD. DSc. Eng. Jens-Uwe Repke, Process Dynamics and Operations Group, Faculty Of Process Sciences, Technical University of Berlin.

1. Introduction

By now, renewable energy has become an important component of Germany's energy mix. In 2014, renewable sources amounted to 26.2% of power generation, and this is increasing further due to the German Government requiring the renewable energy share in power generation to reach 40÷45% by 2025 and 55÷60% by 2035 [14].

Chlorine is one of the most indispensable intermediates in the chemical industry. It is commonly produced through the chlor-alkali process, which is an electrochemical process that decomposes an aqueous solution of sodium chloride by direct current, producing chlorine gas, hydrogen gas, and sodium hydroxide solution. The process's energy consumption dominates the production cost. Given the large-scale introduction of renewable energy sources in Germany's electrical grid, both energy suppliers as well as consumers have to adjust to an increasingly flexible market. Therefore, optimisation of the process has become a major issue to achieve energy conservation and cost effective production. It is important to understand the dynamic and steady-state behaviour of the process in order to optimize the process operation relating to plant energy consumption.

In order to understand the demand response potential of the chlor-alkali process, the dynamic response of the process is modelled. The Butler-Volmer equation and the Nernst equation are used to model the dynamic behaviour of the current density and chlorine production rate. Both of these equations correlate the material balance with the energy consumption of the process.

2. The Process Model

In order to investigate the dynamics of the energy consumption of the chlor-alkali process, a material balance model and an electrolytic cell voltage model were developed. The process consists of two half-cells, which are known as the anode cell and cathode cell. The chemical reactions which are considered in the developed model can be expressed as:

Anode cell : $2Na^+ + 2Cl^- \rightarrow Cl_2 + 2Na^+ + 2e^-$

$2Cl^- \rightarrow Cl_2 + 2e^-$

Cathode cell : $2H_2O + 2e^- \rightarrow H_{2(g)} + OH^-$

$Na^+ + OH^- \rightarrow NaOH_{(aq)}$

Total reaction : $2H_2O + 2NaCl \rightarrow H_{2(g)} + Cl_{2(g)} + 2NaOH_{(aq)}$
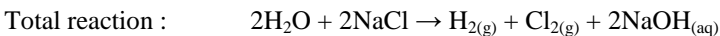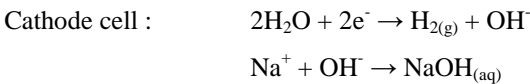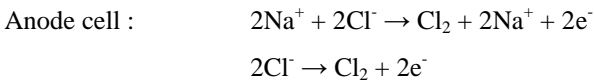
The developed model consists of a material balance model and dynamic model of the energy consumption regarding the dynamics of the material balance in the electrochemical cell. Fig. 1 illustrates the process which is modelled in this study.
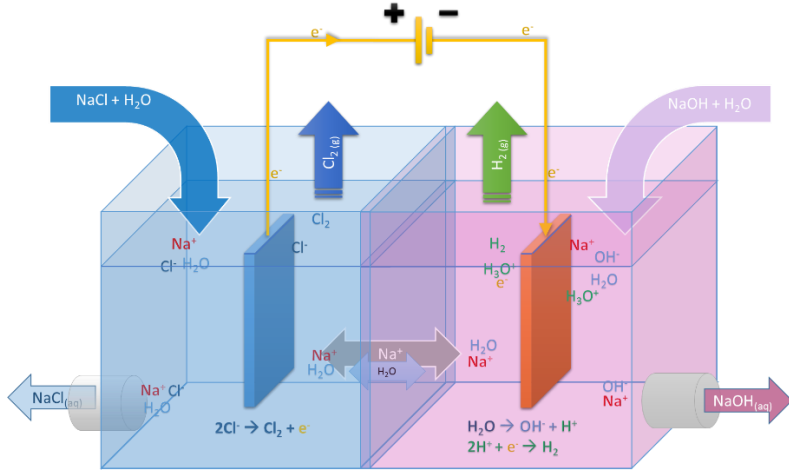
Fig. 1. Diagram of chlor-alkali model

The material balance model considers balances for sodium ions, hydroxide ions, water, and chloride. The liquid volume of each half cell is assumed to be constant and the concentrations of the electrolyte are distributed uniformly. In accordance with Faraday's Law, gas production rates in the chlor-alkali cell can be estimated using the following expressions:

$$\dot{N}_{CatOut}^{H_2} = \frac{i \cdot A}{2F} \tag{1}$$

$$\dot{N}_{CatOut}^{Cl_2} = \frac{i \cdot A}{2F} \tag{2}$$

In these expressions, the current efficiency for producing chlorine and hydrogen gas are assumed to be 100%. The other parallel reactions which appear to be current inefficiency problems are neglected in this model. Tilak and Chen [2] mention that chlorine gas in the anode might dissolve in water to form soluble chlorine, which hydrolyses to form HOCl and OCl⁻. HOCl and OCl⁻ react further to form ClO_3^-. However, based on reference [3], the solubility of Chlorine in water and a solution of NaCl is below 1% of the solution weight when the solution temperature is above 20°C. In accordance with reference [3], Fig. 2 shows that the solubility of chlorine in water, HCl solution, and NaCl solution decreases with increases in temperature and concentration. Hence, the influence of this parallel reactions is minor compared to the other chlor-alkali reactions.
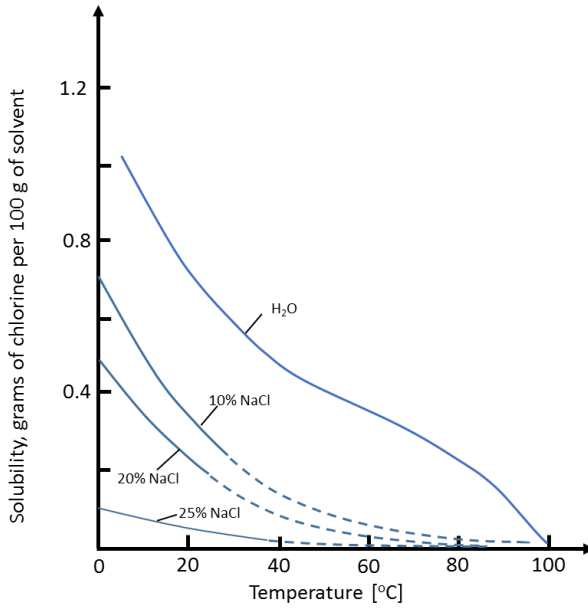
Fig. 2. Solubility of chlorine in water, hydrochloric acid, and sodium chloride solutions, in accordance with reference [3]

1.1. Material Balance Model

In the developed model, the process and ions transport between the anolyte and catholyte does not change the volume of either the catholyte or anolyte. The accumulative volume of the anolyte and catholyte are modelled as:

$$\frac{dV_{CatAcc}}{dt} = \dot{V}_{CatIn} - \dot{V}_{CatOut} \tag{3}$$

$$\frac{dV_{AnAcc}}{dt} = \dot{V}_{AnIn} - \dot{V}_{AnOut} \tag{4}$$

In the simulation, the accumulative volume of the catholyte and anolyte will be assumed to be constant. Both in the anode and cathode, the feed flow rate is equal to the outlet flow.

1.1.1. Sodium Ion Balance

Sodium ions in the modelled process mainly originate from NaCl in the anolyte feed. Some processes consider the feeding of lean concentrations of NaOH as a catholyte input in

order to gain higher NaOH concentration at the cathode outlet. The following equations (equations 5, 6 and 7) formulate the sodium ion balance in the cell.

$$\frac{dN_{CatAcc}^{Na}}{dt} = C_{CatIn}^{NaOH} \cdot \dot{V}_{CatIn} - C_{CatAcc}^{Na} \cdot \dot{V}_{CatOut} + \frac{A \cdot D^{Na}}{\delta} \cdot \left(C_{AnAcc}^{Na} - C_{CatAcc}^{Na} \right) \tag{5}$$

$$\frac{dN_{AnAcc}^{Na}}{dt} = C_{AnIn}^{NaCl} \cdot \dot{V}_{AnIn} - C_{AnAcc}^{Na} \cdot \dot{V}_{AnOut} - \frac{A \cdot D^{Na}}{\delta} \cdot \left(C_{AnAcc}^{Na} - C_{CatAcc}^{Na} \right) \tag{6}$$

$$C_{AnIn}^{Na} = \frac{N_{AnAcc}^{Na}}{V_{AnAcc}} \; ; \; C_{CatIn}^{Na} = \frac{N_{CatAcc}^{Na}}{V_{CatAcc}} \tag{7}$$

Based on some references [13, 15, 16], the concentration gradient of solutions across a polymeric membrane contributes to material transport in the electrochemical cell. In reference [13], it is mentioned that the concentration gradient of water across a proton exchange membrane in a water electrolyser contributed to mass flow inside the cell. The developed sodium balance model also considers the concentration gradient as the driving force of Na^+ ion transport between anolyte and catholyte. In the developed model, the ion exchange rate is proportional to the ion diffusion area, the diffusion coefficient of Na^+ ions, and the concentration gradients between the anolyte and catholyte. Conversely, the exchange rate is inversely proportional to the membrane thickness.

1.1.2. Hydroxide Ion Balance

The hydroxide ions are produced by a cathode reaction which breaks down the water into OH⁻ and H⁺ ions. Based on Faraday's Law, the OH⁻ production rate is proportional to the electrolysis current that drives the cathode reaction. The developed model also assumes that the ion-exchange membrane halts the hydroxide ions transfer from catholyte to anolyte. The OH⁻ ions then cease to exist in the anode compartment. The hydroxide ion balance can be written as:

$$\frac{dN_{CatAcc}^{OH}}{dt} = C_{CatIn}^{NaOH} \cdot \dot{V}_{CatIn} + \frac{i \cdot A_{el}}{2F} - \frac{N_{CatAcc}^{OH}}{V_{CatAcc}} \cdot \dot{V}_{CatOut} \tag{8}$$

1.1.2. Water Balance

In the developed model, concentration of water is also considered as it influences the cathode reaction potential. Water in the cathode mainly stems from the cathode feed. Some water molecules in the anode also move through the membrane to the cathode due to the concentration gradient between the anode and cathode [13, 15, 16]. The water balance in the anode and cathode is expressed as:

$$\frac{dN_{CatAcc}^{H_2O}}{dt} = (55.56 - C_{CatIn}^{NaOH}) \cdot \dot{V}_{CatIn} - C_{CatAcc}^{H_2O} \cdot \dot{V}_{CatOut} - \frac{A \cdot D^{H_2O}}{\delta} \cdot \left(C_{CatAcc}^{H_2O} - C_{AnAcc}^{H_2O} \right) \tag{9}$$

$$\frac{dN_{AnAcc}^{H_2O}}{dt} = (55.56 - C_{AnIn}^{NaCl}) \cdot \dot{V}_{AnIn} - C_{AnAcc}^{H_2O} \cdot \dot{V}_{AnOut} + \frac{A \cdot D^{H_2O}}{\delta} \cdot \left(C_{CatAcc}^{H_2O} - C_{AnAcc}^{H_2O} \right) \qquad (10)$$

where :

D^{H_2O} – Diffusion coefficient of H_2O molecule in the membrane $(2 \cdot 10^{-10}$ m^2/s)[1].

1.1.2. Chloride Ion Balance

In the chlor-alkali cell, chloride ions enter with the anode feed, which is a NaCl solution. The chloride ions in the anolyte are consumed by the anode cell reaction to produce chlorine gas. The reaction rate is estimated by counting the rate of electrons transferred to the chloride ion in the anolyte – this is commonly known as the electric current. So, the developed material balance model describes accumulated chloride ions in the anolyte using the following expression:

$$\frac{dN_{AnAcc}^{Cl}}{dt} = C_{AnIn}^{NaCl} \cdot \dot{V}_{AnIn} - \frac{i \cdot A_{el}}{2F} - \frac{N_{AnAcc}^{Cl}}{V_{AnAcc}} \cdot \dot{V}_{AnOut} \qquad (11)$$

1.2. Energy Consumption Model

The chlor-alkali process consumes electrical energy from an external power supply. Cell voltage is one of most important process variables that defines the energy consumption of the process. In the developed model, the required cell voltage is the accumulation of the following:
- standard electrode potential,
- activation overpotential,
- Ohmic overpotential drop in the membrane, electrolytes, electrodes and conductors.

This cell voltage model is described in the following equations:

$$V_{cell} = E + \mu_{act} + \mu_{ohm} \qquad (12)$$

$$E = E_{An}^0 - E_{Cat}^0 + \frac{R \cdot T}{2 \cdot F \cdot \alpha} \left(ln \left(\frac{\sqrt{p_{an}^{Cl_2}}}{C_{AnAcc}^{Cl}} \right) - 0,5 \, ln \left(\frac{\left(C_{CatAcc}^{H_2O} \right)^2}{p_{Cat}^{H_2} \cdot C_{CatAcc}^{OH}} \right) \right) \qquad (13)$$

$$\mu_{act} = \frac{R \cdot T}{2 \cdot F \cdot \alpha} ln \left(\left(\frac{i}{2i_{an}^o} + \sqrt{\frac{i}{\left(2i_{an}^o + 1\right)^2}} \right) \left(\frac{i}{2i_{cat}^o} + \sqrt{\frac{i}{\left(2i_{cat}^o + 1\right)^2}} \right) \right) \qquad (14)$$

$$\mu_{ohm} = i \cdot A \cdot R_{cell} \qquad (15)$$

1.3. Modelling and Simulation Process

The overview modelling and simulation process is shown by Fig. 3. All of the model components are developed and integrated in the MOSAIC modelling environment. Then, the developed model is simulated in Matlab. The simulation results are discussed further in the subsequent subtitles.
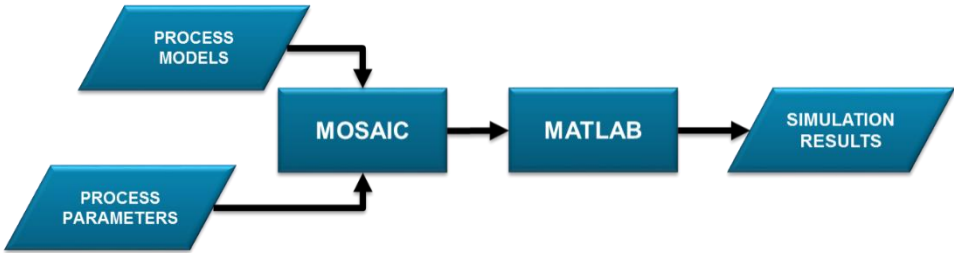
Fig. 3 Modelling and Simulation Process Diagram

3. Model Validation

A model validation is performed by comparing steady-state simulation data with experimental data provided by [4]. The model is constructed in MOSAIC and then simulated in Matlab.

Dias [4] measured some variables from a laboratory-scale chlor-alkali electrolyser to investigate and characterise the membrane cell. The comparison results are expressed in the Fig.4. It shows the polarisation curve of the chlor-alkali cell model and the chlor-alkali electrolyzer. These figures show that the polarization curves of both display a similar trend, although there is an offset between the model values and the experiment values.
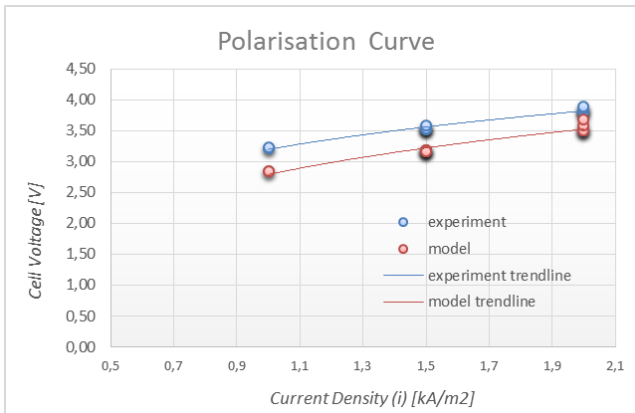
Fig. 4 Polarisation curve of chlor-alkali cell model and chlor-alkali cell electrolyzer

The offset emerges due to the fact that the cell voltage model does not consider the hydrodynamics inside the cell compartment. Some references [4, 6, 7, 8] mentioned that in the experimental cell, the existence of bubbles inside the cell compartment influences the cell voltage. Fig. 5(a) shows that cell voltage tends to increase when the gas void fraction increases – this also increases the difference between the cell voltage and its theoretical value.

Some references [4, 6, 9, 10, 11, 12] mentioned that at the same current density, increasing the volume rate through the cell compartment increases the electrolyte circulation and as a result, decreases the electrolyte resistance due to improved gas removal. As expected, the increase of the volume rate into the cell compartment tends to reduce the offset between the model and experimental data, as shown in Fig. 5(b).

(a)

(b)
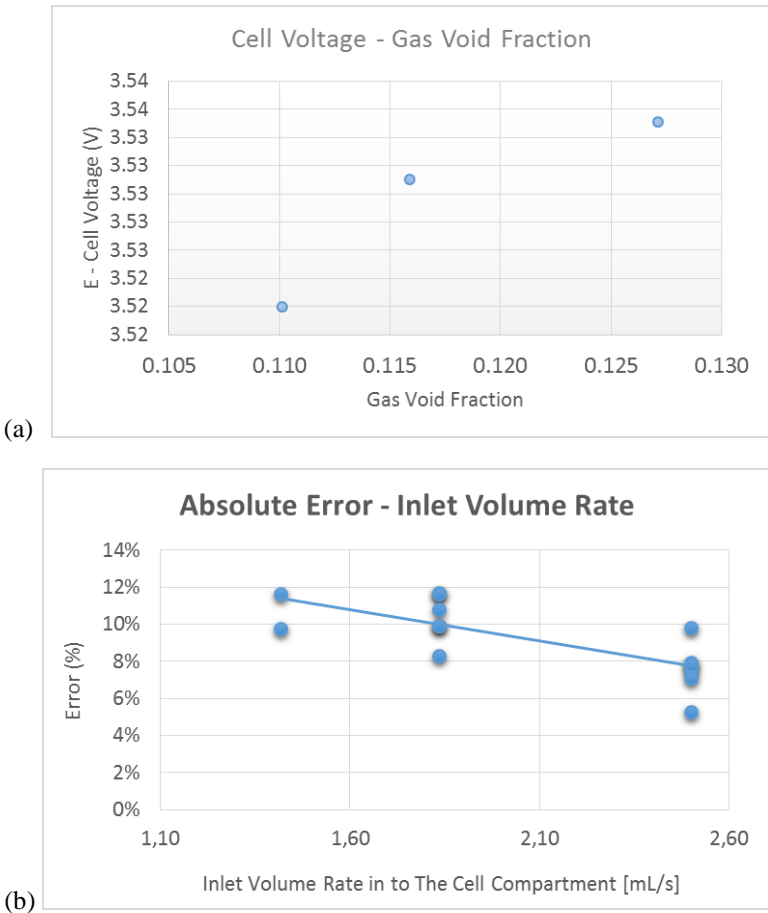
Fig. 5 (a) Cell voltage compared to gas void fraction; (b) Absolute error (model bias) compared to gas void fraction

4. Simulation

Simulations are performed to investigate the dynamic behaviour of the cell when the cell's voltage increases. In this simulation, operation voltage is increased from 0 V to 4 V. The cell is operated in voltage driven mode. The electrolyte volume during the simulation is kept constant. Inlet and outlet volume rates are also constant and have equal values. The simulation parameters are listed in table 1.

Table 1

Simulation Parameters

Process Parameter	Value
[NaCl] at anode inlet (kmol/m^3)	5
[NaOH] at cathode inlet (kmol/m^3)	10
A_{el} / Electrode effective area (m^2)	1
A / Membrane effective area (m^2)	1
$\dot{V}_{AnIn}$, $\dot{V}_{AnOut}$, $\dot{V}_{CatIn}$, $\dot{V}_{CatOut}$ (m^3/s)	$1 \cdot 10^{-3}$; $0.5 \cdot 10^{-3}$; $0.2 \cdot 10^{-3}$
V_{Cat}, V_{An} / volume anolyte and catholyte (m^3)	$5 \cdot 10^{-2}$
α	0.5
D^{Na}	$4 \cdot 10^{-9}$
D^{H2O}	$2 \cdot 10^{-10}$
$E_{An}^0 - E_{Cat}^0$ (V)	2.2
V_{cell} (V)	4
R_{cell} (Ohm)	7.33e^{-5}
R (m^3.kPa/ K.kmol)	8.314
T (K)	363.0
i_{an}^0 (kA/m^2)	$1 \cdot 10^{-10}$
i_{cat}^0 (kA/m^2)	$3 \cdot 10^{-9}$
i / current density (kA/m^2)	0.5 – 2.0

Results of the simulation are shown by Fig. 6, Fig. 7, and Fig. 8. The results show that the process model is a 1st order dynamic system. These results are expected since material transport in the process, which has a1st order dynamic, has the longest time constant compared to the others processes in the electrolysis. Based on these results, it can be concluded that the material transport dictates the process kinetics. This can be seen in Fig.6, which displays current density charts for three different electrolyte circulation rate values (*Vdot*). The electrolyte circulation rate represents the inlet and outlet volume rate of electrolytes (*Vdot*) in the simulation.
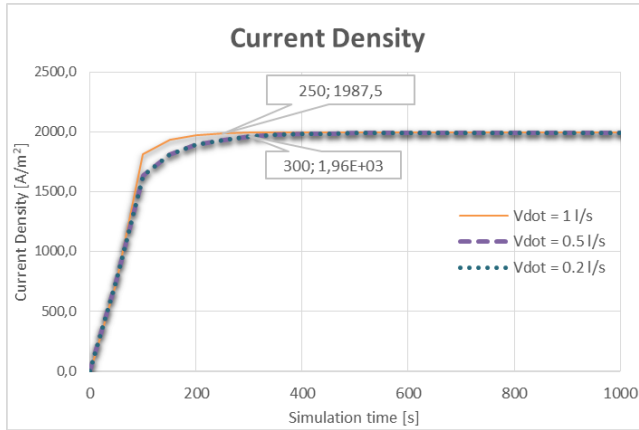
Fig. 6. Current density of simulated chlor-alkali membrane cell

Fig. 6 also shows that higher circulation rates shortens the process' response time. The process' settling time, the time for achieving a steady state, is 250 seconds for a circulation rate of 1 l/s. The settling time increases to 300 seconds for a lower circulation rate at 0.5 l/s.

Fig. 7 shows components of the cell's voltage during the simulation. The figure shows that the decomposition voltage (E) dominate the proportion of total cell voltage. The voltage's value at steady state is lower than its value in the initial condition. The voltage reduction occurs because in the steady state condition the relative activity of the reactants are higher compared to their relative activity at time point zero. The others voltage components, the activation and ohmic voltage, increase along with the increase of electrolysis current.
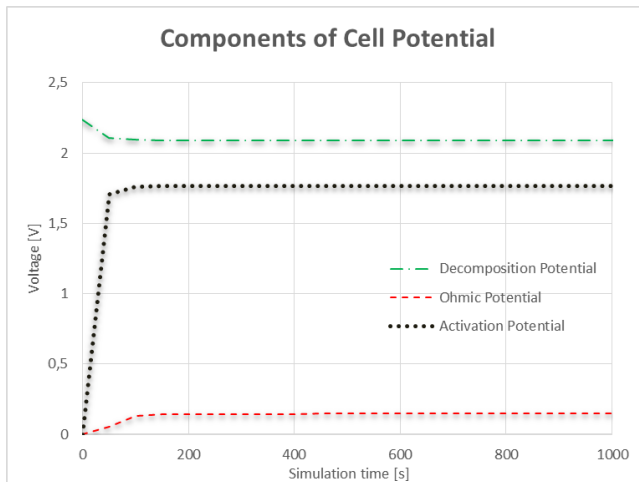
Fig. 7. Decomposition potential, activation potential and ohmic potential of chlor-alkali membrane cell, at $\dot{V} = 1 \; l/s$

Fig. 8 displays the dynamic of the production rate of chlorine gas. The production rate is linear to the current density given that the current efficiency in the model is 100%.
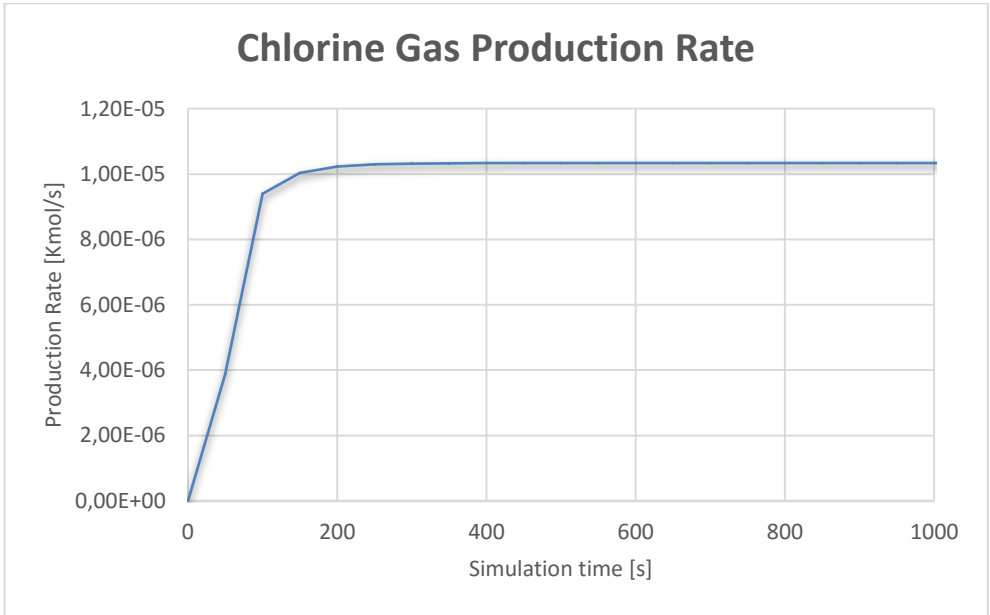
Fig. 8 Cl$_2$ gas production rate, at $\dot{V} = 1\ L/s$

5. Conclusion

In order to investigate the demand response potential of the chlor-alkali membrane process, a dynamic process model of the chlor-alkali membrane process has been developed in the MOSAIC modeling environment and solved in Matlab.

The model considers the dynamic behaviour of the material balance and the relationship between the cell voltage, current density, and ion concentrations in the electrolyte. For the validation, the model shows similar trends to experimental data. However, an offset exists in the voltage value predictions especially at high current density in comparison to lab-scale experimental data. This offset is caused by the simplification of the hydrodynamic behaviour in the model.

The simulation of the developed model shows that material transport dictates the process dynamics. The simulated process achieves steady state approximately after 250 seconds, which increases for lower reactant circulation rates.

For future work, it is important to include a current efficiency estimation model and an ohmic resistance model in the process model in order to achieve a more comprehensive description of the process' dynamic behaviour.

Nomenclature

$\dot{N}_{CatOut}^{H2}$	– production rate of H_2 in the cathode cell, kmol/s,
$\dot{N}_{AnOut}^{Cl2}$	– production rate of Cl_2 in the anode cell, kmol/s,
I	– electrolysis current, kA
F	– faraday constant : 96'485, kCoulomb/kmol·e,)
V_{CatAcc}	– accumulative volume of catholyte, m^3,
$\dot{V}_{CatIn}$	– volume rate of cathode inlet, m^3/s,
$\dot{V}_{CatOut}$	– volume rate of cathode outlet, m^3/s,
$\dot{V}_{AnIn}$	– volume rate of anode inlet, m^3/s,
$\dot{V}_{AnOut}$	– volume rate of anode outlet, m^3/s,
N_{CatAcc}^{Na}, N_{AnAcc}^{Na}	– mole quantity of Na^+ ion in catholyte and anolyte, kmol,
C_{CatIn}^{NaOH}	– concentration of NaOH in the catholyte feed, kmol/m^3,
C_{AnIn}^{NaCl}	– concentration of NaCl in the anolyte feed, kmol/m^3,
C_{AnAcc}^{Na}	– concentration of Na^+ ion in the anolyte, kmol/m^3,
C_{CatAcc}^{Na}	– concentration of Na^+ ion in the catholyte, kmol/m^3,
$\dot{V}_{CatIn}$, $\dot{V}_{AnIn}$	– feeding rate in the cathode and anode compartment, m^3/s,
$\dot{V}_{CatOut}$, $\dot{V}_{AnOut}$	– outlet rate of the cathode and anode compartment, m^3/s,
A	– ion diffusion area in the membrane, 10^{-2} m^2,
D^{Na}	– diffusion coefficient of Na^+ ion in the membrane, $4 \cdot 10^{-9} m^2$/s [1],
δ	– membrane thickness, $2.5 \cdot 10^{-4}$ m [4],
N_{CatAcc}^{OH}	– mole quantity of OH^- ion, kmol,
C_{CatIn}^{NaOH}	– concentration of NaOH in the catholyte feeding, kmol/m^3,
$\dot{V}_{CatIn}$	– feeding rate in the cathode compartment, m^3/s,
$\dot{V}_{CatOut}$	– outlet rate of the cathode compartment, m^3/s,
N_{AnAcc}^{Cl}	– accumulated Cl^- ion in the anode, kmol,
C_{AnIn}^{NaCl}	– concentration of NaCl in the anode feeding, kmol/m^3,
$\dot{V}_{AnIn}$	– feeding rate in the anode, m^3/s,
$\dot{V}_{AnOut}$	– outlet rate of the anode, m^3/s,
V_{cell}	– cell voltage, Volt,
E	– standard electrode potential, Volt,
μ_{act}	– activation overpotential, Volt,
μ_{ohm}	– Ohmic overpotential, Volt,
$E_{An}^0 - E_{Cat}^0$	– standar electrode potential for anode and cathode, Volt,
α	– charge transfer coefficient, symmetry factor = 0.5,

T	– temperature, K,
R	– ideal gas constant: 0.008314, $m^3 \cdot Pa/(K \cdot kmol)$,
i	– current density, kA/m^2,
i_{an}^0	– exchange current density of anode, $1 \cdot 10^{-10}$ kA/m^2,
i_{cat}^0	– exchange current density of cathode, $3 \cdot 10^{-9}$ kA/m^2.

R e f e r e n c e s

[1] Friedfeld B.A. (author), Wellington T.C. (editor), *Modern Chlor-Alkali Technology*, vol. 5, Springer Netherlands 1992.

[2] TILAK B.V., Chen C.-P., *Calculation of the current efciency of the electrolytic sodium chlorate cells*, Journal of Applied Electrochemistry, vol. 29, 1999, 1237-1240.

[3] Schmittinger P., Florkiewicz T., Curlin L.C., Luke B., et.al., *Ullmann's Encyclopedia of Industrial Chemistry – Chlorine*, Wiley-VCH Verlag GmbH & Co. KGaA, Weinheim 2012.

[4] Dias, A.C.d.B.V., *Chlor-Alkali Membrane Cell Process*, PhD Disertation, Chemical and Biological Engineering – University of Porto 2013.

[5] Hardee K.L., *A Simple procedure for evaluating membrane electrolyzer performance*, Modern Chlor-Alkali Technology, vol. 6, 1995, 235-242.

[6] Hine F., Yasuda M., Nakamura R., Noda T., Journal of The Electrochemical Society vol. 122, 1975, 1185-1190.

[7] Xiong Y., Jialing L., Hong S., Journal of Applied Electrochemistry, vol. 22, 1992, 486-490,.

[8] Mandin Ph., Aissa A., Roustan H., Hamburger J., Picard G., Chemical Engineering and Processing, vol. 47, 2008, 1926-1932.

[9] Mirzazadeh T., Mohammadi F., Soltanieh M., Joudaki E., Chemical Engineering Journal, vol. 140, 2008, 157-164.

[10] Kaveh N. S., Ashrafizadeh S.N., Mohammadi F., Chemical Engineering Research and Design, vol. 86, 2008, 461-472.

[11] Jalali A.A., Mohammadi F., Ashrafizadeh S.N., Desalination, vol. 237, 2009, 126-139.

[12] Kaveh N. S., Mohammadi F., Ashrafizadeh S.N., Chemical Engineering Journal, vol 147, 2009, 161–172.

[13] Marangio F., Santarelli M., Calì` M., *Theoretical model and experimental analysis of a high pressure PEM water electrolyser for hydrogen production*, International Journal of Hydrogen Energy, vol. 34, 2009, 1143-1158.

[14] Auer, J., Anatolitis, V., *The Changing energy mix in Germany*. Deutche Bank Research, Curent Issues – Natural Resources, June 26, 2014.

[15] Bird R.B., Stewart W.E., Lightfoot E.N., *Transport phenomena 2nd ed*. John Wiley & Sons Inc., 2002.

[16] Springer T.E., Zawodzinski T.A., Gottsfeld S., *Polymer electrolyte fuel cell model*, Journal of Electrochemical Society, vol. 138, 1991, 2334-2341.

ANETA CELAREK[*], STANISŁAW KUCIEL[**]

AN EVALUATION OF THE CHANGES TO THE MECHANICAL PROPERTIES OF POLYMER BIOCOMPOSITES RESULTING FROM THEIR LONG-TERM STORAGE AT LOW TEMPERATURES

OCENA ZMIAN WŁAŚCIWOŚCI MECHANICZNYCH BIOKOMPOZYTÓW POLIMEROWYCH W PROCESIE DŁUGOLETNIEGO SKŁADOWANIA W NISKICH TEMPERATURACH

Abstract

This paper presents an analysis of the properties of biocomposites that were stored for four years in the refrigerator at 6°C and were investigated for detailed information of mechanical properties like tensile strength and bending. The study was based on test results obtained in 2011. Comparison of changes in the structure of composite materials was carried out an analysis of SEM image. Matrix filling materials were made of wood fibres and tuff.

Keywords: biodegradable composites, strength properties, stores in low temperature

Streszczenie

W artykule przedstawiono analizę właściwości materiałów kompozytowych, które przecho-wywano przez cztery lata w lodówce w temperaturze 6ºC. Wykonano badania wytrzymałoś-ciowe w tym, m.in. testy wytrzymałości na rozciąganie i zginanie. Przeprowadzono również porównania zmian struktury materiałów kompozytowych na podstawie wykonanych zdjęć SEM. W próbkach, jako napełniacz zastosowano mączkę drzewną i tuf wulkaniczny.

Słowa kluczowe: kompozyty biodegradowalne, właściwości wytrzymałościowe, przechowy-wanie w niskich temperaturach

[*] MSc. Eng. Aneta Celarek, Institute of Thermal and Process Engineering, Faculty of Mechanical Engineering, Cracow University of Technology.

[**] PhD. Eng. Stanisław Kuciel, Institute of Material Engineering, Faculty of Mechanical Engineering, Cracow University of Technology.

1. Introduction

Given the state of the environment and the widespread concern for its protection, industry strives to develop methods for the preparation of biocomposites using plastics and natural energy sources. Thus, the development of new plastic products has occurred as a result of desire to protect the environment. These materials have low impact on the environment. Cellulose fibres, starch and wood fibres may be used in production of the natural raw material. The substance with the greatest potential for use is starch because of its low price and wide availability. An additional advantage of starch is that it is highly renewable [7].

Biocomposites form a group of materials where at least one component is biodegradable or a bio-derivative. Frequently, a component has these two features at the same time. To a group of composites we may include polymers of petrochemical origin and polymers with additives natural or synthetic fibers. Fibres are obtained from plants. They may also be, for example, the shells of crustaceans or chitosan, fungi or bacteria. The most interesting group of composites is one considered to be those based on starch and polylactide. These biocomposites are well established on the Polish market and are already produced on a massive scale [3, 8].

The biocomposites includes thermosetting materials (during the manufacture have a plastic properties and can be easily formed) and thermoplastic materials (repeatedly formed in high temperature). In Fig1 the devision of distribution biocomposites are shown [2, 4].
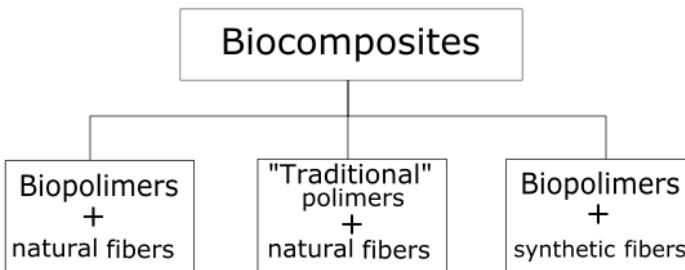
Fig. 1. General division biocomposites [1]

Composites are increasingly used in industry, they are used as decorative elements and components of household appliances. Examples include gears, garden hosepipes and sewer pipes. Composites also started to be incorporated into machines. Research is ongoing and its aim is to expand the use of biocomposites as elements of pressure devices, e.g. tubesheets.

2. Fillers (additives) used in investigated biocomposites

In these tests, the filler was made up of wood fibres and tuff. Below show the short characteristics:

- **Wood fibres –** the natural organic filler**.** These form part of a group of additives being used for the first time in the world. They are most commonly used as an additive for plastics which are of plant origin.

- **Tuff** – this is a natural, inorganic filler obtained from volcanic rock. It was created as a result of the deposition process, as well as the consolidation of products formed during volcanic eruptions.

In the investigation carried out for the 4 types of warps. The types of warp in the industry are identified as BioCérès® BC-LBI01, BioCérès® BC-LBI08, Bio-Flex® F6510 and Biograde® C9555. The information about the particular composition of the warp are kept secret by global companies. For each type of the warp created three types of samples: without additives, with 25% mas wood fibres and with 25% mas tuff. A total were carried out analysis of 12 types of samples which were shown in Tab 1.

T a b l e   1

The compositions and marking tested polymer composites

Lp.	Marking samples	Type of warp	Wood fibres [% mas]	Tuff [% mas]
1	**L1**	BioCérès® BC-LBI01 (wheat starch)	-	-
2	**L1M**		25	-
3	**L1T**		-	25
4	**L8**	BioCérès® BC-LBI08 (wheat starch)	-	-
5	**L8M**		25	-
6	**L8T**		-	25
7	**FF**	Bio-Flex® F 6510 (polylactide + polyester)	-	-
8	**FFM**		25	-
9	**FFT**		-	25
10	**BC**	Biograde® C 9555 (polycellulose)	-	-
11	**BCM**		25	-
12	**BCT**		-	25

3. Test results

The tests were carried out on samples that were stored for 4 years in a refrigerator at 6°C. They were intended to demonstrate the effect of storage conditions on the mechanical properties of the polymer biocomposites during periods of long-term storage.

The mechanical properties of the composites were tested on a MTS 030 Criterion extensometer testing machine. The mechanical properties were determined on the basis of PN-EN ISO 527-1 using a sample in the shape of a dumb-bell – the cross-sectional dimensions were 10×4 mm. The statistic tensile test was performed at room temperature. The investigation carried out of basic mechanical properties: tensile strength σ_m,

E modulus, elongation at break ε_r. Used in research polymer matrix belong to three groups of polymers. The first two (BioCérès® BC-LBI01 and BioCérès® BC-LBI08 are based on wheat starch. The difference between these two webs is primarily the varying content of plasticizers. Two further groups of biopolymers (Bio-Flex® F6510 and Biograde® C9555) are manufactured by the German company, FKuR. The same group of biopolymers (Bio-Flex®) consists of a mixture of polylactide and polyesters in different ratios, depending on the variety. Genre Bio-Flex® F6510 can be formed during of ejaculation and process of blowing up. Biograde® C9555 biopolymer is selected from cellulose-based matrices [5, 6].
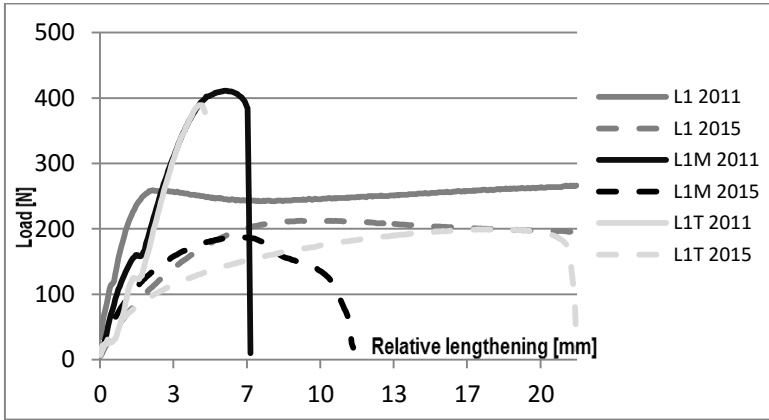
Fig. 2. Stress- strain curve L1 before (2011) and after (2015) storage in low temperature

For each type of samples decrease of the yield strength and tensile strength were noted. The samples with additives change the shape of the graph were observed, lower values of maximum force and increase in value of relative lengthening. The samples without additives were observed large decrease in the value of tensile strength. The graphs shape of the samples before storage is similar.
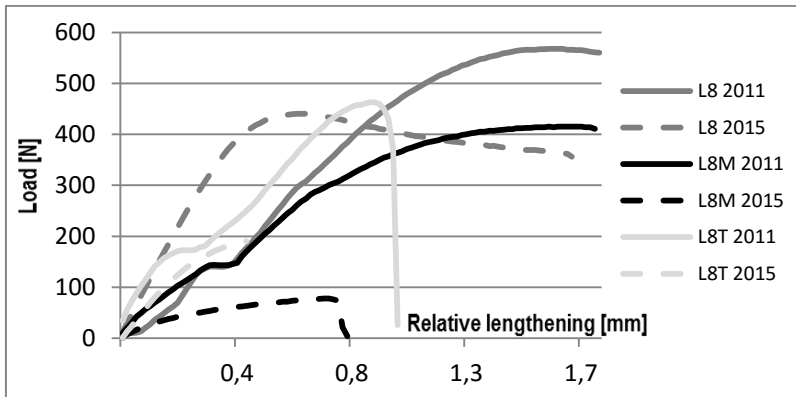
Fig. 3. Stress- strain curve L8 before (2011) and after (2015) storage in low temperature

After four years storage change of the shape of the graph for the type of samples without additives were observed. In this type of samples we observed increase the yield strength and tensile strength. The structure was strengthened. The samples with additives were observed reduction value of relative lengthening.
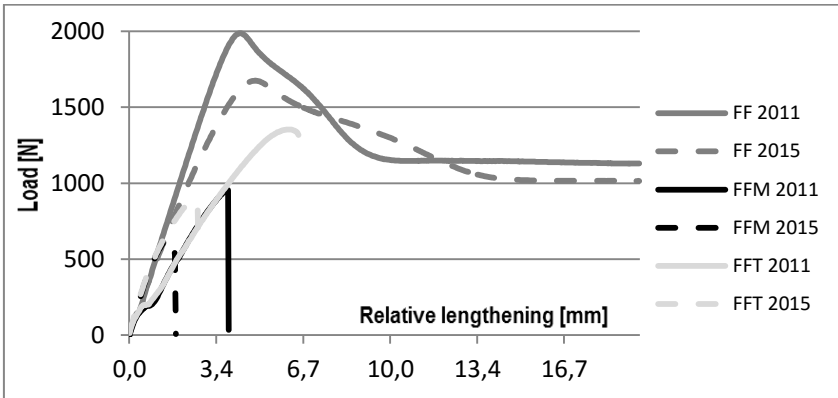
Fig. 4. Stress- strain curve FF before (2011) and after (2015) storage in low temperature

After four years of storage decreases of tensile strength and yield strength and tensile strength were observed. For samples with additives were observed lower relative lengthening. The general conclusion is that the polymers based on cellulose practically no damping a natural and mineral (inorganic) additives. Therefore, the cellulose-based the warp is not used in the biocomposites.
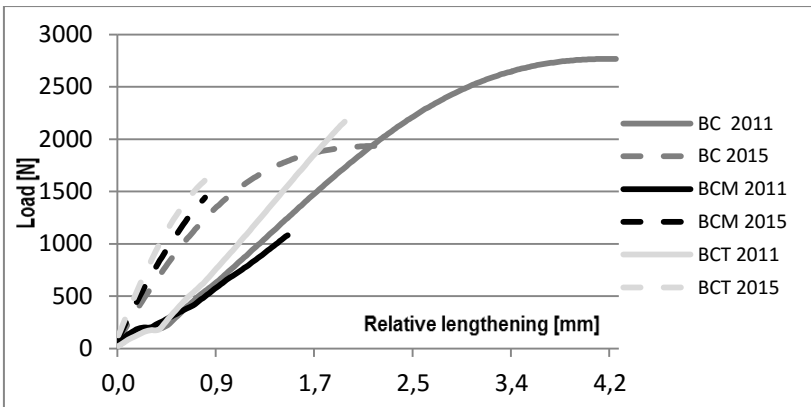
Fig. 5. Stress- strain curve BC before (2011) and after (2015) storage in low temperature

Again, note the decline in the value of tensile strength and yield strength of the samples without additives after the storage period. It is also noted that there was a significant reduction of the elongation of samples after storage. An interesting phenomenon is the tensile strength of the samples in polymers composite with wood fibres after storage.

4. SEM analysis

SEM images were made at the site of samples after fracture. Images were carried out of after static tensile test. The images were made by scanning electron microscope JOEL JSN5510LV and used of different magnifications (x100; x200; x500).

In Fig 5 are shown SEM images of one of the tested composites (L1M) taken before and after storage – the images were taken at different levels of magnification. Changes in the structure that have occurred over the years can be observed in these images; these changes in structure have an obvious negative impact on the strength of the samples.

In the images in Fig. 5, we can see:
- strong connection between the warp and additives after storage,
- the microstructures after storage in this type of samples were more developed surface,
- increase the area of the internal structure of the material,
- looser connections between the matrix and the reinforcement after storage.
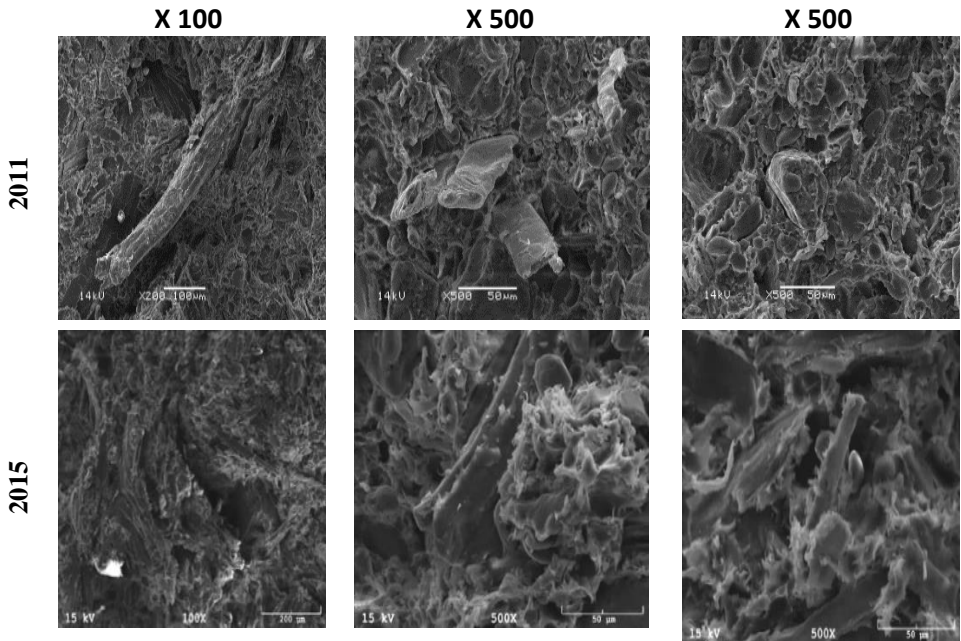
Fig. 6. Comparison of L1M samples before and after the four-year storage period

The following Tab 2 present all results of strength properties before and after storage.

The results of tests of selected strength properties before and after storage

Year	2011			2015		
Material	σ_m [MPa]	E [MPa]	ε_r [%]	σ_m [MPa]	E [MPa]	ε_r [%]
L1	8.02	808	51.7	4.88	487	70.1
L1M	9.22	1847	1.5	4.95	1341	1.1
L1T	10.64	2075	1.5	4.92	684	5.4
L8	14.72	2892	9.3	10.72	3114	1.1
L8M	10.68	2374	1.4	2.03	1303	0.5
L8T	9.68	4196	0.8	4.84	2184	0.45
FF	49.24	2916	127	34.35	2670	131.8
FFM	20.08	3550	1.6	19.91	3005	1.03
FFT	28.22	3609	1.4	23.30	3123	1.31
BC	67.34	6134	3.8	48.04	4601	2.13
BCM	22.36	6517	1.2	34.16	5488	0.76
BCT	44.74	9325	1.7	41.72	6836	0.86

where:

σ_m – is the tensile strength,

E – is the elastic modulus of material at design temperature,

ε_r – is the relative elongation.

5. Conclusion

Despite storage of samples at low temperatures and adverse conditions during the composting biodegradation was noted a decrease in the mechanical properties (tensile strength and yield strength). It confirmed the initial assumptions about the decrease in the value of the mechanical properties. However, there were exceptions described above where increases in the values for different types of thermoplastic polymer matrices and additives were noted.

The unplasticized thermoplastic starch (L8) is a low-biodegradable .The sample-based unplasticized thermoplastic starch (l8) with additives are more biodegradable. It does not depend on the type of supplement.

This is advantageous and resulted in a significant shortening of the life cycle of polymeric materials and the carbon cycle. The work pointed to the need for greater use of biodegradable materials in order to reduce waste and for improved utilisation of biological methods of recycling or composting. This is particularly important in the manufacture of disposable products and those which can easily penetrate the environment causing pollution.

R e f e r e n c e s

[1] Praca zbiorowa pod redakcją S. Kuciela i H. Rydarowskiego, *Biokompozyty z surowców odnawialnych*, Wydawnictwo Columbinum, Kraków 2012.

[2] Kuciel S., Celarek A.: *Polimer*, Nr 4, 2015.

[3] Shalaby W., Burg K.J.L., *Absorbable and Biodegradable Polymer*, CRC Press LLC 2004.

[4] Doli Y., Steinbuchel A., *Biopolymers*, Wiley – VCH Verlag GmbH, 2002.

[5] Kuźniar P., *Biodegradowalne kompozyty na osnowie polimerów z surowców odnawialnych modyfikowanych mączką drzewną lub mineralnym tufem,* Kraków 2010, praca magisterska.

[6] Kuźniar P., Kuciel S., *Biokompozyty z surowców odnawialnych,* PalstNews 4. 2011.

[7] Dyrektywa Parlamentu Europejskiego i Rady 94/62/WE z dnia 20 grudnia 1994r. w sprawie opakowań i odpadów opakowaniowych.

[8] Mohanty A.K., Misra M., Drzal L.T., *Natural Fibers. Biopolymers and Biocomposites*, CRC Press, Broken Sound Parkway, USA, 2005.

PIOTR CYKLIS, PRZEMYSŁAW MŁYNARCZYK[*]

CFD IMPULSE FLOW SIMULATION THROUGH SHAPED NOZZLES

SYMULACJA CFD PRZEPŁYWU IMPULSOWEGO W DYSZACH KSZTAŁTOWYCH

A b s t r a c t

Pressure pulsations in volumetric compressor manifolds are important issues in the compressor plant operation. For pressure pulsation attenuation, mufflers designed using the Helmholtz resonator approach are applied. Nowadays, the variable revolution speed compressors requires new design methods for pressure pulsation damping elements. One of the possibilities to attenuate the pressure pulsations is the introduction of specially shaped nozzles in the gas duct flow. In this paper, the impulse flow simulations conducted in FLUENT/ANSYS. The experimental validation of the simulation results is also presented.

Keywords: pressure pulsations, nozzle, simulation

S t r e s z c z e n i e

Pulsacje ciśnienia są ważnym problemem w instalacjach sprężarek wyporowych. Do projektowania tłumików pulsacji ciśnienia wykorzystuje się metodę Helmholtza Aktualnie coraz większe zastosowanie znajdują sprężarki o zmiennej prędkości obrotowej. Jedną z możliwości jest zainstalowanie dyszy tłumiącej. W artykule tym przedstawiono wyniki symulacji przepływu impulsowego w oprogramowaniu FLUENT/ANSYS Uzyskane wyniki zostały skonfrontowane z wynikami uzyskanymi na stanowisku badawczym.

Słowa kluczowe: pulsacje ciśnienia, dysze, symulacje

[*] Prof. PhD. DSc. Eng. Piotr Cyklis, MSc. Eng. Przemysław Młynarczyk, Institute of Thermal and Process Engineering, Faculty of Mechanical Engineering, Cracow University of Technology.

1. Introduction

Pressure pulsations in volumetric compressor installations are caused by the periodicity of compressor operation. This periodicity induces vibrations, noise and sometimes causes valve failures. In extreme cases, they may cause cracking of the pipelines. The standard method to attenuate pressure pulsation is to apply the Helmholtz theory for the design of mufflers [1, 2]. Such mufflers attenuate only narrow band frequencies close to the designed frequency. In the case of variable revolution speed compressors, this is not efficient since the pressure pulsations have to be attenuated for a wide range of frequencies. This is the reason why other possibilities for pressure pulsation damping are needed [3, 4]. An attenuation method which can be useful is the application of shaped nozzles. It has been found that the shape of the nozzle influences the attenuation of pressure pulsations; however, it also has an impact on the compression power requirement. The nozzle attenuation impact on the pulsation amplitudes is smaller than the Helmholtz resonator. However even 20% of the pulsation attenuation may be sufficient to fill standard requirements in some manifolds. The optimal choice of nozzle dimensions and shape needed to attenuate pressure pulsations requires experimental investigations or the application of a numerical simulation method. Experimental investigations have many disadvantages, and cannot be used in the installation design process for practical reasons. The worked-out CFD-based method consists of two simulations: an impulse excited flow to assess pulsation attenuation; a steady flow through the nozzle to assess increases in pumping power. In the literature, investigations regarding numerical nozzle fluid flow can be found. Some published results are shown in [5, 6 &7]. In this paper, impulse flow simulations using various models and methods conducted in FLUENT/ANSYS are compared. The experimental validation of the simulation results is also described.

2. Numerical model

All of the investigated simulations were conducted using the FLUENT/ANSYS software. For all cases, the 2D axisymmetric, compressible ideal gas isentropic flow model was used with the Reynolds-Stress turbulence model. The simulation was transient with a time step of 2-6 seconds. Impulse flow damping using the QUICK spatial discretisation scheme was conducted for different damping elements. The investigated nozzle shapes were the Venturi orifice, Venturi nozzle and hyperboloidal nozzle with an inner diameter of $d = 15$ mm. The investigated shapes are shown in Figure 1. The outer diameters of the nozzles are 35mm as the installation pipe has the same diameter. For the purpose of verification of the simulations results, experimental investigations were conducted for the same nozzle shapes.

The results obtained in simulations were spatially averaged at the inlet and outlet cross-section to obtain only time-dependent mass flow fluctuations. The output signal has a dampened harmonic form. In order to determine the damping coefficient, the attenuation curves were described by the equation:
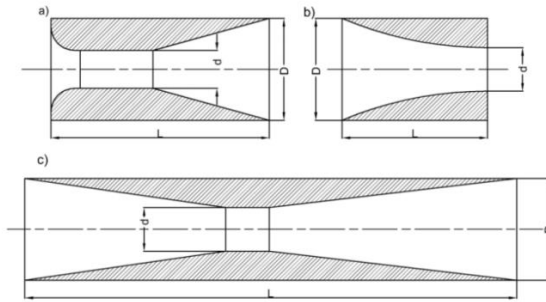
Fig. 1. The investigated geometries: a) Venturi nozzle, b) hyperboloidal nozzle, c) Venturi orifice

$$y(x) = A_0 \cdot e^{B \cdot t} \qquad (1)$$

where

$$B = \frac{\omega}{\zeta} \qquad (2)$$

$$\omega = \frac{2 \cdot \pi}{T} \qquad (3)$$

The curves have to be matched to the obtained signal.
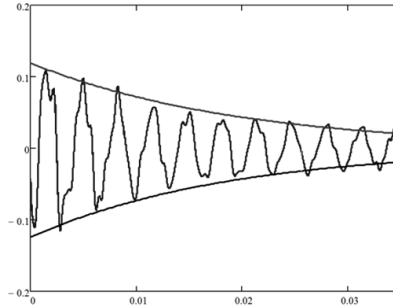
Fig. 2. Signal with both attenuation curves obtained using L-M method

To adjust the attenuation curves for the received signal, an algorithm using the Levenberg-Marquardt (L-M) method was developed. The algorithm is based on the extraction of signal maximum values points, of the time intervals equal to one period for the upper curve. The same procedure was applied for minimum values for the lower damping curve. Then, for the selected points, the curve described by equation $y(x) = A_0 \cdot e^{B \cdot t}$ is fitted using the L-M method. An example of the attenuation curve fit is shown in figure 2.

The signal analysis, using the L-M method, requires further improvement to obtain the damping factor. If the simulation time is too short, the damping curve will not represent the signal attenuation. Besides the first high amplitudes can be misleading and the signal

harmonizes after some periods. The signal after the fast Fourier transform was analysed only for a selected number of the first frequencies.

The numerical model has to be simple and fast to compute; therefore, only four necessary boundary conditions were applied:

- Mass flow Inlet – where the mass flow impulse excitation is 0.1 kg/s. The duration of the impulse excitation is equal to the first, one time step. For the rest of these transient simulation steps, the mass flow inlet boundary is defined as zero. The backflow temperature, if it does occur, is defined as 350 K – close to the flow temperature during experiments.
- Pressure outlet – where the pressure at the outlet is defined as the arithmetical average between the pressure outside the domain and the last cell inside the domain. The backflow temperature, if it does occur, is defined as 350 K.
- Wall – where the tangential stresses are included in the momentum conservation equation. There is no slip condition defined.
- Axis – to determine the appropriate physical value for a particular variable at a point on the axis, the software uses the cell value in the adjacent cell.

An appropriate mesh was prepared for each geometry. For the 2D axisymmetric simulations, the model contains the nozzle shape and a straight pipe fragment. The same geometry as on the test stand installation. In Figure 3, the simulated elements of the mesh are presented.
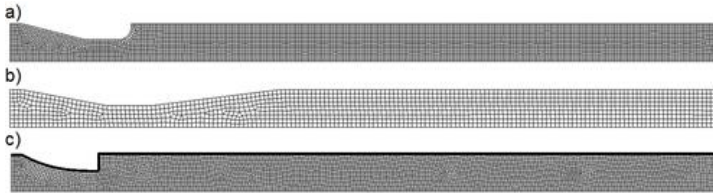
Fig. 3. The mesh models for a) Venturi nozzle, b) Venturi orifice, c) Hyperboloidal nozzle

The geometry and mesh were the same for each shape for all simulations. In Figure 3, three different but still correct meshes are presented. The results of the impulse flow simulation is not strongly dependent on the grid size, the near wall layers addition etc [8]. The most important issue was to obtain the structured mesh, according to the QUICK discretisation scheme requirements. For the presented geometries, a good quality mesh was obtained for approximately 3,500 cells with a cell size ~1 mm.

3. Simulation results

For the selected geometries, numerical simulations were conducted. For each element, the results were spatially averaged at the outlet cross-section to obtain time-dependent mass flow fluctuations [9]. The damping coefficients were estimated using the L-M method with three different approaches. For all approaches, the signal was modified to a number of

first frequencies using fast Fourier transform. The data generation for the first 64 frequencies is obtained using two methods, The third method was used only for the first eight frequencies. In the first method (Method 1) the obtained signal is analysed without any limitations, for all periods. The second method (Method 2) has some limitations, the signal is analysed for only nine periods, and the first lower amplitude peak is not taken into consideration as is shown in Figure 4.
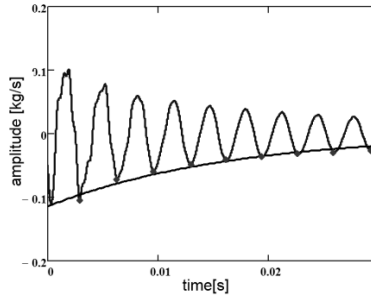
Fig. 4. The points defining the lower attenuation curve for the nine-period analysis, disregarding the first lower amplitude peak

The first eight frequencies had the most significant impact on the signal in the third method (Method 3), therefore only the signals for first eight frequencies were analysed. In the Fig. 5 two signals are presented: the signal obtained in simulation and the signal for the first eight frequencies after FFT.
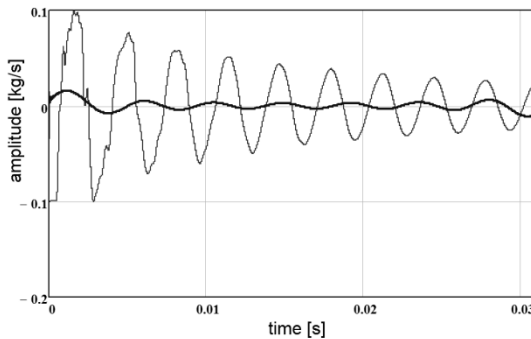
Fig. 5. The signal: ∧ from simulations; ⁓ after the FFT based reduction

The damping factor calculated for the damping curves obtained in the simulations for the different geometries using the described approach are shown in Figures 6-8. In these figures, the results for the impulse propagation through the nozzles are related to the result obtained for the straight, empty pipe geometry. To verify the obtained results, experimental investigations was performed.
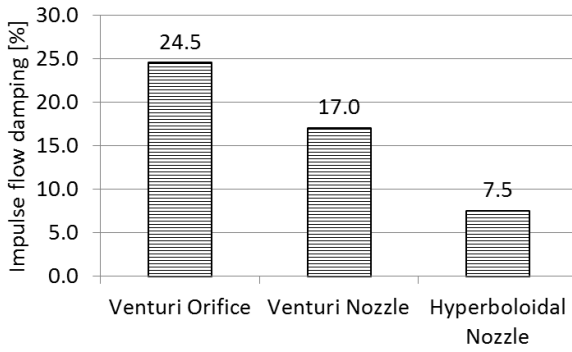
Fig. 6. The impulse flow damping related to the empty pipe (Method 1)
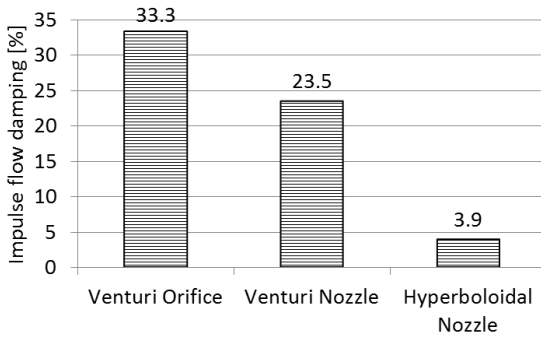
Fig. 7. The impulse flow damping related to the empty pipe (Method 2)
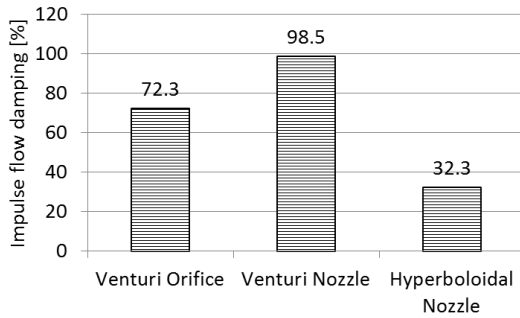
Fig. 8. The impulse flow damping related to the empty pipe (Method 3)

4. Experimental verification

The experimental investigations were performed on a special test stand which was devised to measure, in particular, pressure pulsations in the screw compressor discharge manifold. The test stand and the tests themselves were described in detail in publications [9, 10]. The effect of the nozzle on the pressure pulsations was measured on the test stand for different compressor revolution speeds. In this paper, the average values of the pressure pulsation attenuation for three different geometries are presented. In Figure 9, the pressure pulsations peak-to-peak value decrease for different applied nozzles are shown, related to the empty pipe pulsations for the compressor revolution speed equal to 1615 rev/min.
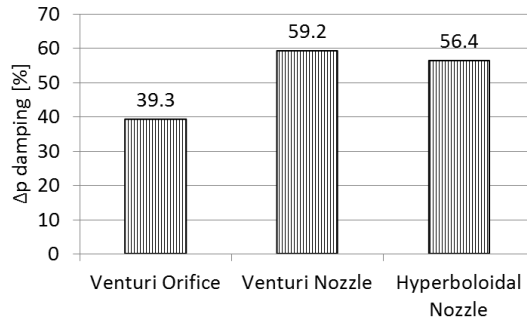
Fig. 9. The pressure pulsations peak-to-peak value decrease compared to the empty pipe pulsations

An exact match of simulation and experimental results cannot be expected in terms of numbers, since the simulation results for the impulse function are related to all frequencies The experimental results are limited only to the chosen investigated frequencies. However, in the case of the third method, the relationships between the compared results for each shape and dimension are similar for both the simulation and experiments. It can be seen that the influence of the hyperboloidal nozzle on the impulse flow damping is under-estimated for all three methods used in the analysis. In this case, the numerical model has to be improved.

5. Conclusions

Numerical simulations of the impulse flow damping coefficient for three different nozzle shapes and three different methods of analysis of the obtained results were presented. The damping factors for the three geometries, calculated using different approaches, were compared with the pressure pulsation damping peak-to-peak values obtained experimentally. It was shown that the method of the 2D simulation results analysis affects the calculated damping coefficient; however, the numerical model still has the highest impact on the coefficient value. The results obtained, using shown numerical simulations and analysis method, corresponds with the experimental results of nozzle pulsations damping. Further method development is necessary to obtain qualitative comparison.

82

Nomenclature

B – damping coefficient for exponential curve [Hz]
ξ   – damping factor [dimensionless]
ω   – natural frequency of the system [Hz]
A_0 – initial amplitude value [Pa]
T – basic period of free pulsation frequency [s]

References

[1] Andersen K.S., *Analyzing Muffler Perfomance Using the Transfer Matrix Method*, COMSOL Conference, Hannover 2008.
[2] Ma Y.-C., Min O.-K., *Pressure calculation in a compressor cylinder by a modified new helmholtz modelling*, Journal of Sound and Vibration, vol. 243, 2001, 775-796.
[3] Lokitsangtong M., Murakami S., Iijima T., *Acoustical Characteristics of Single-Resonator-Type Silencers*, Proceedings of the School of Engineering, Tokai University, Series E 31, 2006, 39-44.
[4] Bilawchuk S., Fyfe K.R., *Comparison and implementation of the varoius numerical methods used for calculationg transmission loss in silencer systems*, Applied Acostics, vol. 64, 2003, 903-916.
[5] Sadamoto A., Tsubakishita Y., Murakami Y., *Sound attenuation in circular duct using slit-like short expansion of eccentric and/or serialized configuration*, Journal of Sound and Vibration, vol. 277, 2004, 987-1003.
[6] Herrmann J., Koreck J., Maess M., Gaul L., von Estorff O., *Frequency-dependent damping model for the hydroacoustic finite element analysis of fluid-filled pipes with diameter changes*, Mechanical Systems and Signal Processing, vol. 25, 2011, 981-990.
[7] Lee S.-H., Ih J.-G., *Effect of non-uniform perforation in the long concentric resonator on transmission loss and back pressure*, Journal of Sound and Vibration, vol. 311, 2008, 280-296.
[8] Cyklis P., Młynarczyk P., *Nozzle suppressed pulsating flow simulation issues*, Technical Transactions, 1-M, 2015, 21-29.
[9] Cyklis P., Młynarczyk P., *An innovative simulation method for the estimation of the nozzle pressure pulsation attenuation*, Journal of Vibration and Control, 2015, doi: 10.1177/1077546315619534.
[10] Młynarczyk P., *Experimental investigations of pressure pulsations damping in screw compressor system,* Proceeding of the Student's conference, Prague 2014.

PAVEL DITL, RADEK ŠULC*

DISPERSION KINETICS MODELLING

MODELOWANIE KINETYKI DYSPERGOWANIA

A b s t r a c t

Stirred tanks for dispersion, the pre-dispersion of two immiscible liquids or particulate solid-liquid suspension are extensively used in the chemical, food, pharmaceutical and metallurgical industries, for purposes such as suspension/emulsion polymerisation, heterogeneous/phase-transfer catalytic chemical reactions, paint production and hydrometallurgical solvent extraction. The aim of this paper is to propose the simple dispersion model enabling the prediction of particle size changes over time and taking into account the type of breakup mechanisms, the non-homogeneity of local turbulent energy dissipation rate in an agitated vessel and the effect of the number of times the liquid passes through the impeller and the impeller zone. The model was successfully tested on data published by Ditl et al. (1981).

Keywords: dispersion kinetics modelling, solid particle-liquid dispersion, tooth impeller

S t r e s z c z e n i e

Mieszalniki do sporządzania mieszanin lub dyspergowania płynów niemieszających się są szeroko stosowane w przemyśle chemicznym, spożywczym, farmaceutycznym, metalurgicznym i wielu innych gałęziach przemysłu. Celem pracy jest przedstawienie prostego modelu dyspersji umożliwiający prognozowanie zmian wielkości cząstek w czasie z uwzględnieniem różnych mechanizmów rozpadu, niejednorodności lokalnych burzliwych szybkości rozpraszania energii w mieszalniku oraz liczby przejść płynu przez obszar mieszadła. Model ten został z powodzeniem przetestowany na danych opublikowanych przez Ditl et al. (1981).

Słowa kluczowe: modelowanie kinetyki dyspersji, układ dyspersyjny cząstki ciała stałego-płyn, mieszadło ścinające

* Prof. PhD. DSc. Eng. Pavel Ditl, Assoc. prof. PhD. DSc. Eng. Radek Šulc, Department of Process Engineering, Faculty of Mechanical Engineering, Czech Technical University in Prague.

1. Introduction

Stirred tanks for dispersion, the pre-dispersion of two immiscible liquids or particulate solid-liquid suspension are extensively used in the chemical, food, pharmaceutical and metallurgical industries, for purposes such as suspension/emulsion polymerisation, heterogeneous/phase-transfer catalytic chemical reactions, paint production and hydrometallurgical solvent extraction [1-3]. Mixing plays a fundamental role in these systems controlling processes such as blending, homogenisation, mass transfer and chemical reactions etc. The quality of product, yield and economy of the processes is therefore significantly affected by mixing. Insufficient or excessive mixing may lead to wastage of processing time and raw material and/or the formation of by-products [4, 5].

The prediction of mean drop/particle size and drop/particle size distribution (DSD) is vital for emulsification, suspension polymerisation, solid particle dispersion or crystallisation. Important process variables such as particle/drop size and size distribution are strongly affected by turbulence kinetic energy dissipation rate ε and its distribution in an agitated vessel.

2. Theoretical background

2.1. Liquid-liquid dispersion

If acting mechanical forces are greater than drop interface surface forces, the drops deform and split into two or more smaller drops. Since this process is random, different sizes of daughter drops are produced. After a period of time, the equilibrium drop size distribution that is independent of the previous history is reached. Two possible mechanisms of dispersion are usually considered: drop break up by viscous forces and drop break up by inertial forces. The drop breakup mechanism is controlled by the turbulent eddy size [6].

If the breakup occurs in the viscous subrange, i.e. $d_p < \eta_K$, the drop breakup is controlled by viscous forces, hence the drop size d_p can be expressed as follows [7]:

$$d_p \propto \frac{\sigma}{\left(\rho_c \cdot \mu_c \cdot \varepsilon\right)^{1/2}},\tag{1}$$

where

ε – the local turbulent energy dissipation rate;
η_K – the Kolmogorov length microscale;
ρ_c, σ, μ_c – the physical properties of continuous fluid, i.e. density, interfacial tension, dynamic viscosity respectively.

If the breakup occurs in the inertial subrange, i.e. $\Lambda > d_p > \eta_K$, drop breakup is controlled by inertial forces, hence the drop size d_p can be expressed as follows [8]:

$$d_p \propto \sigma^{3/5} \cdot \rho_c^{-3/5} \cdot \varepsilon^{-2/5},\tag{2}$$

To characterise equilibrium drop distribution, many authors used Sauter mean diameter d_{32}. Assuming that $\varepsilon \propto N^3 \cdot d^2$, Equation (2) is rewritten into a dimensionless form as follows:

$$d_{32}/d \propto We^{-3/5} \,, \tag{3}$$

where

d	– the impeller diameter;.
We	– the Weber number; $We = \rho_c \cdot N^2 \cdot d^3/\sigma$.

The mentioned correlations are only valid for dilute dispersions with a non-viscous dispersed phase where the viscous energy within the drops is negligible compared to its surface energy and the coalescence phenomenon is negligible. However, in the concentrated coalescing dispersions, the drop size is affected by both the breakup and the coalescence processes. It is assumed that the breakup occurs in the impeller region whilst the coalescence occurs mainly in the bulk region (e.g. [9]). Moreover, the dispersed-phase viscous forces contribute to the drop stability when $\mu_d > \mu_c$.

Many correlations describing the dependence of the Sauter diameter on the physical properties of fluids take both of the influences above mentioned into account by the relation in the following general form:

$$d_{32}/d \propto \left[1 + f_1(\varphi)\right] \cdot \left[1 + f_2(Vi)\right] \cdot We^{-n} \,, \tag{4}$$

where

φ	– the dispersed-phase volume fraction in the system;
Vi	– the viscosity group, $Vi = \mu_d/(d \cdot \rho_d \cdot \sigma)^{1/2}$;
n	– the Weber number´s exponent.

In the breakup region the Weber number´s exponent is 0.6 [8]. In the coalescence region the exponent n is 3/8 [10]. Many authors use the Weber number´s exponent as an adjustable parameter. For example, Desnoyer et al. [11] take into account the effect of the dispersed-phase volume fraction φ on d_{32} considering the effect of the dispersed-phase fraction on the Weber number exponent n and on the constants of proportionality. According to Bałdyga and Podgórska [12], drop size depends on the fine-scale intermittency when the turbulence has intermittent character. In this case, the value of the Weber exponent depends on a intermittency scaling exponent.

The published correlations for d_{32} assume steady state. The time to reach the equilibrium drop size distribution depends on the number of times the liquid passes through the impeller zone and the bulk zone. Following this fact the number of passages through these spaces is crucial for dispersion kinetics modelling as confirmed by Šulc and Ditl [13] for flocculation kinetics modelling.

Currently, the most common approach to predicting drop size distribution and its time evolution in agitated vessels is based on population balance models (e.g. [14, 15]).

However, the quality of the prediction strongly depends on the quality of used breakage and coalescence kernels and the estimation of the local turbulent energy dissipation rate.

2.2. Solid particle-liquid dispersion

Compared with liquid-liquid dispersion, the mechanisms of solid particle-liquid dispersion is less complicated due to the rigid character of solid particles, especially when broken particles do not re-aggregate. In this case, only the breakup process occurs.

The aim of this paper is to propose a simple model of dispersion kinetics for the prediction of the time course of solid particle size taking into account the type of breakup mechanisms, the non-homogeneity of the local turbulent energy dissipation rate in an agitated vessel and the effect of the number of times the liquid passes through the impeller. The model was successfully tested on data published by Ditl et al. [16].

3. Kinetics model

For particle breaking occurring in a mechanically agitated vessel in the inertial subrange, i.e. $\Lambda > d_p > \eta_K$, the following assumptions were postulated: 1) the breaking occurs during passage through the impeller only; 2) broken particles do not re-aggregate; 3) the minimum particle size is limited by the Kolmogorov length microscale η_K corresponding to the mixing intensity in the impeller zone; 4) the change of particle size can be described by first-order kinetics as follows:

$$-\frac{\mathrm{d}(d_p)}{\mathrm{d}t} = k \cdot (d_p - d_{pf}) , \tag{5}$$

where

k	– the breaking rate-constant;
d_p	– actual particle size in time t;
d_{pf}	– the final particle size.

Integrating Equation (5) for the initial condition $d_p (t = 0) = d_{p0}$ the time dependency of particle size d_p can be obtained as follows:

$$\frac{d_p - d_{pf}}{d_{p0} - d_{pf}} = \exp(-k \cdot t) , \tag{6}$$

where

d_{p0}	– the initial particle size.

Taking the number of passages of liquid through an impeller into account, Equation (6) can be rewritten as follows:

$$d_p^* = \frac{d_p - d_{pf}}{d_{p0} - d_{pf}} = \exp(-k^* \cdot N \cdot t) , \tag{7}$$

where

k^* – the dimensionless breaking rate-constant;

d_p^* – dimensionless particle size;

N – the impeller rotational speed.

The Kolmogorov length microscale η_K is defined as follows:

$$\eta_K = \left(\frac{v^3}{\varepsilon}\right)^{1/4} , \tag{8}$$

where

v – the kinematic viscosity of agitated liquid;

ε – the turbulent energy dissipation rate.

The turbulent energy dissipation rate in the impeller zone was estimated from impeller power input using swept volume approach and assuming that the practically whole impeller power is dissipated in the impeller zone. Thus, the final particle size was estimated as follows:

$$d_{pf} \approx (\eta_K)_{imp} = \left(\frac{v^3}{(P/m)_{imp}}\right)^{1/4} = \left(\frac{v^3}{(P/(\rho \cdot V_{imp}))}\right)^{1/4} , \tag{9}$$

where

P – the impeller power input;

$(P/m)_{imp}$ – the specific turbulent energy dissipation rate in the impeller zone;

V_{imp} – the volume occupied by the rotating impeller.

4. Data analysis

The proposed model was tested on data published by Ditl et al. [16]. Ditl et al. [16] studied the time course of the dispersion of TiO_2 particles in liquid. The effect of impeller rotational speed, impeller type, vessel shape, impeller diameter to vessel diameter ratio, and solid particle concentration on dispersion was investigated. The effect of impeller rotational speed was investigated in a square vessel measuring 0.15 m × 0.15 m agitated by a tooth impeller having $D/d = 4.54$. The authors' attention was also focused on the scale-up of dispersion. On the basis of results derived for the disc impeller by Schlichting [17], the authors proposed scale-up rule $N \cdot d^{0.89}$ = const. using which the turbulent shear strength on tooth impeller surface should be maintained constant. The scaling experiments were carried out in cylindrical vessels of various vessel diameters D agitated by a tooth impeller having $D/d = 3$.

The mentioned experimental results were used in this work for the testing of the proposed model. In accordance with the model assumptions, particle sizes measuring less than the estimated Kolmogorov length microscale were not taken into account. The evaluated model parameters are presented in Table 1. The comparison of experimental and predicted dependence of particle size on time is presented in Fig. 1 for data measured in the squared vessel and in Fig. 3 for data measured in the cylindrical vessel. The comparison of experimental data and the time course predicted by the model are presented in dimensionless form for the squared and cylindrical vessel in Fig. 2 and Fig. 5, respectively. The effect of dimensionless time $N.t$ taking the number of times the liquid passes through the impeller into account is visible in Fig. 5. The curves of $d_p^* = f(N \cdot t)$ are more compact than the dependencies $d_p^* = f(t)$ presented in Fig. 4.

T a b l e 1

Model parameters – data Ditl et al. [16]

		N [RPM]	$(P/m)_{imp}$ [W/kg]	k^* [-]	d_{pf} [µm]	R^2 [-]
K1	SQ150-N5000	5 000	4 714	$0.764 \cdot 10^{-5}$	3.816	0.9563
K2	SQ150-N6500	6 500	10 337	$1.476 \cdot 10^{-5}$	3.136	0.9969
K3	SQ150-N7500	7 500	15 867	$1.574 \cdot 10^{-5}$	2.818	0.9882
K4	SQ150-N8800	8 800	25 613	$4.392 \cdot 10^{-5}$	2.500	0.9981
SC1	D300-N3500	3 500	6 440	$1.705 \cdot 10^{-5}$	3.530	0.9955
SC2	D190-N5550	5 550	10 309	$1.549 \cdot 10^{-5}$	3.138	0.9873
SC3	D150-N7600	7 600	16 509	$1.988 \cdot 10^{-5}$	2.790	0.9556
SC4	D100-N11500	11 500	25 485	$1.514 \cdot 10^{-5}$	2.503	0.9278
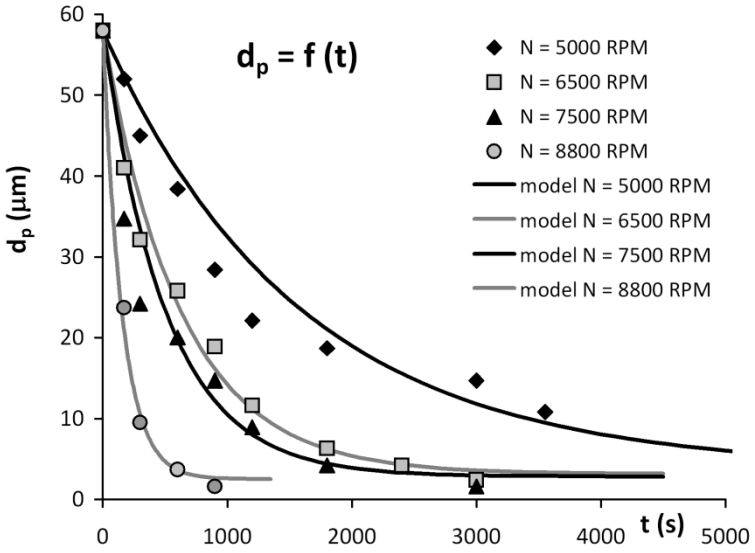
Fig. 1. Experimental data Ditl et al. [16] – squared vessel 150 mm × 150 mm: $d_p = f(t)$
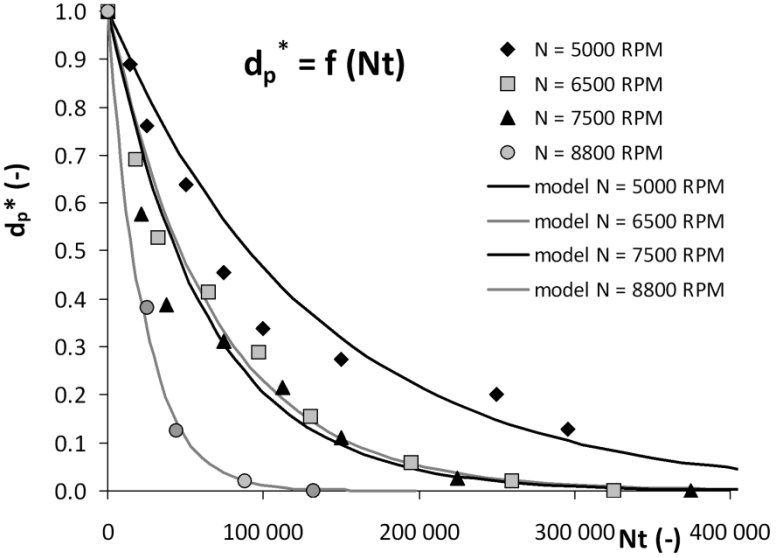
Fig. 2. Experimental data from Ditl et al. [16] – squared vessel 150 mm × 150 mm: $d_p^* = f(N \cdot t)$
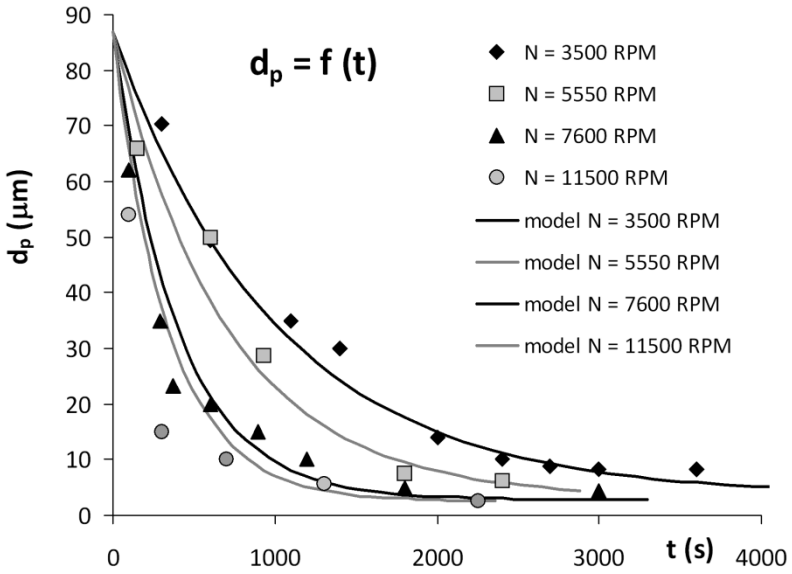
Fig. 3. Experimental data from Ditl et al. [16] – cylindrical vessel scale-up experiment: $d_p = f(t)$
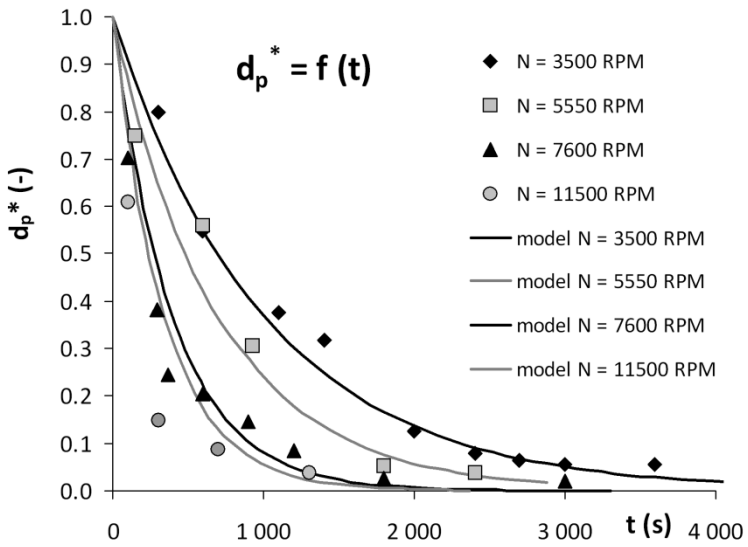
Fig. 4. Experimental data from Ditl et al. [16] – cylindrical vessel scale-up experiment: $d_p^* = f(t)$
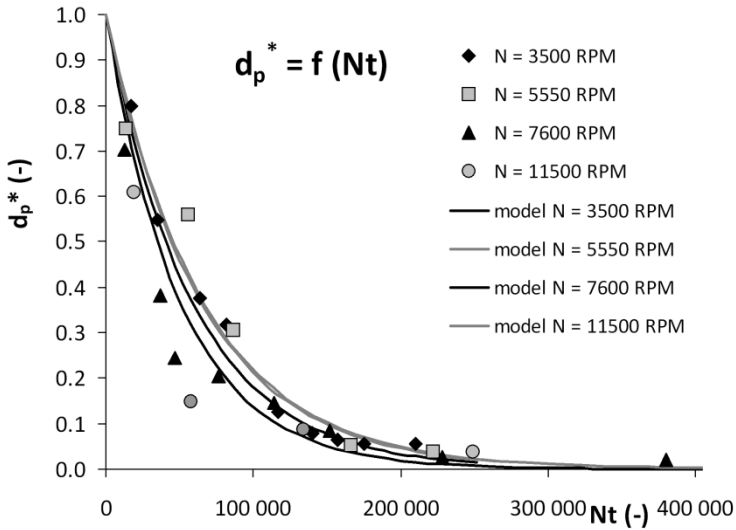
Fig. 5. Experimental data from Ditl et al. [16] – cylindrical vessel scale-up experiment: $d_p^* = f(N \cdot t)$
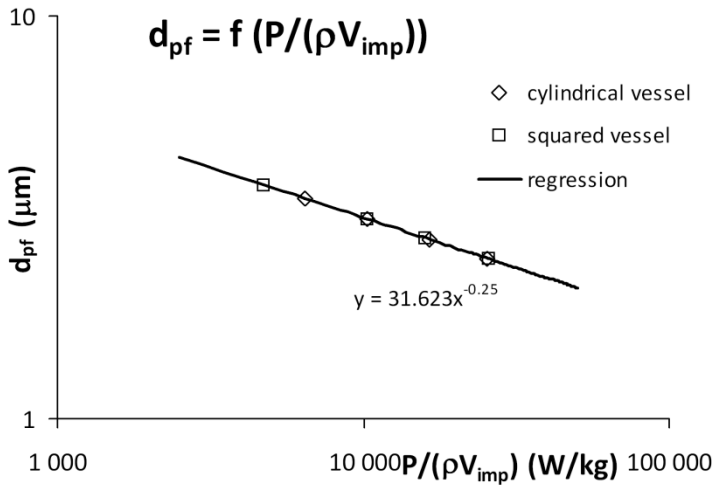
Fig. 6. Experimental data from Ditl et al. [16] – model parameters: $d_{pf} = f(P/(\rho \cdot V_{imp}))$; cylindrical vessel – four different vessel sizes, square vessel – four different impeller speeds
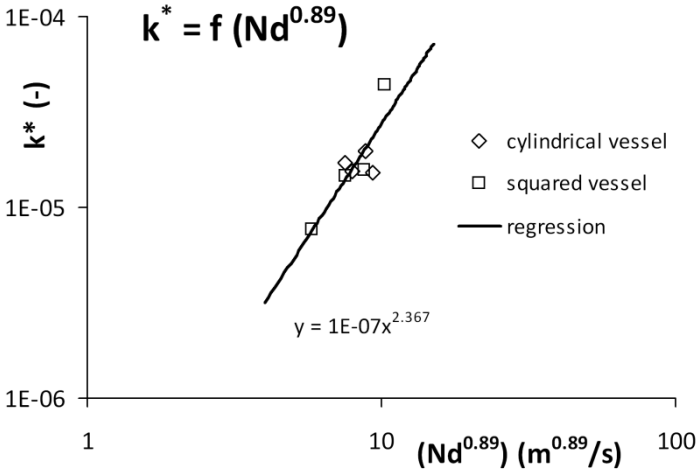
Fig. 7. Experimental data from Ditl et al. [16] – model parameters: $k^* = f(N \cdot d^{0.89})$; cylindrical vessel – four different vessel sizes, square vessel – four different impeller speeds

The following dimensional relationships were found for model parameters d_{pf} and k^*:

$$d_{pf} = 31.623 \cdot (P/(\rho \cdot V_{imp}))^{-1/4} \ (R^2 = 1), \tag{10}$$

$$k^* = 1.178 \cdot 10^{-7} \cdot (N \cdot d^{0.89})^{2.367} \ (R^2 = 0.721), \tag{11}$$

where

d_{pf} [μm], k^* [-], $(P/(\rho \cdot V_{imp}))$ [W/kg], N [RPS] and impeller diameter d [m].

As expected, the model parameter d_{pf} is proportional to the mean dissipation rate in the impeller zone $(P/(\rho \cdot V_{imp}))^{-1/4}$ as follows from Equation (9). The dimensionless rate-constant k^* was found to be proportional to shear strength on impeller surface $((N \cdot d)^{0.89})$. The obtained relationships are graphically shown in Fig. 6 and 7.

5. Conclusions

The following conclusions can be made:

A simple dispersion model enabling the prediction of particle size changes over time was proposed. The model takes into account the type of breakup mechanisms, the non-homogeneity of the local turbulent energy dissipation rate in an agitated vessel and the effect of number of times the liquid passes through the impeller and the impeller zone.

The model was successfully tested on the data published by Ditl et al. [16]. In their study, the dispersion of TiO_2 particles in liquid was investigated.

The dimensional relations $d_{pf} = 31.623 \cdot (P/(\rho \cdot V_{imp}))^{-1/4}$ and $k^* = 1.178 \cdot 10^{-7} \cdot (N \cdot d^{0.89})^{2.367}$ were found for model parameters, where d_{pf} [μm], k^* [-], $(P/(\rho \cdot V_{imp}))$ [W/kg], N [RPS] and impeller diameter d [m].

R e f e r e n c e s

[1] Paul E.L., Atiemo-Obeng V.A., Kresta S.M. (Eds.), *Handbook of industrial mixing. Science and Practice*, Wiley, Hoboken, NJ, 2004.

[2]   Parfitt G.D., *Dispersion of powders in liquids* (2nd ed)., Applied Science Publishers, London 1973.

[3] Lu S., Pugh R.J., Forssberg E., *Interfacial Separation of Particles*, Studies in Interface Science, vol. 20, Elsevier 2005.

[4] Yeoh S.L., Papadakis G., Yianneskis M., *Determination of mixing time and degree of homogeneity in stirred vessels with large eddy simulation*, Chem. Eng. Sci., vol. 60, 2005, 2293-2302.

[5] Cheng D., Feng X., Cheng J., Yang, Ch., *Numerical simulation of macro-mixing in liquid-liquid stirred tanks*, Chem. Eng. Sci., vol. 101, 2013, 272-282.

[6] Sprow F.B., *Distribution of drop sizes in turbulent liquid-liquid dispersions*, Chem. Eng. Sci., vol. 22, 1967, 435-442.

[7] Taylor G.I., *The formation of emulsions in definable fields of flow*, Proc. R. Soc. Lond., A146, 1934, 501-523.

[8] Hinze J.O., *Fundamentals of the hydrodynamic mechanism of splitting in dispersion processes*, AIChE J., vol. 1, 1955, 289-295.

[9] Hu B., Angeli P., Matar O.K., Hewitt G.F., *Prediction of phase inversion in agitated vessels using a two-region model*, Chem. Eng. Sci., vol. 60, 2005, 3487-3495.

[10] Shinnar R., *On the behaviour of liquid dispersions in mixing vessels*, J. of Fluid Mechanics, vol. 10, 1961, 259-275.

[11] Desnoyer C., Masbernat, O., Gourdon, C., *Experimental study of drop size distributions at high phase ratio in liquid-liquid dispersions*, Chem. Eng. Sci., vol. 58, 2003, 1353-1363.

[12] Bałdyga J., Podgórska W., *Drop break-up in intermittent turbulence: maximum stable and transient sizes of drops*, Can. J. of Chem. Eng., vol. 76, 1998, 456-470.

[13] Šulc R., Ditl P., *The effect of process conditions on the flocculation process occurring in an agitated vessel*, Polish J. of Chem. Technology, vol. 14, 2012, 88-96.

[14] Podgórska W., Bałdyga J., *Scale up effects on the drop size distribution of liquid-liquid dispersions in agitated vessels*, Chem.Eng.Sci., vol. 56, 2001, 741-746.

[15] Raikar N.B., Bhatia S.R., Malone M.F., McClements D.J., Almeida-Rivera C., Bongers P., Henson M., *Prediction of emulsion drop size distributions with population balance equation models of multiple drop breakage*, Colloids and Surfaces A: Physicochem. Eng. Aspects, vol. 361, 2010, 96-108.

[16] Ditl P., Novák V., Rieger F., *Dispergace v kapalinách rychloběžnými míchadly (Dispergation in liquids by high-speed impellers)*, Chem.průmysl, vol. 31(56), 1981, 3-10.

[17] Schlichting H., *Boundary layer theory*, McGraw-Hill, New York 1979.

MAXIMILIAN FECHTER, MATTHIAS KRAUME[*]

DIGESTATE TREATMENT TECHNIQUES

PRZETWARZANIE POZOSTAŁOŚCI POFERMENTACYJNYCH

Abstract

Even though digestate is rich in plant nutrients, its value as a fertiliser is low due to its high water content of 90 to 95%. Therefore, the main objective of digestate treatment is to extract clean water in order to concentrate the plant nutrients. These are either in solution or attached to organic particles. Roughly, more than 70% of the digestate's solid particles are smaller than 1 mm and are not easily separated, because of particle size, charge and density. This is one of the reasons why a simple screen separation provides no solution to the problem; however, it is an important step in the treatment chain. During the research project, many different digestate treatment techniques were considered – all of these are recorded in Figure 10.
This article provides an overview of the possible techniques for digestate treatment, how they work, and their central research parameters.

Keywords: digestate, proces engineering

Streszczenie

Pozostałości pofermentacyjne są bogate w roślinne składniki pokarmowe roślin, jednak ich wartość jako nawóz jest niska z powodu dużej zawartości wody od 90 do 95%. Głównym celem przetwarzania pozostał ości jest oddzielenie czystej wody w celu koncentracji składników pokarmowych, które znajdują się w postaci roztworu lub są dołączone do cząstek organicznych, co sprawia, że separacja na pojedynczej membranie jest niewystarczająca. W pracy przedstawiono różne techniki przetwarzania pozostałości pofermentacyjnych.

Słowa kluczowe: pozostałości pofermentacyjne, inżynieria procesowa

[*] MSc. Eng. Maximilian Fechter, Prof. PhD. DSc. Eng. Matthias Kraume, Chair of Chemical & Process Engineering, Faculty of Process Sciences, Technical University of Berlin.

1. Introduction

Digestate treatment has become a major challenge since the latest amendment of the EEG in Germany. The EEG from 2014 states a minimum storage capacity for digestate of 150 days and applies to all fermenters built after 2012 [5]. *The Federal Ministry for the Environment, Nature Conservation, Building and Nuclear Safety* plans to increase the storage time to nine months for biogas plants that cannot apply the digestate on their own fields [7]. Those biogas plants are in urgent need of either digestate treatment or a costly digestate storage tank. The advantages of digestate treatment as opposed to the use of a storage tank are the reduced space requirement, lower transportation costs, and lower fuel and time requirements when applying the digestate onto land due to the reduction in volume. However, even though di-gestate treatment offers many advantages, it also causes many problems. Digestate from a regular mesophilic bio fermenter that is fed with energy-crops and manure, consists of over 90% water. The remainder is biomass, which is rich in plant nutrients and is usually no longer digestible for the majority of bacteria. Around 50% of its particles are smaller than one millimetre and perfectly suspended in the water due to their negatively charged surface. This makes it difficult to separate them. The digestate's high chemical oxygen demand (COD), which takes values between 50 and 120 kg/t [11], rules out the possibility of treating it in the classical method of waste water treatment – nitrification and de-nitrification. This would require a class IV sewage plant, with the capacity to treat the volume of waste water produced by 10,000 to 100,000 people. With the hope for a simple solution to the digestate treatment problem dismissed for the above reason, only more complicated ways of treating contaminated water remain such as evaporation, stripping, flocculation and membrane techniques.

2. Basic Procedure

The first step in digestate treatment is usually the separation of the large particle fraction with a diameter greater 1 mm. This reduces the mass flow by around 10% when using a screw press. Further solid removal can be achieved through the use of vibrating screens,
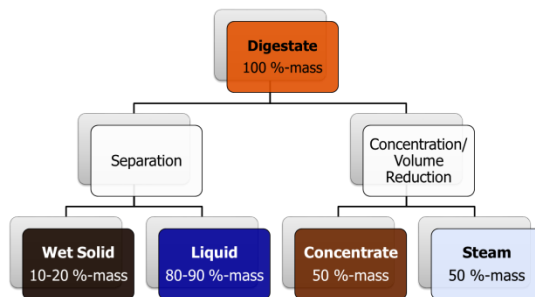
Fig. 1. Basic procedure for digestate treatment. Separation reduces the mass by 10 to 20% by solid removal, concentration leads to higher volume reduction; however, this incurs at higher costs and energy demands. Separation is usually a pre-treatment for more advanced processes

decanters, belt filter presses or flotation. Separation using these techniques can be enhanced by flocculation. The disadvantages of flocculation are the costs for the flocculant and the limitation of synthetic flocculants in fertilisers [6]. When separation is not the first step, an alternative, which is shown in Figure 1, is the volume reduction by the evaporation of water. This technique works well, even without solid removal. In this process, the digestate is concentrated by a factor of two. A maximum dry matter content of 15% can be achieved, this is true for all liquid digestates obtained from mesophilic digesters, as above this level, the digestate loses its ability to be pumped. This technique reaches an efficiency of 0.6÷1.0 l/kWh [20].

3. Concentration

Concentration is performed using the CHP plant's water cooling system which is connected to a water-air heat exchanger. The dryer is either installed between the last digester and the digestate storage tank or parallel to the digestate storage tank as shown in Figure 2. Liquid digestate is pumped into the dryer and dried by the air that is taken from the environment and heated by the waste heat of the CHP plant. The air evaporates water from the digestate and simultaneously extracts some ammonium – this is removed from the exhaust air by a scrubber working with sulphuric acid.
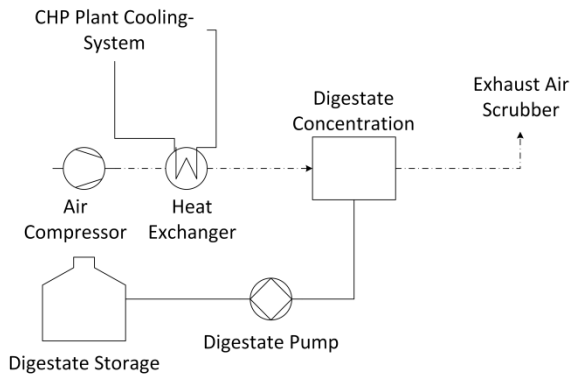
Fig. 2. Digestate dryer used as liquid digestate concentrator, installation parallel to the digestate storage

Such a concentrator device can be constructed with a tank containing the digestate and a drum, belt or disc that dips into the digestate and conveys it to the hot air for evaporation to occur. A large surface area ensures a high water extraction efficiency – the exhaust air should have at least 80% relative humidity. Another method is to use a belt dryer. In order to prevent liquid digestate leaking through the belt dryer's belt it is applied to dried solid digestate at the start. This results in a wet solid digestate which can then be dried. The product of this process cannot be pumped.

4. Separation

The main objective in separation is to achieve a high selectivity, meaning the solid fraction should have a high dry matter content, the liquid fraction should be particle free. Achieving both of these features at the same time is unfortunately impossible; however, with the right combination of separation techniques, it is possible to get a solid with a dry matter content of up to 35÷40% and a liquid phase with less than 2% dry matter content. Generally, it is observed that phosphate tends to stay with the solid fraction, while nitrogen – usually dissolved as ammonium – remains in the liquid phase [11].

As mentioned in Section 2, the first separation step is usually performed by a screw press. This is due to its energy efficiency of around 0.45 kWh/m^3 digestate and its durability. Its' products are a solid with a dry matter content of about 25÷35% and a liquid phase with a reduced dry matter content of between 0.5 and 2 %, depending on the dry matter content of the original digestate and the particle size distribution [11]. In case a particle sensitive treatment techniques follows downstream, the liquid phase needs further solid removal. All separation techniques are shown in Figure 3, the devices for further solid removal usually require an upstream flocculation. For further information about flocculation, see Section 5.

Screw Press In this device, digestate is introduced into a drum screen by a conveyor screw. The screen width varies between 0.5 and 1.0 mm; therefore, particles greater than this size are held back by it while the liquid phase and smaller particles pass through. The remaining solid is compressed towards the end of the drum screen by the conveyor screw, driving out more water. Flaps at the output support the accumulation of solids – these are used to adjust the compression pressure and thus, the dry matter content of the solid phase. A diagram of the screw press is shown in Figure 3(a). For enhanced solid removal, self-cleaning wire wedge filters can be supplemented to the separation system. These work similar to a vertically installed screw press, only with a finer screen and without resulting in the compression of the solid output.

Decanter Centrifuge This device is shown in Figure 3(b). The separation principle is based on gravity and the density difference of particles and liquid. The decanter consists of a fast rotating encasing drum and a slightly faster rotating conveyor screw, resulting in a relative rotational speed of the screw against the drum. The digestate is introduced through the drive shaft into the middle of the encasing drum. Due to their higher density, particles gather on the encasing drum's surface and are driven towards the output by the conveyor screw. The liquid squeezes through the slits between the drum and the screw to exit the decanter through the liquid's output. An overflow weir prevents particles from exiting at the liquid output. The process can be influenced by the rotational speed of drum and screw, the difference in rotational speed between drum and screw, the over flow weirs position and the mass flow through the centrifuge. The decanter centrifuge produces a very clear liquid fraction; however, the solid fraction still has a relatively high water content. Compared to the screw press, this is more sensitive to mechanical malfunction and its energy consumption is between 3 and 5 kWh/m^3 of digestate [11].

Belt Filter Press A diagram of the belt filter press operating principle is shown in Figure 3(c). The digestate is fed onto the belt filter, pre-dewatering is accomplished by gravity. Optionally, a vacuum can be applied in this zone to enhance the water extraction.

After the initial drainage, sludge is compressed between two filter belts that run between several rollers. The increased pressure drives out water as does the slight relative movement of the two filter belts. At the output, the belts separate and the solids are scraped off. Afterwards, the filter belts are spray washed. The solids output has a high dry matter content, the liquid phase quality depends on the belt filter and on flocculation. It consumes around 0.88 kWh/m^3 of sludge.

(a) Screw press

(b) Decanter centrifuge

(c) Belt filter press

(d) Flotation

(e) Vibrating screen
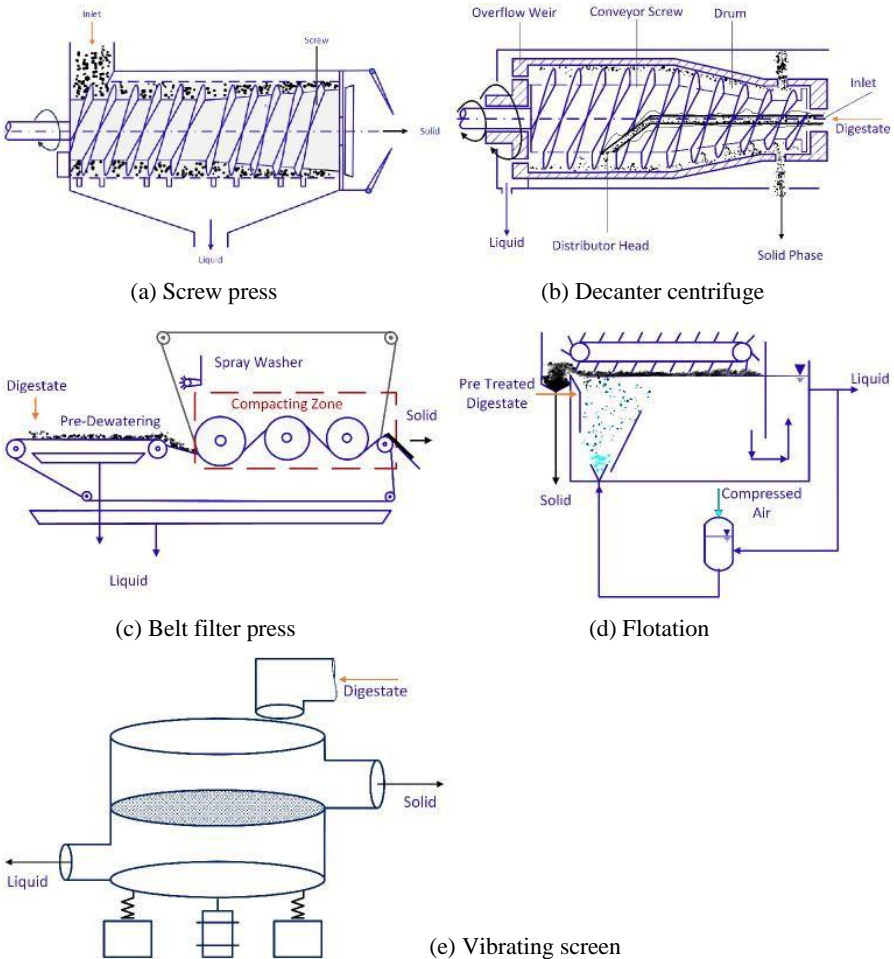
Fig. 3. Devices used for separation and further solid removal

Flotation The flotation separates particles by taking advantage of bubble formation on particle surfaces and hence, the density difference between liquid and the agglomerate of particle and bubble. Figure 3(d) illustrates the method of operation of this device. Air is diluted in liquid digestate under pressure, the air-saturated liquid is then fed into the flotation tank though a relaxing valve. The diluted air changes state to gas and small bubbles form on

the particles' surface. The bubble-particle agglomerate is elevated by buoyancy and floating sludge builds up at the surface. This is scraped towards the overflow weir for the flotation sludge. For a cleaner liquid fraction, the output is partly recycled into flotation. The advantage of flotation is a very clean, near particle free liquid fraction. The flotation sludge still has a very high water content. This technique is only used for solid removal from liquids that already have a low dry

Vibrating Screen A vibrating screen is normally used for further solid removal after using a screw press or a decanter centrifuge, because even though a decanter produces very clean very high water content. This technique is only used for solid removal from liquids that already have a low dry matter content. Flotation takes around 0.2 kWh/m^3 treated liquid, particles with a density lower than water can get through the gravitational field of a decanter. Figure 3(e) shows the application of a vibrating screen. Digestate is introduced onto the screen, liquid and small particles pass through whilst the remaining solid particles stay on top of the screen and move towards the solid outlet due to screen vibration. The typical width of a screen slit width is 150÷250 μm [11].

5. Flocculation

In order to enhance the separation processes, flocculation is often used in industrial applications. The trouble with digestate and its particles that won't sediment is that the particles repel each other because of their negatively charged surfaces. This prevents their agglomeration to bigger particles that are easier to remove [11]. Flocculation becomes important when a particle free liquid needs to be provided for membrane technologies. A reverse osmosis membrane is very sensitive to particles and requires pre-treatment by ultra-filtration – this involves high energy consumption when the concentration of solids is high. Therefore, whilst a well-performed flocculation reduces energy consumption, it requires extra operating resources such as the flocculant and the flocculant aid polymer.

Flocculation of digestate is carried out in two steps. Firstly, the flocculant – usually a water soluble metal salt such as iron-III-chloride – is added to the digestate. The highly-charged cations formed by the metal salt effect that the negatively charged particles suspended in the digestate agglomerate to slightly bigger particles, see Figure 4 on the left. Since these particles are still too small for separation, a flocculant aid polymer is added. This can be imagined as a long chain with negatively charged arms where the particle loaded metal cations connect to form a huge particle that can be easily separated.
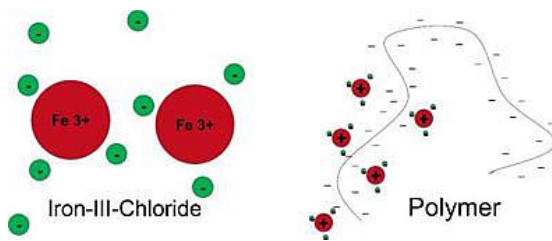
Fig. 4. Principle of flocculation

6. Further Treatment

After separation, a solid phase with a dry matter content of 25÷35% and a liquid phase with 1÷8% are obtained. Both can individually be treated further in order to remove more water, isolate certain plant nutrients and produce highly concentrated fertilisers as well as clean water.
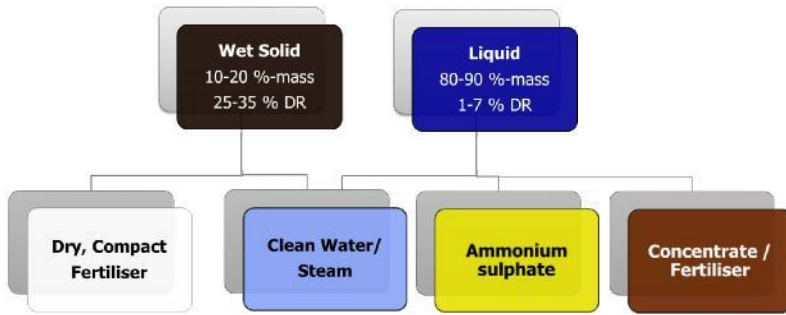
Fig. 5. Products of further treatment

6.1. Solid Phase

The further treatment of the solids amounts to further water removal and compaction. The devices used for these two steps work in similar ways. For the drying process the belt dryer is shown as an example, other constructions of dryers, such as drum dryer, feed-and-turn-dryer etc. follow the same working principle. Drying the solid phase of a digestate is only appropriate when there is enough heat available from the CHP plant. For pelleting the solid phase, its dry matter content should be between 86 and 90%; thus, if pellets are desired as a final product, drying is inevitable. The working principle of drying solids is the same as described for concentration in section 3. Using steam instead of air as a drying medium is more efficient due to the enhanced energy recovery [23]. However, steam dryers are not in standard usage for digestate drying – they are seldom used and expansive.

(a) Belt Dryer   (b) Pelleting machine [16] as an example for compacting solid digestate
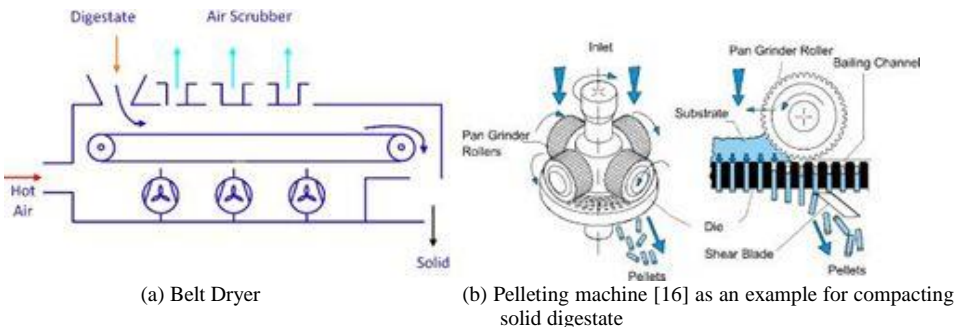
Fig. 6. Devices for further solid treatment

Dried solids have a bulk density of 250÷350 kg/m^3 whereas pellets bulk density ranges from 700÷750 kg/m^3. This is a great advantage when the solids are supposed to be sold as a

commercial fertiliser since it improves the handling considerably. The compacting generally works by applying pressure to the solid material and forcing it through a tight die. This can be achieved either with a conveyor screw like in an extruder or by grinder rollers, that are used in a pelleting machine. Inside the bailing channels, the material is homogeneously compressed. The pellets' surface is coated with a thin shiny layer, which is the result of the effect of high pressure and temperature on lignin and cellulose. Figures 6(a) and 6(b) illustrate how both processes operate.

6.2. Vacuum Evaporation

The liquid digestate from the separation can be further concentrated through the use of vacuum evaporation. The benefit of using vacuum evaporation is that the boiling point of water is reduced to 40÷70°C, depending on the absolute pressure. This enables the use of cooling water from the CHP plant that has a temperature of approximately 85°C. Furthermore, it reduces the amount of thermal energy needed to heat the digestate to its boiling point. In Figure 7, a flow chart for a single-step vacuum evaporator is presented to demonstrate the working principle. Liquid digestate enters the evaporator, which is connected to the CHP plant's cooling system. The applied vacuum reduces the boiling point to around 60°C, water is evaporated and dissolved gases like carbon dioxide and ammonia escape the liquid. Since digestate contains a lot of ammonium, the produced steam is rich in ammonia; this needs to be removed in order to obtain clean water. This is done by an acidic scrubber using sulphuric acid to turn the ammonia into ammonium sulphate. Afterwards, the steam is condensed and stored in a water tank. In order to remove all heat from the system, this water is used in an evaporative cooler. The energy demand of such a plant is around 13kWh electricity per cubic meter of digestate while 1.4 litres of water are removed with one kilowatt hour of thermal energy [21].

If evaporation takes place in more than one evaporator, it is possible to reuse the thermal energy. This is done by applying different pressures in the evaporation tanks and hence, achieve different boiling temperatures. The steam from the hottest evaporator is cooled and condensed in the first condenser while digestate from the second evaporator, working at lower temperatures, is heated and evaporated. Commercial systems use up to three evaporation steps, reaching a very high level of thermal energy efficiency.
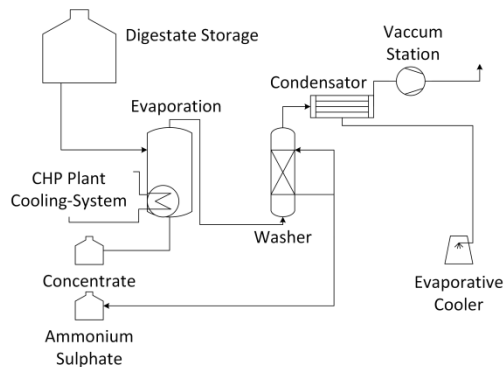

Fig. 7. Working principle of a single-step vacuum evaporation system

6.3. Ultra-Filtration and Reverse Osmosis

The membrane process is the most sensitive of the three described further treatment techniques. Even though ultra-filtration is used for the express purpose of removing particles, it can only cope with a maximum sludge concentration of 25 mg/l which is about equal to a dry matter content of 2.5%. [3] Therefore, an elaborate separation technique should be installed upstream. Therefore, the energy demand of ultra-filtration is increased by higher solid concentrations because this thickens the liquid and results in higher pressure loss. Another issue is the cleaning interval which also depends on the solid concentration in the input liquid. It is important that the ultra-filtration step reliably removes all particles form the liquid. This is because of the small liquid channels inside the reverse osmosis modules that are blocked by particles very easily.

The way the membrane system as shown in Figure 8 works is, that the ultra-filtration removes all solids from the liquid digestate. Usually, a feed and bleed circuit is used in these kind of systems. This means that a small pump ensures the required transmembrane pressure difference in the ultra-filtration cycle and a large pump circulates the fluid through the membrane. The retentate is rich in organic matter and usually recycled to the fermenter. The permeate is introduced into the reverse osmosis process. This works in two steps: firstly, most salts and dissolved substances are removed. Since ammonium always stays in a state of dynamic equilibrium with ammonia, the permeate of the first step still contains a major fraction of it. Ammonia is not held back by membranes; therefore, sulphuric acid is added to the permeate of the first reverse osmosis step turning ammonia into ammonium, which can be held back by the membrane in the second reverse osmosis step. The permeate of the second step is clean water, that can be introduced into the environment[1]. The retentate is reintroduced to the first step of reverse osmosis. The first step retentate is therefore rich in ammonium sulphate.

The operation costs are dominated by the use of electrical energy. Processing one cubic meter of digestate with a membrane process requires approximately 21 kWh of electricity. This also includes digestate separation prior to the membrane process [27].
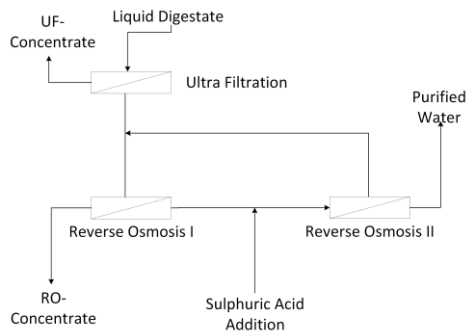
Fig. 8. Membrane process for total digestate treatment

---

[1] The permeates concentration of pollutants is very low and should not cause a problem for the environment; however, there is no mention of waste water from bio-digesters in the German waste water decree, making it hard to achieve permission for waste water discharge.

6.4. Stripping

The stripping process is used to remove ammonium from the digestate and fermentation process. It involves the separation of solids before stripping, which however, is not as complicated as for the membrane process. Unlike vacuum evaporation and membrane treatment, clean water is not obtained through this process. Figure 9 shows a flow chart of an ammonia stripping process connected to a digester.

For this process, the coarse solid fraction is removed from the digestate. The liquid phase is heated and sodium hydroxide is added to increase the pH and hence, move the ammonia/ammonium equilibrium toward the ammonia side to increase its volatility.
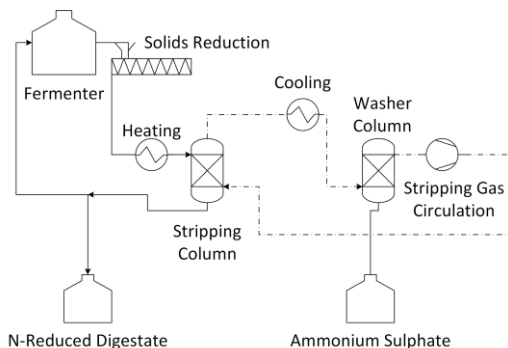
Fig. 9. Stripping process to reduce the ammonium concentration in the digestate and inside the fermenter

Afterwards, the liquid is introduced into a column, where a stripping gas (mostly steam) is used to extract the ammonia from the liquid. After this stage, the nitrogen-reduced liquid digestate either flows back into the digester or to a storage tank. The stripping gas needs to be recovered. Thus the stripping gas is introduced in a washer column where the ammonia is removed with the aid of sulphuric acid, forming ammonium sulphate – the second product of ammonia stripping.

The advantage of ammonia stripping is high flexibility in the choice of substrate for the digester, enabling the use of dry chicken faeces in large proportions. The energy demand of a stripping system is 90 kWh thermal energy and 7 kWh electrical energy per cubic meter of digestate [12].

7. Summary

All described steps of digestate treatment can be summarised in a digestate treatment flow chart shown in Figure 10. Each step involves a greater effort but simultaneously, a higher value product. The only exception in this chart is the stripping, which is a process that not only treats the digestate but also influences the behaviour of the fermenter. The actual effort for stripping equals a three-step treatment such as vacuum evaporation or membrane treatment.
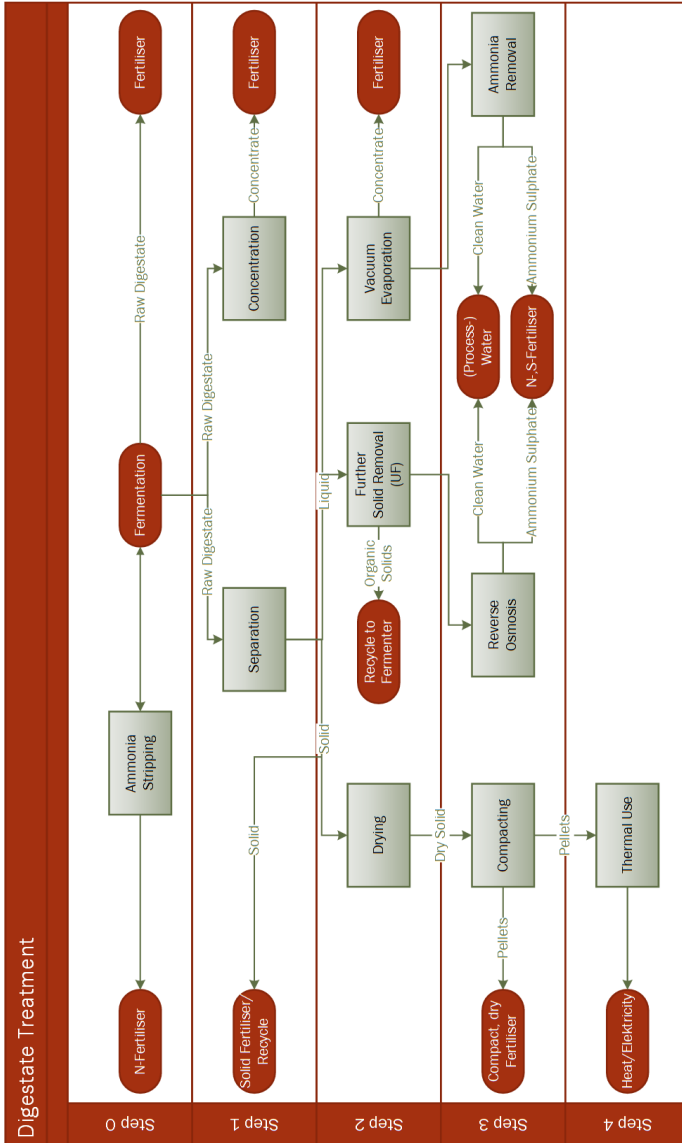
Fig. 10. Digestate treatment techniques flow chart

R e f e r e n c e s

[1] Amlinger F., Peyr S., Hildebrandt U., Müsken J., Cuhls C., Clemens J., S*tand der technik der kompostierung*, Bundesministerium für Land- und Forstwirtschaft, Umwelt und Wasserwirtschaft, 2005.

[2] Bauermeister U., *Erzeugung von konzentriertem Stickstoffdünger aus Gärprodukten – Einsatzmöglichkeiten und Prakxiserfahrungen des ANAStrip-Verfahrens,* 2013.

[3] Berghof Membrane Technology GmbH & Co. KG., *Bioflow Membrane Manual*, http://adurna.in/documents/Bioflow.pdf.

[4] BIGATEC – Ingenieurbüro für Bioenergie. http://www.bigatec.de.

[5] Bundesministerium der Justiz und für Verbraucherschutz. Gesetz für den Ausbau erneuerbarer Energien (Erneuerbare-Energien-Gesetz-EEG 2014): EEG2014.

[6] Bundesministerium der Justiz und für Verbraucherschutz. Verordnung über das Inverkehrbringen von Düngemitteln, Bodenhilfsstoffen, Kultursubstraten und Pflanzenhilfsmitteln (Düngemittelverordnung - DüMV), 2012.

[7] Bundesministerium für Umwelt, Naturschutz, Bau und Reaktorsicherheit. Verordnung über Anlagen zum Umgang mit wassergefährdenden Stoffen (AwSV). http://www.bmub.bund.de/fileadmin/Daten_BMU/Download_PDF/Binnengewaesser/awsv_bf.pdf.

[8] Dorset Agrar- und Umwelttechnik GmbH.

[9] Fachverband Biogas e.V., editor. *23. Jahrestagung und Fachmesse: Aufbereitung und Vermarktung von Gärprodukten,* 2014.

[10] Förstner U., *Umweltschutztechnik* (German Edition), Springer, 8. aufl. 2012.

[11] Fuchs W., Drosg B., Peter H., Klummp H., *Technologiebewertung von Gärrestbehandlungs- und Verwertungskonzepten*, Eigenverlag der Universität für Bodenkultur, Wien 2010.

[12] GNS – Gesellschaft für Nachhaltige Stoffnutzung mbH. www.gns-halle.de.

[13] Hornung A., *Konzept der Biobatterie,* 2013.

[14] HUNING Umwelttechnik GmbH & Co. KG.

[15] Jung R., *Effizienzsteigerung von Biogasanlagen durch Pyrolyse von Gärresten,* 2014.

[16] Kaltschmitt M., Streicher W., *Energie aus Biomasse*, Springer, 2 edition, 2009.

[17] Köhnlechner M., *Volumenreduktion und Veredelung von Gärprodukten* [in] *Fachverband Biogas* e.V., editor, 23. Jahrestagung und Fachmesse, 2014, 28-36.

[18] Lehmann T., *Aufbereitung von Gärresten zur stofflichen und energetischen Nutzung,* 2013.

[19] Lehmann Maschinenbau GmbH.

[20] Burkhard Meiners, 2014.

[21] MKR Metzger GmbH.

[22] Röhren- und Pumpwerk BAUER GmbH.

[23] Seefeldt F., Berewinkel J., Lubetzki Ch., *Energieeffizienz in der Industrie*, Springer, 2009.

[24] Sommer K., *CULTAN-Düngung: physiologisch, ökologisch, ökonomisch optimiertes Düngungsverfahren für Ackerkulturen, Grünland, Gemüse, Zierpflanzen und Obstgehölze*, Mann 2005.

[25] Steros GmbH.

[26] Thermo-System GmbH.

[27] Brüß U., *MPS Verfahren zur Totalaufbereitung von Gärresten* [in] *Fachverband Biogas e.V*., 23. Jahrestagung und Fachmesse, 2014, 13-27.

[28] Drasden Venturi GmbH Energieanlagen and GMBU e.V., Halle, *Untersuchung zur Rohstoffseparation aus Gärresten,* 2013.

MARKUS ILLNER[*], TOBIAS POGRZEBA[**], MARCEL SCHMIDT[**],
DAVID MÜLLER[*], ERIK ESCHE[*],
REINHARD SCHOMÄCKER[**], JENS-UWE REPKE[*], GÜNTER WOZNY[*]

HYDROFORMYLATION OF 1-DODECENE IN MICROEMULSIONS: OPERATION AND VALIDATION OF LAB RESULTS IN A MINIPLANT

HYDROFORMYLOWANIE 1-DODEKANU W MIKROEMULSJACH: WARUNKI I MOŻLIWOŚCI STOSOWANIA WYNIKÓW BADAŃ LABORATORYJNYCH W MINI-INSTALACJI

A b s t r a c t

A method of hydroformylation to convert long- chained olefins, using tunable microemulsion systems, tests were conducted on a mini-plant at the center InPROMPT/TRR 63. Surfactant allowing a quasi-homogeneous reaction of olefin in aqueous Rhodium catalyst solution.

Keywords: hydroformylation, microemulsions, mini-plant, long term operation

S t r e s z c z e n i e

W pracy przedstawiono metodę hydroformylowania w celu konwersji długołańcuchowych olefin, z wykorzystaniem przestrajalnych układów mikroemulsji, badania przeprowadzono na mini-instalacji w ośrodku InPROMPT/TRR 63. Stosowano surfaktant umożliwiający quasi-jednorodną reakcję olefin 1- dodecenu w wodnym roztworze katalizatora rodowego.

słowa kluczowe: hydroformylowanie,, mikroemulsje, mini-instalacja

[*] MSc. Markus Illner, DSc. Eng. David Müller, DSc. Eng. Erik Esche, Prof. DSc. Eng. Jens-Uwe Repke, Prof. PhD. DSc. Eng. Günter Wozny, Process Dynamics And Operations Group, Faculty Of Process Sciences, Technical University of Berlin.

[**] MSc. Eng. Tobias Pogrzeba, MSc. Marcel Schmidt, Prof. Dr. Rer. Nat. Reinhard Schomäcker, Department For Chemistry, Faculty Of Mathematics And Natural Sciences, Technical University of Berlin.

1. Introduction and Motivation

Within the chemical industry, hydroformylation is one of the main reaction processes used in the formation of aldehydes, a major class of base chemicals used for polymer or solvent products, flavourings, and detergents [1]. The reaction itself was discovered in 1938 by Otto Roehlen [5]. Nowadays, the application is usually realised as a homogenously catalysed process – this offers advantages with regard to high product selectivity and mild reaction conditions [2-4]. Here, olefins react with hydrogen and carbon monoxide in the presence of transition metal catalysts (cobalt, rhodium) towards the linear aldehyde and branched byproducts (Fig. 1).
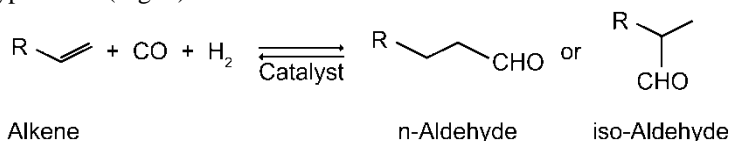
Fig. 1. Reaction equation of the hydroformylation reaction, R denotes an alkyl group [6,7]

Recently, industrial applications have focussed upon rhodium-based catalysts in which the modification of the metal complex with tailored ligands offers higher degrees of selectivity and activity [1, 8]. As a major drawback, the increasing costs of catalysts necessitate efficient catalyst recovery. Dissolving the catalyst in an aqueous phase and thus enabling a biphasic process concept tackles this obstacle. Highly active catalyst-ligand complexes maintain high reaction rates, while catalyst recovery is efficiently achieved through basic phase separation (see the Ruhrchemie-Rhône Poulenc Process, described in [3]). However, with the increasing chain length of the applied olefin, the miscibility of the oily reactant phase and the aqueous catalyst solution decreases. Additionally, the reaction rates decrease, as the interfacial area between the reactants and the catalyst is reduced. Therefore, state of the art biphasic process concepts are not applicable in case new feedstocks, such as bio-based long-chained olefins, are to be used.
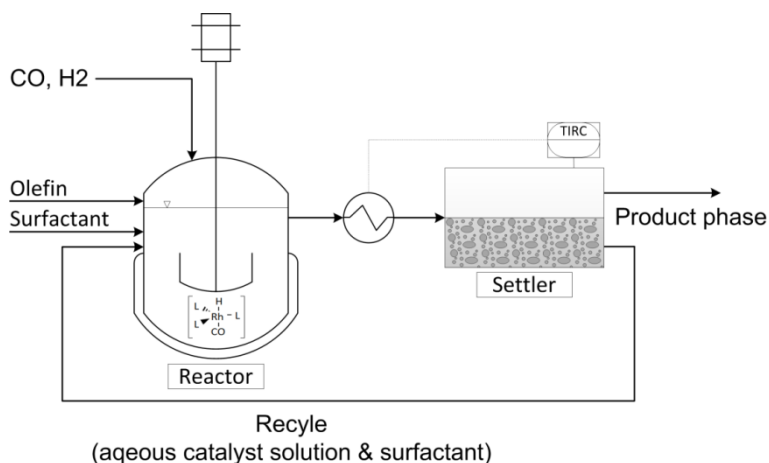
Fig. 2. General process concept for the hydroformylation in microemulsions, derived from [10]

In this contribution we examined a new process concept for the hydroformylation of long-chained olefins in microemulsion systems, which is currently investigated within the collaborative research centre InPROMPT / TRR 63 in Germany. Here, a surfactant is used to increase the miscibility between the nonpolar reactants and the aqueous catalyst phase by the formation of micelles. Again, a water-soluble ligand-modified rhodium catalyst is used to achieve good reaction performances, as described by Hamerla et al. in [9]. After the reaction step, the thermomorphic behaviour of micellar systems is exploited to separate and collect a pure product containing oily phase, while the catalyst and the surfactant are recycled back into the reactor [9, 10]. The general process concept is depicted in Fig. 2.

In the scope of this study, an integrated process development approach was carried out. This consisted of initial lab scale experiments to determine suitable reaction conditions, the phase separation behaviour, and the general component and fluid properties. In addition, a mini-plant was constructed to investigate the technical and economic feasibility.

Besides tackling the main challenges (homogenous reaction and stable phase separation) of this novel process concept, also the applicability of early stage laboratory scale results on the technical system are of interest. For that, preliminary lab results of the reaction performance and the phase separation are presented.

From this data, an operational set point for the mini-plant has been derived and operated during a 200 hour campaign. The resulting data is then discussed in comparison to previous findings to highlight additionally needed investigations on the laboratory scale.

2. Background Information

In this section, the constitution of surfactant containing multiphase systems and occurring phenomena are discussed. Moreover, information on the applied component system and the constructed mini-plant is given.

2.1. Microemulsion systems

Microemulsion systems are formed with the addition of a specific amount of surfactant to a mixture of polar and nonpolar components. In a thermodynamically favourable state, micelles are formed as microscopic scale structures trapping either oil (nonpolar component) or water (polar component). As a consequence, the interfacial area between oil and water is increased. On a larger scale, this multiphase system can be regarded as homogeneous, thus enabling efficient catalytic reactions.

The formation of micelles and additional excess phases of either oil or water is influenced by the concentrations of the components in the system and the temperature of the system. Here, different phase separation states are possible, which could be exploited in a phase separation step. For the description hereof, Kahlweit's fish diagram, a cross-section of Gibb's phase prism at a constant oil to water ratio of 1:1, is used.

Relating to Fig. 3, it is obvious that the phase distribution and the emulsion state depends on temperature and surfactant concentration. Regarding the process concept a pure oil phase (light grey in Fig. 3) containing the reaction product and a catalyst rich aqueous phase (dark in Fig. 3) for efficient catalyst recycling are desirable. Therefore, only the three phase (3) and the two-phase region (2) are feasible for the plant operation. As described by

Pogrzeba et al. [13], the phase separation dynamics show a distinct reduction of the time needed to achieve full separation in the three-phase region; therefore, an operational temperature interval is given for the settler operation.
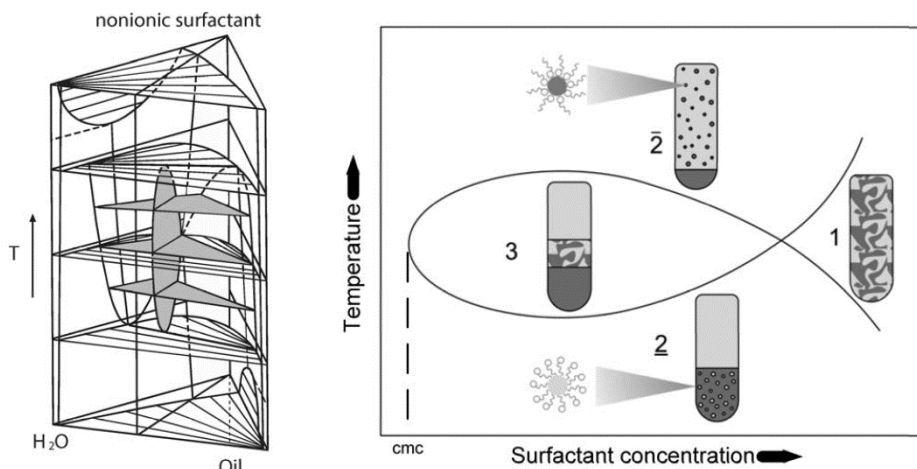
Fig. 3. Left: Temperature dependent Gibb's phase prism for an oil, water, and non-ionic surfactant mixture, taken from [11], Right: Kahlweit's fish [12]

2.2. Mini-plant Set-up

The constructed mini-plant at the Process Dynamics and Operations Group at Technische Universität Berlin consists of three main sections, as depicted in Fig. 4. The feed section contains tanks for the long-chained olefin, catalyst solution, surfactant, and synthesis gas containers. Piston pumps deliver a maximum alkene feed of 840g/h to the reaction section. Herein, a stirred tank reactor with 1.5 L total and 0.8 L liquid volume, gassing stirrer, and gauge glass, as well as the self-constructed settler are located. The latter is equipped with knitted wire internals to enhance phase separation and offers quick volume and functionality adaption through a modular design [14]. The heating of both units is regulated by thermostats. In the product section a part of the oil phase is purged from the process and stored for further processing.

The plant is fully automated by the process control system SIEMENS PCS7. Operators are supplied information from more than fifty sensors and may enforce operation trajectories through twenty actuators. Here, pumps for liquid flows, thermostats for temperature control and control valves for gas and product streams are selectable.

To provide additional information, especially for component concentrations inside the settler and the reactor two offline gas chromatographs are employed; additionally, an ICP-OES is used to determine the rhodium concentration in the product phase. For online-concentration measurements the Raman spectroscopy is carried out. Sampling positions and Raman probe locations are indicated in Fig. 4.

The plant was constructed to meet ATEX Explosion Zone 2 specifications.
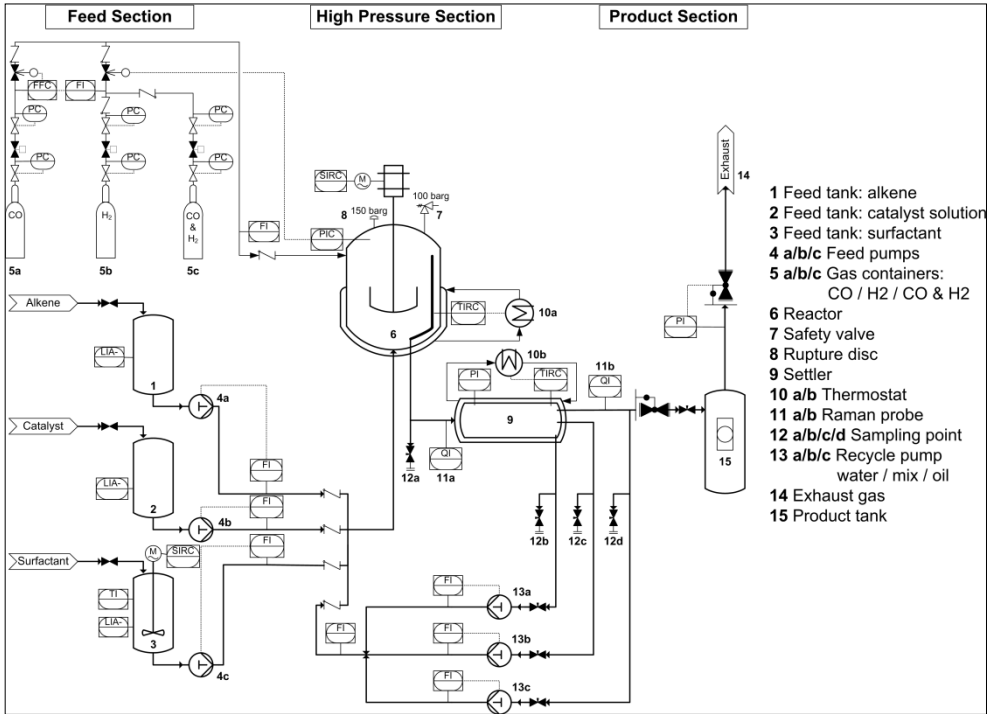
Fig. 4. Simplified P&ID of the mini-plant for the hydroformylation of long-chained olefins

2.3. Applied substances

For preliminary laboratory experiments and mini-plant operations, an exemplarily multiphase system was used in this study.

As a long-chained olefin 1-dodecene (C_{12} alkene) was used. The synthesis gas was set to a composition of 1:1 vol.-% of $CO:H_2$ with a purity of 5.0. The applied catalyst complex was aggregated from a Rhodium precursor [Rh(acac)(CO)2] (CAS: 14874-82-9), sponsored by Umicore N.V., and the water soluble ligand SulfoXantPhos (sulfonated form of XantPhos, CAS: 161265-03-8, Molisa GmbH). To maintain a microemulsion system, the non-ionic surfactant Marlipal 24/70 (CAS: 68439-50-9), sponsored by Sasol Germany GmbH, was applied. Additionally, small amounts of Na_2SO_4(1 wt.-%) were used to enhance the phase separation.

Expected products according to the reaction equation in Fig. 1 are 1-tridecanal and its isomers. Additionally, isomers of 1-dodecene and dodecane as a hydrogenation product were expected as by-products.

3. Preliminary investigations

The proposed novel process concept poses two major challenges: maintaining a reaction step which meets the advantageous features of a homogenous catalysis; maintaining a fast and robust phase separation. Although the overall mixer-settler set-up is comparatively simple, these major aspects need to be faced in advance on a smaller scale.

3.1. Reaction kinetics

Determining the reaction set point also requires detailed investigations on the influence of reactor operation parameters such as educt and surfactant concentration, synthesis gas pressure, and temperature.

For this purpose, various experiments were carried out to identify the overall aldehyde yield, reaction selectivity regarding all products, and the n/iso selectivity, marking the fraction of linear to branched aldehydes. As an example, the influence of pressure and temperature were examined in this study. Laboratory results are depicted in Table 1 and Fig. 5 and are subsequently discussed.

The concentrations of educt (Oil content) and surfactant for these experiments and accordingly, the mini-plant operation are fixed to

$$\text{Oil content: } \alpha = \frac{m_{Oil}}{m_{Oil} + m_{Water}} = 0.46 \tag{1}$$

$$\text{Surfactant content: } \gamma = \frac{m_{Surfactant}}{m_{Total}} = 0.08 \tag{2}$$

using mass fractions of 298 g/g Rh(acac)(CO)2 and 4530 g/g SulfoXantPhos(see [9, 15, 16]).
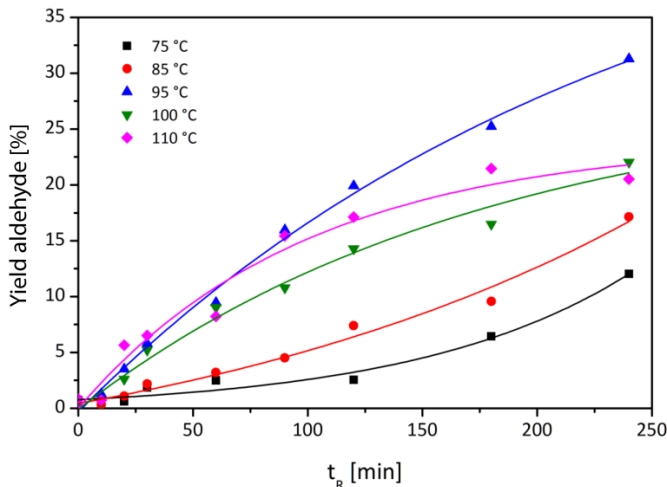
Fig. 5. Temperature influence on the yield of 1-tridecanal at 15bar and a reaction volume of 50mL, results taken from [16].

Experimental results of kinetic experiments at 95°C reaction temperature for the above given component composition after 240 min in a reaction volume of 50mL, results taken from [16]

Reaction pressure	Aldehyde [wt-%]	Selectivity [%]	Selectivity [n/iso] aldehyde	TOF_{Ald} [h^{-1}]
3 bar	15.9	83.1	97/3	94
15 bar	19.2	89.5	97/3	102
20 bar	20.4	87.5	99/1	106
30 bar	21.7	89.0	98/2	114
40 bar	15.7	82.6	97/3	77

Obviously, a reaction temperature of $T_R = 95°C$ is desirable, as the highest 1-tridecanal yields could be achieved. The decreasing aldehyde yield and changing curvature for other reaction temperatures is mainly due to changing catalyst selectivity and activity [15].

Regarding the pressure influence, there is a payoff between maximum yield and reaction selectivity. Given the results in Table 1 $p_R = 15$ bar is favoured given the high total selectivity, n/iso selectivity, and high aldehyde yield at a low pressure level.

At this point, operation conditions can be fixed for the reaction step of the mini-plant. Using the given temperature and pressure set point for a mini-plant, a product yield of roughly 30 % after 240 minutes could be expected in batch mode.

3.2. Phase separation

To maintain a stable phase separation in a microemulsion system, a specific optimal operation temperature needs to be applied, as described in section 2.1. A systematic approach for phase separation system investigations, model development and equipment design is given by Müller et al. [14]. Following this guideline, a systematic mapping of the three-phase region is achieved, which can be implemented into empirical correlations. Fig. 6 depicts a set of collated experimental data, whereas the upper and lower temperature limit of the desired three-phase region was tracked with respect to the surfactant concentration.

By also taking the product content X as 1-tridecanal yield and the oil content α into account, parameterised empiric correlations could be introduced (see Eq. 3 and 4). Fitting the parameters $P_i^{max/min}$ to experimental data enables the prediction of the settler temperature during the mini-plant operation based on the concentration data from GC samples at position 12a in Fig. 4.
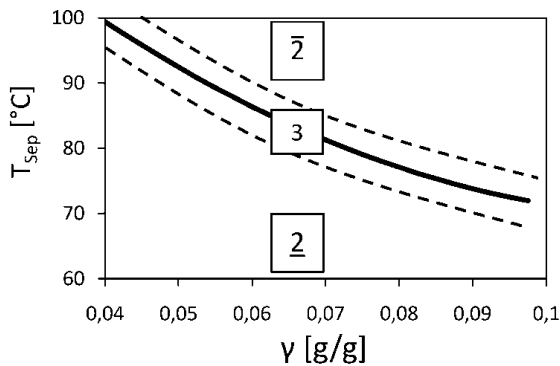
Fig. 6. Optimal separation temperature (solid line) and lower and upper limit (dashed lines) for maintaining the three-phase state, dependent on surfactant concentration γ. Oil content α was kept constant at 0.5 g/g, aldehyde yield was set to $X = 0$g/g.

$$
\begin{aligned}
T_{max} = \ & P_1^{max} + P_2^{max} \cdot \alpha + P_3^{max} \cdot \gamma + P_4^{max} \cdot X \\
& + P_5^{max} \cdot \alpha^2 + P_6^{max} \cdot \gamma^2 + P_7^{max} \cdot X^2 + P_8^{max} \cdot \alpha^2 \cdot \gamma^2 \\
& + P_9^{max} \cdot \alpha \cdot \gamma + P_{10}^{max} \cdot \alpha \cdot X + P_{11}^{max} \cdot X \cdot \gamma
\end{aligned}
\tag{3}
$$

$$
\begin{aligned}
T_{min} = \ & P_1^{min} + P_2^{min} \cdot \alpha + P_3^{min} \cdot \gamma + P_4^{min} \cdot X \\
& + P_5^{min} \cdot \alpha^2 + P_6^{min} \cdot \gamma^2 + P_7^{min} \cdot X^2 + P_8^{min} \cdot \alpha^2 \cdot \gamma^2 \\
& + P_9^{min} \cdot \alpha \cdot \gamma + P_{10}^{min} \cdot \alpha \cdot X + P_{11}^{min} \cdot X \cdot \gamma
\end{aligned}
\tag{4}
$$

4. Results and Discussion: Long-term mini-plant operation

Before detailing the measurement data from long-term mini-plant operations, the operational conditions and pursued schedules are outlined. Reaction data concerning product and by-product formation and an evaluation of the phase separation state and success is given and connected to the operation schedule.

4.1. Process Conditions and Schedule

In accordance with section 3.1 the reaction pressure is set to 15 bar gauge pressure, the reaction temperature is kept constant at 368 K. Depending on the emulsion state, the stirring speed is varied between 700 and 1200 rpm. Gassing is always ensured in this range.

Over a 200-hour period of operation, several operational modes where applied to investigate the dynamic process behaviour in terms of reaction performance and phase separation robustness. For these modes, the feed rate for the continuous operation and the internal recycle streams for the surfactant and the catalyst solution were adapted. Table 2 presents the main operational parameters of the three investigated modes SP1-3.

Mini-plant operation schedule overview with operational conditions and modes for different set points (SP)

	SP1	SP2	SP3
Duration	50 h	10 h	60 h
Residence time reactor	0.45 h	2.6 h	2.6 h
Residence time settler	0.55 h	3.2 h	3.2 h
Alkenefeed	100 g/h	0 g/h	30 g/h
Operation mode	Continuous	Full recycle	Continuous

The reaction started once synthesis gas was introduced into the process. This is marked as operation hour 0 in the following figures. Following the start up a steady state was obtained and operated in a continuous plant operation mode (SP1). Afterwards, a new set point was approached with a full recycle mode in SP2, without any alkene feed. SP3 again marks continuous operation. In this mode, the feed rate and the internal recycle were reduced to increase the residence times in reactor and settler and achieve a higher aldehyde yield.

4.2. Reaction yield and selectivity

In this section, the reaction performance within the mini-plant operation is shown regarding overall product yield and selectivity of the reaction. Depicted diagrams are sorted by the operation modes SP1-3, in terms of constant residence time and alkene feed rate.
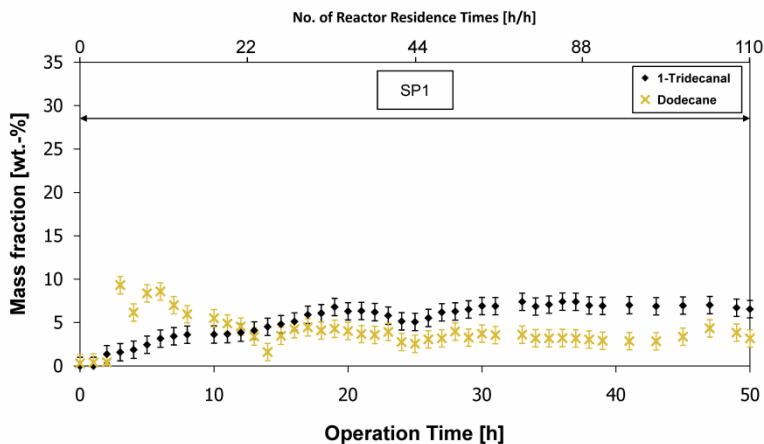
Fig. 7. Results for the main product (1-tridecanal) and one by-product (dodecane) as mass fractions in the reactor for mini-plant operation state SP1

With regard to product formation Fig. 7 and Fig. 8 confirm a significant formation of 1-tridecanal. A steady state concentration was achieved in all continuous operation modes. Due to the different residence times, a maximum mass fraction of roughly 7wt.-% for SP1 and 20wt.-% 1-tridecanal for SP3 are reasonable. In the qualitative comparison to the reaction performance in Fig. 5 a minor reduction in product yields is obvious, which is caused by the different geometric set up (scale-up) and non-ideal mixing in the reactor.
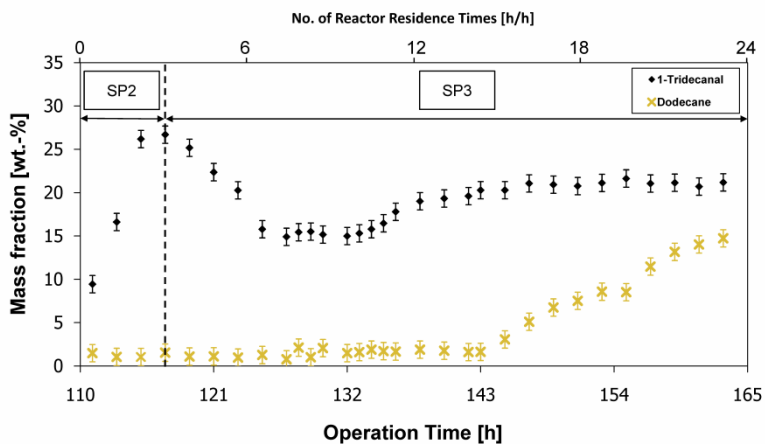

Fig. 8. Mass fractions of main the product (1-tridecanal) and one by-product (dodecane) in the reactor for mini-plant operation modes SP2 and SP3
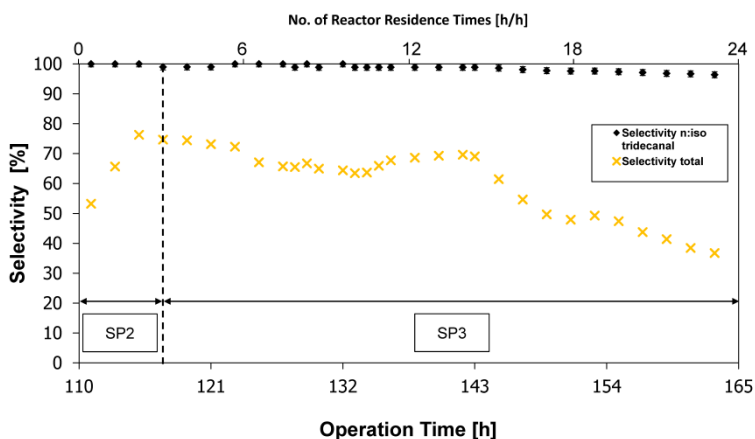
Fig. 9. Selectivity of the reaction expressed as the fraction of linear to branched aldehydes (n/iso) and the total selectivity towards 1-tridecanal. Data is given for the for mini-plant reactor at operation states SP2 and SP3

However, large quantities of the undesired by-product dodecane are also produced. This undesired hydrogenation is dominating for the start-up of the operation at operation time 0 to 10h and reoccurs in mode SP3 beginning with operation time 143 (see Fig. 8). This reaction performance is rather unexpected as only slightly higher hydrogenation was found by Pogrzeba et. al for higher reaction temperatures [16].

Taking a closer look at the reaction selectivities in Fig. 9 the finding described above is emphasised. Table 1 displays a total reaction selectivity of 89.5% for previous batch experiments. In the mini-plant operation, this remains unobtainable with isomerisations further lowering the selectivity. By contrast, the selectivity of linear to branched aldehydes meets prior findings and periodically tops the proposed value of 97% linear aldehyde.

Interestingly, the operational mode has a strong influence on reaction performance and selectivity. This is perfectly clear for the effect of residence time on the expected yield. However, the strong affection on the by-product formation is rather unexpected (compare total selectivity for SP2 and SP3). Given the fact, that the active catalyst species is formed via the addition of a carbon monoxide molecule (see [9]), it is possible that a temporary transformation of the catalyst species occurs within the separation step and the internal recycle which leads to a different reaction performance once the recycled catalyst re-enters the reactor. Consequently, as a feedback to laboratory experiments, operation modes and catalyst conditions need to be investigated regarding by-product formation in order to identify infeasible operation conditions for the mini-plant or conceptual or constructional requirements for improvement.

4.3. Phase separation performance

The phase separation performance is evaluated by the purity of the gathered oily top phase of the settler. For this, sample point 12d (Fig. 4) is used to analyse the total amount of oily components (n/iso-dodecene, dodecane, n/iso-tridecanal) using gas chromatography. The results for operation mode SP2 and SP3 are given in Fig. 10.

Fig. 10. Phase separation quality embodied by the total amount of oily components in the oil phase of the settler. Data given for operation state SP2 and SP3

In general, the phase separation was successfully achieved for both operation set points as the mass fraction of oily components is permanently hi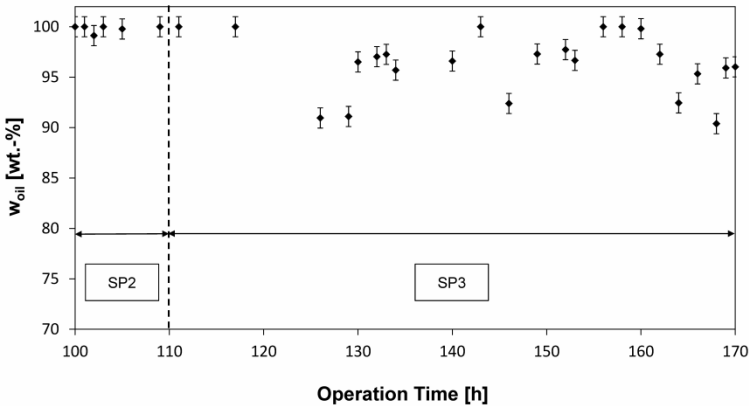gher than 90 wt.%. Periods of perfect phase separation with 100 wt.% oil component mass fraction are achieved for SP2 and around 160 hours of operation. However, reduced oil phase purity is mainly due to the dissolution of larger amounts of surfactant and consequently also traces of the catalyst solution. The corresponding phase separation state is the two upper region, where for a higher temperature, the solubility of surfactant in the oil phase increases [13]. In case of SP3 in Fig. 10, the three-phase region could not efficiently be tracked and operated throughout plant operation – this might be due to concentration shifts caused by the reaction and applied recycle ratios between the recycle pumps 13a-c in Fig. 4. Moreover, the applied model prediction is partly invalid, as the large byproduct formation is not taken into account.

Referring to section 4.2, a possible influence of the settler operation on the catalyst needs to be investigated in terms of the prevention of by-product formation. Here, the reaction performance under varied settler residence times will be investigated. Additionally of interest are the component distribution within the settler phases and possible accumulation of the catalyst and the surfactant in this unit.

5. Conclusions and Outlook

In this contribution, a proof of concept for a novel process for the hydroformylation of long-chained olefins is presented with experimental data of a long-term operation of a mini-plant. The applicability of preliminary lab scale results on the plant operation are discussed and future demand for investigations is highlighted.

In general, the main aspects of the developed process concept, a quasi-homogenously catalysed reaction, as well as a stable phase separation could be proven for a long-term operation of a mini-plant. However, some challenges arise from the conducted plant experiments which show a mismatch with preliminary lab experiments. Here, severe by-product formation is present, which drastically reduces the reaction selectivity. This contrasts the economically beneficial homogenous catalysis. Transformations of the active catalyst species are supposed to account for this undesired effect. Additional kinetic experiments and constructional modifications of the mini-plant will be carried out to overcome this issue. The concurrent conduction of lab scale and mini-plant scale experiments show a possible reduction of process development time, as arising obstacles can be tackled at an early stage. Concerning the phase separation, the increased byproduct formation leads to a certain model-plant mismatch This makes the controllability of the phase separation tedious and shows the complexity of this system. Early stage identification on the influential parameters of the phase separation in a technical system offers a more systematic approach to determining phase separation behaviour.

For further investigations, the described challenges in reaction and separation procedures are to be analysed in the lab to provide updated information for future mini-plant operations. Additionally, advanced process control strategies are to be implemented to enhance controllability and observability of the mini-plant. Advanced (online) analytics,

such as Raman spectroscopy, are to be tested for fast and reliable concentration identifycation for in situ tracking reaction and phase separation.

R e f e r e n c e s

[1] Franke R., Selent D., Börner A., *Applied Hydroformylation*, Chem. Rev, vol. 112 (11), 2012, 5675-5732.

[2] Röper M., *Homogene Katalyse in der Chemischen Industrie*, Chemie Unserer Zeit, vol. 40, 2006, 126-135.

[3] Kohlpaintner C.W., Fischer R.W., Cornils B. *Aqueous Biphasic Catalysis: Ruhrchemie/Rhône-Poulenc Oxo Process*, Appl. Catal. A Gen.,vol. 221(1-2), 2001, 219-225.

[4] Wiese K.-D., Obst D., *Catalytic Carbonylation Reactions: Hydroformylation* [in:] Beller M. (Eds.): *Topics in Organometallic Chemistry*, Springer, Berlin Heidelberg, 2006.

[5] Cornils B., Herrmann W. A., *Applied Homogeneous Catalysis with Organometallic Compounds: A Comprehensive Handbook in Three Volumes*, Wiley, 2002.

[6] Kupka J., *Hydroformylierung von 1-Octen in Mikroemulsion*, PhD thesis, Technical University of Braunschweig, 2006.

[7] Miyagawa C.C., Kupka J., Schumpe A., *Rhodium-Catalyzed Hydroformylation of 1-Octene in Micro-Emulsions and Micellar Media*, J. Mol. Catal. A Che, vol. 234(1–2), 2005, 9-17.

[8] Leeuwen P.W.N.M. (Eds.), Claver C., *Rhodium-Catalyzed Hydroformylation*, Kluwer Academic Publishers, Dordrecht 2001.

[9] Hamerla T., Rost A., Kasaka Y., Schomäcker R., *Hydroformylation of 1-Dodecene with Water-Soluble Rhodium Catalysts with Bidentate Ligands in Multiphase Systems,* Chem. Cat. Chem., vol. 5(7), 2013, 1854-1862.

[10] Müller M., Kasaka Y., Müller D., Schomäcker R., Wozny G., *Process Design for the Separation of Three Liquid Phases for a Continuous Hydroformylation Process in a Miniplant Scale*, Ind. Eng. Chem. Res, vol. 53, 2013, 7259-7264.

[11] Schwarze M., Pogrzeba T., Volovych I., Schomäcker R., *Microemulsion Systems for

Catalytic Reactions and Processes, Catal. Sci. Technol.,vol. 5(1), 2015, 24-33.

[12] Lade O., *Charakterisierung, Modellierung und Polymerisation von Mikroemulsionen aus Alkylmethacrylaten*, PhD thesis, Universität Köln, 2001.

[13] Pogrzeba T., Müller D., Illner M., Schmidt M., Kasaka Y., Weber A., Wozny G., Schomäcker R., Schwarze M., *Superior Catalyst Recycling in Surfactant Based Multiphase Systems – Quo Vadis Catalyst Complex?*, Chem. Eng. Process. Process Intensif, vol. 99, 2015, 155-166.

[14] Müller D., Esche E., Pogrzeba T., Illner M., Schomäcker R., Wozny G., *Systematic Phase Separation Analysis of Surfactant Containing Systems for Multiphase Settler Design*, Ind. Eng. Chem. Res, vol. 54(12), 2015, 3205-3217.

[15] Hamerla T., *Hydroformylierung langkettiger Olefine mit zweizähnigen Rhodium-Komplexen in mizellaren Lösungen und Mikroemulsionen*, PhD thesis, Technical University of Berlin, 2014.

[16] Pogrzeba T., Müller D., Hamerla T., Esche E., Paul N., Wozny G., Schomäcker R., *Rhodium catalysed hydroformylation of long-chain olefins in aqueous multiphase systems in a continuously operated mini-plant*, Industrial & Engineering Chemical Research, vol. 54(48), 2015, 11953-11960.

RYSZARD KANTOR, PRZEMYSŁAW MŁYNARCZYK[*]

WATER JACKETS AS EFFICIENT HEAT SHIELDS IN HIGH TEMPERATURE DIFFERENCE CASES – CFD MODELLING OF CONVECTIVE AND RADIATIVE HEAT TRANSFER IN VACUUM SYSTEMS

PŁASZCZ WODNY JAKO EFEKTYWNA IZOLACJA CIEPLNA W APLIKACJACH O DUŻEJ RÓŻNICY TEMPERATUR - MODELOWANIE CFD KONWEKCYJNEJ I RADIACYJNEJ WYMIANY CIEPŁA W SYSTEMACH PRÓŻNIOWYCH

Abstract

Many experimental high-energy installations, e.g. ITER (Cadarache), CERN (Geneva), SOLARIS (Krakow), require an ultra-high quality of vacuum. To meet these requirements, a vacuum void and its adjacent diagnostic systems are exposed to elevated temperatures (baking) after assembly to outgas all volatile surface contaminants. The baking temperature peaks as high as 250°C for up to 24 hours.

Keywords: vacuum systems, heat transfer, water jacket, heat shield

Streszczenie

W eksperymentalnych instalacjach wysokich energii, m. in ITER (Cadarache), CERN (Genewa), SOLARIS (Kraków), istnieje konieczność uzyskania próżni o wysokiej jakości. W tym celu przestrzeń próżniowa oraz znajdujące się w niej urządzenia diagnostyczne wystawiane są na bardzo wysokie temperatury by pozbyć się resztek zanieczyszczeń z układu. Podczas tego procesu wygrzewa się instalację w temperaturze dochodzącej do 250°C przez nawet 24 godziny.

Słowa kluczowe: system próżniowe, wymiana ciepła, płaszcz wodny, izolacja termiczna

[*] DSc. Eng. Ryszard Kantor, MSc. Eng. Przemysław Młynarczyk, Institute of Thermal and Process Engineering, Faculty of Mechanical Engineering, Cracow University of Technology.

1. Introduction

The concept of a water jacket cooled by water, assumes that it is a sufficiently efficient heat shield. It serves as a thermal barrier between high and low temperature zones. The water jacket should be, as much as possible, thermally isolated from the high temperature structure. The most efficient thermal insulation system is based on a vacuum layer (one or more if needed) enclosed by surfaces characterised by their low thermal emissivity coefficient. In practical applications, the thermal barrier is not fully efficient in steady state conditions and gains heat from the adjacent hot walls. The excessive heat must be removed from the thermal barrier in order to maintain it at the required temperature and this is provided by cooling water circulating along walls of the thermal barrier. For less strict requirements and also for reasonably low temperature differences between hot and cold regions, the heat shield is often designed as a metal shield made of material which is characterised by its high thermal conductivity [1]. The temperature of the heat shield is controlled by water circulating through loops of pipes which are attached to the external or internal surfaces of the heat shield. For more thermally loaded cases and also for high thermal requirements, the only efficient solution is the one based on the water jacket concept.

The aim of proposed paper is to compare the efficiency of the multilayer insulation thermal shield structures, based on the water jacket concept, by the use of 3D CFD simulation in ANSYS Fluent software. The surface-to-surface (S2S) model is applied to simulate heat transfer by radiation. In addition, the paper includes discussion about multilayer solutions, characterised by a high thermal resistance, and particularly dedicated to vacuum transfer lines with high temperature differences.

2. Water Jacket Geometries

The water jacket geometries for the comparison between single- and double-layer vacuum solutions have been modelled in the Autodesk Inventor software. The layout of the single-layer vacuum system is shown in Figure 1.

The water jacket layout is based on two axisymmetric cylinders made of stainless steel, one inserted into the other forming a thin layer between the walls which is filled with circulating water. An internal space, within the internal cylinder (1) is allotted for the installation of diagnostic instruments. It is assumed that the inner wall (0) of the internal cylinder (1) is ideally thermally connected with diagnostic instruments; thus, their temperatures are considered to be the same. The temperature of the internal cylinder is regulated by the temperature of the circulating water (2). It is assumed that all diagnostic instruments are thermally connected with the internal cylinder (1) and the entire thermal load is absorbed by the water (2) through the internal cylinder (1). The middle cylinder (3) absorbs the heat by radiation, through the vacuum (4) layer, emitted by the adjacent surfaces of the external shell (5). Moreover, the supporting elements (6) are indispensable to fix the water jacket, however they constitute additional thermal bridges. In the proposed solution, the supporting elements are formed in a pattern of full length rectangular rods, parallel to the axis of the water jacket cylinders. To ensure thermal resistance of the

proposed solution, the emissivity coefficient of walls adjacent to the vacuum should be as low as possible and the number, size and thermal conductivity of the supporting elements should be minimised. It is conservatively assumed that four full-length supporting elements (6) is the maximum number and size and in the final design phase, it would be reduced. The double-vacuum layer water jacket layout is presented in Figure 2.
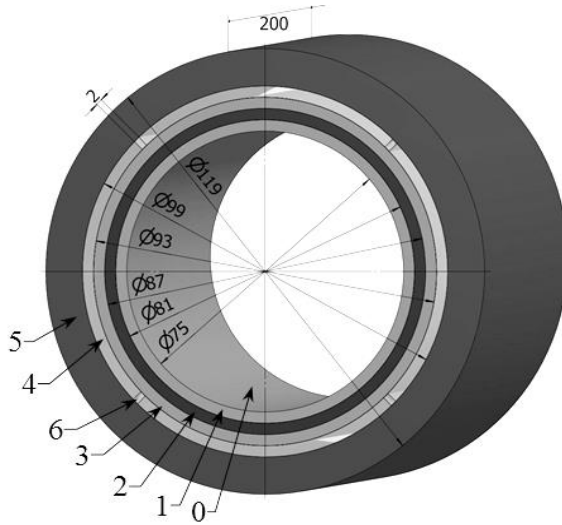
Fig. 1. Concept of the water jacket with single-layer vacuum

The water jacket zone names and basic dimensions are presented in Table 1.

<div align="right">T a b l e 1</div>

The water jacket with single-layer vacuum - zone names and basic dimensions

No	Name	Dimension [mm]	Description
0	Inner Wall	75	Diameter
1	Internal Cylinder	3	Thickness
2	Water	3	Thickness
3	Middle Cylinder	3	Thickness
4	Vacuum	3	Thickness
5	External Shell	10	Thickness
6	Supporting Element	2	Width
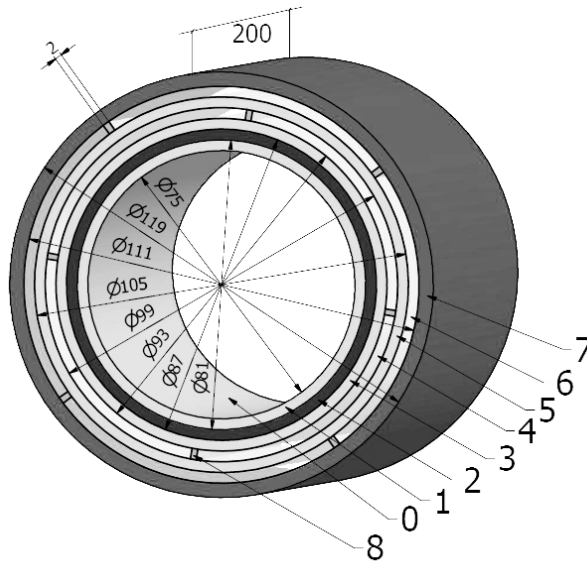
Fig. 2. The water jacket with double-layer vacuum

The double-layer solution is founded on the single-layer water jacket concept. Zone names and basic dimensions are presented in Table 2.

<div align="right">T a b l e 2</div>

The water jacket with double-layer vacuum - zone names and basic dimensions

No	Name	Dimension [mm]	Description
0	Inner Wall	75	Diameter
1	Internal Cylinder	3	Thickness
2	Water	3	Thickness
3	Middle Cylinder	3	Thickness
4	First Vacuum layer	3	Thickness
5	External Cylinder	3	Thickness
6	Second Vacuum layer	3	Thickness
7	External Shell	3	Thickness
8	Supporting Element	2	Width

Most of the features and components of the double-layer vacuum solution are the same as in the single-layer concept. As an additional component, it contains the external cylinder (5), separating two vacuum layers (4 and 6), all located outside of the water layer (2). The external cylinder (5) and the second vacuum layer (6) are inserted by removing the internal fragment of the external shell (7). The external cylinder (5) is supported on both sides by two sets of four evenly distributed supporting elements (8). The second set of supporting elements is orientated at an angle of 45° relative to the first set in order to minimise heat transfer by thermal conduction.

3. Boundary conditions and numerical model

All CFD simulations have been performed with the ANSYS Fluent software. Numerical meshes in both geometries were generated by the sweep method. The 3D mesh of the single-layer vacuum model is presented in Figure 3. The global boundary conditions and material properties are listed in Table 3.
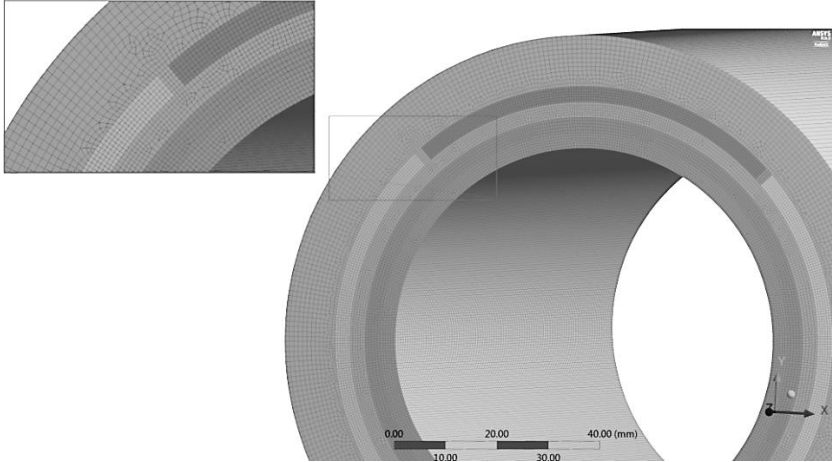
Fig. 3. 3D structural mesh

T a b l e 3

Global boundary conditions and material properties

Boundary condition	Value
Inlet Water Temperature	293 K
External Shell Temperature	513 K
Heat load from diagnostic instruments	2 W
Water Inlet Velocity	0.5 [m/s]
Internal radiation emissivity coefficient	0.5
Material of all structural components	Stainless Steel 316L
Thermal conductivity (316L)	16.27 W/mK
Cooling Water properties	Demineralised water, reference pressure 1 atm
Vacuum properties	Vacuum: air at constant density, max. 10 Pa

The major heat transfer rate to the water jacket is transferred from the external shell to the external cylinder, by radiation, surface to surface, and locally by thermal conduction through the supporting elements. It is assumed that the contribution of thermal conduction and convection effects to the overall heat transfer through the vacuum layer is negligible [2], this is mainly due to the extremely low density of the gas and the thin vacuum gap.

The additional minor heat load, generated by diagnostic instruments during their operation is a maximum of 2 watts. Diagnostic instruments are located in the space within

the inner wall (0). In the simulation, it is defined as a constant heat flux boundary condition on the inner wall of the internal cylinder.

According to ANSYS Fluent Documentation [3], the recommended optimal numerical models are as follows:

- pressure based, steady-state model for flow calculations;
- k-ε realisable turbulence model;
- surface-to-surface radiation model.

4. Simulation results comparison

Preliminary calculations indicate, assuming that layout and dimensions are constant, that the influence of three parameters is dominant: water flow rate, internal emissivity and the thermal conductivity of solid materials. The above mentioned parameters are defined in the simulation task as constant boundary conditions and material properties.

Steady-state simulation results are very promising and indicate that the idea of the heat shield by the water jacket is very effective in both cases. Temperature contours on the symmetrical (in the middle of the length) cross-sections and selected walls are shown in Figure 4. The temperature of the internal cylinder (1) is, in both cases, uniformly maintained at a low level, close to the temperature of the water. The high temperature gradient, particularly in the supporting elements (6) of the single-layer vacuum layout, may generate thermal stress problems. This effect should be studied later, during the final design stage.
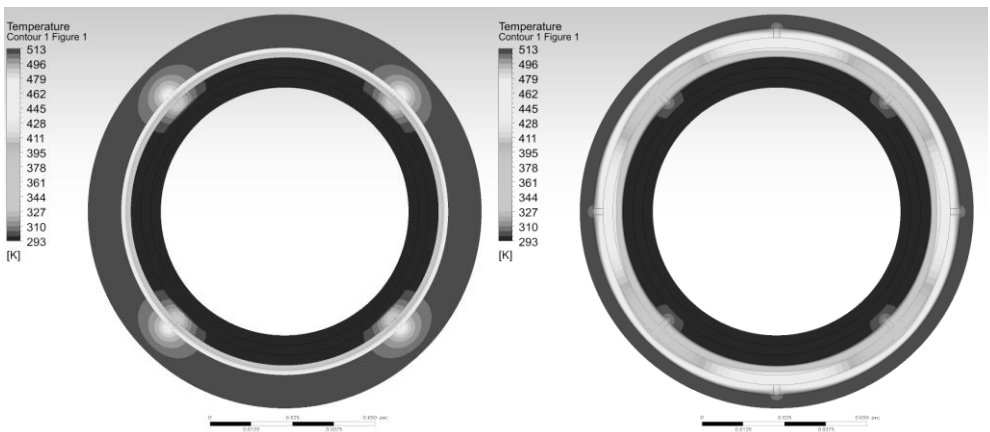
Fig. 4. Temperature contours at cross section: a) single-layer Vacuum layout, b) double-layer Vacuum layout

For more strict thermal requirements, e.g. narrow range of acceptable temperature, the impact of the supporting elements may cause problems with thermal uniformity. Contours of temperature along the inner wall (0) are shown in Figure 5.

The entire water jacket is of almost uniform temperature, with the exception of regions with direct solid-to-solid contacting areas by the supporting elements. The temperature rise is 0.6 K in the single-layer vacuum layout and 0.3 K in the double-layer vacuum layout.
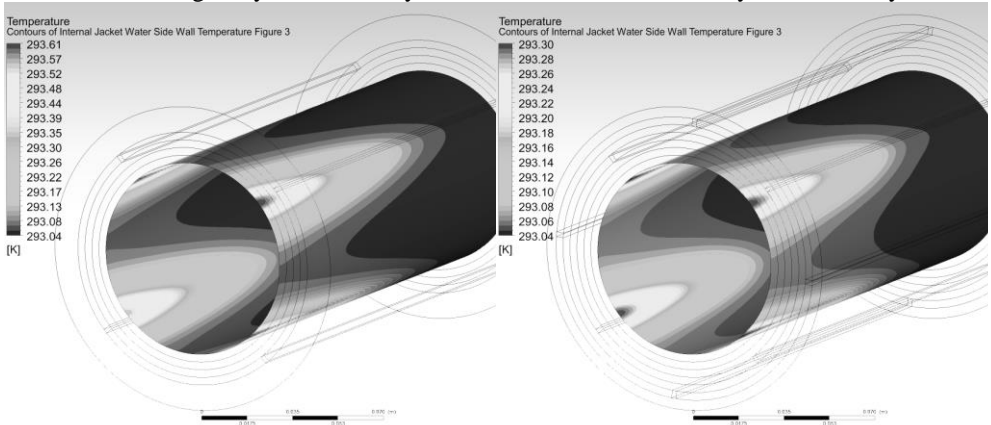
Fig. 5. Temperature contours on the inner wall (0) of: a) single-layer vacuum layout, b) double-layer vacuum layout

There are two possible ways to limit heat transfer by conduction through the supporting elements – by using insulating materials with low thermal conductivity and/or by limiting the thermal contact area; for instance, the quantity and length of the supporting elements can be limited.

Contours of temperature along the middle cylinder (3) and the supporting elements (6, 8) are shown in Figure 6.
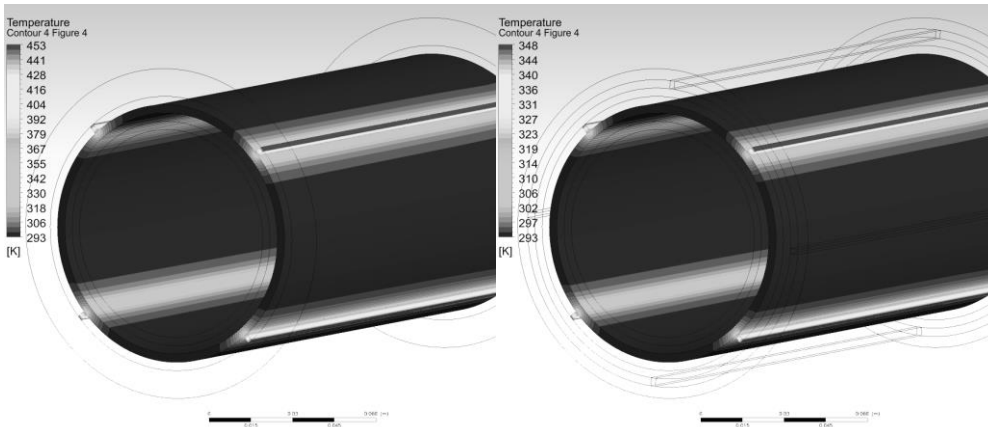
Fig. 6. Temperature contours on the middle cylinder (3) of: a) single-layer vacuum layout, b) double-layer vacuum layout

The analysis of both cases in Figure 6 shows that the influence of the intermediate element – the external cylinder (5) is extremely positive and the double-layer vacuum layout may be chosen as a final solution. The double-layer vacuum layout in principle solves the problem of high temperature gradient, decreasing temperature by around 100 K. Moreover, it allows the decreasing of the overall heat transfer by around three times. The final results are shown quantitatively in Table 4.

T a b l e   4

Final quantitative results – comparison both layouts

Name	Single-layer Vacuum layout	Double-layer Vacuum layout
Water Mass flow Rate [kg/s]	0.000396	0.000396
Increase of Water Average Temp. [K]	0.5	0.2
Increase of Inner Wall (0) Average Temp. [K]	0.6	0.3
First Vacuum (4) – Radiative Heat Transfer Rate W]	63.5	24.6
First Vacuum (4) – Conductive Heat Transfer Rate through the Supporting Elements [W]	691	242
Total Heat Transfer Rate [W]	756.5	268.6

A particularly important conclusion derived from Table 4 is that it is strongly recommended to restrict the heat transfer by conduction through the supporting elements since their contribution to the overall heat transfer is dominant.

5. Conclusions

The double-layer vacuum layout is significantly more effective as a thermal barrier. The overall heat transfer dropped from 691 W in the single-layer layout to 242 W in the double-layer layout. Additionally, the temperature of the inner wall (0) can be better controlled and maintained more uniformly in the narrow range. However, there is the possibility of further limitation of heat transfer through the water jacket and in consequence the cooling demand. There are several possible ways to decrease the heat transfer occurring as a result of conduction through the supporting elements by:
1. using low-thermal-conductivity insulating materials;
2. limiting the thermal contact area;
3. limiting the number and length of the Supporting Elements.

It is strongly recommended to take into consideration the above mentioned recommendations, since their influence on the overall heat transfer is dominant. Moreover, the contribution of the radiative heat transfer (see Table 4) to the overall heat transfer should be limited by applying a special surface finish.

R e f e r e n c e s

[1] Kantor, R., *Optimization of the LUCID detector heat shield cooling*, 20th International Conference of Process Engineering and Chemical Plant Design, Berlin 2014, 165-177.
[2] *VDI Heat Atlas Second Edition*, Springer-Verlag, Berlin-Heidelberg 2010.
[3] ANSYS Fluent Documentation, v. 16.0.

MARKUS KOLANO, MANUEL BREHMER, MATTHIAS KRAUME[*]

NUMERICAL SIMULATION OF VISCOELASTIC FLUID FLOW IN STIRRED VESSELS

SYMULACJA NUMERYCZNA PRZEPŁYWU PŁYNÓW LEPKOSPRĘŻYSTYCH W MIESZALNIKU

Abstract

In this work, a tool for calculating viscoelastic flows with rotating geometries in OpenFOAM based on the finite-volume method is presented. The tool combines the split-stress tensor approach and viscoelastic differential constitutive equations with the sliding-mesh technique. With this tool, a CFD simulation was run for a geometry of a spherical stirrer in an aqueous solution of carboxyl cellulose. Additionally, a rheological characterisation of that solution was conducted. For validation, the simulations were compared with flow field data acquired through particle image velocimetry measurements.

Keywords: viscoelasticity, White-Metzner, PIV, OpenFOAM, dynamic mesh

Streszczenie

W pracy przedstawiono program OpenFOAM do wyznaczania przepływów płynów lepkosprężystych przy użyciu metody objętości skończonych. Program łączy założenia dla tensora naprężeń dzielonych z konstytutywnymi równaniami różniczkowymi płynów lepkosprężystych oraz techniką przesuwnych oczek siatki. Symulacje CFD przeprowadzono w mieszalniku wodnego roztworu celulozy karboksylowej, badano również charakterystykę reologiczną roztworu. W celu weryfikacji symulacje zostały porównane z wartościami przepływu w mieszalniku uzyskanymi metodą PIV.

Słowa kluczowe: lepkosprężystość, model White-Metzner'a, PIV, OpenFOAM, dynamiczna siatka

[*] MSc. Eng. Markus Kolano, MSc. Eng. Manuel Brehmer, Prof. PhD. DSc. Eng. Matthias Kraume, Chair of Chemical & Process Engineering, Faculty of Process Sciences, Technical University of Berlin.

1. Introduction

Most of the fluids encountered in the chemical, food or cosmetic industries exhibit non-Newtonian flow behaviour. Viscoelastic effects can occur, altering flow patterns and dynamics in comparison to Newtonian fluids, especially when dealing with polymeric and biological fluids. In stirred tanks, these effects can lead to cavern formation and inversion of flow fields around impellers i.e., influencing mixing times, power input, shear stress, etc. For process design, the ability to quantify and predict these effects numerically is therefore of high interest in order to be able to choose optimal stirrer and tank geometries and process conditions.

In general, viscoelastic fluids can be viewed as a combination of a viscous and an elastic material. In contrast to Newtonian fluids, time-dependent stress relaxation is observed. When subjected to shearing, viscoelastic fluids develop normal stress differences, leading to phenomena like the Weissenberg effect [1]. Furthermore, stretching of these fluids causes elastic forces. Additionally, the viscosity dependence on shear rate is commonly non-linear.

For a rotating sphere stirring a viscoelastic fluid in a vessel, Ide et al. [2] found out that dependently of the viscoelasticity of the continuous phase, the general direction of the secondary flow field is changed: for polystyrene-styrene solutions with low concentrations (up to 20wt-%), both the primary and the secondary flow field are qualitatively similar to those of a Newtonian fluid; for higher concentrations (50wt-% or more), the fluid flows inwardly at the poles of the sphere and is expelled at the equator. Similar phenomena were found for a disc and a flat turbine.

Numerical simulations of these effects have already been conducted for a sphere with the finite element method, i.e. [3], but a tool to simulate viscoelastic flows for rotating geometries with a finite-volume method in non-commercial CFD software hasn't yet been developed. In this work, a tool capable of calculating viscoelastic fluid flow for complex rotating geometries is presented. For validation, a CFD simulation for a rotating sphere in an aqueous carboxymetyhl cellulose solution was compared to particle image velocimetry measurements. For the simulation, a rheological characterisation of the used solution was also conducted.

2. Materials and Methods

2.1. Mathematical Model

To calculate isothermal incompressible flows of viscoelastic fluids, the equations for mass conservation:

$$\nabla \cdot (u) = 0 \tag{1}$$

and momentum conservation:

$$\frac{\partial (\rho u)}{\partial t} + \nabla \cdot (\rho u u) = -\nabla (p) + \nabla \cdot \tau \tag{2}$$

have to be solved, with ρ denoting the density of the fluid, p the pressure, u the velocity vector and τ the stress tensor.

By splitting the stress tensor into a Newtonian solvent contribution τ_s and an polymeric contribution τ_p, both the influence of the solvent and the polymeric liquid can be taken into account:

$$\tau = \tau_s + \tau_p \tag{3}$$

with τ_s being defined by:

$$\tau_s = 2\eta_s D \tag{4}$$

where η_s is the dynamic solvent viscosity and D is the deformations rate tensor:

$$D = \frac{1}{2}\left(\nabla u + [\nabla u]^T\right) \tag{5}$$

In literature, numerous constitutive models have been developed to describe viscoelastic flow behaviour with a polymeric contribution to the stress tensor [4]. In this work, the differential White-Metzner model [5] is used:

$$\tau_p + \lambda_p(\dot{\gamma})\breve{\tau}_p = 2\eta_p(\dot{\gamma})D \tag{6}$$

with η_p being the polymeric dynamic viscosity, λ_p the relaxation modulus and the shear rate $\dot{\gamma}$ being defined by:

$$\dot{\gamma} = \sqrt{2D:D} \tag{7}$$

In Equation (6), $\breve{\tau}_p$ denotes the upper convected derivative of the stress tensor:

$$\breve{\tau}_p = \frac{D}{Dt}\tau_p - \left[\nabla u^T \cdot \tau_p\right] - \left[\tau_p \cdot \nabla u\right] \tag{8}$$

where $\dfrac{D}{Dt}$ is the material derivative:

$$\frac{D}{Dt}\tau_p = \frac{\partial}{\partial t}\tau_p + u \cdot \nabla\tau_p \tag{9}$$

Both the shear rate dependence of the relaxation modulus and the viscosity can be modelled by a Cross correlation:

$$\eta_P(\dot{\gamma}) = \frac{\eta_{P,0}}{1 + (k\dot{\gamma})^{1-m}} \tag{10}$$

$$\lambda_P(\dot{\gamma}) = \frac{\lambda_{P,0}}{1 + (L\,\dot{\gamma})^{1-n}} \tag{11}$$

where $\eta_{P,0}$ and $\lambda_{P,0}$ are the constant dynamic viscosity and relaxation modulus at a zero shear rate respectively; k, m, L and n are adjustable parameters. Instead of a model, Carreau-Yasuda-models can also be used:

$$\eta_P(\dot{\gamma}) = \eta_{P,0}\left[1 + (k\,\dot{\gamma})^a\right]^{\frac{m-1}{a}} \tag{12}$$

$$\lambda_P(\dot{\gamma}) = \lambda_{P,0}\left[1 + (L\,\dot{\gamma})^b\right]^{\frac{n-1}{b}} \tag{13}$$

To take into account a constant dynamic viscosity $\eta_{P,\infty}$ and relaxations modulus $\lambda_{P,\infty}$ at high shear rates, a variation of the Carrau-Yassuda equation can be used:

$$\eta_P(\dot{\gamma}) = \eta_{P,\infty} + \left(\eta_{P,0} - \eta_{P,\infty}\right)\left[1 + (k\,\dot{\gamma})^a\right]^{\frac{m-1}{a}} \tag{14}$$

$$\lambda_P(\dot{\gamma}) = \lambda_{P,\infty} + \left(\lambda_{P,0} - \lambda_{P,\infty}\right)\left[1 + (L\,\dot{\gamma})^b\right]^{\frac{n-1}{b}} \tag{15}$$

With a and b being additional adjustable parameters.

2.2. Model Implementation in OpenFOAM®

In 2010, Favero et al [6] developed a volume of fluid tool to calculate transient, incompressible viscoelastic flows. They implemented numerous differential viscoelastic constitutive equations and released them in the OpenFOAM® Extend Project. Additionally, dynamic mesh handling is a supported feature in OpenFOAM® [7], allowing for both dynamic mesh movement as well as refinement.

The tool presented in this work combines the aforementioned features to calculate viscoelastic flows for rotating geometries. For velocity-pressure-stress coupling, a so-called PIMPLE algorithm is used, a method that results from combining the SIMPLE [8] and PISO [9] algorithms. The procedure used in the tool to solve the problem of viscoelastic fluid flow for rotating geometries can be summarised as follows:

1. As a first step, the initial mesh is altered according to the predefined mesh motion, updating boundary conditions, calculating relative fluxes with the given fields of velocity u, pressure p and stress tensor τ and interpolating them at arbitrary mesh interfaces.
2. Subsequently, the PIMPLE algorithm starts: the pressure gradient and the stress divergence are calculated explicitly and the momentum equation is solved implicitly for each velocity component.
3. With the new velocity field estimate, the pressure equation is solved and corrected.
4. If desired, an inner PISO corrector loop can be started, which repeatedly solves and corrects the pressure equation to obtain more accurate pressure and velocity fields.
5. Finally, the stress tensor field is calculated according to equation (6).
6. Steps 2, 3, 4 and 5 can be repeated as many times as desired before the PIMPLE-loop for the next time step starts at step 1 again.

2.3. Computational Grid and Solver Parameters

For the CFD simulations, the computational grid was created with the snappyHexMesh utility – an OpenFOAM meshing tool capable of refining the mesh at specific surfaces, feature lines and within certain cell. The dimensions of the grid were 0.3 m in all directions, with a sphere of 0.04 m diameter being in the centre of the mesh. The rotating region of the mesh was a cylindrical region with a diameter of 0.2 m and a length of 0.2 m, with the front and back side of cylinder being oriented normal to the x-axis, which was also the axis of rotation. The overall number of cells was 71,540, with 67,080 of them being hexahedra, 24 prisms and 4,436 polyhedra. The arbitrary mesh interface consisted of 21,053 faces, while the dynamic mesh region contained 67,538 cells. Convergence criteria for the velocity, pressure and stress tensor fields were a residual of $4\ 10^{-7}$ with a relative tolerance of 0, respectively. The time-step size was adjusted dynamically to a maximum Courant number of 1.
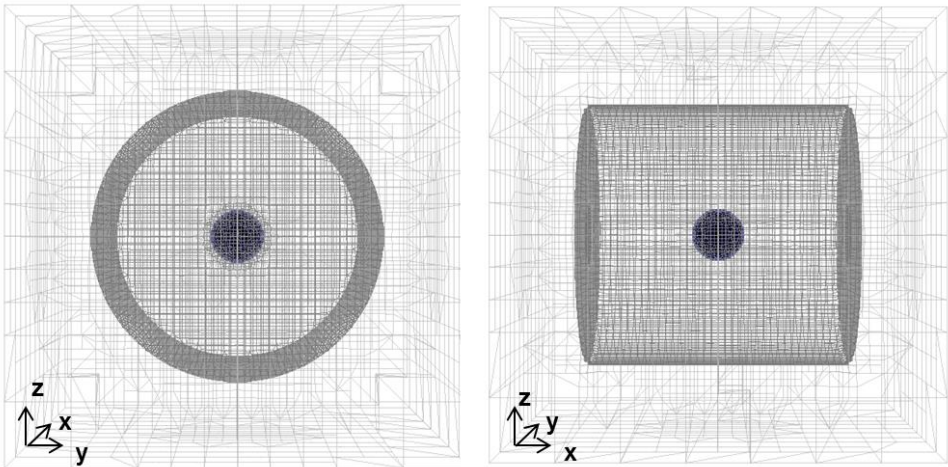
Fig. 2. Computational domain: surface mesh of sphere in black, dynamic mesh part in dark grey

2.4. Experimental Setup

For the experimental determination of velocity fields using the PIV-technique, a rectangular vessel was used. Length, height and width were 1m, 0.5 m and 0.5 m respectively. The material of the vessel walls was glass with a width of 0.01 m, allowing a laser light to pass through with a minimum of absorption and reflection from the vessel walls. As a stirrer, a stainless steel sphere with a diameter of 0.04 m was used. The sphere was connected to a horizontal shaft and was driven by a motor at a stirring speed of 1000 rpm and positioned in a central position 0.25 m away from the fluid surface and the vessel walls, except for the wall where the shaft was put through (0.15 m distance).

A LaVision FlowMaster 2D-PIV system was used for the PIV measurements in this study. It consisted of a pulsed Nd:YAG laser with a maximum double pulse rate of 15 Hz and the progressive-scan Imager Pro SX 5M CCD camera with a 12 bit range and a maximum resolution of 2456 by 2058 pixels. PIV-calculations were performed with the DaVis 8 software. To prevent damage to the camera due to uncontrolled reflections, fluorescent tracer particles in combination with a cut-off filter lens were used.

The laser was positioned at the same height as the stirrer on the opposite site of the motor, illuminating the symmetry plane normal to the vessel floor. Images were taken with a frame rate of five double images per second.
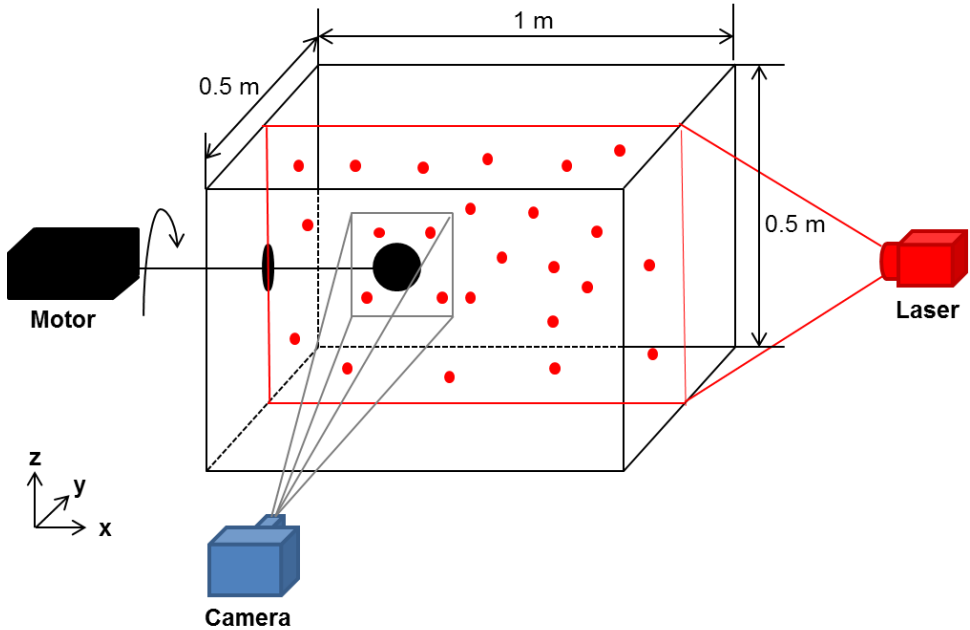
Fig. 2. Experimental setup for PIV measurements; the laser illuminates the symmetry x-z plane

2.4. Model Liquids and rheological characterisation

An aqueous carboxymethyl cellulose (Blanose) solution with a concentration of 5 g kg^{-1} was used as a viscoelastic model liquid. At higher concentrations, these solutions can become too opaque to allow for optical flow field measurements via the PIV method. Rheological measurements were carried out at 20°C with an Anton Paar MCR302 device, using a cone-and-plate system.

3. Results

3.1. Dynamic Viscosity and 1. Normal Stress Difference

In Figure 3, the results for the rheological measurement of the dynamic viscosity of the 5-wt% CMC solution as well as corresponding fits are presented. At shear rates lower than 0.06 s^{-1}, the accuracy of the used rheometer is not high enough to allow for exact measurements.

In general, the 5-wt% CMC solution exhibits shear thinning behaviour with a constant dynamic viscosity at low shear rates (about 0.22 Pas). With all aforementioned models, it is possible to acquire satisfactory fits, with the Carreau-Yasuda type models being capable of predicting the slope of the viscosity curve most accurately.
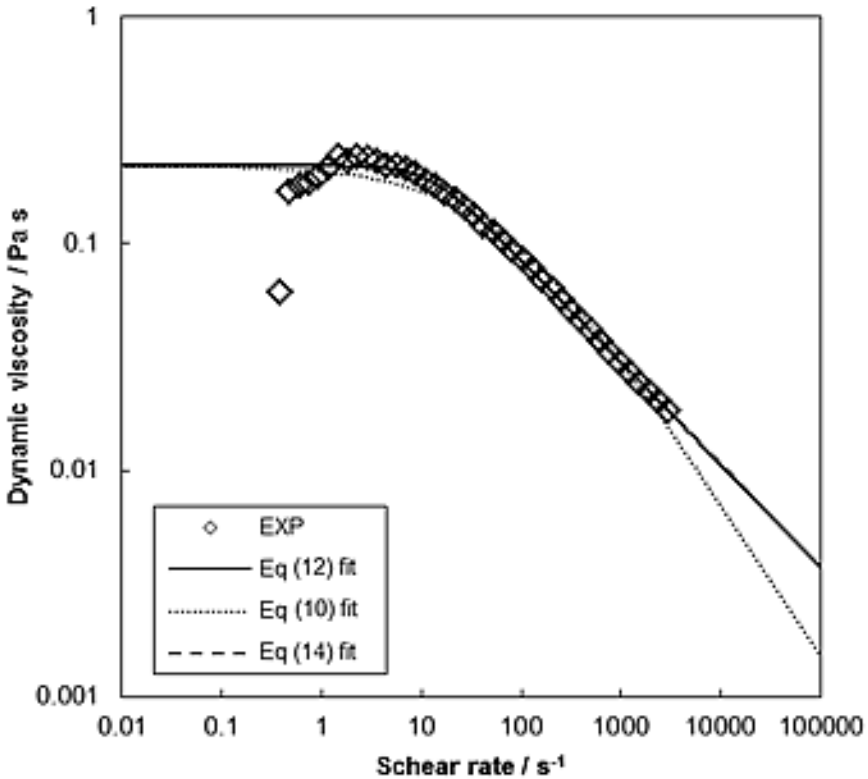
Fig. 3. Measured dynamic viscosity curve for 5-wt% CMC and corresponding fits

In Figure 4, the measured 1. normal stress differences for the same solution are shown. With increasing shear rate, the 1. normal stress differences rise. It has to be noted that measuring normal stress differences at low shear rates with the used rheometer is difficult

or impossible, since the measurement accuracy is too low to resolve the normal forces occurring under those conditions. The relaxation moduli were calculated from the dynamic viscosity and the 1. normal stress difference:
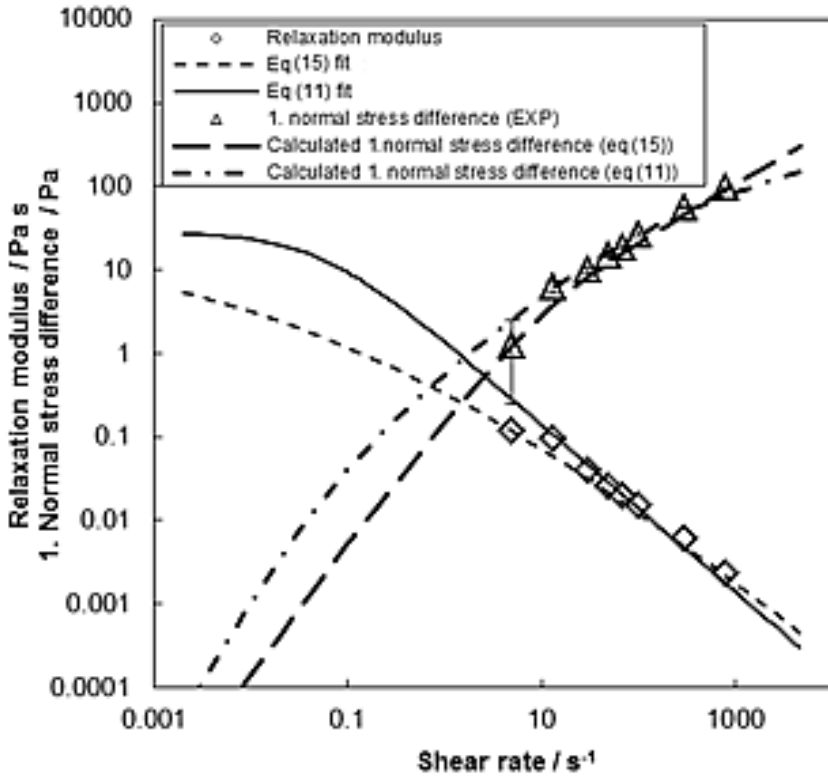
Fig. 4. Measured 1. normal stress differences for 5-wt% CMC and corresponding fits for relaxation moduli

Equations (11) and (15) were used to model the dependence of the relaxation modulus on shear rate, as shown in Figure 4. The best fit was achieved for the Carreau-Yasuda type model (Equation [15]).

$$\lambda_P = \frac{N_1(\dot{\gamma})}{2\eta_P(\dot{\gamma})\dot{\gamma}^2} \tag{16}$$

Finally, the model parameters for the fits in Figures. 3 and 4 are presented in Tables 1 and 2.

Model parameters for the different viscosity models

	$\eta_{P,\infty}$ Pa s	$\eta_{P,0}$ Pa s	k s	m	a
$\eta_P\left(\dot{\gamma}\right)=\dfrac{\eta_{P,0}}{1+\left(k\,\dot{\gamma}\right)^{1-m}}$	–	0.220	0.016	0.331	–
$\eta_P\left(\dot{\gamma}\right)=\eta_{P,0}\left[1+\left(k\,\dot{\gamma}\right)^{a}\right]^{\frac{m-1}{a}}$	–	0.220	0.085	0.550	2.209
$\eta_P\left(\dot{\gamma}\right)=\eta_{P,\infty}+\left(\eta_{P,0}-\eta_{P,\infty}\right)\left[1+\left(k\,\dot{\gamma}\right)^{a}\right]^{\frac{m-1}{a}}$	10^{-5}	0.220	0.085	0.550	2.210

Model parameters for the different relaxations modulus models

	$\lambda_{P,\infty}$ Pa s	$\lambda_{P,0}$ Pa s	L s	n	b
$\lambda_P\left(\dot{\gamma}\right)=\dfrac{\lambda_{P,0}}{1+\left(L\,\dot{\gamma}\right)^{1-n}}$	–	28	20	0.001	–
$\lambda_P\left(\dot{\gamma}\right)=\lambda_{P,\infty}+\left(\lambda_{P,0}-\lambda_{P,\infty}\right)\left[1+\left(L\,\dot{\gamma}\right)^{b}\right]^{\frac{n-1}{b}}$	10^{-5}	28	8.637	0.002	0.213

3.2. Simulation Results

In Figures 5 and 6, velocity profiles for both the PIV measurements and CFD simulations are presented. In Figure 5, the velocities along the line through the origin and parallel to the x-axis are shown, while in Figure 6, the line is parallel to the z-axis. The transient simulation was stopped after a simulated time of 6 seconds.

Fig. 5. Velocity profiles along the *x*-axis

Fig. 6. Velocity profiles along the *z*-axis

Except for the x-component along the z-axis, the simulations fit well to the PIV measurements from a qualitatively perspective. The locations of the velocity maxima coincide, especially for the x-components in Figure 5 and the z-components in Figure 6. Also, general flow field characteristics like an inward flow at the poles and an outflow at the equator are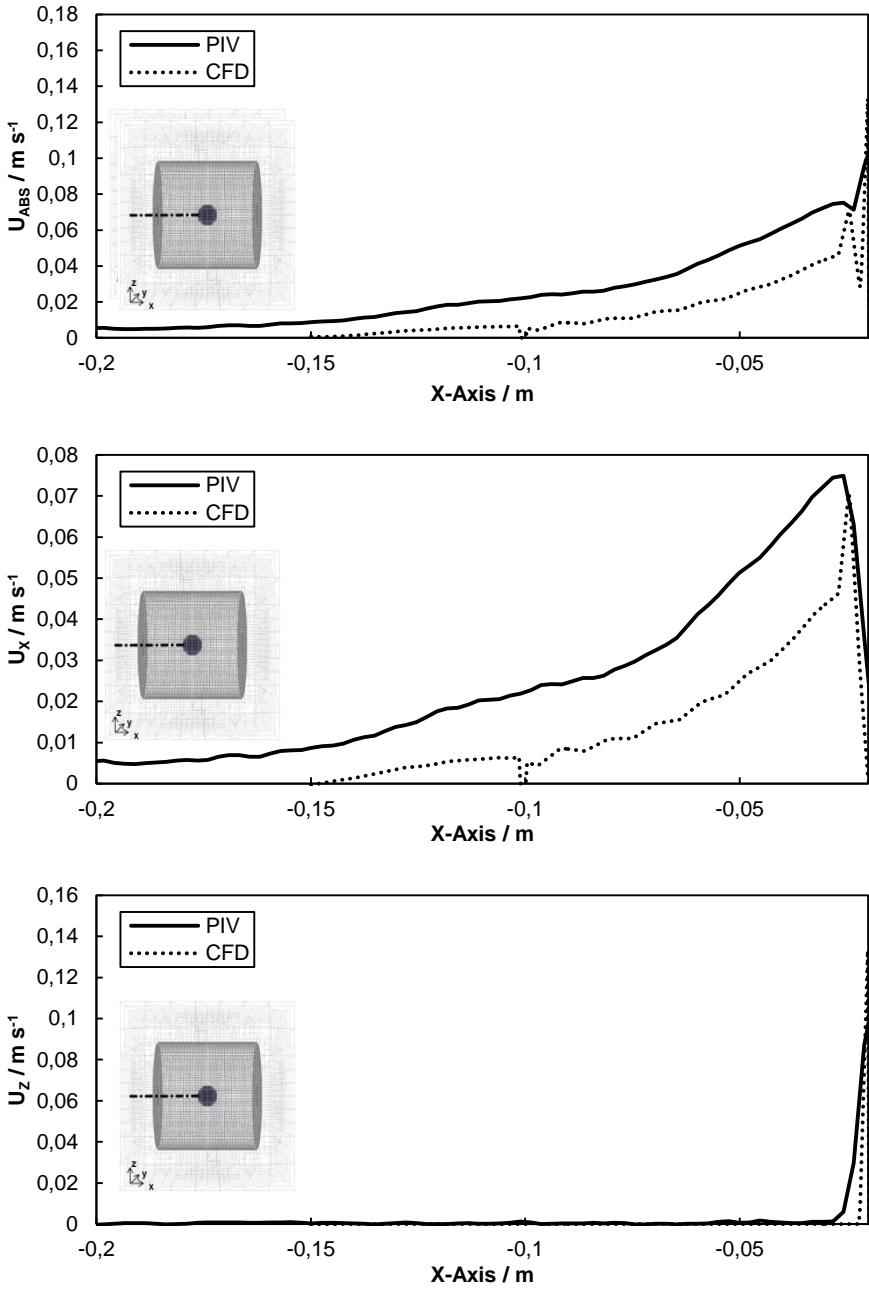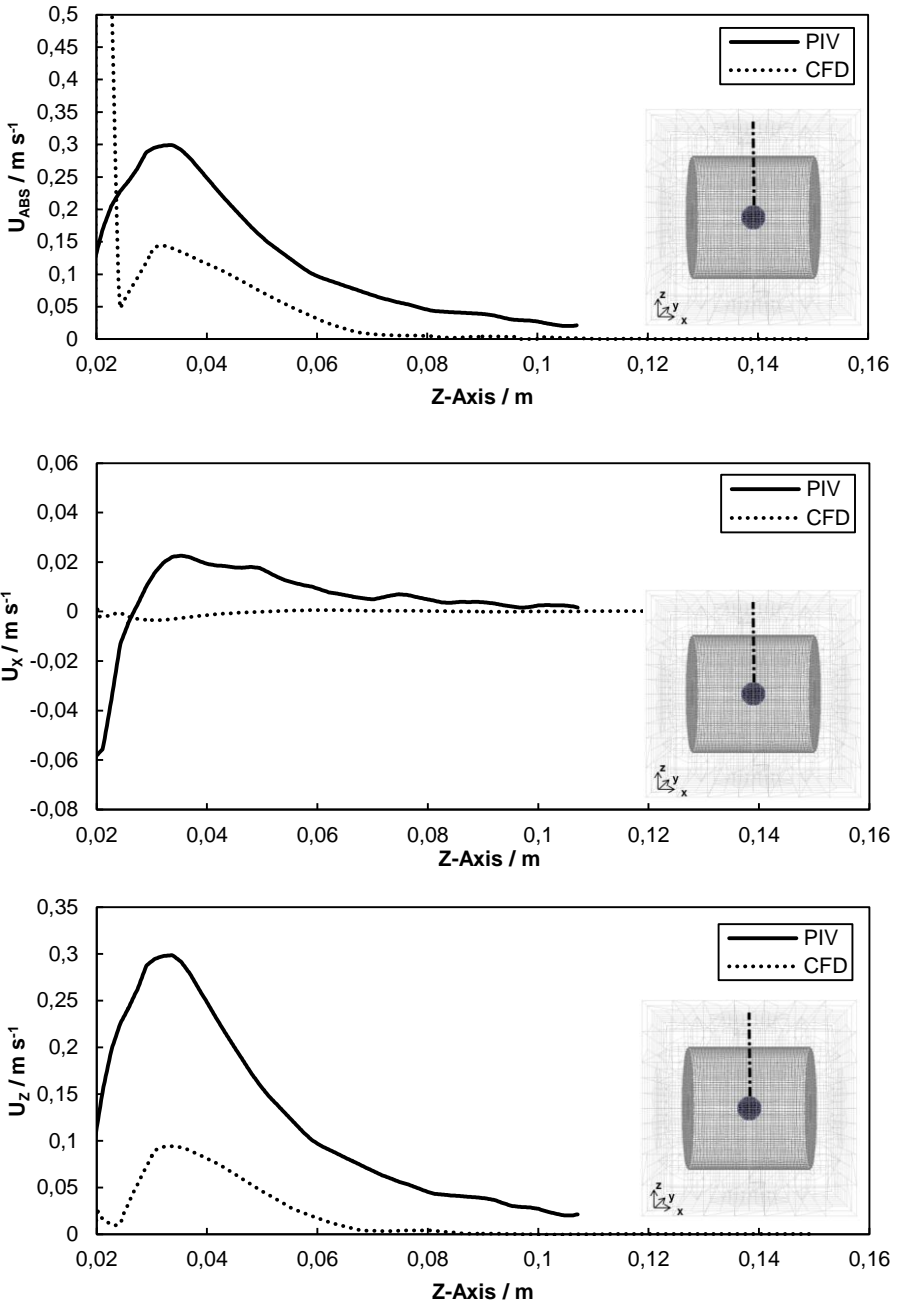 predicted correctly. Quantitatively, the magnitude of all velocity components is underestimated. One explanation for this could be the relatively coarse mesh, which may not be sufficient to resolve the flow field accurately, especially in the vicinity of the sphere.

4. Conclusion

The OpenFOAM® tool used to calculate viscoelastic flows in rotating geometries presented in this work shows promising results. Compared to PIV measurements, the predicted flow field around a rotating sphere in a CMC solution simulated with a White-Metzner constitutive model fits qualitatively well; quantitatively, the velocity magnitudes were underestimated by a factor of roughly 3. In future works, simulations with finer meshes will be conducted to minimise numerical errors. Additionally, different differential constitutive models – especially multi-mode variants like Giesekus and Phan-Thien-Tanner – will be tested for improvement of simulation accuracy. Both PIV measurements and CFD simulations will also be conducted for more complex stirrer geometries like Rushton turbines and propellers.

R e f e r e n c e s

[1] Weissenberg K., *Abhandlungen der Königlichen Preußischen Akademie der Wissenschaften zu Berlin Nr. 2*, 1931.
[2] Ide Y., White J.L., *Rheological phenomena in polymerization reactors: Rheological properties and flow patterns around agitators in polystyrene–styrene solutions*, Journal of Applied Polymer Science, vol. 18(10), 1974, 2997-3018.
[3] Garuno I.E., Tamaddon-Jahromi H.R., Webster M.F., *Oldroyd-B numerical solutions about a rotating sphere at low Reynolds number*, Rheologica Acta, vol. 54(3), 2015, 235-251.
[4] Cherizol R., Sain M., Tjong J., *Review of Non-Newtonian Mathematical Models for Rheological Characteristics of Viscoelastic Composites*, Green and Sustainable Chemistry, vol. 5(1), 2015, 6-14.
[5] White J.L., Metzner A.B., *Development of constitutive equations for polymeric melts and solutions*, Journal of Applied Polymer Science, vol. 7, 1963, 1867-1889.
[6] Favero J.L., Secchi A.R., Cardozo N.S.M, Jasak H., *Viscoelastic flow analysis using the software OpenFOAM and differential constitutive equations*, Journal of Non-Newtonian Fluid Mechanics, vol. 165, 2010, 1625-1636.
[7] Jasak H., *Dynamic Mesh Handling in OpenFOAM*, 47th AIAA Aerospace Sciences Meeting Including The New Horizons Forum and Aerospace Exposition, Orlando, Florida, 2009, 1-10.
[8] Versteeg H., Malalasekera W., *An Introduction to Computational Fluid Dynamics: The Finite Volume Method*, Pearson Education Limited 2007.
[9] Issa R.I., *Solution of implicitly discretized fluid flow equations by operator-splitting*, Journal of Computational Physics, vol. 93(2), 1991, 388-410.

BARBARA LARWA, KRZYSZTOF KUPIEC, TADEUSZ KOMOROWICZ,
MONIKA GWADERA, MIKOŁAJ TEPER[*]

MODELLING OF HEAT TRANSFER IN GROUND HEAT EXCHANGERS

MODELOWANIE PRZENOSZENIA CIEPŁA W WYMIENNIKACH GRUNTOWYCH

Abstract

The results of the numerical simulation of heat conduction in ground with a horizontal, tubular (parallel pipes) heat exchanger installed are presented in this paper. On the basis of analysis of courses of temperature isolines in the ground, a simplified mathematical heat transfer model in a horizontal ground exchanger was developed. The ground thermal diffusivity was assumed to be a variable of location. On the basis of the model, the temperature profiles in the ground with a heat exchanger installed were determined.

Keywords: ground heat exchangers, non-homogeneous ground thermal properties

Streszczenie

Przedstawiono wyniki symulacji numerycznej przewodzenia ciepła w gruncie, w którym znajduje się szereg równoległych, poziomych rur wymiennika ciepła. Na podstawie analizy przebiegów izolinii temperatur w gruncie opracowano uproszczony model matematyczny przenoszenia ciepła w poziomym gruntowym wymienniku. W modelu przyjęto, że dyfuzyjność cieplna gruntu jest zmienna z położeniem. Wykorzystując opracowany model wyznaczono profile temperatur w gruncie z zainstalowanym wymiennikiem.

Słowa kluczowe: gruntowe wymienniki ciepła, niejednorodne właściwości termiczne gruntu

[*] MSc. Eng. Barbara Larwa; Assoc. Prof. Krzysztof Kupiec; DSc. Eng. Tadeusz Komorowicz; DSc. Eng. Monika Gwadera; MSc. Eng. Mikołaj Teper, Chair of Chemical and Process Engineering, Faculty of Chemical Engineering and Technology, Cracow University of Technology.

1. Introduction

Ground heat exchangers are the essential components of ground-source heat pump installations. A basic criterion of ground heat exchangers is their orientation – this paper deals with horizontally heat exchangers. An overview of the application of ground heat exchangers and numerical models relating to them was presented by Florides and Kalogirou [1].

Ground temperature varies according to its depth and is the result of both a periodic variability of the ground surface temperature and the ground thermal inertia. During cold periods, the ground temperature exceeds the ground surface temperature by several degrees K – the reverse situation occurs during warm periods. An analysis of receiving heat from various ground depths in different time periods was presented by Gan [2]. If the heat is received from the ground during cold periods, it is better to place the exchanger pipes deep down. Conversely, if the heat is received during warm periods (e.g. for heating water in swimming pool) it is advantageous to place the pipes at a shallow depth, close to the surface.

The thermal properties of the ground are characterised by thermal diffusivity:

$$a = \frac{k}{c \cdot \rho} \tag{1}$$

where: k – heat conduction coefficient, c – heat capacity, ρ − density.

Ground typically consists of three phases: solid, liquid and gaseous. Fluid phases, i.e. water and air, fill the spaces between the grains. Therefore, the ground is a multi-phase system [3]. For modelling the heat transfer in the ground, it is convenient to use a substitute thermal diffusivity coefficient taking into account both the heat conduction in the solid and the heat transport in the fluid filling the void space. Because the ground humidity depends on the ground location, the variability in thermal diffusivity should be taken into account when modelling.

The aim of this work is to determine the temperature profiles in the ground in which an exchanger associated with a heat pump is installed. The calculations were carried out for ground physical parameters varying with the position with the application of the model based on one-dimensional heat conduction equation with an internal heat source. A possibility of application of 1D model has proved the simulations performed with the use of the ANSYS Transient Thermal application. The effect of the physical ground properties on the temperature distribution in the ground affecting the operation of the ground heat exchanger associated with a heat pump is analysed.

2. Simulation of heat conduction in the ground cooled with a system of horizontal pipes using the ANSYS application

In cases of slight changes between the inlet and the outlet temperature of the operating fluid in a horizontal ground heat exchanger, the ground heating and the ground cooling can be considered as a two-dimensional problem. In this paper, the flow through three parallel,

coupled, horizontal pipes located in the ground is analysed. The problem can be described by the two-dimensional transient heat conduction equation:

$$\frac{\partial T}{\partial t} = a\left(\frac{\partial^2 T}{\partial x^2} + \frac{\partial^2 T}{\partial y^2} \right)$$

(2)

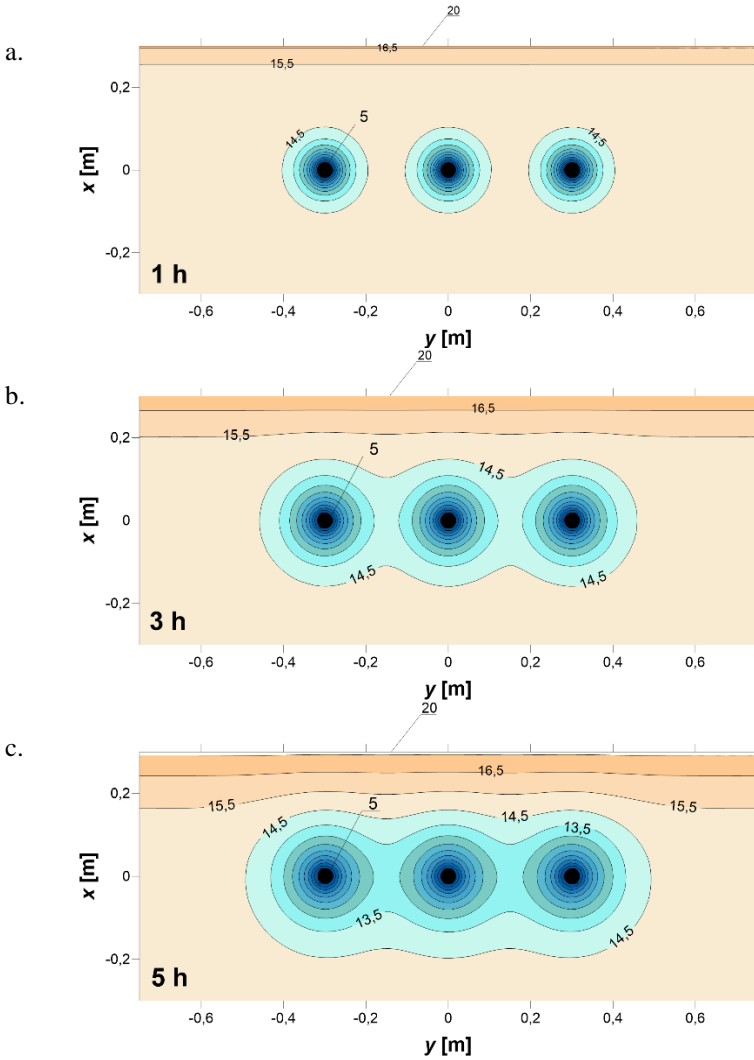where: T − temperature, t − time, x, y – position coordinates.

Fig.1. The cooling of ground with exchanger pipes
a)   1hr, b) 3hrs, c) 5hrs

The initial condition results from the assumption of the uniform ground temperature at the beginning of the process. The boundary condition is related to the constant (in time and space) value of temperature of all the tubes surface. For calculations, the following data were used: $a = 0.384 \cdot 10^{-6}$ m^2/s, temperature of pipe surface 5°C, initial ground temperature $T_i = 15$°C, and dimensions of the analysed ground block – 1.5m×0.6m×0.3m (number of nodes: 381270). Furthermore, the following assumptions were made: the outer diameter of pipes was 38 mm, the distance between the axes of pipes was 300 mm, the ambient temperature was 20°C, the heat transfer coefficient between the environment and the ground h_0 was 10 W/m^{2}K. The calculations relate to ground of homogenous thermal properties. The results of the calculations are presented in Figs. 1a, b, c [4]. The figures are related to the cross-section of the system of pipes. As can be seen, at the beginning, each pipe cools down the ground individually, independently of the other pipes. However, after some time, the temperature fronts come together and isolines become more rectilinear and parallel to the horizontal position. Thus, the system behaves similarly to cooling down the ground by infinite plate. The similarity is even larger when there are more pipes installed, and the more densely arranged they are side by side. Therefore, in the case of large number of pipes the heat transfer in the considered system is practically 1D.

3. Heat transfer in ground with non-homogenous thermal properties

3.1. Heat conduction in porous materials

The ground thermal properties change considerably even if the parameters affecting the heat transfer only change slightly. The heat transfer process in the ground is determined by the heat conduction of the grains of minerals present in the ground, the heat conduction of the air and water in the ground void space, possible natural convection inside the void space and the thermal resistance at contact points between the grains. In humid ground below 0°C, the heat transfer process is more complicated because of the phase transition of the water portion into ice.

Russel derived the following relationship to calculate the effective heat conductivity of porous material as a function of the properties of solid and fluid matter [5]:

$$k = k_s \cdot \frac{\varepsilon^{2/3} + \kappa}{\varepsilon^{2/3} \cdot \left(1 - \varepsilon^{1/3}\right) + \kappa} \tag{3}$$

where ε is the porosity and κ is defined with the formula:

$$\kappa = k_s / \left(k_f - k_s\right) \tag{4}$$

where k, k_s and k_f respectively denote the heat conductivity of porous material, solid and fluid matter.

If the pores are filled with water, usually $k_f > k_s$, then $\kappa > 0$ and finally $k > k_s$. However, if $k_f < k_s$, which is always valid for the case of gas in pores, then $\kappa < 0$ and $k < k_s$. In the first case, the greater the porosity (water content), the greater the heat conduction coefficient. In

the case of gas filling the pores, the greater the porosity, the lower the heat conduction coefficient of the system. The Russel model meets the following conditions: for $\varepsilon = 1$, there is equality $k = k_f$ but for $\varepsilon = 0$, there is $k = k_s$. Moreover, the Russel model describes well an effect of a kind of phase filling the ground on the heat conduction coefficient.

3.2. Mathematical model of ground exchanger

On the basis of the heat transfer simulation it should be noted that the constant temperature lines do not differ significantly from those which occur when the exchanger is used as a flat slab. This provides the basis for utilising the one-dimensional equations of heat conduction for the modelling of horizontal ground heat exchangers. It is assumed that the only mechanism of heat transport in the ground was conduction.

The equation of heat conduction has the form [6-8]:

$$\frac{\partial T}{\partial t} = \frac{\partial}{\partial x}\left[a(x)\frac{\partial T}{\partial x}\right] + \frac{q_v}{c\rho} \tag{5}$$

where: x – position coordinate (distance from the ground surface), q_v – rate of heat generation per volume unit.
The boundary condition at the surface of the ground has the form:

$$x = 0 \qquad T = T_0 \tag{6}$$

The ground surface temperature T_0 varies in time according to the formula:

$$T_0 = T_b + B \cdot \cos\left[\frac{2 \cdot \pi}{t_c} \cdot (t - t_{max})\right] \tag{7}$$

where $t_c = 365$ days. The following values, valid for climatic conditions in Cracow, were used in calculations: $T_b = 8.5°C$, $B = 10.4$ K, $t_{max} = 198$ days.

The second boundary condition is related to the ground at a great depth, where the temperature is constant:

$$x \rightarrow h_{inf} \qquad T = T_b \tag{8}$$

The rate of heat generation q_v in equation (5) is the thermal power produced in a volume $\Delta V = A_g \cdot \Delta x$ [9]. This quantity is connected with the rate of heat transfer $\dot{Q}$ between the working liquid flowing in a ground heat exchanger and the ground. The calculations were done for N nodes so $\Delta x = h_{inf}/N$. Since exchanger pipes are arranged at distance h from the ground surface, then:

$$q_v = \begin{cases} 0 & \text{for} \quad i < n \\ -\dot{Q}_{GHE}/\Delta V & \text{for} \quad i = n \\ 0 & \text{for} \quad i > n \end{cases} \tag{9}$$

where $i = 1, 2,…, n, ..., N; n = \text{Int} (h/\Delta x)$.

The ground thermal diffusivity is described with a step function because the variation of ground humidity with the ground depth is step. Two cases are considered:

a) The thermal diffusivity in the outer ground layer (< 2 m deep) is higher than the diffusivity in the bottom layer. The function $a(x)$ has the form:

$$a(x) = \begin{cases} 1.0 \cdot 10^{-6} \text{ m}^2/\text{s} & \text{for} \quad x < 2 \text{ m} \\ 0.2 \cdot 10^{-6} \text{ m}^2/\text{s} & \text{for} \quad x \geq 2 \text{ m} \end{cases} \tag{10}$$

In this case, the ground heat exchanger is placed at a depth of 1 m.

b) The thermal diffusivity in the upper ground layer (< 1 m) is lower than the diffusivity in the bottom layer. The function $a(x)$ has the form:

$$a(x) = \begin{cases} 0.2 \cdot 10^{-6} \text{ m}^2/\text{s} & \text{for} \quad x < 1 \text{ m} \\ 1.0 \cdot 10^{-6} \text{ m}^2/\text{s} & \text{for} \quad x \geq 1 \text{ m} \end{cases} \tag{11}$$

In this case, the ground heat exchanger is placed at a depth of 2 m.

3.3. Computational temperature profiles in the ground

If the thermal diffusivity is high, the temperature gradients are low; therefore, the lines of temperature profiles are steep. Conversely, if the thermal diffusivity is low, the temperature gradients are high; thus the inclination angle of temperature profiles lines is small. In the case of high thermal diffusivity, the temperature in the outer layer approximates the ground temperature whereas in the case of low thermal diffusivity, the outer ground layer is a kind of buffer isolating the bottom layer from the impact of the ground surface.

The presence of a heat exchanger installed in the ground is connected with the heat collection from the ground which results in disturbance of natural temperature profiles. The calculations were carried out for the heat flux collected from the ground $\dot{Q} = 5000$ W and for the ground surface area $A_g = 500$ m^2.

The results of calculations of temperature profiles are depicted in Figs. 2 and 3. The calculations relate to the following operating conditions: the average twenty-four-hour ambient temperature is lower than 7.5°C, the ground temperature at the depth of the arrangement of exchanger pipes is higher than 1°C [10].

Fig. 2. Ground temperature profiles with heat exchanger installed in the case of higher thermal diffusivity in the outer ground layer

Fig. 2 presents the ground temperature profiles if the exchanger is located at a depth of 1 m, while in the depth range from 0 to 2 m, the ground thermal diffusivity is higher than in deeper layer. The shapes of temperature profiles result from the collection of heat mainly from the ground surface because of good thermal diffusivity and a shallow location of exchanger. The low thermal diffusivity ground layer below 2 m has a slight influence in the heat transfer process.

Fig. 3 presents the results of calculations relating to the location of a ground heat exchanger at a depth of 2 m while below a depth of 1 m, the ground thermal diffusivity is lower than in deeper layers. The low thermal diffusivity of the upper ground layer (0÷1 m) hampers the heat transfer between the ground surface and the cooled ground at the depth of the arrangement of the exchanger pipes. Therefore, the heat is transferred from the deeper ground layer which results in the deformation of their temperature profiles. At a depth of 10 m, the ground temperature is unstable over time – this is in contrast to the previous case.
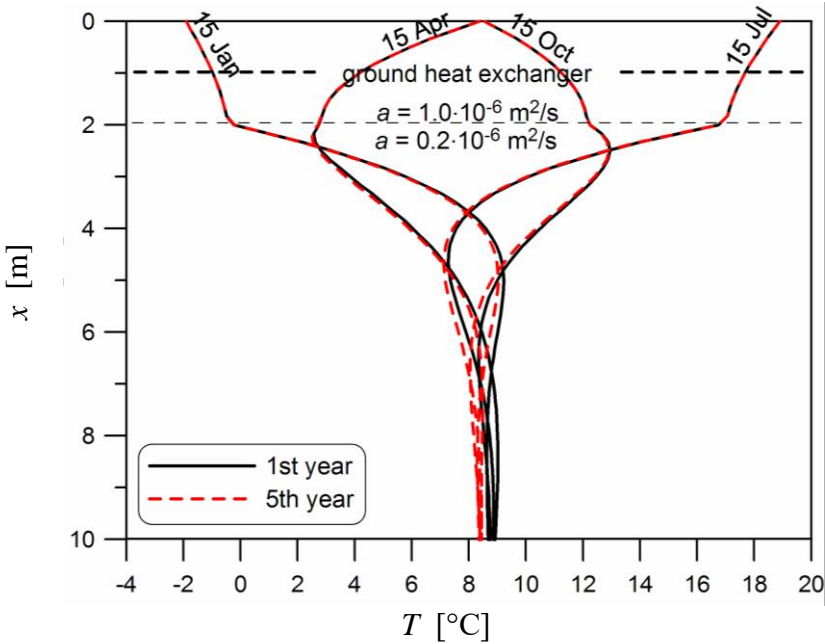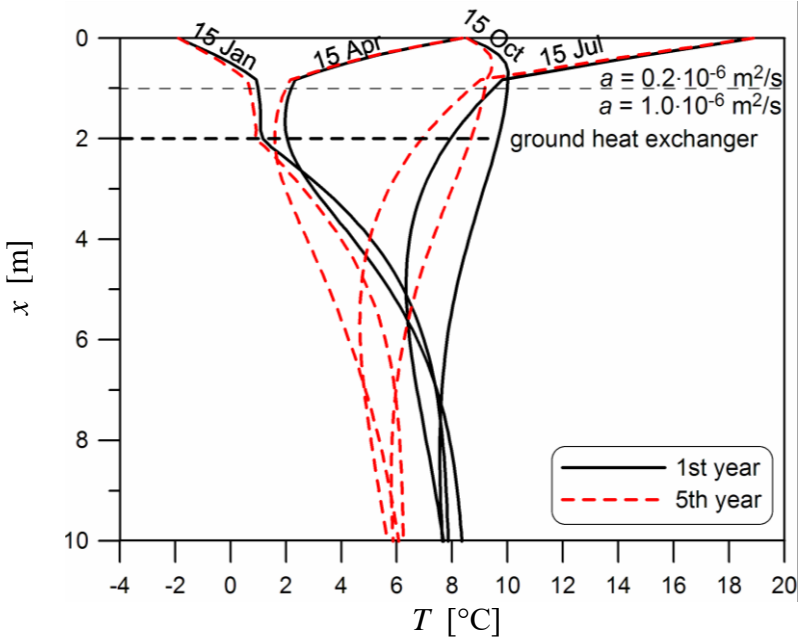
Fig. 3. Ground temperature profiles with heat exchanger installed in the case of lower thermal diffusivity in the outer ground layer

The significant differences in the courses of temperature profiles for the first and the fifth year of operation only occur in the case presented in Fig. 3. In numerical calculations, it was necessary to properly adjust the ground depth where the temperature is stabilised (h_{inf}). For the ground thermal diffusivity described with formula (11), it was necessary to assume the value $h_{inf} = 50$ m.

4. Conclusions

- It was noticed that for the simulation of heat conduction for a system of parallel pipes of a ground heat exchanger that after some time, the temperature isolines are similar to straight lines. This gives a basis for using one-dimensional equations of heat conduction for the modelling of horizontal ground heat exchangers.
- If a higher diffusivity ground layer is located above a lower diffusivity layer, the upper layer does not affect the temperature distribution in the lower layer because the upper layer temperature approximates the ground surface temperature.
- If a higher diffusivity ground layer is located below a lower diffusivity layer, the upper ground layer is a buffer isolating the bottom layer from the impact of the ground surface.
- When a heat exchanger is installed in the ground and the thermal diffusivity

of the upper layer is low, the temperature profiles in the bottom layer undergo considerable and long-term changes over time. After several years of the operation of an exchanger in such conditions, ground could be cool down significantly. This is due to not enough compensation of the heat transfer from the surroundings.

Nomenclature

a – thermal diffusivity of the ground, m^2 /s,
A_g – area of the ground surface, m^2
B – annual amplitude of the ground surface temperature, °C,
c – ground heat capacity, J/(kgK)
h – distance between the heat exchanger and the surface of the ground, m
h_{inf} – distance from the surface of the ground where the ground temperature is undisturbed, m
k – ground thermal conductivity, W/(mK)
q_v – rate of heat generation per unit volume, W/m^3
$\dot{Q}$ – rate of heat transfer, W,
t – time, s
t_{max} – time lag from the beginning of the year to the occurrence of the highest temperature in a year, s
T – temperature of the ground, °C,
T_0 – average daily ground surface temperature, °C,
T_b – average annual ground surface temperature, °C,
x – position coordinate, m
ρ – ground density, kg/m^3

References

[1] Florides G., Kalogirou S., *Ground heat exchangers – A review of systems, models and applications*, Renewable Energy, vol. 32, 2007, 2461-2478.
[2] Gan G., *Dynamic thermal modelling of horizontal ground-source heat pumps*, International Journal of Low-Carbon Technologies, vol. 8, 2013, 95-105.
[3] Al-Khoury R., *Computational Modeling of Shallow Geothermal Systems*, CRC Press, 2012.
[4] Larwa B., *Numerical and experimental analysis of heat transfer in ground exchangers* (*Analiza numeryczna i eksperymentalna przenoszenia ciepła w wymiennikach gruntowych*), PhD Thesis, Kraków 2016.
[5] Woodside W., *Calculation of the thermal conductivity of porous media*, Can. J. Phys., Volume, vol. 36, 1958, 815-823.

150

[6] Carslaw H.S., Jaeger J.C., *Conduction of heat in solids*, second ed., Clarendon Press, Oxford 1959.

[7] Cengel Y., Ghajar A., *Heat and mass transfer: fundamentals and applications*, McGrawHill 2010.

[8] Staniszewski B., *Wymiana ciepła – podstawy teoretyczne*, WNT, Warszawa 1979.

[9] Kupiec K., Larwa B., Gwadera M., *Heat transfer in horizontal ground heat exchangers*, Applied Thermal Engineering, vol. 75, 2015, 270-276.

[10] Kupiec K.,, Larwa B., Komorowicz T., Neupauer K., *Temperature profiles in the ground with non-uniform physical properties* (*Profile temperatur w gruncie o niejednorodnych właściwościach fizycznych*), Inżynieria i Aparatura Chemiczna, vol. 54(6), 2015, 332-333.

MICHAL NETUŠIL, PAVEL DITL[*]

AUTOMOTIVE CATALYST PRODUCTION – CHALLENGES FOR CHEMICAL ENGINEERS

PRODUKCJA KATALIZATORÓW SAMOCHODOWYCH WYZWANIEM DLA INŻYNIERÓW CHEMIKÓW

Abstract

The goal of this paper is to explain the chemical engineering backgrounds for operations participating on catalyst production in the automotive industry. It is shown that chemical engineering knowledge can help to a better understanding and optimisation of the production process. Besides the contribution mentioned above this paper brings the description of the up to date and interesting technology developed and patented by the worldwide leader in the chemical engineering - BASF. The car catalyst production process consists of two steps. Firstly, the coating slurry is produced and secondly, it is applied to the substrate. This paper focuses on the slurry production especially with regard to its dispersion, mixing, particle size reduction, and the influence of parameters affecting this process.

Keywords: plant design, automotive catalyst, process control

Streszczenie

Celem niniejszego opracowania jest przedstawienie podstaw inżynierii chemicznej procesów stosowanych przy produkcji katalizatorów w przemyśle motoryzacyjnym. W pracy przedstawiono opis nowoczesnej technologii opracowanej i opatentowanej przez światowego lidera w inżynierii chemicznej - BASF. Proces produkcji katalizator samochodowy składa się z dwóch etapów: produkcja zawiesiny i nanoszenie na podłoże. W pracy opisano wytwarzanie zawiesiny ze szczególnym uwzględnieniem dyspersji, mieszania, zmniejszenia rozmiaru cząstek i oddziaływania parametrów procesowych.

Słowa kluczowe: projektowanie instalacji, katalizator samochodowy, kontrola procesu

[*] PhD. DSc. Eng. Michal Netušil, Prof. PhD. DSc. Eng. Pavel Ditl, Department of Process Engineering, Faculty of Mechanical Engineering, Czech Technical University in Prague.

1. Introduction

The process and control of slurry production are described in general without detailed information. The details depend on a vendor selection. The block diagram in Fig.1 below displays the basic configuration of a catalyst coating plant. The main steps in slurry preparation are colour coded in accordance with the key.
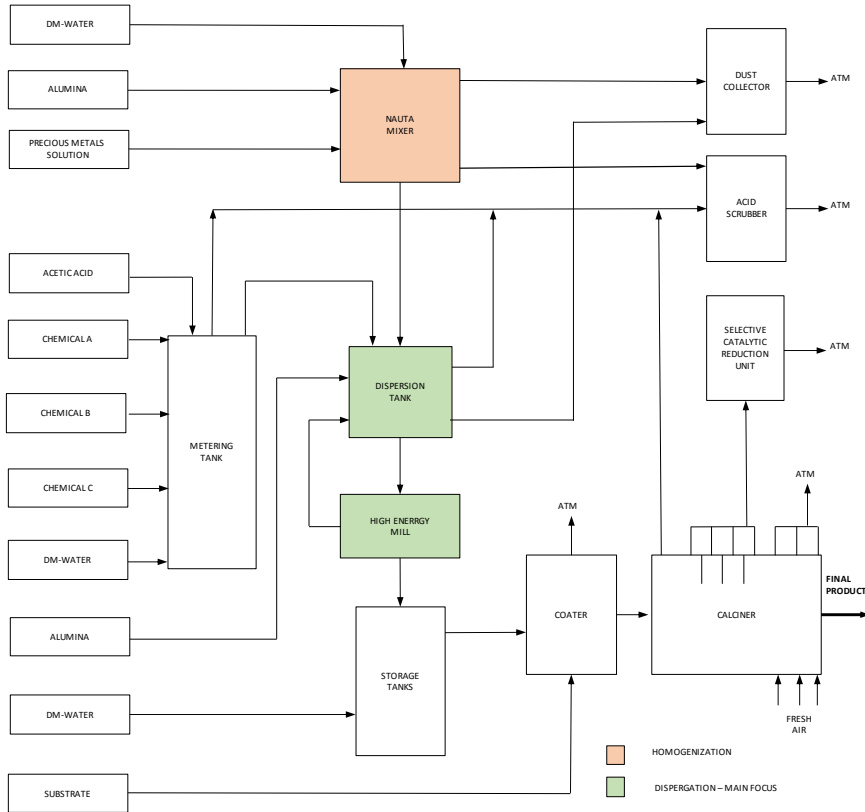
Fig. 1. Slurry preparation and coating block diagram

With respect to the material flow, the slurry preparation is set up in a building containing the ground, the first and the second floor. On the second floor, the raw material is dosed and mixed in Nauta mixers. Mixing occurs with the minimal addition of fluids. On the same floor, high-speed shear machines are placed. These machines are used for the purpose of reducing the size of ingredient particles. From the second floor, the mixture flows to the first floor where dispersion tanks are located. In the dispersion tanks, solutions are added and homogenisation proceeds. From the first floor, the mixture flows to the ground floor where it is milled by high-energy mills. The mixture from the mill is circulated back to the dispersion tank until the desired particle size is achieved. The ready mixture (slurry) is pumped to storage tanks located on the first floor. From the storage tanks

the slurry is dosed into portable tanks on the ground floor. The portable tanks containing the slurry are manually transported to the production area where they feed the coating lines.

Coating lines coat the substrates. The substrates are dipped into the slurry and dried. The new types of coating lines have also a pre-drying step. After drying, the substrates continue to the calciner. The calciner is of a tunnel type, it is a circulating hot air oven consisting of heating and cooling zones. The maximum temperature is 600°C and the overall residence time is around 90 mins. During calcination, residual moisture evaporates and the organic ingredients of the wash coats are oxidised. In the case of precious metal (PM) coats, the composition of the ammine solution used for stabilising the precious metal solution leads to the release of oxides of nitrogen (NO_x). Each zone is equipped with its individual circulating fans and burners. Substrates covered with a calcined coat leave the oven and are loaded onto pallets.

For gas treatment, two different units are needed. The acid scrubber treats acid gases. These gases are created as a result of acetic acid evaporation (acetic acid is one of the base chemicals used in slurry preparation). The principle of gas treatment is chemical absorption by means of the spraying of a base solution whereas selective catalytic reduction (SCR) mainly treats the NO_x created within the high temperature zones of the coater. Principe is reduction of NO_x to nitrogen by ammonia. The reaction occurs within the presence of O_2. The by-product is H_2O.

2. Control description

The process control of automotive catalyst plants consists of three major sections. Slurry preparation, coating section, and the scrubber and SCR system. All the system cabinets, including power distribution panel and marshalling panels, are installed in a control room. All operator stations have monitors for the visualisation of the process flow and recipe management. The interface of the programmable logic controller (PLC) panels with the drives in motor control center (MCC) is through interposing relay panel/profibus.

2.1. Slurry preparation

Slurry required for coating is prepared on demand as per the relevant confidential recipe. The equipment involved in slurry preparation is a Nauta mixer and the associated raw material handling system, dispersion tanks, milling and slurry storage. Slurry preparation is monitored and controlled by PLC and supervisory control and data acquisition (SCADA) system. The remote terminal unit is in the plant operation room. Terminals are used for the operator's manual interventions – access is password-protected. The recipe management is implemented for both the batch and discrete parts of the process. The batch recipe management stores information about the dynamic configuration of the recipe and works for batch functions with pre-programmed batch cycles and compositions. The system enables changing the batch recipes as required. Based on actual compositions, mix ratios and quantities the formula settings are derived. The formulas for each batch are stored. Data stored also contains the time record of vessels charging.

A wireless type barcode reader system enables exact material charging according to the PLC system of the slurry section. The input from the barcode reading system is verified by

the recipe management system to ensure that the correct material is charged into the equipment as per the recipe.

A radio-frequency identification (RFID) system is implemented for the connection of hoses. The RFID system is installed in field providing information about the connection of each hose to the equipment. The system is comprised of the RFID controllers and RFID tags and it is connected to the main control system. The RFID controller is mounted at the flange of the equipment. The RFID tags are at both the ends of the hoses. The RFID controller reads the RFID tag number on the hose and the information is cross-referenced by the control system – if the numbers match, the equipment valves are opened.

In the functional area of the Nauta mixer (Fig. 2) is the PM solution tank, the dosing pumps, the Nauta mixer and the vacuum conveying system for alumina dosing. The raw material is barcoded and a barcode scanner sends the information before charging. Any mismatch in the barcode cross-referencing will not allow the batch to proceed. Remotely operated switches for all drives are shown on screen in the operation room. Based on the

Fig. 2. Nauta mixer

batch preparation recipe, the operator takes a premeasured amount of PM from the PM vault. The PM vault contains a CCTV surveillance system and an intrusion detection system. The PM solution is manually added into the PM solution tank. Use of barcode reader avoids adding the PM into wrong solution tank. The PM solution tanks are refilled regularly. Refilling of PM solution tanks is allowed only if the scrubber suction valve is open and scrubber blower is switched on. A weight measurement is displayed both in field and on the remote display panel. PM solutions are charged to the Nauta mixer using the dosing pumps. When the batch starts, the inlet valves of dosing pumps opens. Material is charged to the Nauta mixer. Charging of material to the Nauta mixer is controlled by weighing scale. The speed of agitation is automatically controlled. Mixers are fully automated and the sequence of operations follows the required recipe. The sequences involve a dust collection system, the switching on and off of valves, the addition of alumina through a vacuum conveyor, agitation, PM addition, suction to the acid scrubber system, PM solution tank rinsing, and drainage to the dispersion tank. Alumina is usually received in bulk bags which are fed into the Nauta mixer by a vacuum conveying system. Before starting alumina charging, the operator has to ensure that the dust collection system is switched on. Alumina is added in accordance with the recipe and the weighing system on the Nauta mixer trips the vacuum conveyor after the required amount is added. Powder from bags is transported through flexible hoses and charging is performed in multiple cycles with various quantities of powder according to the recipe. When the batch in the Nauta mixer is ready, the operator connects the Nauta mixer to the selected dispersion tank. Based on the connection check, the operator in the control room initiates the transfer operation. The weighing system informs the operator about the state of transfer.

The functional area of dispersion contains the base chemical storage tanks, the metering tank, the dispersion tank (Fig. 4) and the vacuum conveying system. There are usually 4-5
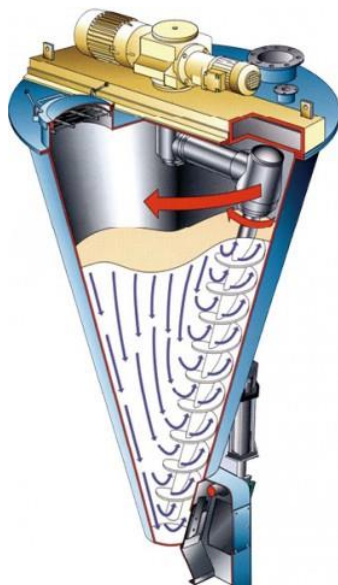
base chemical storage tanks. To avoid mixing different loads in the base chemical tanks, charging of chemicals from the drum does not proceed if the barcode doesn't match. Level switch is provided to stop the air operated double diaphragm (AODD) dosing pumps when the required level is reached. Fixed quantities of base chemicals are added to the metering tank based on the selected batch recipe. On/off valves at the inlet of the metering tank close after pre-set quantities of base chemicals are added. Flexible hose connections are provided from the demineralized (DM) waterline for rinsing of the metering tank. The dispersion tank is a jacketed vessel with an agitator. The agitator is provided with a variable frequency drive (VFD) for agitation speed adjustments. The sequence of dispersion tank operation starts with filling the dispersion tank jacket with cold water. Cleanliness of the tank is checked and chilled DM water is added to the dispersion tank. Dust collection and acid scrubber suction are turned on. The Nauta mixer output is transferred into the dispersion tank and mixing with the base chemical proceeds. Agitation lasts at least 20 minutes. Slurry from the dispersion tank is fed to the energy mill via a peristaltic pump. The mill outlet overflows into a small tank and is recirculated back to the dispersion tanks. The temperature control loop is connected to the chilled water system. The vacuum conveying system for alumina dosing works in the same way as for the Nauta mixer – alumina is added in multiple steps.

Dispersion tank capacity 600 Lts

EQUIPMENT DESCRIPTION

SECTION	SLURRY MACHINE	WEIGHT	680	Kg.
CAPACITY	000 EA./hr.	TANK VOLUME	600	Litre.
VOLTAGE CONNECTION	380/N/PE WITH AGITATOR INVERTER			

BILL OF MATERIAL

NO.	DESCRIPTION	MATERIAL	DIMENSION	Q'TY.	REMARKS
1	TOP PLATE	SUS304	6mm. thk.	1	--
2	TANK SHELL	SUS304	#1150 x 4.5thk.	1	--
3	WALL SHELL	SUS304	#1286 x 4.5thk.		2 FIXED, 2 SWIVEL
4	BOLTS	SUS304	M14x	12	
5	COVER	SUS304	400x260	1	
6	BUFFLE PLATE	SUS304	95x800x8thk.	1	
7	SPIRAL PLATE	SUS304	--	1	
8	BLIND FLANGE	SUS304	#50mm. JIS10K	1	
9	BOTTOM VALVE	SUS304	#40mm. JIS10K	1	
10	VALVE	SUS304	#1/2" NPT	1	
11	PROPERLER	SUS304	--	1	
12	SHAFT	SUS304	--	1	
13	GEAR MOTOR	HICO+YEN	11kW./4 Pole	1	300~900 rpm./inverter
14	JACKET	SUS304	2mm. thk.	1	
15	TANK SUPPORT	STEEL	L100x100x6thk.	4	

NOZZLE SCHEDULE

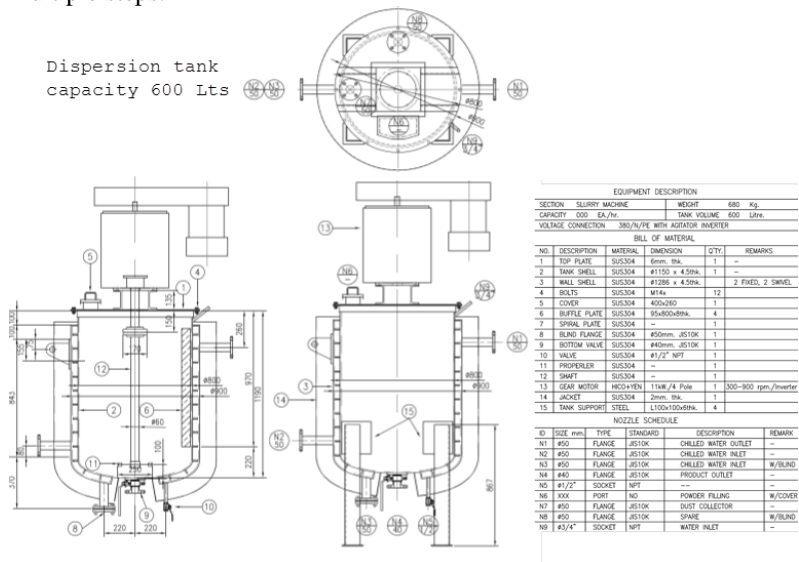| ID	SIZE mm.	TYPE	STANDARD	DESCRIPTION	REMARK
N1	#50	FLANGE	JIS10K	CHILLED WATER OUTLET	--
N2	#50	FLANGE	JIS10K	CHILLED WATER INLET	--
N3	#50	FLANGE	JIS10K	CHILLED WATER INLET	W/BLIND
N4	#40	FLANGE	JIS10K	PRODUCT OUTLET	--
N5	#1/2"	SOCKET	NPT	--	--
N6	XXX	PORT	NO	POWDER FILLING	W/COVER
N7	#50	FLANGE	JIS10K	DUST COLLECTOR	--
N8	#50	FLANGE	JIS10K	SPARE	W/BLIND
N9	#3/4"	SOCKET	NPT	WATER INLET	--

Fig. 3. Technical drawing of 600L dispersion tank with equipment description and nozzle schedule

Equipment involved in functional area of the high-energy mills do not require the recipe management The energy mill is regulated with speed controls using VFD. The mill operation is controlled from the operation room. The sequence of milling operations starts with connecting the dispersion tank to the mill peristaltic pumps. The mill outlet pumps are connected to both the storage tanks and the dispersion tanks. The level of seal liquid for the mill is checked and flow rate is set. The mill RMP is set and the milling operation begins. During milling, the particle size reduction is checked and when the desired particle size is

achieved, the mill outlet is discharged to the storage tanks; otherwise, it is recirculated back to the dispersion tank. The speed of agitating in the storage tanks and the chilled water flow in the tank jacket are controlled automatically. An alarm triggered by weight alerts the operator to stop filling the storage tank. Based on production requirements, the storage tank outlet is manually connected to mobile storage tanks by a flexible hose. Once the source and destination hose clamps fit the valve can be opened. Mobile storage tanks mixing has the VFD control panel. RPM is set up manually by the operator. Mobile storage tanks transfer the slurry into the coating area.

2.2. Substrate coating

The coating area consist of coating production lines. Lines are usually provided as a package including all the associated instrumentation related to the systems. The substrate is manually unloaded from pallets on to a conveyor belt. The substrate marked with barcodes is conveyed to the coating machines. The substrate can be placed manually or by robots onto a rotating index table. Prior to coating, the dry weight of the substrate is measured. The substrate is rotated into the dip pan. The lower part of the substrate is dipped into the slurry. Applying a vacuum to the upper part of the substrate allows sucking in a predefined quantity of slurry. After coating, the weight gain of the substrate is measured. The coated substrate is placed horizontally on the conveyor belt by which is fed into the dryer. The substrates are dried by passing a large quantity of air heated to 150°C through the cells until the moisture content is removed. The substrate spends around 10-12 minutes in the dryer.

After drying, the substrates are rotated to a vertical position and aligned on the feeding conveyor belt to the calciner, either by robot or manually. The calciner is tunnel type oven in which hot air is circulated. Calciners consist of 7-9 different heating-cooling zones. The max temperature is 600°C and the overall time spent in the calciner is around 90 mins. During calcination, residual moisture evaporates and the organic ingredients of the wash coats are oxidised. In the case of PM coats, the composition of ammine solution used for stabilising the PM solution leads to release of NOx. The oven is heated by burners placed in each section. The sections are also equipped with individual circulating fans. The calcined substrate leaves the oven on the conveyor belt and is manually loaded onto pallets.

2.3. Gas treatment, utilities

The acid scrubber system is provided to scrub out any volatile organic compound (VOC) or acetic acid vapour in the off-gas sucked from both the slurry preparation and coating section. A NaOH solution is used for scrubbing. A blower at the scrubber outlet maintains a slight draft in the system and vents to the atmosphere. Fresh raw water makes up the portion of stream routed to wastewater treatment plant. For acid scrubber operation, standby pumps and blowers are recommended. The scrubber usually has its own control panel. Only the information about the pressure drop across the packed column and the run/trip status of blowers is send to the SCADA. A visual alarm for a high pressure drop across the scrubber is provided in the coater area.

The SCR (DeNO$_x$) system processes off-gas from the calciner and consists of two types of catalysts a DeNO$_x$ catalyst to remove the NO$_x$ and an oxidation catalyst to remove the total organic carbon and CO. The off-gas is filtered and heated up to the working

temperature of the catalyst (the SCR unit is preheated to a minimum of 350°C). NH_3 is required for DeNOx reaction while the O_2 content in the off-gas is sufficient for the oxidation reaction. The mixture of the off-gas and the NH_3 reacts on the catalyst surface. NH_3 sorbs to the V_2O_5 molecules of the catalyst and reacts with the NO_x, forming N_2 and H_2O. After desorption of the reacted products, the reduced catalyst is re-oxidised to the active initial state. Hydrocarbons and unreacted NH_3 are partially oxidised after the $DeNO_x$ catalytic reaction. Downstream the catalyst oxidises the pollutants to harmless chemicals. O_2 and VOC migrate to the catalyst surface by gas diffusion and are adsorbed onto the catalyst active sites on the surface of the catalyst where oxidation occurs. The oxidation reaction products are then desorbed from the active sites and transferred by diffusion back into the gas stream. The fan installed at the outlet provides the static pressure to overcome the total pressure drop of the system and provides a constant pressure at the inlet of the system. The cleaned off-gas goes to stack. In the stack NO, NO_2 concentration is measured. Based on the NO, NO_2 concentration results the feed of the NH_3 is controlled. The SCR usually has its own PLC to control the operation.

The utility packages commonly have their own control system. The compressed air, chilled water, DM water, wastewater treatment plant and NG are basic utilities of the process. There is only few hardwire interfaces with SCADA. Hardwired are usually flow or pressure indicators. A dedicated uninterruptible power supply shall be provided for entire instrumentation system. Redundancy is provided for the field instrument and the control system. Back-up time 30 minutes is sufficient.

3. Dispersion and milling

The theoretical background for the dispersion step present in the slurry preparation process is applied. For the determination of the final dispersion size, the balance between force from dynamic turbulent stresses and surface tension force is defined according to [1] as follows:

$$\frac{d_{32}}{D} = C_1\,(1+C_2\cdot c^{V})\cdot Po^{-0.4}\cdot\left(\frac{T}{D}\right)^{1.2}\cdot We^{-0.6} = C_3\cdot We^{-0.6} \tag{1}$$

where

d_{32}	–	Sauter mean particle size [mm], ($d_{32} = 0{,}67\cdot d_{max}$)
D	–	diameter of the impeller [mm],
C_1, C_2	–	constants depending on the system geometry [-],
c^{V}	–	volumetric concentration of dispersed phase [-],
Po	–	power number [-],
T	–	diameter of the tank [mm],
We	–	Weber number [-].

Details for deriving the constant C_3 are shown [1]:

$$C_3 = f\left(Po, T/D, c^{V}, \zeta, Vi\right) \approx 0.063 + 3.3\cdot c^{V} \tag{2}$$

where

ζ – ratio of local dissipation energy related to its maximal value; $\varepsilon_{max}/\varepsilon_{mean}$,

Vi – square root of viscosity ratio of dispersed and continuous phase; $(\mu_d/\mu_c)^{1/2}$.

By combining the previous equations, the final result is obtained:

$$d_{32} \approx C_3 \cdot \rho^{-0.2} \cdot \sigma^{0.6} \cdot \varepsilon^{-0.4} \approx \varepsilon^{-0.4} \qquad (3)$$

where

ρ – density of mixture [kg/m^3],

σ – interfacial surface tension [N/m],

ε – local energy dissipation per unit of mass [W/kg]

The result relates the final particle size to local dissipation energy. The graphical dependence of d_{max} [µm] vs. ε [W/kg] is shown on the graph below (Fig. 4).

From the balance of surface and shear stress forces, it is seen that the maximal shear stress and ε define d_{32}. If equipment with the uniform ε distribution and long enough dispersion time is applied, then the required particle size with narrow particle size distribution is achieved. Shear stress and circulation generated by an impeller in dispersion tanks should be in proportion [1].
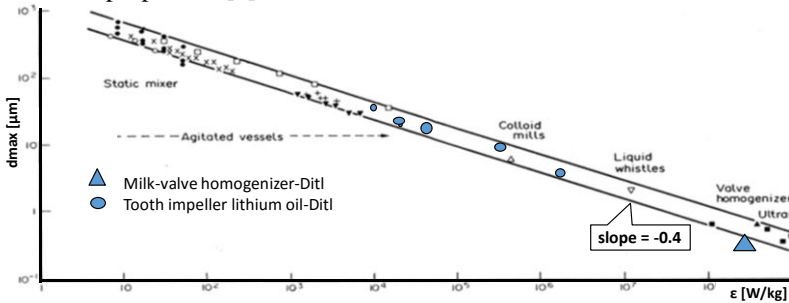
O to the agitated tanks of Calabrese *et al.* (1986a,b) and Wang and Calabrese (1986); □ to the agitated tank of Sprow (1967). Points ▼ and + refer to the agitated vessel of Davies *et al.* (1986) for the dispersion of cyclohexane and decalin respectively. Points ● refer to the data for a Kenics mixer, calculated (as d_{omax} values) by the present author from the data of Berkman and Calabrese (1985). They refer to xylene, silicone oil and paraffin oil. Points △, ▽ and ▲ refer to local P_M data calculated (Davies, 1985) from the specifications and operating conditions of a colloid mill, a liquid-whistle homogenizer, and a fine-clearance valve homogenizer, respectively. Points ■ are deduced from data of Walstra (1974) for a valve homogenizer, and * refers to his ultrasonic homogenizer.

Fig. 3. Generalisation of dispersion results d_{32} vs. ε

The homogenised slurry from dispersion tanks is milled. In mills at temperature 20°C, its specific gravity varies from 1.0 to 1.8. Slurry with a nominal feed size of P95 is 2-3 mm and has an extremely high viscosity of 20,000 – 4 cP. Milling is used to increase the surface area and induce defects in the particles. Milling increases the proportion of regions of high activity in the surface. If a cubic solid is broken down into smaller cubes, each of side 1/n of the original cube, the specific surface area is increased n-times, the broken down mass contains n^2-times the original length of edges and n^3-times the number of corners [2]. The most conventional mechanical milling methods are shown in Fig. 5.

Attritors are very effective for the milling of slurry, these consist of a cylindrical grinding chamber with a drive shaft that has multiple impellers protruding from it (Fig. 6). The power input is not used for rotating or vibrating a heavy grinding chamber but it goes

directly to agitating the media. The rotating shaft stirs the fine media, beads and liquid. The impellers energise the beads' charge, causing powder size reduction thanks to their mutual impact [3]. 10-800 µm ZrO_2 beads with a density of 5.7 g/cm^3 and very good abrasion resistance are used and the shaft rotates up to 4,200 rpm. Use of milling beads of the same size has been shown to produce tracks. Consequently, the beads roll along a well-defined trajectory. Therefore, it is necessary to use a combination of smaller/larger beads to randomise their motion [3, 4]. In the attritors 70-80% of the milling chamber is filled. Attritors processing hard-to-mill materials like slurry are operated in batches. There is a loop between the attritor and the dispersion tank for material circulation. Milling in attritors assures high shear stress, uniformity and short milling time.
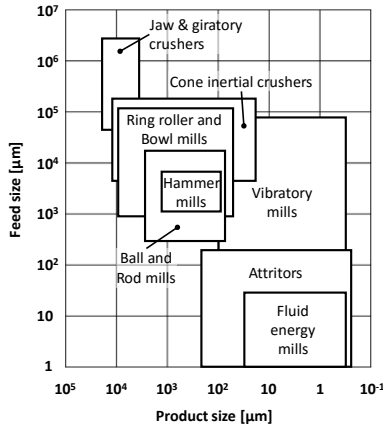
Fig. 5. Application range of mechanical milling methods

Thorough investigation of milling process has shown that three milling stages can be clearly distinguished: the Rittinger stage, the aggregation stage, the agglomeration stage. In the Rittinger stage, the energy input is approximately proportional to the new surface area formation. During the aggregation stage, particles adhere to each other – the degree of dispersion is still increasing significantly and the adherence takes place in consequence of van der Waals forces of the magnitude 0.04-4 kJmol^{-1} [5]. These aggregates can be dissolved by slight mechanical intervention. During the agglomeration stage, the surface area may even decrease because of particle agglomerate growth. Growth proceeds thanks to solid bridges, interfacial forces and capillary pressure on freely movable liquid surfaces, adhesion/cohesion and attraction forces. The distance between particles and the number of contacts plays an important role in the appearance of adhesion. The presence of fine particles along with coarse particles promotes the formation of aggregates. Plastic deformation at contact points increases the area of the adhesion forces and, thereby increases the strength, compactness, and resistance to mechanical effects of the agglomerates [2, 5]. Particles in the nanometer size range have a strong tendency to agglomerate owing to their large specific surface area which accentuates their van der Waals interactions. They must be stabilised against aggregation into larger particles by adding surfactants into the system.
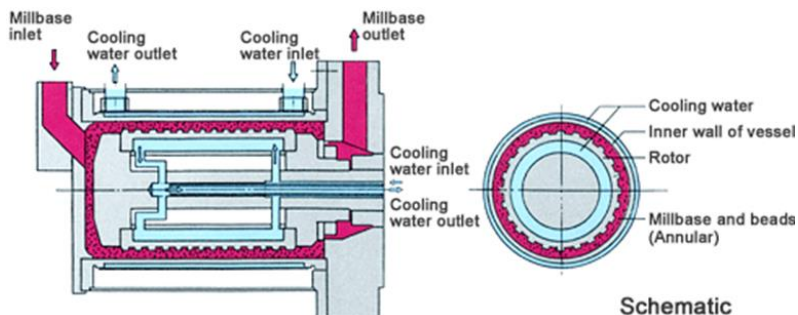
Fig. 4. Attritor scheme

In high-energy milling, surfactants have been used at a level of about 1–5 wt.% of the total powder charge into the mill. The nature and quantity of surfactants used and the type of powder milled would determine the final size, shape, and purity of the powder particles. Use of a larger quantity of surfactants normally reduces the particle size by an order of magnitude of 2–3 [4].

5. Conclusion

On the example, it is shown that chemical engineering affects many branches. Historically, theoretical principles were developed mainly in the chemical industry. Therefore, it is useful to apply this knowledge in newly evolving non-traditional areas. It can be seen in the example that it is essential to analyse the process in the first step and divide the process into separate physical operations. Following the application of already derived dependences in chemical engineering and their synthesis helps the production assessment and optimisation. Professor Ditl jokes about the role of a 'postal pigeon' in this knowledge transfer process. In the article knowledge obtained from the process department at Czech Technical University in Prague was applied on the example.

References

[1]   Ditl P., *Selected Problems in Dispersion Mixing*, DECHEMA, Proceedings of Annual Meeting on Extraction and Mixing Processes Working Groups, Heidelberg, 15-17 March 2015.
[2]   Welch A., *The reaction of crystal lattice discontinuities to mineral dressing*, Developments in Mineral Dressing, 1953, The Institution of Mining and Metallurgy, London, 387-392.
[3]   Rhodes M., *Introduction to Particle Technology*, John Wiley and Sons, 1998.
[4]   Suryanarayana C., Ivanov E., Boldyrev V., *The science and technology of mechanical alloying*, Materials Science and Engineering A, 2001, 304-306, 151-158.
[5]   Juhász A., Opoczky L., *Mechanical Activation of Minerals by Grinding: Pulverizing and Morphology of Particles*, Ellis Horwood, Chichester 1990.

PRZEMYSŁAW DANIEL PASTUSZAK[*], KONRAD NERING[**]

AN EVALUATION OF DELAMINATION IN COMPOSITE STRUCTURES BY COOLING DOWN THERMOGRAPHY (CDT): NUMERICAL STUDIES

OCENA DELAMINACJI W STRUKTURACH KOMPOZYTOWYCH Z UŻYCIEM TERMOGRAFII OCHŁADZANIA: BADANIA NUMERYCZNE

A b s t r a c t

This paper is devoted to numerical studies of composite structures with delaminations made with the use of CDT. Analysis of temperature distribution provides the opportunity to determine the geometry of subsurface defects. Results confirm the validity of the FE model in comparison to previous experimental investigations.

Keywords: Cooling Down Thermography (CDT), Composite Plates, Delamination, Finite Element Method (FEM)

S t r e s z c z e n i e

Praca jest poświęcona badaniom numerycznym struktur kompozytowym z delaminacjami z wykorzystaniem CDT. Analiza rozkładu temperatury daje możliwość określenia grubości defektów podpowierzchniowych. Wyniki potwierdzają słuszność opracowanego modelu numerycznego w porównaniu do wcześniejszych badań eksperymentalnych.

Słowa kluczowe: termografia ochładzania, płyty kompozytowe, delaminacja, metoda elementów skończonych (MES).

[*] MSc. Eng. Przemysław Daniel Pastuszak, Institute of Machine Design, Faculty of Mechanical Engineering, Cracow University of Technology.

[**] DSc. Eng. Konrad Nering, Institute of Thermal and Process Engineering, Faculty of Mechanical Engineering, Cracow University of Technology.

1. Introduction

Nondestructive tests (NDT) are able to provide subsurface defect information without compromising the structural integrity of the examined object. Among the broad variety of NDT techniques is Infrared Thermography (IRT) – this has several unique advantages that distinguishes it from the other techniques: speed of measurement, lack of contact, cost effectiveness, inspection of large flat and/or curved areas. Furthermore, this non-invasive technique creates opportunities to apply it practically in any process where temperature plays a crucial role.

The advancement of IR system technology triggered extensive research in many fields of science. Despite numerous studies, there remains a lot of space for cognisance and the development of IRT methods. In Ref. [1], a new procedure for the thermal/infrared non-destructive testing of composite plates is presented. The authors of this work proposed an application of the thermoelectric module as a source of the heat flux change. The investigated samples were firstly cooled down and they were then exposed to a higher ambient temperature. An infrared camera monitored the surface temperature variation in both the cooling and heating stages in order to reveal subsurface flaws. Nevertheless, the conducted experiments were limited to several specimens due to the high costs of the examined composite structures and time.

The CDT approach creates new possibilities for testing components which cannot be heated due to, for example, thermal expansion or space limitation of the excitation source. In addition, this approach provides a high speed of measurement. It should also be noted that the shown procedure presents some disadvantages in terms of versatility.

Numerical analysis is useful for considering nonlinear phenomena, complex geometries, various boundary conditions, anisotropic materials, etc., without the expense of the manufacturing and testing of many specimens. Analytical solutions are restricted to idealistic scenarios with regard to shapes, selected boundary conditions and isotropic materials that are free of defects – of course, such limitations are impractical for industrial applications. The two most popular numerical approaches in engineering are the Finite Difference Method (FDM) and the Finite Element Method (FEM). The FEM offers capabilities to better understand the thermal processes, which are the basis of thermographic analysis. The numerical investigation can be conducted in order to simulate the heat flow through the material as well as the stress and strain distributions during loading conditions including both mechanical and/or thermal loads.

Numerical modelling and its further comparison to experimental data provides a unique opportunity to study the particular effects on thermal behaviour of the investigated object. Examples where the FEM was successfully applied to simulate classical thermographic tests of multi-layered composites [2, 3] and fibre metal laminates [4] can be found in the literature.

The main aim of this work is to simulate the CDT tests of composite structures with various delaminations and to investigate their impact on thermal response.

2. Active Infrared Thermography

The theoretical aspects of AIRT are well known; therefore, they are not discussed in this work. However, an outline of the most important procedures is presented in order to highlight their novel approach. Broad considerations of the issues presented in this paragraph connected with the fundamentals of AIRT can be found, for example, in Refs. [5-7].

In short, Infrared thermography (IRT) is the field of science that allows visualisation of the emitted infrared radiation in the form of thermal images. Additionally, it includes further signal processing, modelling, computation and analyses of the temperature patterns. Generally, infrared non-destructive testing methods can be divided into active and passive techniques. The difference between them is the origin of the infrared radiation emitted by the investigated surfaces. In the passive thermography, the temperature of the examined object is monitored either during normal operation or immediately after the end of the work – this is in contrast to active techniques which require external stimulation source.

Active infrared thermography is based on the monotonic or periodic supply of external energy to the investigated object. In order to reveal hidden flaws with this type of method, a dynamic temperature field (heating or cooling) is generated. This procedure is caused by equal temperatures of the defective and healthy (non-defective) areas of the examined material during steady state; therefore, it is necessary to excite it. Depending on the form and quantity of supplied energy, AIRT can be divided into the following approaches: pulse thermography (PT), lock-in thermography (LT) and vibrothermography (VT) [8-10].

The pulsed IRT approach is currently the most popular among the AIRT approaches due to its speed of inspection and ease of deployment with regard to field measurements and data interpretation. It uses an energy excitation source to rapidly induce the surface of the investigated material, an infrared camera then records a series of thermograms at constant intervals in the time domain during both heating and cooling stages. When the thermal waves reach the defect, they change their propagation rate producing a thermal contrast on the surface. Pulsed thermography is an indirect process because the subsurface features of a material are inferred by the surface temperature response. It should be noted that the pulse period must be carefully chosen to prevent the failure of an analysed material. The results are visualised throughout the creation of thermal image sequences (thermograms) which map the temperature distribution on the surface of the examined object in the time domain. Among the broad possibilities of pulsed thermography application, it is also important to determine the limitations of this method caused by the research equipment and the investigated objects.

It should be noted that the arrangement of the heat generator and recording equipment could be done by two schemes: one- and two-sided (in reflection or in transmission). It has influence on a measurement, for example, in many practical cases, the transmission method cannot be applied due to inaccessibility of the back surface. Reflection configuration allows the provision of information about the defect depth but only near the investigated surface – this is in contrast to the two-sided method, which is able to reveal deeper defects [8-10].

3. Thermal contrast

Subsurface flaws may be identified by their temperature signals on the examined surfaces. The basic and most commonly used measure of defects is the temperature difference between the pre-selected reference area, which is assumed to be non-defective, and the defective area. This simplest case in thermal non-destructive testing and evaluation (TNDT&E) nomenclature is called an absolute thermal contrast C_a [6]. The main drawback of this basic measure used for defect detection and quantification is the linear dependence on the amount of absorbed energy during the heating stage. It can be described, for CDT two-sided procedure, as follows:

$$C_a(t) = T_d(t) - T_{nd}(t) \tag{1}$$

where T_d is the temperature of the defective region and T_{nd} is the temperature of the non-defective region of the examined specimen.
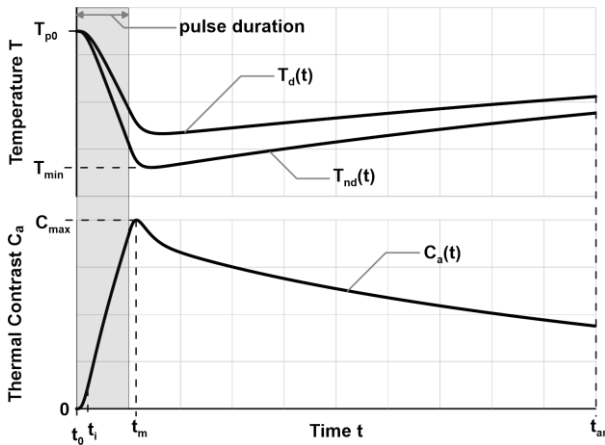
Fig. 1. Temperature and thermal contrast curves with distinction of characteristic points of CDT analysis

The thermal contrast defined in Eq. (1) unfortunately depends strongly on heat flux transmitted through the analysed specimen (assuming uniform one-directional heat flux through the specimen) which in many cases, may be defined incorrectly. Therefore, the dimensionless thermal contrast for the two-sided method of IR-NDT is proposed herein:

$$C_{ar}(t) = \frac{T_d(t) - T_{nd}(t)}{T(t_0) - T_{min}} = \frac{C_a(t)}{T(t_0) - T_{min}} \tag{2}$$

where $T(t_0) = T_{p0}$ is the temperature at the beginning of analysis and T_{min} indicates the minimum temperature of the specimen (in the non-defective area) occurring during analysis (Fig. 1). It is assumed that the difference between the defective and non-defective temperatures at the beginning of analysis ($t = t_0$) is zero.

Values of the defined contrast vary between 0 and 1. A zero value indicates a lack of defect in the analysed specimen $\forall_t T_d(t) = T_{nd}(t)$, and a value of 1 may only occur in time t_m in the case when the temperature of the defective area remains equal to T_{p0} $\forall_t T_d(t) = T(t_0)$. A value 1 indicates infinite heat flux resistance of delamination.

The impact of initial conditions, heat flux and thermal properties on this type of contrast is mitigated which creates an opportunity to compare various thermographic results.

4. Numerical studies

4.1. Description of FE model

In order to predict the thermal behaviour of the investigated object, transient heat transfer analyses were performed for 2D model with various artificial defects. A commercially available ANSYS package version 12.1 was used for this purpose. Implementation of the model was carried out with the use of the ANSYS parametric design language (APDL). This provides the opportunity to automate both simple and complex tasks associated with the creation of areas, meshing, boundary conditions etc. APDL scripting language was also used to retrieve information from the ANSYS database after calculations such as temperature runs and distributions.

Fig. 2 shows the schematic geometry of a composite structure with distinction of the delamination location and boundary conditions. It was assumed that the investigated specimen was in equilibrium with the environment at the beginning of the analysis; therefore, measured ambient temperature in the laboratory $T_{amb} = 25°C$ was used in the numerical model both as a boundary and as initial conditions. The convective coefficient corresponds to the value recommended in the literature for natural convection in a still air environment ($h = 10$).
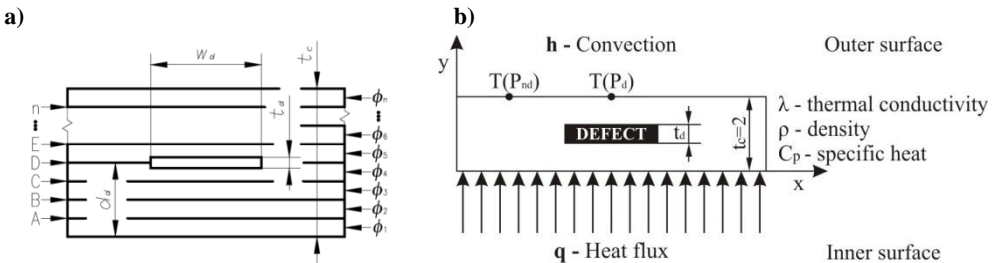
a)

b)

Fig. 2. a) Geometry and location of the delamination, b) boundary conditions

All simulations were carried out in the transmission mode where heat flux was applied on the inner surface and the outer surface was observed during both heating and cooling stages. The entire thermal analysis last for 100 seconds and consisted of two load steps. In the first loadstep, the density of the heat flux was set to -8000W/m² in order to simulate negative heat flux such as in the thermoelectric module. It was instantaneously and uniformly imposed on the inner surface and last continuously for 10 seconds while the front surface was being cooled by natural convection. In the second stage, the heat flux was

removed and the investigated structure was cooled by natural convection on the both surfaces.

In the present investigation, the PLANE77 element was used – this is a higher order version of the 2D, 4-node thermal element (PLANE55) and it has one degree of freedom (temperature) at each node. It is also worth mentioning that selected to current analysis 8-node elements is well suited to model curved boundaries and mitigate curvature effects. PLANE77 can be applied to a steady-state and/or, what is more important for this work, transient thermal analysis. In this element, orthotropic material directions correspond to the element coordinate directions. Convection or heat flux (but not both) and radiation may be input as surface loads on the element faces. Heat generation rates may be input as element body loads at the nodes. If the model containing this element is also to be analysed structurally, the element can be replaced by an equivalent structural element (such as PLANE183) [13].

Artificial delamination was simulated by the area with different thermal properties. This is justified by similar conditions in experiments [1] where the defect was simulated by PTFE foil in the form of a single square inserted between individual layers of the laminate during the manufacturing stage. In order to accurately represent the thermographic process in the composite structure it is necessary to define the biased mesh around the delamination – this is shown in Fig. 3.
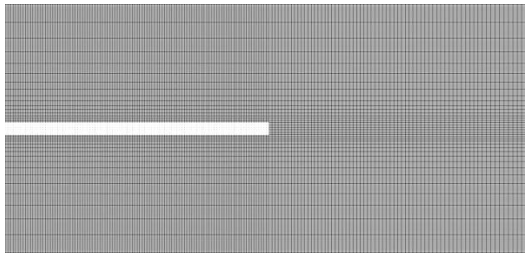

Fig. 3. Magnification of the biased mesh of the delaminated area.

The thermophysical properties of selected materials used during the modelling of CDT are given in Table 1. It should be noted, that these values can considerably differ for other types of laminates or even of the same type composed of identical reinforcement and matrix but performed with the use of a different curing cycle. Therefore, only compatible and experimentally validated data provided by research centers is given herein.

Table 1

Thermophysical properties of selected materials

Material	Thermal conductivity λ [W/mK]	Density ρ [kg/m³]	Specific heat capacity C_p [J/kgK]	Reference
GFRP (∥fibre) along the fibres	0.929	1960	840	[11]
GFRP (⊥fibre) transverse	0.544			
PTFE (Teflon ®)	0.250	2170	1050	[12]

4.2. Results and discussion

After the solution of the posed problem of the thermal response of the composite structure with delamination it is possible to illustrate the computation results. It can take the form of temperature distributions in the model at any moment in time of the analysis, as well as the temporal evolution of the temperature in the chosen points and/or areas. This information is used for further computations of thermal contrasts which are measures of defects. Characteristic points on the contrast evolution curves, such as the time of maximum contrast occurrence t_m and inflection time of the contrast evolution t_i are especially considered.

The presence of the defect alters the heat flow through the laminate resulting in abnormal temperature distribution on both surfaces of the investigated composite structure. This can be observed in Fig. 4.
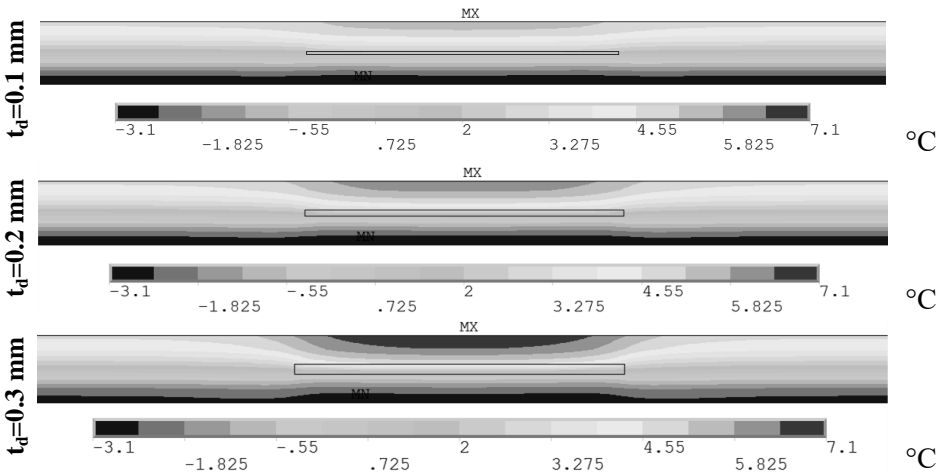
Fig. 4. Temperature distribution through the thickness of the composite structure with various delaminations captured at the time of maximum contrast t_m

In Fig. 5, the temperature profiles on the outer surfaces of the investigated composite structure with various delaminations at the time of maximum contrast t_m are presented. It can be stated that an above average temperature on the outer surface reveals the presence of a resistive defect in the structure. This temperature contrast indicates the presence of a defect and pinpoints its location. It should also be mentioned that a constant temperature in the non-defective area results from neglecting noises from the surroundings and the research equipment.
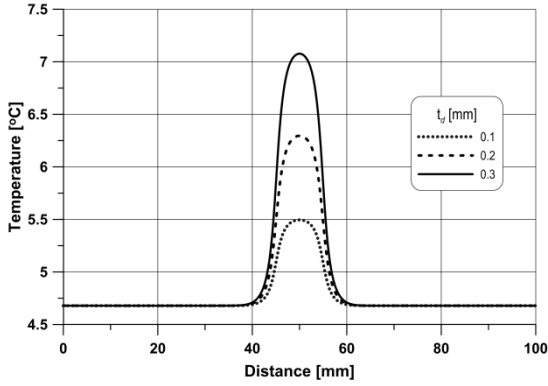
Fig. 5. Temperature profiles on the outer surfaces of the investigated composite structure with various delaminations at the time of maximum contrast t_m
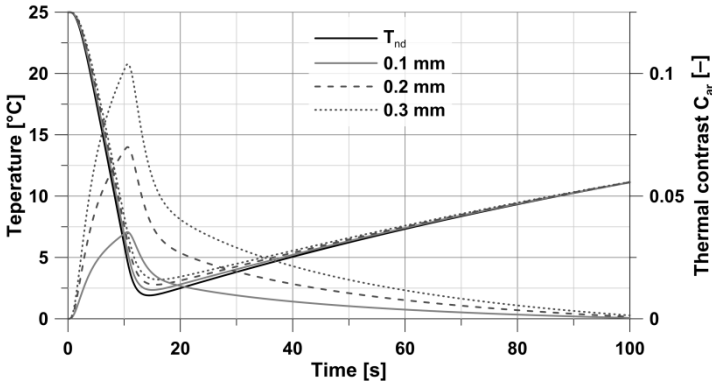
In Fig. 6, the temperature runs within the defective and non-defective areas and thermal contrast evolution C_{ar} for different delamination thicknesses t_d are presented. Initially, there is drastic decrease of temperature during the cooling stage. In the heating stage, after reaching maximum thermal contrast C_{ar} at time t_m, there is a near steady increase of temperature towards the final equilibrium with the environment.

Fig. 6. Temperature runs within defective and non-defective areas and thermal contrast evolution C_{ar} for different delamination thicknesses t_d

Given the ability of the present parametric FE model to account for change in the defect thickness, an analysis of the magnitude of maximum thermal contrast C_{ar} and inflection time t_i versus thickness of the defect t_d was carried out – the results are plotted in Fig. 7. One can observe that in both cases, there is linear correlation between considered variables. It can also be stated that the thicker defects show a higher C_{ar} and t_i which consequently leads to easier and faster detection of such a defect. It should also be noted that the time of maximal contrast occurrence t_m is constant for all thicknesses of the defect (10.6 seconds) and inflection time of the contrast evolution t_i is heat flux independent.
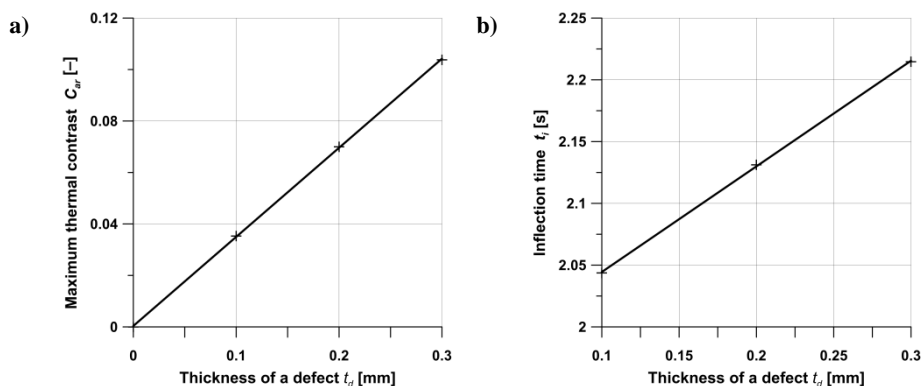
Fig. 7. Maximum thermal contrast C_{ar} and inflection time t_i versus thickness of a defect t_d

5. Conclusions

This paper has shown that CDT can be successfully and effectively simulated by FE numerical modelling. It creates an opportunity to investigate various cases in a short period of time. The thickness of a defect can be determined by the maximum thermal contrast C_{ar} and inflection time t_i which change linearly and are independent from heat flux. Further experimental and numerical studies are needed to investigate other types of defects with various thermal properties.

Acknowledgment

References

1. Pastuszak P.D., Nering K., Muc A., *Detection of defects in composite plates by Cooling Down Thermography (CDT)*, Composites Theory and Practice, nr 2, 2014 111-115.
2. Krishnapillai M., Jones R., Marshall I. H., Bannister M., Rajic N., *Thermography as a tool for damage assessment*, Composite Structures, 67, 2005, 149-155.

3.   Krishnapillai M., Jones R., Marshall I. H., Bannister M., Rajic N., *NDTE using pulse thermography: Numerical modelling of composite subsurface defects*, Composite Structures, 75, 2006, 241-249.
4.   Mabrouki F., Genest M., Shi G., Fahr A., *Numerical modeling for thermographic inspection of fiber metal laminates*, NDT&E International, 42, 2009, 581-588.
5.   Maldague X.P.V., Moore P.O., eds., *Nondestructive Testing Handbook*, Vol. 3: Infrared and Thermal Testing, 3rd ed., American Society for Nondestructive Testing, Columbus, Ohio 2001.
6.   X. P. V. Maldaque, *Theory and practice of infrared technology for nondestructive testing*, John Wiley & Sons, Inc., New York - Toronto 2001.
7.   Vollmer M., Mollmann K.P., *Infrared Thermal Imaging; Fundamentals*, *Research and Applications*, WILEY-VCH Verlag GmbH& Co. KGaA, Weinheim, Germany 2010.
8.   Maldaque X.P.V., *Introduction to NDT by Active Infrared Thermography*, Materials Evaluation, 6(9), 2002, 1060-1073.
9.   Ibarra-Castaneda C., Piau J.-M., Guilbert S., Avdelidis N.P., Genest M., Bendada A., Maldague X.P.V., *Comparative study of active thermography techniques for the nondestructive evaluation of honeycomb structures*, Research in Nondestructive Evaluation, 20(1), 2009, 1-31.
10. Ibarra-Castanedo C., Avdelidis N.P., Grenier M., Maldague X., Bendada A., *Active thermography signal processing techniques for defect detection and characterization on composite materials*, Proc. SPIE 7661, Thermosense XXXII, 76610O (May 03, 2010); doi:10.1117/12.850733.
11. Hagenbeek M., *Characterisation of Fibre Metal Laminates under Thermo-mechanical Loadings*, PhD thesis, Faculty of Aerospace Engineering, Technische Universiteit Delft, Delft 2005.
12. Ibarra-Castanedo C., *Quantitative subsurface defect evaluation by Pulsed Phase Thermography: Depth retrieval with the phase*, PhD thesis, University Laval, 2005.
13. ANSYS, Inc., *Element Reference*, Release 12.1, November 2009.

SEBASTIAN PATER, JANUSZ MAGIERA, WŁODZIMIERZ CIESIELCZYK[*]

HYBRID HEATING AND COOLING SYSTEM WITH RENEWABLE ENERGY SOURCES

HYBRYDOWA INSTALACJA GRZEWCZA I CHŁODNICZA Z ODNAWIALNYMI ŹRÓDŁAMI ENERGII

Abstract

This paper presents hybrid heating and cooling system with four heating devices, three of which are producing heat from renewable energy sources. The systems operate in real conditions in residential and commercial building near Cracow. Geothermal heat pumps have an additional working mode that can be used for passive cooling during summertime for the cooling of building interiors. Results from several years of installation operation with a particular emphasis upon performance, the consumption of electricity, and the amount of heating and cooling production achieved by the individual devices have been presented.

Keywords: hybrid installation, renewable energy sources, geothermal heat pump

Streszczenie

W artykule omówiono hybrydową instalację grzewczą i chłodniczą z czterema urządzeniami grzewczymi, przy czym trzy z nich wytwarzają ciepło z odnawialnych źródeł energii. System pracuje w warunkach rzeczywistych w budynku mieszkalno-usługowym w okolicy Krakowa. Gruntowa pompa ciepła posiada dodatkowy tryb pracy, tj. chłodzenia pasywnego, który jest używany w czasie lata do chłodzenia pomieszczeń budynku. Przedstawiono wyniki kilkuletniej pracy instalacji ze szczególnym uwzględnieniem uzyskiwanej sprawności, zużycia energii elektrycznej oraz ilości wyprodukowanego ciepła i chłodu przez poszczególne urządzenia.

Słowa kluczowe: instalacja hybrydowa, odnawialne źródła energii, gruntowe pompy ciepła

[*] DSc. Eng. Sebastian Pater, Prof. PhD. DSc. Eng. Janusz Magiera, PhD. DSc. Eng. Włodzimierz Ciesielczyk, prof. CUT; Chair of Chemical and Process Engineering, Faculty of Chemical Engineering and Technology, Cracow University of Technology.

1. Introduction

In recent decades, energy demands have been growing due to the increase in the global population, suburbanisation and industrial development [1]. This increase in energy consumption, and in particular fossil fuels, has had a considerable impact on the environment and this has become a substantial cause of universal concern. Utilising renewable energy sources (RES) as much as possible whilst simultaneously focussing on energy efficiency initiatives will probably direct countries on the path to decreasing greenhouse gas emissions and mitigating climate changes and environmental pollution [2].

Space conditioning of buildings is area with a high potential for effective energy production, carbon savings, and reducing energy demands where efficient devices which use RES can make a significant contribution. Households were responsible for approximately one quarter of the final energy consumption in the European Union and Poland in 2013 (Fig. 1).
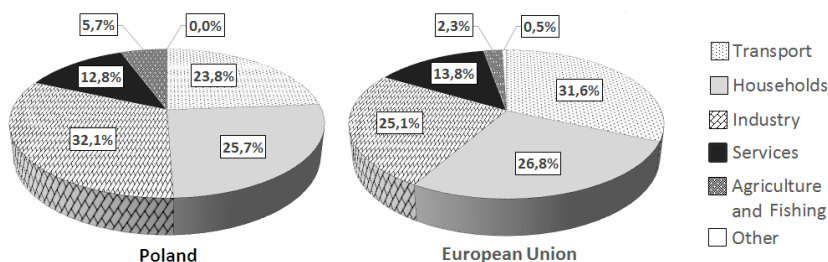
Fig. 1. Final energy consumption by sector in EU and Poland in 2013 [3]

In general, there is a need to develop heating and also, due to climate changes, cooling systems that are environmentally friendly and less reliant upon fossil fuels [4]. Such systems which meet economical and technical challenges often require a combination of technologies. Currently, hybrid installations are becoming more and more popular in central heating (CH) systems, as well as in systems for domestic hot water (DHW) preparation in residential buildings [5]. The work of these systems is based upon mutual cooperation of at least two devices using different energy sources, including renewable sources. In Polish conditions, such systems most commonly use heat pumps, solar panels and biomass boilers, as well as devices that use traditional fuels (gas boilers and solid fuel boilers). Combining different technologies significantly raises the reliability of systems but also complicates the process of their design and optimisation compared to single-technology systems, this is due to the need to integrate detailed control strategies in the design process [6].

An important issue is the operation of the hybrid system in the way that compensate advantages and disadvantages of system devices, because most of RES produce a variable stream of energy in the course of the year, day and even hour [1]. The heat is usually produced by the device which has the lowest operating costs. In addition, hybrid systems use the fluctuating energy more efficiently by matching the energy supply with demand [7]. The enormous energetic potential of hybrid systems that use RES is as important as the ecological aspect of their application because of the reduced emissions of air pollutants and

greenhouse gases. By contributing to energy efficiency, it significantly reduces the negative environmental impact from conventional energy sources, it increases the potential uptake of some renewable energy technologies, it amplifies the potential of sustainable energy development and it subsequently leads to better energy security.

The great importance of hybrid systems that contribute to the development of efficient and affordable technologies based on renewable sources has been strongly highlighted by adding them to the list of strategic priorities for research and innovation of the European Technology Platform on Renewable Heating and Cooling [8].

The aim of this work is to present and analyse selected operational aspects of hybrid system for CH, cooling and DHW preparation in residential and commercial building around Cracow since September 2011. The systems consist of four heat sources, including three which use RES as well as other components and loops. The integration of all heat sources takes place through an advanced cascade combination of two control systems which play an important role in energetic and ecological balance of system. Additionally control systems enables the continuous recording and acquisition of measurements among other temperatures of fluids, generated heat streams by individual heat source devices, solar irradiance.

2. Description of hybrid installation

2.1. Heating and cooling devices

Table 1 presents basic technical data of heating and cooling devices in the considered installation. The bottom heat source (BHS) for a geothermal, brine-water heat pump is a vertical ground heat exchanger in the form of three boreholes, each of which have a depth of 70 meters. The boreholes with diameters of 135mm was made in one line, with seven meters intervals and at six meters distance from the northern wall of the building. In each borehole, a single polyethylene U-tube was mounted. The intermediate fluid which passes energy from the ground to the evaporator is 40% v/v aqueous propylene glycol solution with a freezing point of -21.7ºC.

In the summertime, at high ambient temperatures, the heat pump can operate in a passive cooling mode which involves the use of the additional heat exchanger and appropriately controlled three-way valves. In this mode, the heat from the interior of the building is transferred to the soil which surrounds the bottom heat source without using the compressor of the heat pump. This process occurs because in temperate climates, during the year the soil temperature below 10 meters is constant at around 10-11°C, which is lower than the interior of the building [9]. The temperature of the upper layers of the soil varies sinusoidally throughout the year [10].

In a biomass boiler, which is actually a fireplace with a heat exchanger and water jacket, heat is generated from the combustion of beech common (*Fagus sylvatica*) wood logs. Thermal energy produced in the process is transported to the buffer tank with a capacity of 1500 L without coils, loaded directly (Fig. 2).

Basic technical data of heating and cooling devices in the installation

Device	Technical data	
Heat pump	Heating power in B0/W35, B5/W55	10.4kW, 11.0kW
	COP in B0/W35, B5/W55	4.4, 3.2
	Cooling power in 18/22ºC	6.2kW
Biomass boiler	Total heating power	24kW
	Heating power of water circuit	21kW
Solar collectors	Number of collectors	five collectors with 20 tubes each one collector with 12 tubes
	Type	vacuum-tube with heat-pipe
	Aperture area	$1.866m^2$ for 20 tubes and $1.200m^2$ for 20 tube collector
	Optical efficiency	61.8%
Gas condensing boiler	Heating power	adjustable from 7.2kW to 19.5kW

Solar collectors mounted on the south-facing slope of the building with a roof pitch of 35° is composed of two parallel connected groups of collectors (three collectors for each group). The total aperture area of collectors participating in the collection of solar radiation is 10.53 m^2. Generated heat in the first instance is used for the heating of the water surrounding the inner tank of the combined tank (total capacity 800 L; 200 L for inner tank). If the appropriate temperature of the DHW is reached, the three-way valve is triggered and heat from the collectors is directed to the buffer tank (Fig. 2). Solar fluid, which mediates in the transferring of heat from the collectors to the tanks, is de-ionised water.

The gas condensing boiler (the only conventional heating device in the installation) passes generated heat either directly to the water in the buffer tank or by the upper coil to the DHW in the inner tank of the combined tank (Fig. 2). Fuel which is delivered from the gas network for the combustion process in the boiler is natural methane gas (Group E) with a gross calorific value of not less than 38.0MJ/m^3.

2.2. The heating circuits, ventilation system, other components

During the year, the appropriate thermal comfort in most rooms of the building is maintained by blowing heated or cooled air into them by the air handling unit. In the building, four ventilation zones were separated. For each zone, was assigned channel, water air heater– the heat for these appliance is provided by four heating circuits (OB 1-4 in Fig. 2). Circuit OB 4 is a heating circuit of convection heaters installed in basement rooms, bathrooms and two rooms of the building. Circuit OB 6 is a heating circuit of the industrial air heater mounted in the storage room of the building. One more circuit, named OB 7, can be also distinguished in the installation – this delivers and receives heat from air in the air handling unit during cooperation with a heat pump.
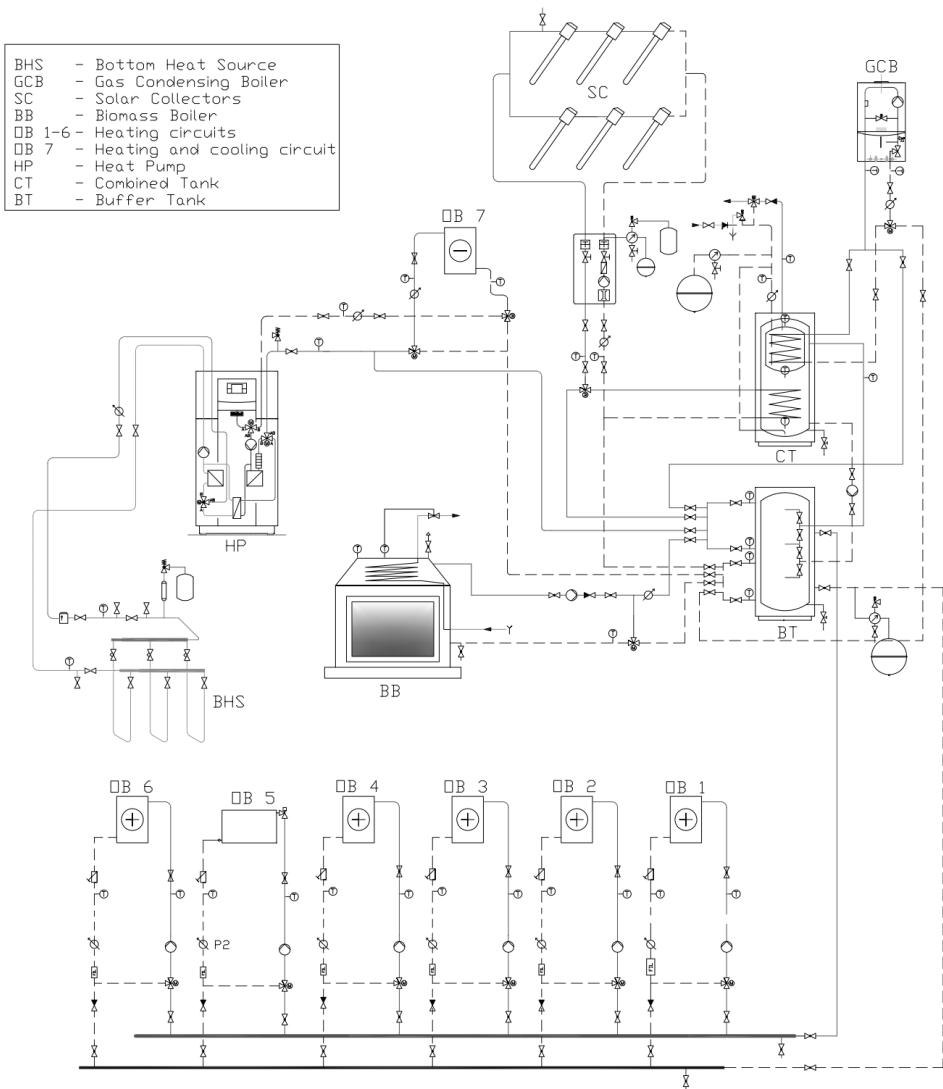
Fig. 2. Simplified layout of hybrid installation with the main components and loops

The fluid temperatures in the installation was measured by temperature sensors with platinum resistance sensing element Pt1000 belonging to accuracy class A according to EN 60751:2009 and outer casing type OG.

The volume flow rate of water in the heating circuits in the system was determined by dry running single-jet water meters. For other circuits, dry running multi-jet water meters were used. Both meters were equipped with transmitters of electric pulses.

A secondary standard-class pyranometer was used for measuring the direct and diffused solar radiation intensity, this was mounted on the roof of the building parallel to the surface of the solar collectors. Measuring the amount of electricity consumed by the main devices in the system, the control system and the air-handling unit was performed by single-phase and three-phase electricity meters which had a SO pulse output.

The volume of high-methane gas consumed by the gas boiler was measured using a bellows gas meter with a 2 L measurement chamber and freely suspended synthetic membranes in the measuring mechanism.

2.3. Control system

For the sake on presence of several heating and one cooling devices was used dedicated especially for hybrid systems [11] two DigiENERGY control systems in a cascade control. The master DigiENERGY is directly responsible for the work of the heat pump, gas boiler, solar collectors, three heating/cooling circuits, and the preparation of DHW; it also takes part in the transfer of control signals for the automation of the air-handling unit. In the main window (Fig. 3), the part of the installation and the current parameters are presented.
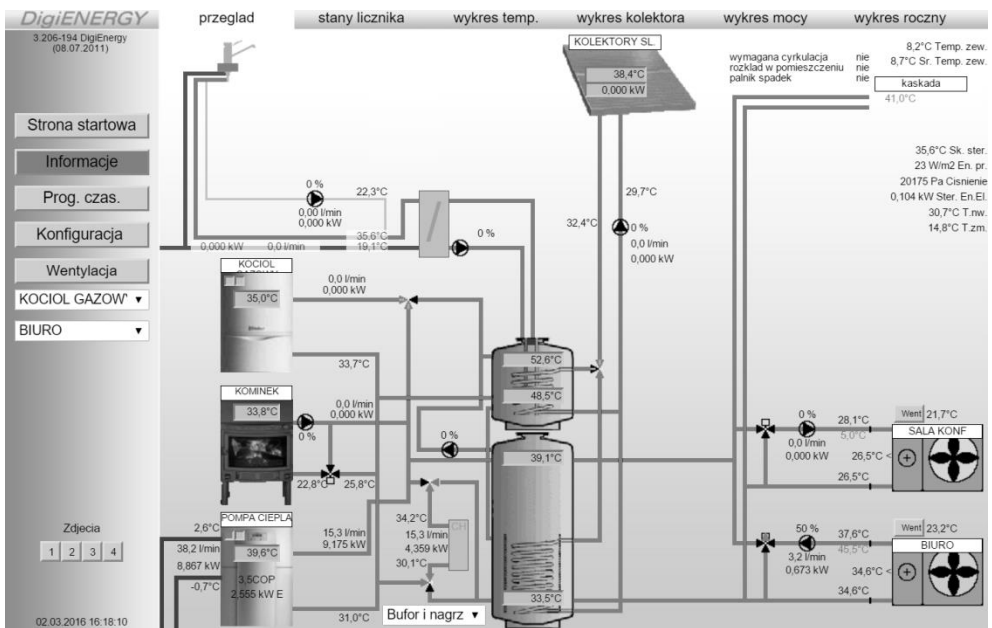
Fig. 3. The main window of the installation of the master DigiENERGY control system

The slave DigiENERGY is directly responsible for the work of the biomass boiler, four heating circuits, the registration data from the pyranometer and taking part in the transfer of control signals for the automation of the air-handling unit.

The operation of the heat pump, the biomass boiler and the gas boiler is controlled by DigiENERGY through the determination of the on and off heating hysteresis, the minimum

and maximum working temperatures, breaks in work caused by exceeding the limits of the allowable working temperatures, delay time of temperature measurement and time period of the priority in preparation of DHW. Other parameters of the boilers are chosen by their built-in drivers.

3. Results and discussion

The daily values of heat production by the individual heating devices of the considered installation and the average daily ambient temperature values from January 2012 until January 2016 are shown in Fig. 4. The heat pump was connected to the installation on 22 January 2012 and from that moment, it started the production of heat. In the winter months, due to the low outside temperature and the simultaneous increase in energy demand for heating the rooms of the building, all heating devices were working. The gas condensing boiler, the biomass boiler and the heat pump generated heat mainly from the beginning of November until the end of April when the average daily ambient temperature was below 10°C.

In the period from early May to the end of September each year, energy produced by solar collectors was, on most days, sufficient to cover 100% of the heat demand for central heating and preparation of the DHW. From November until the beginning of March, the amount of heat produced by the collectors, compared to other heating devices in the installation were much smaller. During these periods were several dozen days when the solar collectors didn't produced a single unit of heat – for example, from 1 November 2014 until 15 March 2015, there were 68 such days.

From February 2015 to October 2015, the biomass boiler wasn't working because in the installation was tested bivalent cooperation of heat pump and gas condensing boiler. Therefore, a much higher level of heat production by the gas boiler for this period in comparison to such periods in the other years can be observed.

The device which globally supplied the biggest amount of heat in each of the first three years of operation of the investigated system was the biomass boiler (Fig. 5). In 2015, the quantity of heat produced by the heat pump (i.e. 35.2 GJ) was only slightly higher than by the biomass boiler. In each year, the least heat was generated by the solar collectors and reached a maximum value of 14.34GJ (3.98 MWh) in 2012. From 2012 to 2015, the total annual heat production did not differ much from each other and was approximately 110GJ (30.6 MWh).

Heat from RES amounted to 69.2%, 73.4%, 76.7% and 64.0% for the years 2012, 2013, 2014 and 2015, respectively, considering the fact that in the case of the heat pump, energy was partially produced from the electricity consumed by the scroll compressor. The gradual increase of this value in first three years was the result of the application of appropriate improvements in the control system. The result obtained in 2015 was caused by suspending use of the biomass boiler for several months.

The electricity consumption of the following units of the installation was measured:
- heat pump (electronics, compressor and circulation pumps of the lower and upper heat sources);
- air-handling unit (electronics, fans and actuators);

- control system and additional electrical devices (circulation pumps, three-way and mixing valves, electronics of gas and biomass boilers).
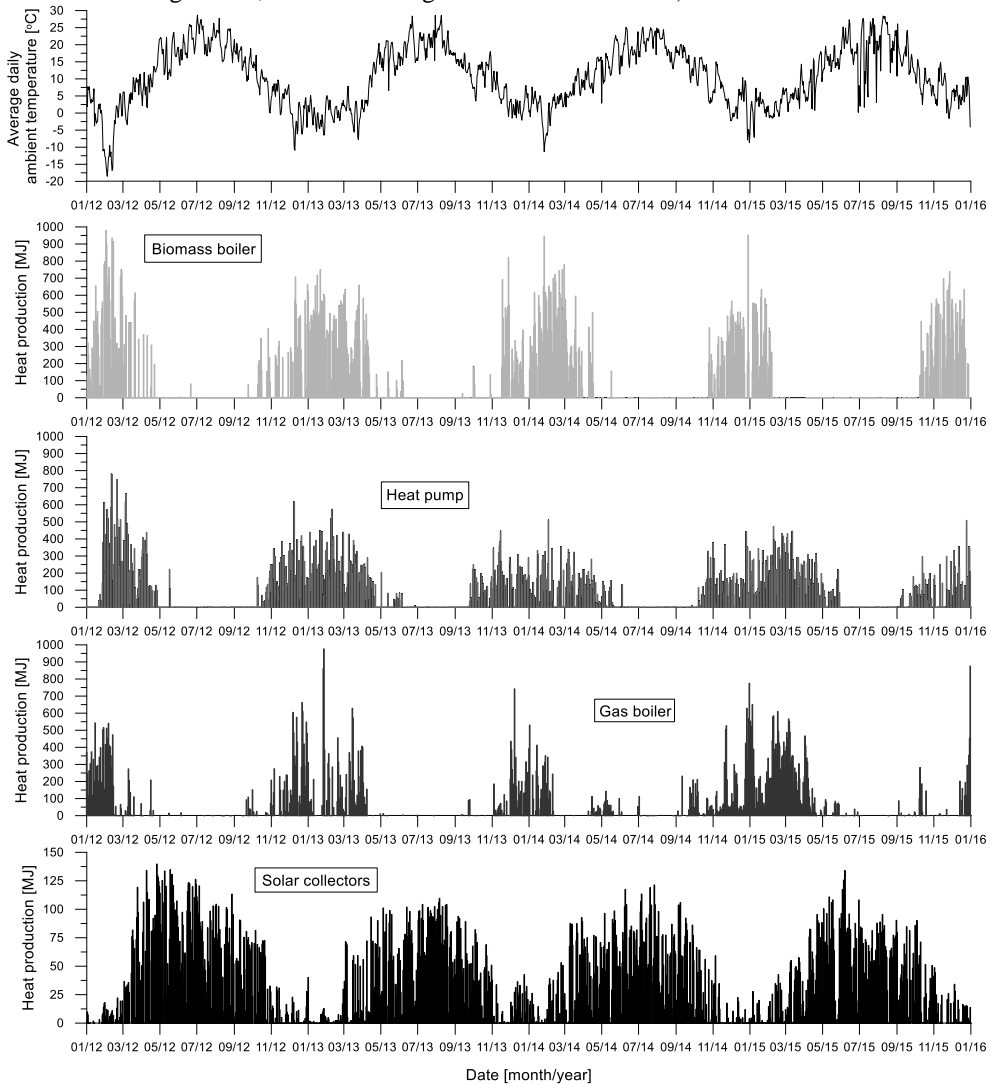

Fig. 4. Daily values of heat production by individual heating devices and the average daily ambient temperature values in the installation from January 2012 until January 2016

The highest electricity consumption (Table 2) in each year was recorded for the heat pump (about 60% of the total electrical energy consumed), which works both in the heating and cooling mode. The second highest electricity consumption was that of the air handling unit.
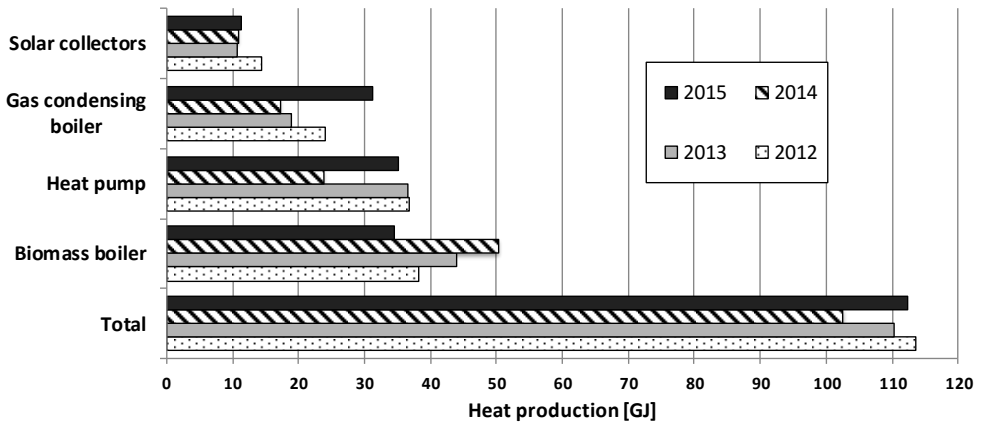
Fig. 5. Annual production of heat by each heating device in the installation for years 2012-2015

Electricity consumption in the installation

Device	Annual electricity consumption			
	2012 [GJ]	2013 [GJ]	2014 [GJ]	2015 [GJ]
Control system and additional electrical devices	2.59	2.94	3.00	3.36
Air-handling unit	4.41	4.49	3.24	2.97
Heat pump	11.19	10.80	6.76	9.63
Total	**18.19**	**18.24**	**11.64**	**15.96**

In the years under consideration, the passive cooling mode of heat pump was used in the period from the beginning of June until the end of August (such a period in the year will be henceforth be referred to as the cooling season). Cooling was carried out in office rooms and the conference hall located on the north-west side of the ground floor of the building, with a total usable area of 103 m^2. During the process, the central heating coil inside the air handling unit was working as an air cooler, lowering the temperature of the air blowing into the rooms. Due to the nature of the use of facilities, passive cooling was mainly carried out during the working hours of office workers (between 0700 and 1800 on business days excluding holiday breaks, vacations) when the outside air temperature exceeded 25°C.

The value of the seasonal cooling performance factor (SPF$_C$) of the heat pump in the cooling seasons was defined by Formulas 1 and 2. Equation 2 also takes into account the electricity consumption in the standby mode of the heat pump.

$$\text{SPF}_{C1} = \frac{Q_C}{P_C} \tag{1}$$

$$\text{SPF}_{C2} = \frac{Q_C}{P_C + P_P} \tag{2}$$

where

Q_C – amount of cooling energy produced by heat pump in the season, J,

P_C – amount of electricity consumed by compressor, controller, circulation pumps of heat pump in the cooling season, J,

P_p – amount of electricity used in standby mode of heat pump in season, J.

From 2012 to 2014, the number of days with active passive cooling were similar and reached approximately twenty-five days, whereas in 2015, there were forty-six such days. The highest SPF_C values were achieved in the year 2014 (Table 3). Taking into account the amount of electricity consumed in standby mode in the calculation reduces the SPF_C values by an average of 15÷24%.

Table 3

SPF_C values of heat pump in cooling seasons

Cooling season	2012	2013	2014	2015
SPF_{C1}	8.38	8.77	11.45	8.50
SPF_{C2}	6.43	6.92	8.69	7.17

The seasonal performance factor (SPF) of the heat pump in the heating mode (excluding months in which the heat pump was working in the cooling mode) had a maximum value of 3.83 in 2015 and a minimum value of 3.37 in 2012. SPF obtained in 2015 was satisfactory in comparison to data submitted in [12], where dozens of installations with ground heat pumps cooperating with low temperature heating in real conditions achieved average SPF values from 3.63 to 3.79.

The average annual efficiency of heat generation by the gas condensing boiler varied from 78% to 82%, which was a result similar to that noticed in [13] where dozens of boilers received an annual performance of 82.5% ± 4.0%. However, the average efficiency of the water circuit of the biomass boiler was identified at the level 47.9%.

The annual efficiency of solar collectors in the installation varied in the range from 32% to 38%. Taking into account the fact that some part of the heat generated by collectors was consumed for the needs of the frost protection system of solar fluid in the calculation, the annual efficiency was reduced to approximately 3%.

4. Conclusions

Through the integration of several heating devices and by applying appropriate improvements in the control system of the hybrid installation, up to 76.7% coverage of annual heat demand for CH and preparation of DHW from renewable energy sources was achieved in 2014 while maintaining high energy efficiency of individual heating units.

Additionally, owing to the passive cooling mode of the heat pump, it was possible to obtain a suitable thermal comfort in the occupied rooms of the building during summertime and with low energy consumption by the cooling process.

Stimulation of growth with rational use of conventional resources while simultaneously respecting the environment is one of the challenges confronting the Polish. It seems that the logic of the near future will be to increase the use of RES because of their wide availability, ecological purity, the possibility of decentralisation of their use, and thus increasing the energy security of country. The latter aspect plays a large role in the global, political and economic trends.

Already, special emphasis is placed on the solutions lowering the energy consumption of residential buildings. The presented work includes such solutions and at the same time, fits into popular trends in the development of environmentally friendly technologies.

A b b r e v i a t i o n s

RES   – Renewable Energy Sources
CH   – Central Heating
DHW   – Domestic Hot Water
BHS   – Bottom Heat Source
SPF   – Seasonal Performance Factor
SPF_C – Seasonal Cooling Performance Factor

R e f e r e n c e s

[1] Peerez-Navarro A. et al., *Experimental verification of hybrid renewable systems as feasible*, Renewable Energy., vol. 86, 2016, 384-391.

[2] DeLlano-Paz F., *The European low-carbon mix for 2030: The role of renewable energy,* Renewable and Sustainable Energy Reviews, vol. 48, 2015, 49-61.

[3] European Commission, *EU energy in figures. Statistical pocketbook 2015,* Publications Office of the European Union, Luxembourg 2015.

[4] US 8733429 B2, *Hybrid heating and/or cooling system*, 2014.

[5] Joniec W., Rybka K., Orysiak A., *ISH 2015*, Rynek Instalacyjny, vol. 4, 2015, 8-12.

[6] Qi Z. et al., *Status and development of hybrid energy systems from hybrid ground source heat pump in China and other countries,* Renewable and Sustainable Energy Reviews, vol. 29, 2014, 37-51.

[7] Li F., Zheng G., Tian Z., *Optimal operation strategy of the hybrid heating system composed of centrifugal heat pumps and gas boilers*, Energy and Buildings, vol. 58, 2013, 27-36.

[8] Sanner B. et al., *Strategic Research and Innovation Agenda for Renewable Heating & Cooling*, Publications Office of the European Union, Luxembourg 2013.

[9] Geetha N. B., Velraj R., *Passive cooling methods for energy efficient buildings*, Energy Education Science and Technology Part A: Energy Science and Research, 29, 2012, 913-946.

[10] M. Rubik, *Pompy ciepła w systemach geotermii niskotemperaturowej*, Oficyna Wydawnicza Multico, Warsaw 2011.

[11] Neupauer K., Głuszek A., Magiera J., *Sterownik nowego typu dla instalacji hybrydowych z odnawialnymi źródłami energii*, Inżynieria i Aparatura Chemiczna, 49, 2010, 87-88.

[12] Miara M. et al., *Heat Pump Efficiency Analysis and Evaluation of Heat Pump Efficiency in Real-life Conditions*, (online) homepage: http://wpeffizienz.ise. fraunhofer.de/download/final_report_wp_effizienz_en.pdf (date of access: 24.02.2015).

[13] Energy Saving Trust, *Final Report: In-situ monitoring of efficiencies of condensing boilers and use of secondary heating,* (online) homepage: https://www.gov.uk/government/uploads/system/uploads/attachment_data/file/1809 50/Insitu_monitoring_of_condensing_boilers_final_report.pdf (date of access: 29.04.2015).

ALBERTO PENTEADO, ERIK ESCHE, DANIEL SALERNO, HAMID REZA GODINI,
JENS-UWE REPKE, GÜNTER WOZNY[*]

THE SYSTEMATIC DESIGN
OF CO_2 CAPTURE PROCESSES
APPLIED TO THE OXIDATIVE COUPLING OF METHANE

USUWANIE DITLENKU WĘGLA PRZY UTLENIAJĄCEJ KONWERSJI METANU

Abstract

The oxidative coupling of methane is the catalytic conversion of methane into ethene. Carbon dioxide is generated as a reaction by-product and must be removed from the gaseous stream. In this paper, the application of a hybrid carbon dioxide removal process including absorption with amines and gas separation membranes is investigated through simulations and cost estimations.

Keywords: carbon dioxide capture, oxidative coupling of methane, absorption, membranes

Streszczenie

Utleniające łączenie cząsteczek metanu do etenu możliwe jest na drodze katalitycznej konwersji metanu. Dwutlenek węgla powstaje jako produkt uboczny reakcji i musi być usuwany z gazowego strumienia. W niniejszym artykule, przedstawiono hybrydowy proces usuwania CO_2: absorpcji z aminami i separacji membranowej oraz szacunek kosztów.

Słowa kluczowe: wychwyt CO2, utleniające łączenie metanu, absorpcja, mambrany

[*] Chem. Eng. Alberto Penteado, DSc. Eng. Erik Esche, DSc. Eng. Daniel Salerno, DSc. Eng. Hamid Reza Godini, Prof. PhD. DSc. Eng. Jens-Uwe Repke, Prof. PhD. DSc. Eng. Günter Wozny, Process Dynamics and Operations Group, Faculty of Process Sciences, Technical University of Berlin.

1. Introduction

Carbon capture and storage (CCS) has been suggested as a critical component to the reduction of greenhouse gas (GHG) emissions without limiting energy usage in the near future [1]. There has been an increasing number of publications in this field. A search on Science Direct with the keyword "carbon capture" filtering years 2000 to 2010 returns around 56,000 publications. The same search for the time frame from 2010 to 2016 yields nearly 90,000 results. CCS is also not to be limited solely to power plants. The scenario entitled '2DS' developed by the International Energy Agency describes how technology across sectors may be transformed by 2050 in order to limit the average global temperature increase to 2K. In this scenario, nearly half of the CO_2 captured between 2015 and 2050 is from industrial sources, such as from the production of steel, chemicals, and cement [1]. Within this context, this contribution aims to study and further develop the carbon dioxide capture section for the oxidative coupling of methane process.

The oxidative coupling of methane (OCM), which is the catalytic conversion of methane into ethene (ethylene), has been extensively investigated for the past thirty years due to its potential for methane utilisation. The OCM allows for the conversion of methane containing feedstock, such as natural gas or biogas, into ethylene. Thus, OCM enables the production of value-added chemicals directly from C1, avoiding the costly intermediate step involving syngas [2]. The ethylene product is the raw material for the production of nearly all plastic commodities, such as high and low density polyethylene, polyethylene terephthalate, polyvinyl chloride, and polystyrene. The global ethylene capacity in 2012 is estimated to be above 140 million tons per year [3], which is almost entirely covered by naphtha or ethane cracking.

The USA has recently undergone the so-called shale revolution, bolstered by the exploration of deep underground shale formations through hydraulic fracturing and horizontal drilling [4]. Wet shale gas typically requires gas processing to produce pipeline-quality natural gas for energetic purposes and an ethane rich stream which is cracked to produce ethylene. In this sense, OCM could be of significant advantage by increasing the ethylene output through the further conversion of methane. In 2015, the first OCM demonstration plant was commissioned in Texas [5].
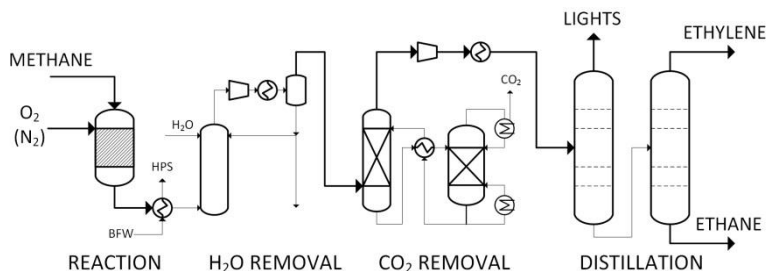

Fig. 1. Conceptual Flow Diagram for the OCM Process

The activation of most OCM catalysts occurs at temperatures around 973K, which also favours secondary reactions and limits the product yield. It is suggested in literature that the combined ethylene and ethane yield in the OCM reactor should not exceed 28% [6],

evidencing the need for efficient downstream separation sections. The carbon dioxide is an undesired by-product which is of major concern. The stream leaving the OCM reactor can be compressed, cooled, and flashed for bulk water removal. The removal of the unconverted methane and the C_2 fractionation can be achieved through cryogenic distillation, even in a shared distillation section if OCM is to be an add-on unit for an ethane cracker. However, the carbon dioxide formed in the OCM reactor must be removed from the gas stream by a CO_2 removal section before it can enter the distillation section. A conceptual process flow diagram for the OCM process is presented in Fig. 1. This contribution focuses on the design and improvement of an industrial scale CO_2 separation section in the downstream section of an OCM reactor producing 100 kton of C_2H_4 per year.

2. Motivation

Absorption with amines is the most commonly employed carbon dioxide removal technology for flue gas CO_2 capture, natural gas sweetening, and biogas upgrading; therefore, it is an obvious initial candidate for OCM and also for industrial/process gas streams. Aqueous solutions of monoetanolamine (MEA), normally limited to 30wt% due to their corrosive nature, are widely used as solvents and are considered as the benchmark for comparison with new technologies.
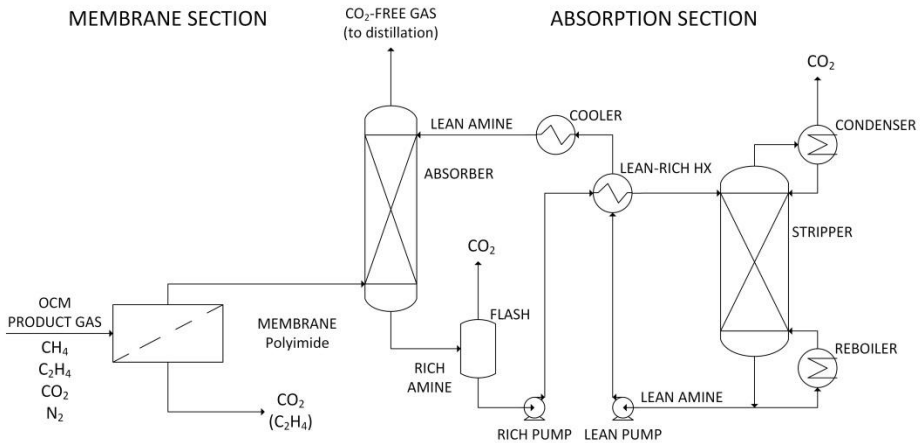
Fig. 2. Process flow diagram of a hybrid CO_2 removal process employing a polyimide gas separation membrane and absorption

In the absorption column, i.e. structured packing column, the amine solution is fed at the top and contacts the gas stream containing CO_2, which is fed at the bottom. The amine chemically binds with the carbon dioxide releasing a CO_2-free gas at the top and a rich amine solution, loaded with CO_2, at the bottom. The rich amine stream is then flashed to near atmospheric conditions to partially remove the CO_2, then pre-heated in a heat exchanger and fed to a stripping column. Heat is added through the reboiler in the stripper in order to reverse the reactions, producing a CO_2 rich gas stream at the top and a lean

amine solution at the bottom which is cooled and recycled back to the absorber. A process flow diagram for the described process is presented on the right-hand side of Fig. 2.

The current research and development in the field of CO_2 capture concentrates on three different focal points according to [7]:

- the development of new energy-efficient solvents;
- process synthesis and optimization;
- integration with the energy plant and CO_2 compression system.

An example of the first focal point is the utilisation of functionalised ionic liquids in order to increase the absorption rate and capacity as described in [8]. Within the second focal point, a generalized framework for the optimal design of CO_2 capture flowsheets is presented in [9]. The models applied therein are based on inexpensive equilibrium calculations and orthogonal collocation on finite elements, resulting in a flexible superstructure that can handle flowsheets with multiple column segments in series and parallel, as well as side feeds and withdrawals. An example of research within the third focal point is the rigorous rate-based simulation of an integrated gasification combined cycle with pre-combustion CO_2 capture as in [10].

Herein, a fourth focal point for carbon capture research and development is suggested – this involves alternative separation technologies. While absorption with amines is the most well established process, emerging technologies such as gas-separation membranes, low temperature distillation with controlled CO_2 freezing, and pressure swing adsorption are also being investigated and comprehensively reviewed in [11].

In this sense, membrane-based gas separation offers significant advantages such as simple operation, reduced start-up time, and easy and modular installation [12]. A major disadvantage of gas separation membranes is that scale-up occurs mainly by adding more modules operating in parallel. This results in an approximately linear increase of the capital investment cost, while well-established technologies, such as absorption, tend to scale up better. Nevertheless, membranes have been successfully employed for natural gas treatment, notably for small to medium capacities or even for large capacities in off-shore or remote applications [12]. Gas separation membranes can also offer significant contribution for biogas upgrading [13].

These four focal points are considered when developing the carbon dioxide capture section for the OCM process. Stünkel et al. investigated the absorption section experimentally in a mini-plant in Technische Universität Berlin, testing different solvents and operating conditions within the scope of the OCM process downstream section [14]. The use of gas separation membranes in combination with absorption in a hybrid process was described in [15]. A membrane module or cascade of modules was applied in order to remove the bulk CO_2, with the remaining fraction being removed through absorption as seen in Fig. 2. In [16], the hybrid CO_2 capture mini-plant was optimised to minimize the energy demand. The integration of the carbon dioxide capture section with the other sections of the OCM mini-plant in a superstructure was proposed and optimised in [17].

Given the successful proof of concept at the mini-plant scale, the design and economic evaluation of a hybrid system for CO_2 removal at industrial scale was performed in [18]. Therein, the benchmark solvent 30wt% MEA was considered for the absorption section. This contribution is herein further extended by analysing the effect of switching the solvent to an aqueous solution containing 37wt% N-methyldiethanolamine (MDEA) and 3wt%

piperazine (PZ). The MDEA reacts slower with CO_2 in the absorber, but its regeneration in the stripping column should demand less energy. The PZ is added to overcome the first disadvantage, for it reacts quickly with CO_2. The membrane and absorption sections were modelled and simulated. A design was carried out aiming at the removal of 97% of the inlet CO_2. The considered OCM reactor produces 100 kton of C_2H_4 per year. Two new design configurations were proposed, one is a standalone absorption process with the mixed solvent, while the other is a hybrid process employing a polyimide membrane and the mixed solvent. The size of the equipment is calculated, and the utility and equipment costs are estimated. The performance of the new process configurations was analysed by comparison with a benchmark process consisting of standalone absorption with 30wt% MEA.

3. Modelling

The absorption section was modelled in Aspen Plus with an Electrolyte NRTL model for the liquid phase and the Redlich-Kwong equation of state for the vapour phase. The solubility of gaseous components in amine solutions was described by Henry's law. The simulations made use of the example files in the software's library, which are based on [19]. The implemented thermodynamic and reaction kinetic parameters from various literature sources were kept. The columns were simulated with rigorous rate-based models, using Aspen Plus's built-in correlations for mass, heat, and momentum transfer, and for the packing hold-ups. Sulzer Mellapak 350X and 350Y were selected as the structured packings of the absorption and stripping columns respectively. The remaining units were modelled using the traditional MESH approach.

A high-capacity, flat sheet, envelope-type membrane module was considered for this application. The applied membrane material was polyimide (PI), which has a high CO_2 selectivity towards hydrocarbons. This means that the permeate is a CO_2 rich stream, while the other components tend to remain on the retentate stream. The membranes and modules were produced by research partners at Helmholtz-Zentrum Geesthacht Centre for Materials and Coastal Research, Germany, as outlined in [13].

A one-dimensional, solution-diffusion model based on balance and flux equations was applied [20]. Secondary transport effects such as pressure drop and concentration polarisation were neglected based on mini-plant experimental results. The flow was assumed to be isothermal with the permeate being 5K cooler to account for the Joule-Thomson effect. The permeances were calculated using an Arrhenius type equation. Fugacities were calculated on the retentate side using the Peng-Robinson equation of state [21]. The set of differential algebraic equations was discretised using orthogonal collocation on finite elements (OCFE) with fourth-order Lagrangian polynomials on Radau roots. Ten finite elements were employed, as this provided reasonable computation time and identical results to simulations employing twenty finite elements.

The model was first created using the online modelling environment MOSAIC, which allows for the automatic code generation for the numerical solution using different programming and domain-specific languages [22]. As an example, for the optimisation of the CO_2 capture mini-plant performed in [16], an AMPL code for the membrane model was

automatically generated in MOSAIC to allow for its solution using the IPOPT solver [23]. Herein, the membrane model at mini-plant scale was further extended inside MOSAIC to allow for the simulation of industrial plants by applying a scale-up by numbering up approach. The inlet flow was divided by the design flow of a single membrane module, resulting in the required number of parallel operating modules. A single module was then simulated and the resulting flows were multiplied back by the number of parallel modules. The code was automatically generated in MOSAIC using the Aspen Custom Modeler modelling language, allowing for the model to be compiled and included as a custom unit operation in Aspen Plus simulations. Hence, MOSAIC offers a convenient modelling platform, allowing facilitated model exchange, reuse, and application across platforms.

4. Simulations

The simulations were carried out using Aspen Plus version 8.8 with the available unit operation models of the software library and the custom membrane model exported from MOSAIC. Utility and equipment costs were calculated using Aspen Economic Analyzer, which allows for the process synthesis and the cost estimation steps to be performed simultaneously. The default utility costs of the software were kept.

Different OCM reactor concepts, such as packed bed, fluidised bed, and membrane reactors, as well as different feeding policies, such as CH_4-O_2 ratio, N_2 or CO_2 dilution, are currently under investigation [24]. It has been previously demonstrated that membrane-based CO_2 separation is unlikely to bring any economic advantage unless CO_2 is used as dilution gas in the OCM reactor [18]. When employing N_2 for dilution, the driving force for the CO_2 separation through permeation is not high enough, implying too high a product (ethylene) loss in the permeate stream. Therefore, a CO_2 diluted gas stream was considered in this paper. It was assumed that the OCM reactor outlet gas stream is compressed, cooled and passed through the water removal section, thus delivered to the CO_2 removal section at 10bar, 313K, and dry, with the following molar composition: CO_2: 24.5%; C_2H_4: 4.5%; N_2: 8.0%; CH_4: 63.0%.

4.1. Absorption Section

Given the degree of complexity of the absorption/desorption system with electrolytes, reactions, and rate-based calculations; no actual optimisation was performed in Aspen Plus. The design of this section was thus performed in terms of extensive simulations and sensitivity analyses. A similar systematic has been previously detailed in literature [7].

The absorption column was designed based on the liquid to gas ratio (L/G), which is determined as the ratio between the total liquid and gas mass flow rates in the column. Initially, one wants to use as little amine solution as possible for a given CO_2 capture duty, which means the L/G ratio should be as small as possible. A reduction in the L/G ratio can be achieved by increasing the packed height of the absorber. On the other hand, increasing the packed height also increases the capital investment cost for the column. For the sensitivity analysis in Fig. 3, the packed height was varied and the necessary amine flow rate to achieve the given CO_2 capture duty of 97% was calculated for each case.
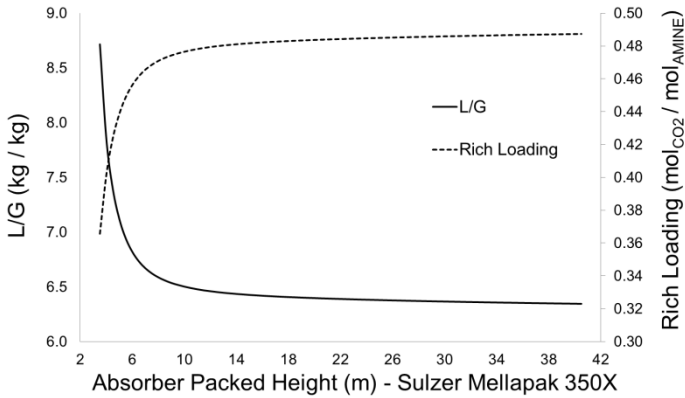
Fig. 3. Sensitivity analysis for the packed height in the absorber

It is clear from Fig. 3 that after a packing height of 14m, the effect of adding more packing in order to reduce the L/G ratio is greatly reduced. For steady operation out of the region where the L/G ratio dramatically increases, a packing height of 20 m was chosen for the absorber. The achieved rich loading in the bottom (α_{RICH}), expressed in mol_{CO2}/mol_{AMINE}, is also shown on the secondary axis.

The design of the stripper was achieved through the NQ-curve shown in Fig. 4, which illustrates the relationship between the number of stages, in this case represented by the column's packed height, and the heat duty. The CO_2 mass fraction on the top of the stripper was fixed at 0.9 by varying the distillate rate, and consequently, the reflux ratio and condenser duty. The lean amine loading at the bottom of the column was fixed by varying the reboiler duty. A higher packed height implies lower energy consumption, but increased capital investment cost. It is clear that from 4.5 m of packing, the reboiler duty stabilises at around 3.05 MJ/kgCO$_2$. Hence, a packed height of 6m was selected for the stripper.
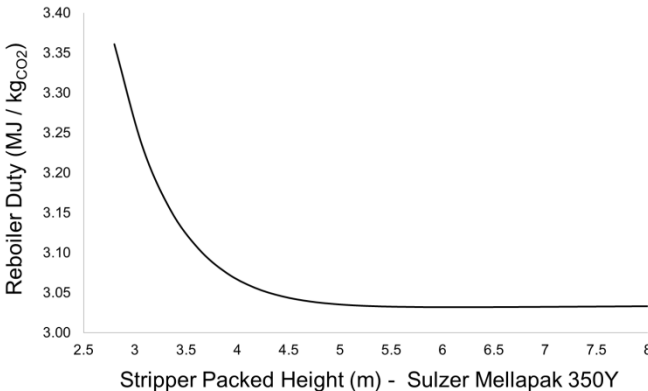
Fig. 4. NQ-Curve for the stripping column

The columns' diameters were calculated taking into consideration the fractional approach to maximum capacity. The maximum capacity corresponds to a gas load of 5÷10% below the flooding point so the column could still operate under these conditions. Sulzer recommends a fractional approach to maximal capacity between 0.5 and 0.8 – a value of 0.75 was taken. The columns operate under pressure (10 bar for the absorber and 2.2 bar for the stripper); therefore, pressure drop is not as critical as for flue gas CO_2 capture. The resulting diameters for the absorber and stripper were 4.3 m and 5.8 m respectively. The pressure drop calculated by the built-in vendors' correlation were 2.4 mbar/m and 0.4 mbar/m, which are within the recommended values.

The ideal operating point of the absorption/desorption system was investigated through a sensitivity analysis for the lean loading of the amine solution (α_{LEAN}), which was set by varying the reboiler duty in the stripping column. The rich loading at the bottom of the absorber is limited by the amine solution absorption capacity. Feeding a leaner amine to the absorber implies a reduced L/G ratio and recirculation rate; however, amine regeneration occurs at the expense of reboiler duty. The sensitivity analysis was carried out by varying the set point for the lean loading and computing the utility costs, comprising cooling water, electricity, and medium pressure steam, for the entire system. The energy efficiency of the newly considered solvent can be seen in Fig. 5, where the optimal lean loading is rapidly achieved at around 0.04 mol_{CO2}/mol_{AMINE}. This value typically ranges from 0.1÷0.25 mol_{CO2}/mol_{AMINE} for the benchmark 30wt% MEA, indicating that the regeneration of the second one demands more energy.
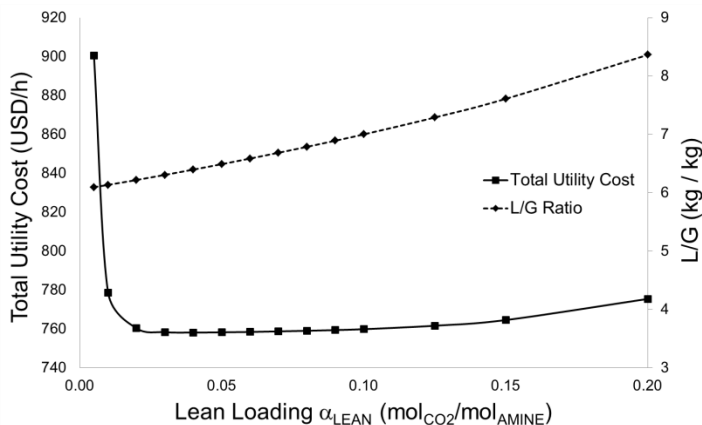
Fig. 5. Sensitivity analysis for the lean loading

4.2. Membrane Section

The membrane section was designed through sequential optimisation with an SQP solver in Aspen Plus. The objective function to be minimised was a cost function containing the cost to treat the remaining CO_2 in the retentate stream through absorption, and a penalty cost applied to the C_2H_4 loss in the permeate stream. The optimisation variables were the membrane area per module and the permeate pressure.

The penalty cost for the ethylene loss was based on its current market price, which can vary drastically according to oil price fluctuations. Applying a price of 1200 USD per ton of C_2H_4 led the solver to bring the membrane area to its lower bound of 0.1 m² in order to keep ethylene loss as low as possible, but capturing only 2.3% of the inlet CO_2. For a price of 600 USD per ton of C_2H_4, an area of 2.1 m² was found to be optimal, resulting in 36.7% CO_2 capture and 2.8% ethylene losses. The optimisation was thus used to provide a reasonable range of values for the membrane areas. The optimal permeate pressure was found to be at its lower bound of 1.1bar for all the cases, given that a higher pressure differential across the membrane increases the CO_2 selectivity towards C_2H_4.

Ultimately, a value of 1.5 m² was selected for the membrane area, allowing as much as 28.6% of the CO_2 to permeate through the membrane, while losing only 2.0% of the inlet C_2H_4. Hence, the addition of the membrane section to remove the bulk of the CO_2 allows for a major reduction in the required amine recirculation rate and reboiler and cooling duties in the absorption section. The design of the absorption section to remove the remaining CO_2 was carried out through the same previously described methodology.

For the given gas flow rate, as much as 3,030 parallel membrane modules were required. This generates additional capital investment costs. On the other hand, the equipment in the absorption section was reduced. While carbon steel can be applied in the membrane section, the equipment in the absorption section needs to be constructed of stainless steel given the corrosive behaviour of the solvent. Therefore, a trade-off in the total equipment cost was observed.

5. Results and Discussion

The main results from the economic analysis are presented in T a b l e   1 . These are the utility cost, installed equipment cost, and total cost calculated by annualising the equipment cost according to the following formula, where i is the interest rate of 15%, and n is the operating life of the plant, which was assumed to be 20 years:

$$TotalCost = UtilityCost + EquipmentCost\left(\frac{i(1+i)^n}{(1+i)^n - 1}\right) \tag{1}$$

The three scenarios correspond to standalone absorption with MEA (benchmark), standalone absorption with MDEA+PZ, and hybrid process employing PI membrane and absorption with MDEA+PZ.

The application of the energy-efficient solution containing MDEA and PZ in the absorption section allowed for utility cost savings in comparison with the benchmark MEA. This is mainly attributed to the reduced reboiler duty in the stripping column. Despite requiring a higher solvent recirculation rate, which causes the absorber and other equipment to be larger, the stripper column was significantly shortened. The NQ-Curve for the stripper column using MEA showed that around 15m of packing are necessary to bring the energy requirement down to 3.59 MJ/kgCO_2. For MDEA+PZ a value of 3.03 MJ/kgCO_2 could be reached with only 6m of packing. Hence, both the capital and operating cost could be reduced by switching the solvent from MEA to MDEA+PZ. This process configuration

should be applied when N_2 dilution is used in the OCM reactor and the use of membranes is uneconomical due to the high ethylene losses in the permeate stream.

Results of the economic analysis forthe different process configurations

Process Configuration	Utility Cost kUSD/y	Equipment Cost kUSD	Total Cost kUSD/y
MEA	6,653	15,653	9,154
MDEA + PZ	6,309	15,146	8,729
PI+MDEA+PZ	4,781	15,625	7,277

When adding the membrane unit on the upstream of the absorption section, the energy required for the CO_2 separation was reduced to 2.30 MJ/kgCO_2, which led to the low operating cost for this configuration. It is also shown that the reduction in the equipment size on the absorption section nearly covered the costs of the membrane modules. The absorption section for this process configuration was estimated at 11,807 kUSD, while the membrane section was estimated at 3,818 kUSD. The downside of this process configuration is that the ethylene loss was 2.7%, while for standalone absorption, this value was typically between 1.0÷1.5%. However, this lost is most likely still acceptable for industrial purposes, indicating that gas separation membranes can be applied if CO_2 dilution is used in the OCM reactor. It is also clear that the benefit brought by the addition of the membrane section is much higher than the benefit from switching the solvent.

6. Conclusion

A systematic methodology for the design of energy efficient carbon dioxide absorption processes based on rigorous rate-based simulations and the execution of sensitivity analyses through the use of commercial flowsheeting software was presented. The methodology was applied to the CO_2 removal section of the oxidative coupling of methane process. The use of a new solvent, an aqueous solution of 37wt% MDEA and 3wt% PZ, was considered as an opportunity for process improvement on an industrial scale. Different process configurations were considered and the configuration employing a PI gas separation membrane and absorption with MDEA and PZ in a hybrid concept provided the most cost-efficient solution for this application.

It is evident how emerging technologies, such as absorption fluids and membranes, can play a major role in reducing the cost of carbon dioxide sequestration, thus enabling its application across different industrial segments. It is also clear how the application of hybrid processes, which exploit the pros and cons of different separation mechanisms, can provide significant energy and cost savings for chemical processes.

R e f e r e n c e s

[1] EA, *Technology Roadmap: Carbon Capture and Storage*, International Energy Agency, Paris 2013.

[2] Ashcroft A.T., Cheetham A.K., Foord J.S., Green M.L.H., Grey C.P., Murrell A.J., Vernon P.D.F., *Selective oxidation of methane to synthesis gas using transition metal catalysts*, Nature, vol. 344, 1990, 319-321.

[3] True W., Global ethylene capacity continues advance in 2011, Oil & Gas Journal, vol.7(110), 2012.

[4] Kinnaman T.C., *The economic impact of shale gas extraction: A review of existing studies*, Ecological Economics, vol. 7, 15 May 2011, 1243-1249.

[5] Fischer J., *Methane-to-Ethylene Plant Comes Online in Texas*, NGI Weekly Gas Market Report, 06 April 2015.

[6] Su Y.S., Ying J.Y., Green Jr. W.H., *Upper bound on the yield for oxidative coupling of methane*, Journal of Catalysis, vol. 218(2), 2003, 321-333.

[7] Agbonghae E.O., Hughes K., Ingham D.B., Ma L., Pourkashanian M., *Optimal Process Design of Commercial-Scale Amine-Based CO_2 Capture Plants*, Ind. Eng. Chem. Res., vol. 38, 2014, 14815-14829.

[8] Feng Z., Cheng-Gang F., You-Ting W., Yuan-Tao W., Ai-Min L., Zhi-Bing Zhang, *Absorption of CO_2 in the aqueous solutions of functionalized ionic liquids and MDEA*, Chemical Engineering Journal, vol. 1, 2010, 691-697.

[9] Damartzis T., Papadopoulos A.I., Seferlis P., *Generalized Framework for the Optimal Design of Solvent-Based Post-Combustion CO_2 Capture Flowsheets*, Chemical Engineering Transactions, 2013.

[10] Moioli S., Giuffrida A., Gamba S., Romano M.C., Pellegrini L., Lozza G., *Pre-combustion CO_2 capture by MDEA process in IGCC based on air-blown gasification*, Energy Procedia, vol. 63, 2014, 2045-2053.

[11] Rufford T.E., Smart S., Watson G.C.Y., Graham B.F., Boxall J., Diniz da Costa J.C., May E. F., *The removal of CO_2 and N_2 from natural gas: A review of conventional and emerging technologies*, Journal of Petroleum Science and Engineering, vol. 94-95 2012, 123-154.

[12] Bernardo P., Drioli E., Golemme G., *Membrane Gas Separation: A Review/State of the Art*, Ind. Eng. Chem. Res., 2009, 4638-4663.

[13] Brinkmann T., Naderipour C., Pohlmann J., Wind J., Wolff T., Esche E., Müller D., Wozny G., Hoting B., *Pilot scale investigations of the removal of carbon dioxide from hydrocarbon gas streams using poly(ethyleneoxide)-poly(butylenetere-*

phthalate) PolyActiveTM) thin film composite membranes, Journal of Membrane Science, vol. 489, 2015, 237-247.

[14] Stünkel S., Illmer D., Kraus R., Wozny G., *On the design, development and operation of an energy efficient CO_2 removal for the oxidative coupling of methane in a miniplant scale*, Applied Thermal Engineering, vol. 43, 2012, 143-147.

[15] Song S., Esche E., Stünkel S., Brinkmann T., Wind J., Shishatskiy S., Wozny G., *Energy, Equipment and Cost Savings by Using a Membrane Unit in an Amine-Based Absorption Process for CO_2 Removal*, Chemie Ingenieur Technik, vol. 8, August 2013,1221-1227.

[16] Esche E., Müller D., Song S., Wozny G., *Optimization during the process synthesis: enabling the oxidative coupling of methane by minimizing the energy required for the carbon dioxide removal, Journal of Cleaner Production*, vol. 91, 2015,100-108.

[17] Esche E., *MINLP Optimization under Uncertainty of a Mini-plant for the Oxidative Coupling of Methane*, PhD Thesis, Technische Universität Berlin, 2015.

[18] Penteado A., Esche E., Wozny G., *Implementation of a Customized Gas-Separation Membrane Model into Commercial Flowsheeting Software to Simulate a Hybrid CO_2 Removal Process for Oxidative Coupling of Methane*, AIChE Annual Meeting 2015, Salt Lake City, US, 2015.

[19] Zhang Y., Chen C.-C., *Thermodynamic Modeling for CO_2 Absorption in Aqueous MDEA Solution with Electrolyte NRTL Model*, Ind. Eng. Chem. Res., vol. 1, 2011, 163-175.

[20] Ohlrogge K., Ebert K., *Membranen: Grundlagen, Verfahren und industrielle Anwendungen*, Weinheim, Germany: WILEY-VCH Verlag GmbH & Co. KGaA, 2006.

[21] Peng D.-Y., Robinson D.B., *A new two-constant equation of state*, Ind. Eng. Chem. Fundament., vol. 1, 1976, 59-64.

[22] Kuntsche S., Arellano-Garcia H., Wozny G., *MOSAIC, an environment for web-based modeling in the documentation level*, Computer Aided Chemical Engineering, vol. 29, 2011, 1140-1144.

[23] Wächter A., Biegler L.T., *On the implementation of an interior-point filter line search algorithm for large-scale nonlinear programming*, Math. Progr. Ser., 2005, 25-57.

[24] Godini H.R., Jašo S., Xiao S., Arellano-Garcia H., Omidkhah M., Wozny G., *Methane Oxidative Coupling: Synthesis of Membrane Reactor Networks*, Ind. Eng. Chem. Res., vol. 51(22), 2012, 7747-7761.

KAZIMIERZ RUP,[*] AGATA DRÓŻDŻ[**]

NUMERICAL MODELLING OF PULSE WAVE PROPAGATION IN THE HUMAN THORACIC AORTA

MODELOWANIE NUMERYCZNE PROPAGACJI FALI TĘTNA W PIERSIOWYM ODCINKU AORTY

A b s t r a c t

In this paper, a solution to the numerical simulation of blood flow in the human thoracic aorta is presented. *In vivo* measurements of pulsewave waveforms were performed and used as the initial condition for numerical calculations. Equations resulting from the analysis of the general mass and momentum balance for blood flow were used for the description of aortal haemodynamics. The system of differential equations has been solved with the method of characteristics, which is often used in hydrodynamic problems. Numerical simulations were employed for the cases of three people of differing ages. As a result, time-dependent profiles of blood pressure and velocity as well as deformation of the arterial wall were determined.

Keywords: blood flow; pulse wave propagation; haemodynamics

Streszczenie

W pracy dokonano numerycznej symulacji przepływu krwi w odcinku piersiowym aorty człowieka. Jako warunek początkowy w obliczeniach numerycznych wykorzystano wzięte z pomiarów *in vivo* przebiegi fali tętna. Równania wynikające z analizy bilansu masy i pędu dla przepływu krwi oraz równowagi dla materiału ścianki zostały użyte do opisu hemodynamiki krwi odcinka aorty. Układ równań różniczkowych rozwiązany został za pomocą metody charakterystyk. Przeprowadzono symulacje numeryczne dla przypadków trzech osób w różnym wieku. W wyniku przeprowadzonych obliczeń numerycznych wyznaczono zmienne w czasie profile prędkości i ciśnienia krwi oraz deformację ścianek odcinka aorty.

Słowa kluczowe: przepływ krwi, propagacja fali tętna; hemodynamika

[*] Prof. PhD. DSc. Eng. Kazimierz Rup, Institute of Thermal and Process Engineering, Faculty of Mechanical Engineering, Cracow University of Technology.

[**] MSc. Agata Dróżdż, Jagiellonian Centre for Experimental Therapeutics, Jagiellonian University.

1. Introduction

Blood flow in major arteries is caused mainly by cardiac function. The total energy of systole consists of the elastic potential energy required to deform the arterial walls, the kinetic energy of blood and the potential energy of position required to overcome the force of gravity [4].

In the case of heart and blood vessel haemodynamics, measurements of pressure changes and blood velocity are most commonly used and, recently, the results of numerical simulations and theoretical considerations have been also employed.

A description of many works on the numerical simulation of blood flow in the major arteries, assuming both rigid and resiliently deformable walls, is shown in [6]. The results of numerical calculation on the self-excited oscillation velocity and pressure in selected sections of the aorta, taking into account the local constriction, are shown in [8]. In [3] and [7], the flow of blood as a Newtonian fluid in the thoracic aorta has been analysed, assuming that the wall has the characteristics of linear elasticity. The known dependence of blood flow on time [3] or the corresponding pressure changes in time [7] have been used as the initial condition for numerical calculations.

The purpose of this article is to develop a non-linear, one-dimensional model of pulse wave propagation in the human thoracic section of the aorta. The model includes partial differential equations resulting from the balance of mass and momentum for the fluid area and the balance equation for the area of the vessel'swall. Pressure changes over time, measured *in vivo* using an applanation tonometer (SphygmoCor, AtCor Medical), were used as the initial condition in the calculations. In the performed numerical calculations, the average blood velocity during systole was taken into account. Based on the determined velocity fields and blood pressure, the elastic deformation of the thoracic aorta wall has also been determined.

2. Formulation of the problem

To describe the haemodynamics of the human thoracic aorta (Fig. 1a),methods known in the field of technical hydrodynamics have been used. Schematic diagrams of the considered flow are shown in Figures1a and 1b. The following assumptions have been taken into account:

- the blood vessel has the shape of a circular cylinder with varying cross-sectional area $S = S(s, t)$, constant wall thickness b, and constant length L;
- in a vessel filled with blood, the flow is unsteady and laminar under isothermal conditions;
- the vessel wall is undergoing substantial elastic deformation only in a radial direction;
- blood filling the vessel is a Newtonian fluid with a constant viscosity and a slight compressibility.

Including the above assumptions, the considered blood flow in the thoracic aorta is described by the following system of equations:

$$\frac{d\upsilon}{dt} + \frac{1}{\rho}\frac{\partial p}{\partial s} + g\frac{dz}{ds} + \frac{\lambda}{2D}\upsilon|\upsilon| = 0 \tag{1}$$

$$a^2 \frac{\partial v}{\partial s} + \frac{1}{\rho}\frac{dp}{ds} = 0 \tag{2}$$

where:

$$\frac{dv}{dt} = \frac{\partial v}{\partial t} + v\frac{\partial v}{\partial s} \tag{3}$$

$$\frac{dp}{dt} = \frac{\partial p}{\partial t} + p\frac{\partial p}{\partial s} \tag{4}$$

v is the velocity of blood, g is the gravitational acceleration, and λ is the friction coefficient.
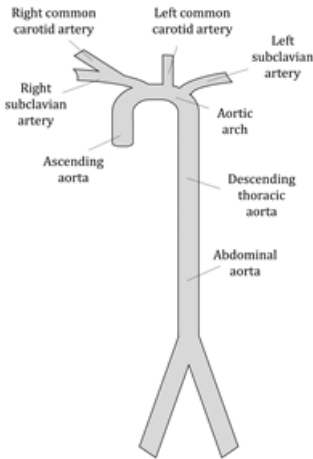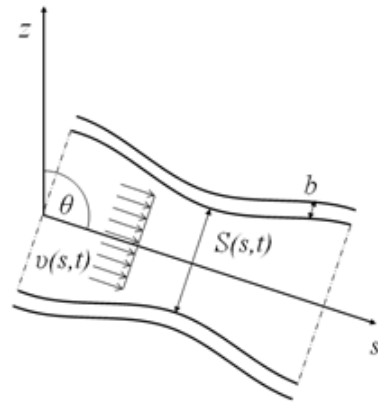

Fig. 1a. Human aorta   Fig. 1b. Coordinate system

Equations (1) and (2) result from the analysis of the general mass and momentum balance for blood flow in the considered region of the aorta. The equilibrium condition for the elastic vessel wall has also been included in the above equations. The velocity of the pressure wave (sound) propagation in blood within an elastic vessel (where ρ is blood density, κ is the modulus of volume elasticity, D is the vessel diameter, and b is the wall thickness) can be written as [5]:

$$a = \frac{\sqrt{\dfrac{\kappa}{\rho}}}{\sqrt{1 + \dfrac{\kappa}{E}\dfrac{D}{b}C}} \tag{5}$$

In Formula (5), there are the following values: modulus of circumferential elasticity E and parameter C, taking into account the wall thickness of the vessel. For a thick-walled vessel ($b/D > 1/40$), fixed at both ends, parameter C takes the form of [5]:

$$C = \frac{1}{1+\dfrac{b}{D}}[(1+\mu^2)+2\frac{b}{D}(1+\mu)(1+\frac{b}{D})]\qquad(6)$$

Where μ is the Poisson's ratio for the vessel wall material.

To solve the system of equations (1) and (2), taking into account relationships (3 ÷ 6), the method of characteristics is commonly used in hydrodynamics (Rup & Dróżdż, 2014; Larock, Jeppson & Watters, 1999). The main idea behind the method of characteristics is to replace the partial differential equations with an equivalent system of ordinary differential equations:

$$\frac{d\upsilon}{dt}+\frac{g}{a}\frac{dH}{dt}-\frac{g}{a}\upsilon\frac{dz}{ds}+\frac{\lambda}{2D}\upsilon\,|\,\upsilon\,|=0\qquad(7)$$

$$\frac{d\upsilon}{dt}-\frac{g}{a}\frac{dH}{dt}+\frac{g}{a}\upsilon\frac{dz}{ds}+\frac{\lambda}{2D}\upsilon\,|\,\upsilon\,|=0\qquad(8)$$

It should be noted that equation (7) is valid only for the C^+ characteristic, described by the relationship:

$$\frac{ds}{dt}=\upsilon+a\qquad(9)$$

In contrast, equation (8) is only valid along the C^- characteristic:

$$\frac{ds}{dt}=\upsilon-a\qquad(10)$$

Where H is the hydrostatic pressure of a blood column, described by the relationship:

$$p=\rho\cdot g\cdot(H-z)\qquad(11)$$

Initial and boundary conditions are based on the measurements performed *in vivo*. In particular, on measurements taken from three subjects of different ages. Using an applanation tonometer (SphygmoCor, AtCor Medical) with a piezoelectric transducer, three curves of the pressure wave in the aorta were obtained. The characteristics of the values obtained are summarised in Table 1.

T a b l e   1

Characteristic values of the pulse wave

Age (years)	Cardiac period (s)	Number of points[a]	Maximal pressure (mmHg)	Minimal pressure (mmHg)
27	0.998	186	108.3	75.9
40	0.841	216	132.2	86.8
70	0.892	64	138.5	86.1

[a] Readout in discrete form

For the purposes of numerical calculations, pressure changes were converted according to Equation (11), obtaining in the vessel inlet section:

$$H_{P_1}(t) = \frac{p(t)}{\rho \cdot g} \tag{12}$$

In order to perform numerical integration of Equations (7) and (8) with the initial and boundary conditions listed above, numerical code in FORTRAN was designed and made compatible with the method of characteristics. The measured waveform of the pressure $p(t)$ was interpolated using the spline function [7] in the calculation process.

3. Analysis of the obtained results

The numerical computations take into account the following values of parameters describing the physical properties of blood and the thoracic aorta wall at $T = 37°C$. These parameters are taken from Reference [2]:

1. Characteristics of blood
   Dynamic viscosity $\eta = v \cdot \rho = 0.0035$ N·s·m^{-2}
   Density $\rho = 1060$ kg·m^{-3}
   Bulk modulus $\kappa = 2.15 \cdot 10^9$ Pa
2. Characteristics of the aortic wall
   Internal diameter $D = 20$ mm
   Wall thickness $b = 1.2$ mm
   Length $L = 160$ mm
   Poisson's ratio $\mu = 0.5$

The values of the circumferential modulus of elasticity and pulse wave velocity equation (5) with regard to the age of the person are shown in Table 2. The table also contains parameter C calculated in accordance with Formula (6) and the corresponding value of time step.

Table 2

Morphometric properties of systemic circulation in human subjects

Age (years)	E [2] (Pa)	C	a (m/s)	Δt (ms)
27	$5.5 \cdot 10^5$	0.8875	5.92	0.92
40	$7.0 \cdot 10^5$	0.8875	6.68	0.83
70	$14.5 \cdot 10^5$	0.8875	9.61	0.57

The calculations take into account that the average velocity of blood in the aorta is considered to be v_0; additionally, it is assumed that the vessel is in a vertical orientation. A section of the considered aorta was divided into twenty-nine segments with a length $\Delta s = 5.52$ mm in the calculation process.

Selected results obtained from numerical calculations during the 50th cardiac cycle from the start of the simulation, are shown in the graphs (Figures 2 ÷ 5).
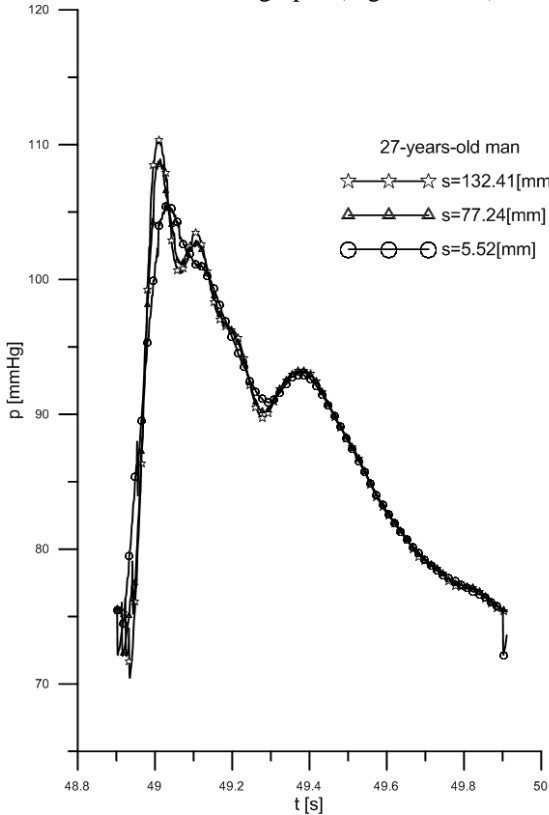
Fig. 2. Simulation of the pressure waveforms in the 27-year-old subject

Figure 2 shows three curves of the pressure wave in a selected cross-section of the 27-year old man's thoracic aorta. These cross-sections are described by the values of the s coordinate measured along its axis. Curves of the pulse wave at the beginning of segment 2, that is at a distance $s = 5.52$ mm from the initial cross-section, are marked with circles in Figure2.

As presented in Figure 2, the pressure wave curves illustrate an increase in the maximal pressure of flowing blood with increasing distance from the initial cross-section of the aorta segment. Thus, in the case of the pressure wave in the cross-section that is a distance of $s = 132.4$ mm from the inlet and marked with stars, the corresponding value of the maximum pressure is $p = 110.4$ mmHg. This increase in the maximum pressure is noted particularly in the initial part of each of the 50 cardiac cycles.

Figure 3a shows blood velocity changes calculated for 50th cardiac cycle in the same cross-sectionsas above. The maximum blood velocities in the vessel cross-sections are:
$\circ - \upsilon_{max}(s = 5.52$ mm$) = 0.660$ m/s, $\quad \Delta - \upsilon_{max}(s = 77.24$ mm$)\ 0.522$ m/s, $\quad * - \upsilon_{max}(s = 132.41$ mm$) = 0.368$ m/s.

The corresponding, real blood velocity waveform in the 27-year-old subject's aorta cross-section, measured by the Doppler ultrasound method, is shown in Figure 3b.
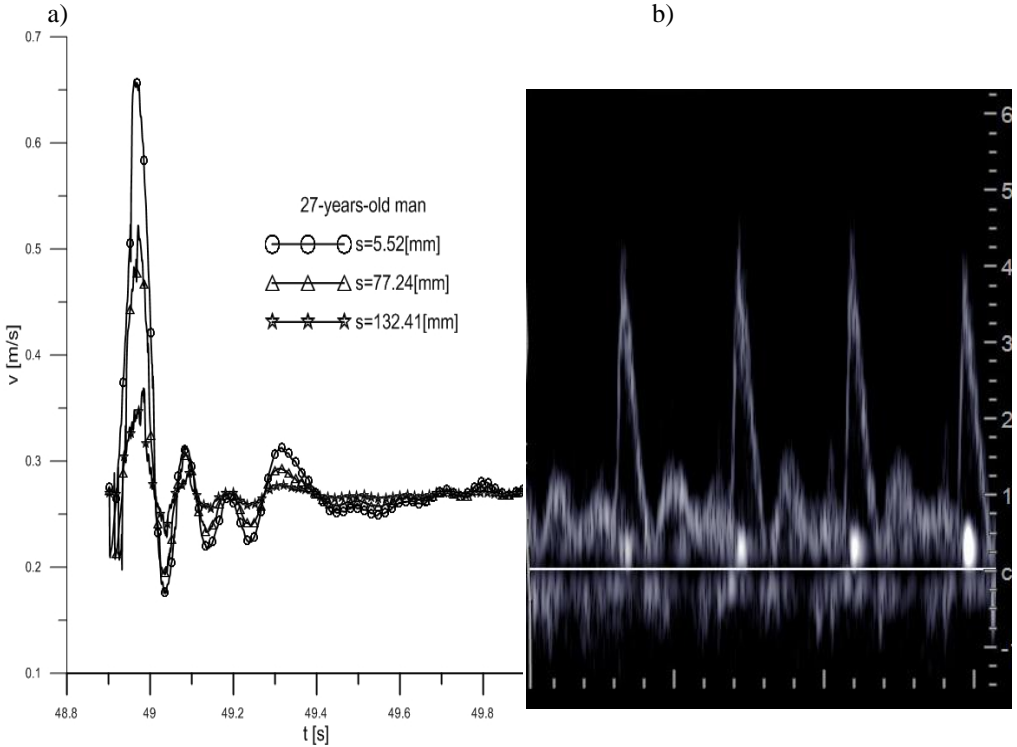
Fig. 3a, b. Simulated and measured blood velocity waveforms

Corresponding changes of blood velocity for people aged 40 are shown in Figure 4. Velocity changes over time in the particular sections of the aorta are characterised by decreasing extreme values with increases in the person's age.

It should be noted that the areas of blood velocity disorders extend over a greater length of the aorta in the elderly.

On the basis of the blood pressure and velocity changes in the thoracic aorta, relative elastic deformation of the vessel wall was determined. Taking into account the influence of a pulsatile blood flow on the elastic vessel wall, the following relationship was introduced:

$$\frac{\delta D}{D}(s,t) = \frac{D}{2b} \cdot \frac{C}{E} \left[p(s,t) - \rho \cdot a(\upsilon(s,t) - \upsilon_0) \cdot (1 + \upsilon(s,t)/a) \right] \tag{13}$$

The variables used in equation (13) have been previously described in the text. The relative elastic deformation of the aorta wall according to equation (13) is shown in Fig. 5.
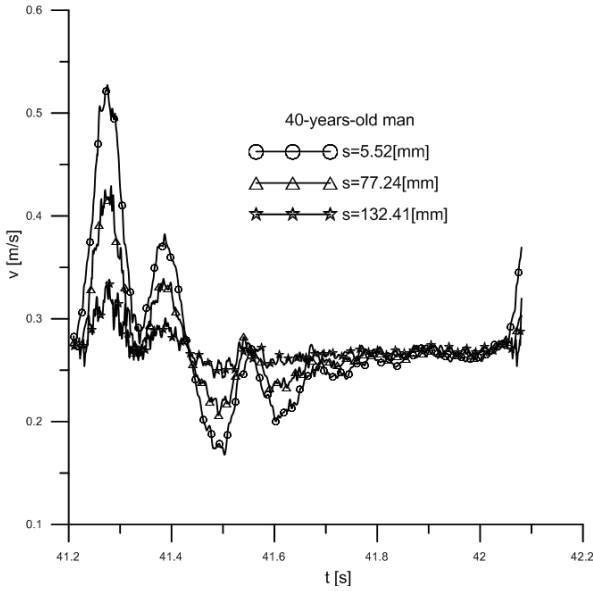
Fig. 4. Simulated velocity waveforms in the 40-year-old subject
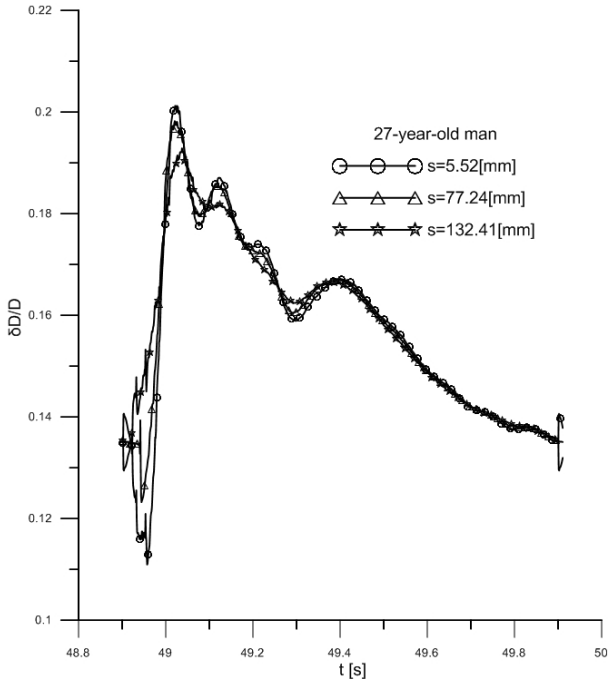
Fig. 5. Simulated relative deformation in the 27-year-old subject

Extreme values of the relative deformation of the vessel wall are observed in Figure 5 in the initial part of each of the fifty cardiac cycles. In the case of the younger age groups, in which blood vesselshave greater elasticity ($E = 5.5 \cdot 10^5$ Pa), local relative deformation reaches an extreme value of $\delta D / D (s = 5.52$ mm, $t = 49.0308$ s$) = 0.200$.

4. Final remarks and conclusions

This paper is an attempt to develop a non-linear, one-dimensional model of blood flow in the human thoracic aorta. The developed model includes measurements of the blood pressure changes performed *in vivo*. Furthermore, in the considered model,pulsatile blood flow caused by elastic deformations of the vessel wall is included.

The model includes partial differential equations resulting from the mass and momentum balance recorded for blood flow and the power balance condition for the area of the vessel wall.

The method of characteristics was used for integration of the equations. The analysis obtained from numerical calculations is limited to fifty cardiac cycles. It is worth noting that in each of the fifty cardiac cycles, as the initial condition for pressure, pulse waveforms measured by an applanation tonometer were used.

The analysis shows a high degree of result stability obtained throughout the whole considered temporal and spatial area.

The numerical results describing the velocity and pressure of blood flow are characterised by high intensity of changes at the beginning of each cardiac cycle. These changes are manifested by a build-up of their peak values with increasing distance of the segment from the initial section of the vessel. The relative increase in peak blood pressure is 4.5% at $s = 132.4$ mm from the inlet section for a 27-year-old person. In the case of results obtained for the blood velocity, the intensity of changes is more intense in the initial part of the considered part of the aorta – the relative maximum velocity increase is 144% for this person.

Elastic deformations of the considered vessel section are associated with the propagation of the pressure wave. Changes in blood velocity are, in turn, coupled to pressure changes. Consequently, the relative intensity of the elastic deformation of the wall is similar to changes in blood velocity. The elastic deformation of the wall takes extreme values in the initial part of the vessel and in the initial phase of systole. The maximum relative strain is about 0.200 in the 27-year-old person.

The numerical results for the velocity, blood pressure and deformation of the vessel wall obtained for 40- and 70-year-old subjects are characterised by lower intensity of changes, as compared with the corresponding results for a younger person.

R e f e r e n c e s

[1] Bergant A., Simpson A.R., Vitkovsky J., *Developments in unsteady pipe flow friction modelling*, Journal of Hydraulic Research, vol. 39(3), 2001, 249-257.

[2] Black J., Hastings G., *Handbook of Biomaterial Properties*, Springer Science & Business Media1998.

[3] Filipovic N., Mijailovic S., Tsuda A., Kojic M., *An implicit algorithm within the arbitrary Lagrangian-Eulerian formulation for solving incompressible fluid flow with large boundary motions*, Computer methods in applied mechanics and engineering, vol. 195(44), 2006, 6347-6361.

[4] Konturek S., *Human physiology cardiovascular system*, vol. II, Jagiellonian University, Krakow 2001.

[5] Larock B.E., Jeppson R.W., Watters G.Z., *Hydraulics of Pipeline Systems*, CRC Press, 1999.

[6] Liu Y., Lai Y., Nagaraj A., Kane B., Hamilton A., Greene R., McPherson D.D., Chandran K.B., *Pulsatile flow simulation in arterial vascular segments with intravascular ultrasound images*, Medical Engineering & Physics, vol. 23(8), 2001, 583-595.

[7] Rup K, Dróżdż A. *Numerical modelling of the pulse wave propagation in large blood vessels based on liquid and wall interaction*, Journal of Physics: Conference Series 530, 2014, 012010.

[8] Tang D., Yang J., Yang C., Ku D.N., *A nonlinear axisymmetric model with fluid-wall interactions for steady viscous flow in stenotic elastic tubes*, Journal of Biomechanical Engineering, vol. 121(5), 1999, 494-501.

[9] Tiselj I., Gale J., *Integration of unsteady friction models in pipe flow simulations*, Journal of Hydraulic Hydraulic Research, vol. 46(4), 2008, 526-535.

AZIS BOING SITANGGANG[*], ANJA DREWS[**], MATTHIAS KRAUME[***]

AUTOMATED MEMBRANE REACTORS FOR THE EARLY PROCESS DEVELOPMENT OF ENZYME PROMOTED BIOCONVERSION

ZAUTOMATYZOWANE REAKTORY MEMBRANOWE DLA PROCESU WCZESNEGO ROZWOJU ENZYMU WSPOMAGANEGO BIOKONWERSJĄ

Abstract

In general, there is always a trade-off between the information output and the process throughput. The automation of micro- to small-scale bioreactors is considered necessary as this can facilitate a straightforward bioprocess development to reach its commercial success. A small-scale, dead-end enzymatic membrane reactor system has been realised. Reactor system was tested for the continuous transgalactosylation of lactulose using commercial β-galactosidase.

Keywords: enzymatic membrane reactor, bioprocess, transgalactosylation, enzyme

Streszczenie

Zawsze mamy do czynienia z kompromisem pomiędzy informacją wyjściową a przepustowością procesu. Jeżeli skala maleje, dostępne jest mniej informacji z powodu zmniejszonego monitorowania i kontroli. Automatyzacja mikro- do mini- bioreaktorów jest konieczna aby osiągnąć sukces komercyjny. Zbudowano reaktor membranowy w skali mini, w którym badano ciągłą transgalaktozylację laktulozy z użyciem komercyjnej beta-galaktozydazy.

Słowa kluczowe: enzymatyczny reaktor membranowy, proces biologiczny, transgalaktozyla-cja, enzym

[*] MSc. Azis Boing Sitanggang, Chair of Chemical & Process Engineering, Faculty of Process Sciences, Technical University of Berlin and Bogor Agricultural University, Indonesia.

[**] Prof. PhD. DSc. Eng. Anja Drews, Hochschule für Technik und Wirtschaft Berlin.

[***] Prof. PhD. DSc. Eng. Matthias Kraume, Chair of Chemical & Process Engineering, Faculty of Process Sciences, Technical University of Berlin.

1. Introduction

Small-scale reactors are generally used to reduce the amount of reactants, samples and biocatalysts. It is worth mentioning that small reactors possess a number of benefits in terms of reaction performances, as high surface area to volume ratios allow the chemical reactions to be more rapid [1]. However, according to Betts and Baganz [2], there is a trade-off between the information output and the experimental throughput at different reactor sizes during enzyme-promoted bioconversions. As the size of the reactor gets smaller, less information is available due to reduced monitoring and control. Therefore, automated micro- to small-scale reactor is of importance as this can facilitate a straightforward bioprocess development to reach its commercial success. This study aimed to establish a small-scale enzymatic membrane reactor (EMR) system which is also able to generate more information output. Several industrially relevant parameters, such as continuous substrate dosing with a constant flow rate (flux), online pH and temperature evaluation, and the control of enzyme activity could be performed. The reactor system was intended for bioprocess characterisations of enzyme-promoted bioconversions where continuous long-term operation (> 100 h) and product separations can be realized. To show the applicability of this developed reactor, a long-term continuous synthesis of lactulose using commercial *A. oryzae* β-galactosidase in the presence of lactose and fructose was performed at a maintained enzyme activity.

2. Materials and methods

2.1. Experimental rig

Two parallel reactors were built in an enzymatic membrane reactor (EMR) system [3, 4]. Each reactor consisted of a pressure-stable glass container and a body (holder) which was modified from the XFUF-047 dead-end stirred cell produced by Merck Millipore Darmstadt, Germany. The maximum working volume of the reactor was 90 mL. The reactor was equipped with a pressure-stable pH electrode produced by ProSense BV, The Netherlands. For the permeate measurement, a Kern EW 620-3NM precision balance was used (Kern & Sohn GmbH, Germany). In addition, a proportional pressure regulator (PPR) MPPE with a precision of ± 20 mbar from Festo AG & Co. KG, Germany was installed. For the realisation of the enzyme dosing, micro-solenoid valves from ASCO Numatics GmbH, Germany were used. A *normally closed* (2/2 NC) valve was used to control the flow of the enzyme into the reactor, whereas a *normally open* (2/2 NO) valve was installed for the substrate feed. The used membranes (diameter = 47 mm, surface area = $12.38 \cdot 10^{-4}$ m^2) were polyethersulfone (PES) with molecular weight cut-off (MWCO) of 5, 10 and 20 kDa (Microdyn-Nadir GmbH, Germany), polysulphone (UFX10), cellulose acetate (RC70PP) with a MWCO of 10 kDa (Alfa Laval Mid Europe GmbH, Germany). A constant flux operation (thus providing a constant hydraulic residence time HRT) and the maintenance of enzyme activity (through the addition of "fresh" enzymes) were realised by a proportional-integral-derivative (PID) controller, developed by using Laboratory Virtual Instrument Engineering Workbench (LabVIEW) software [5].
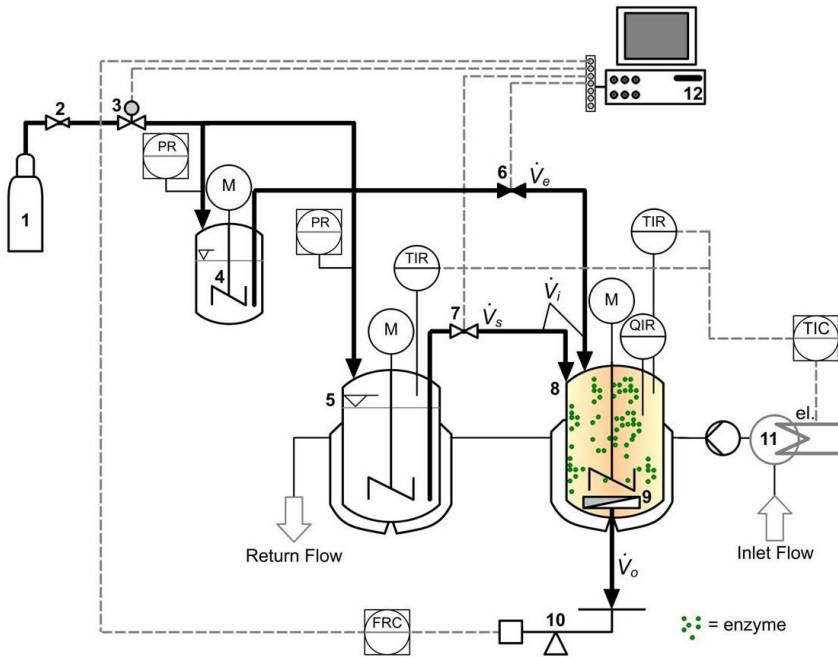
Fig. 1. Process flowsheet of a single reactor in the EMR system with an automatic procedure of enzyme dosing: (1) N$_2$ bottle, (2) pressure reducer, (3) PPR, (4) enzyme tank, (5) substrate tank, (6) 2/2 NC valve, (7) 2/2 NO valve, (8) reactor, (9) flat-sheet UF membrane, (10) precision balance, (11) heating system, (12) PC. Q = quality parameter, pH [5].

2.2. Chemicals

The enzyme β-galactosidase from *Aspergillus oryzae* (G5160), acetonitrile (271004), lactulose (61360), D-fructose (F0127), lactose (17814), 2-nitrophenyl β-D-galactopyranoside (ONPG, 73660) and 2-nitrophenol (ONP, 19702) were purchased from Sigma-Aldrich, Germany.

2.3. Continuous synthesis of lactulose

Lactose and fructose were used as substrates for lactulose synthesis using a commercial *A. oryzae* β-galactosidase. The total sugar concentration C_s was 500 g/L, with a molar ratio of lactose to fructose m_L/m_F = 1/8 or 1/4, dissolved in 150 mM phosphate-citrate buffer pH 4.5 and with an enzyme concentration $[E]$ = 3 or 10 U/mL. The continuous synthesis was performed at 40°C and agitated at 350 rpm. A long-term operation was carried out by dosing the "fresh" enzymes.

2.4. Enzyme activity determination and analytical method

A. oryzae β-galactosidase activity was determined according to Sigma–Aldrich enzymatic assay of β-galactosidase using ONPG as the substrate. One unit of enzyme activity is defined as the amount of enzyme required for hydrolysing 1 μmol ONPG to ONP and D-galactose per minute at pH 4.5 and 30°C [5]. Lactose and lactulose were analysed by means of HPLC [6].

3. Results and discussion

3.1. Constant flux operation and enzyme dosing

As shown in Fig. 2a, two types of PID controller (with normal and fast setting according to Kuhn [7]) were used to control the flux (e.g., process variable of flux J_{PV}) during the filtration of ultrapure water at a set point of flux $J_{SP} = 25$ L/(m²h). The PID controller with a fast setting had a smaller over-shoot response (Fig. 2a). Therefore, the control error ($error = (|J_{SP} - J_{PV}|/J_{SP})\cdot 100\%$) of fast setting PID controller was smaller than that of normal one. To have a more stable J_{PV}, the influence of the number of averaged points in the filter of moving average n was investigated for the fast setting PID controller. As can be seen in Fig. 2b, a higher value of n led to a poorly reactive response. Within this study, $n = 50$ points was selected to filter the flux data points.
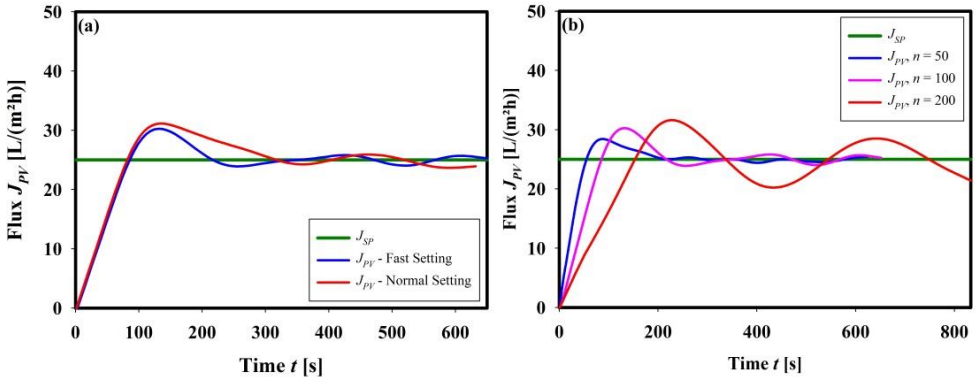
Fig. 2. (a) Testing PID controllers – normal setting *vs*. fast setting during ultrapure water filtration with $n = 100$ data points and (b) The influence of number of data points being averaged n on the stability of J_{PV} with the PID controller of fast setting: $J_{SP} = 25$ L/(m²h), PES membrane with MWCO 5 kDa, agitation = 350 rpm, $T = 40^{\circ}$C.

To maintain the enzyme activity during a long-term operation, an open-loop control (i.e., due to off-line product analysis) with automatic procedure of enzyme addition was also established. To have a constant flux operation during the enzyme dosing, the enzyme valve (2/2 NC) is opened whereas the substrate valve (2/2 NO) is closed [5]. Through the opening, the enzyme tank still experiences the same pressure as the substrate tank since the N_2 inlet gas for the substrate and enzyme tank are connected with a T-pipe joint (see

Fig. 1). The dosing accuracy was evaluated by using ultrapure water to replace both the enzyme and the substrate solution with the set dosing volume V_{sD} in the range of 0.5-10 mL. During the dosing, the enzyme tank was placed on the balance. The reduced weight of the enzyme tank should be due to some amount of ultrapure water pumped (or dosed) into the reactor (actual dosing volume V_{aD}). As shown in Fig. 3, the average inaccuracy of the developed dosing system was less than 2%.
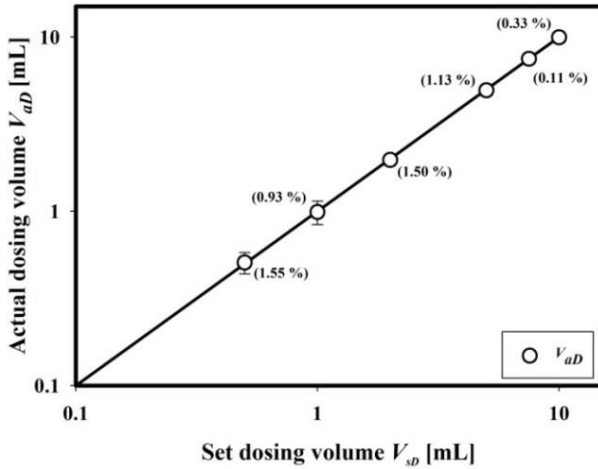
Fig. 3. Evaluation of dosing accuracy in the developed EMR with the averaged errors in parentheses

3.2. Continuous synthesis of lactulose

3.2.1. Membrane selection

The suited membrane was selected from three membrane types, PES (10, 20 kDa), UFX10 (10 kDa) and RC70PP (10 kDa). As can be seen in Fig. 4(a), lactulose concentrations between PES 10 and 20 kDa were almost identical. It indicates that by a higher membrane MWCO for PES membrane, the enzyme permeation did not occur. There was a slight difference between lactulose concentrations for those three membranes where the PES membrane clearly prevailed. However, the transmembrane pressure ΔP increased rapidly for both cut-offs of the PES membrane as reflected by their higher fouling rates. Although, the smallest fouling rate was found for the RC70PP membrane, its initial ΔP was the highest one compared to the other membranes (870 mbar). Hence, the UFX10 membrane was selected for further study as it had the smallest initial ΔP (257 mbar) with a compromised fouling rate.
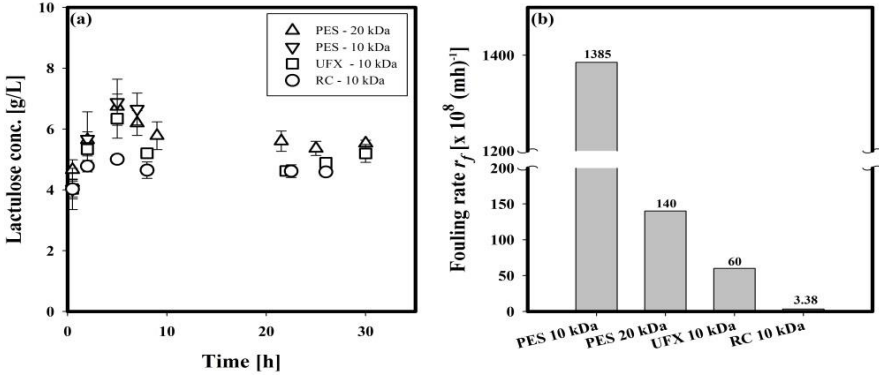
Fig. 4. (a) Lactulose concentrations of different membrane types and (b) fouling rates r_f of different membranes used for continuous lactulose synthesis using *A. oryzae* β-galactosidase in an EMR system with conditions: $C_S = 500$ g/L, $m_L/m_F = 1/8$, $[E] = 3$ U/mL, $HRT = 7$ hour, 150 mM citrate-phosphate buffer pH 4.6, agitation = 350 rpm, $T = 40°C$. Fouling rate was calculated as

$$r_f = \frac{\Delta P}{\Delta t} \cdot \frac{1}{\eta_{(T)} \times J} \quad \text{with } \eta_{(T)} = 0.0393 \text{ Pa·s}$$
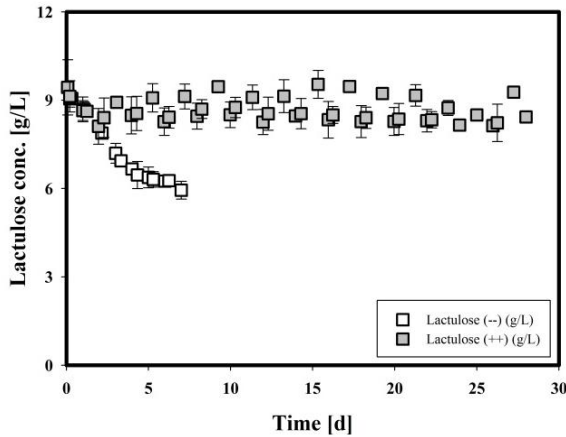
Fig. 5. Long-term continuous synthesis of lactulose by maintaining *A. oryzae* β-galactosidase activity in the EMR system (enzyme dosing: 10% of initial enzyme amount per 48 hours); (--) experiment without enzyme addition and (++) with enzyme addition. Both experiments were carried out with the same operating conditions: $C_S = 500$ g/L, $m_L/m_F = 1/4$, $[E] = 10$ U/mL, $HRT = 9$ hours, 150 mM citrate-phosphate buffer pH 4.6, agitation = 350 rpm, $T = 40°C$, UFX membrane MWCO = 10 kDa.

3.2.2. Long-term operation of continuous lactulose synthesis

In Fig. 5, a prolonged reaction was carried out for one week without the addition of enzymes into the reactor. At 48 hours, 100 hours and 168 hours, the reductions of lactulose concentration were about 10%, 28.7% and 34.4%, respectively. In our previous study [6], using *K. lactis* β-galactosidase, after 168 hours of reaction, lactulose concentration was reduced by 31 %. Mayer et al. [8] also reported the production of lactulose in an EMR using free β-glycosidase from *P. furiosus* (CelB*). The lactulose concentration decreased to almost zero after 96 hours. Another prolonged reaction was carried out with the addition of enzymes as much as 10% of the initial enzyme amount every 48 hours. Herein, a lactulose outlet concentration of 8.67 g/L could be kept constant for 28 days (with the number of enzyme additions was 13 times (see Fig. 3)).
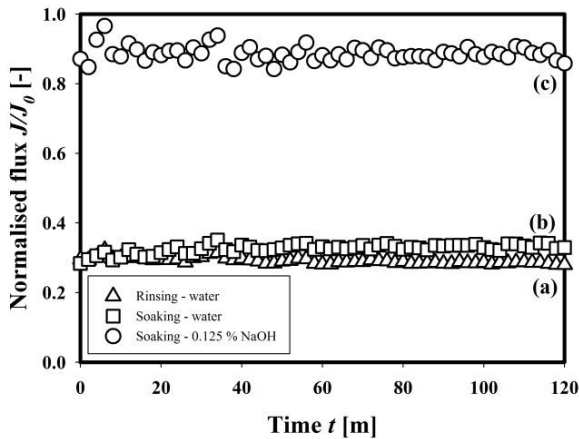
Fig. 6. The efficiencies of serial cleaning for the UFX membranes used in a long-term continuous synthesis of lactulose (see Fig. 5 for operating conditions).

The effectiveness of physical and chemical cleaning were also investigated for the used UFX membranes in the long-term operation of continuous lactulose synthesis (Fig. 5). The cleaning was done successively from rinsing → soaking (with water) → chemical soaking (0.125% NaOH). In Fig 6, through rinsing, the recovered flux was only 29.14%. Moreover, by soaking the membranes overnight in ultrapure water was not efficient as the recovered flux was only enhanced by 3% from the previous cleaning. Through overnight chemical soaking, the recovered flux was about 88.57%.

4. Conclusions

An automated small-scale EMR system was realised. Both constant flux operation (thus HRT) and maintenance of the enzyme activity could be performed (with a control error of less than 2%) besides online temperature and pH monitoring. Through the long-term

continuous synthesis of lactulose with a maintained enzyme activity, the applicability of the developed reactor was proven. Conclusively, the automated membrane reactor is claimed to be a useful bioreactor for studying the engineering aspects of enzyme-promoted bioconversions at lab-scale.

R e f e r e n c e s

[1] Jensen K.F., *Microreaction engineering – is small better?*, Chemical Engineering Science, vol. 56(2), 2001, 293-303.

[2] Betts J., Baganz F., *Miniature bioreactors: Current practices and future opportunities*, Microbial Cell Factories, vol. 5(21), 2006, 1-14.

[3] Sitanggang A.B., Drews A., Kraume M., *Rapid transgalactosylation towards lactulose synthesis in a small-scale enzymatic membrane reactor* (*EMR*), Chemical Engineering Transactions, 38, 2014, 19-24

[4] Sitanggang A.B., Drews A., Kraume M., *Continuous synthesis of lactulose in an enzymatic membrane reactor reduces lactulose secondary hydrolysis*, Bioresource Technology, vol. 167, 2014, 108-115.

[5] Sitanggang A.B., Drews A., Kraume M., *Development of a continuous membrane reactor process for enzyme-catalyzed lactulose synthesis*, Biochemical Engineering Journal, vol. 109, 2016, 65-80.

[6] Sitanggang A.B., Drews A., Kraume M., *Influences of operating conditions on continuous lactulose synthesis in an enzymatic membrane reactor system: A basis prior to long-term operation*, Journal of Biotechnology, vol. 203, 2015, 89-96.

[7] Kuhn U., *Eine praxisnahe Einstellregel fur PID-Regler*: *Die T-Summen-Regel*, Automatisierungstechnische Praxis, vol. 5, 1995, 10- 16.

[8] Mayer J., Kranz B., Fischer L., *Continuous production of lactulose by immobilised thermostable β-glycosidase from Pyrococcus furiosus*, Journal of Biotechnology, vol. 145, 2010, 387- 393.

JOLANTA STACHARSKA-TARGOSZ, KONRAD NERING[*]

ANALYSIS OF PRESSURE LOSSES IN THE CROSS FLOW FAN HEAT EXCHANGER AT VARIOUS THERMAL AND FLOW CONDITIONS

ANALIZA STRAT CIŚNIENIA W WENTYLATOROWYM WYMIENNIKU CIEPŁA DLA RÓŻNYCH WARUNKÓW CIEPLNYCH I PRZEPŁYWOWYCH

Abstract

In this paper the analysis of performance characteristics of a cross flow fan working as an element of the unit incorporating heat exchanger as well as performance characteristics of the unit are presented. These experimental results were basic for consideration of pressure losses arising as an effect of direct connection of a cross flow fan and a heat exchanger located in the charging zone of the fan as a resistance. Analysis of an influence of rotational speed variation as well as a medium temperature on aerodynamic characteristics of heat exchanger let to propose a method for the local pressure loss estimation.

Keywords: cross flow fan heat exchanger, performance characteristics, local pressure losses

Streszczenie

W artykule przedstawiono analizę charakterystyk pracy wentylatora poprzecznego jako elementu układu z wymiennikiem ciepła oraz charakterystyk układu. Wyniki eksperymentalne stanowiły podstawę do przeprowadzenia analizy strat ciśnienia spowodowanych bezpośrednim połączeniem wentylatora poprzecznego z wymiennikiem ciepła umieszczonym w jego strefie tłoczenia. W wyniku analizy wpływu zmiany prędkości obrotów wirnika wentylatora jak i temperatury medium w wymienniku ciepła na charakterystyki aerodynamiczne wymiennika, zaproponowano metodę oceny lokalnej straty ciśnienia.

Słowa kluczowe: wentylatorowy wymiennik ciepła, charakterystyki pracy, lokalne straty ciśnienia

[*] Prof. PhD. DSc. Eng. Jolanta Stacharska-Targosz, DSc. Eng. Konrad Nering, Institute of Thermal and Process Engineering, Faculty of Mechanical Engineering, Cracow University of Technology.

1. Introduction

Cross flow fan cooperation with a heat exchanger seems to be more useful solution than the use of axial or radial fans due to the relatively low noise and a uniform velocity distribution at its inlet and outlet cross sections. The dimension of rectangular inlet or outlet cross section of the fan is adapted to rectangular inlet cross section of the heat exchanger reducing the local pressure losses. Fig. 1 shows an example of direct connection of both elements of the unit, where the cross flow fan (1) is directly connected to the heat exchanger (2) mounted at the fan suction zone [1].
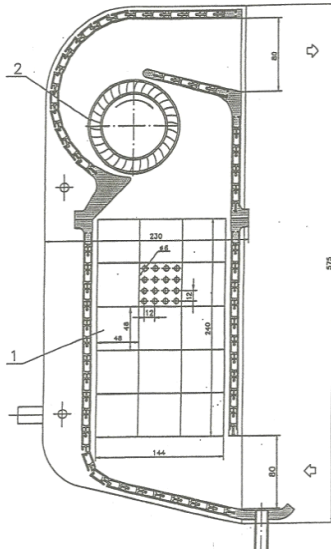
Fig. 1. Cross flow fan heat exchanger

Cross flow fan heat exchanger as the air curtain or as an element of air conditioning system forming perpendicular laminar air stream is applied for example in hospital operating rooms for separating the places which require special conditions of clean air free from microorganisms.

Lengthening of the impeller (limited by strength of material) gives a possibility to increase the volumetric flow rate and adapt to the requirements of particular application. Its rectangular cross sections in the suction and discharging zones enabling the direct connection with the heat exchanger are an advantage in local losses reducing.

Among whole literature one can find only a few studies taking into account a heat exchanger application in the air conditioning unit. An effect of heat exchanger as a suction resistance on internal flow in a room air conditioner was investigated and presented in [2]. The total pressure was stable inside the both suction and discharging zones when the cross flow fan worked without a heat exchanger. The size and magnitude of vortex depended on the setting of heat exchanger as an element of the unit which created the turbulence. In [3] the authors considered three different casing designs of a unit containing the same cross flow fan and heat exchanger indicating an influence of the design of a cross flow fan

parameters on the air conditioning unit performance. The study has been carried out numerically and experimentally for the heat exchanger located at the suction zone of the cross flow fan.

2. Some experimental results of cross flow fan heat exchanger investigations

As mentioned above a heat exchanger usually is mounted at the suction zone of the cross flow fan. Experiments carried out for the cross flow fan model (L/D = 180/60) with throttling at inlet and outlet cross section indicated higher values of the dimensionless pressure coefficient and efficiency for the case of throttling realized at the discharging zone [4].

The aim of investigations presented in this paper is an evaluation of local loss aroused on connection of the cross flow fan WPU 450/100 constructed at the Cracow University of Technology and the mass-produced heat exchanger GP6/7 forming together a unit. The quantitative estimation of the flow structure effect was based on the analysis of aerodynamics and efficiency curves obtained for different flow and thermal conditions comparing the performances made for a cross flow fan operating separately and as an element of the unit with the built-in heat exchanger. Some selected experimental results showing the influence of the rotational speed on the unit performances were presented in [5]. An increase of the rotational speed from $n = 5$ 1/s to $n = 20$ 1/s caused the increase of dimensionless static and total coefficients of the unit about 97 % for $\psi_s{}''$ and 58% for $\psi_t{}''$ as well as efficiency which reached $\eta_t{}'' = 40$ % for the flow coefficient $\varphi = 0.85$.

In Fig. 2 the scheme of measurements of the static pressure (p_1, p_2, p_3) averaged at the cross sections (A_1, A_2, A_3) is shown.

$$A_1 = 0.07440 \text{ m}^2$$
$$A_2 = 0.04465 \text{ m}^2$$
$$A_3 = 0.05390 \text{ m}^2$$
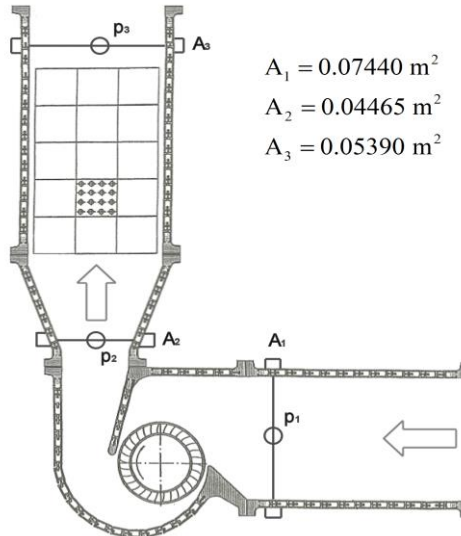
Fig. 2. Scheme of static pressure measurements for a unit: the cross flow fan – the heat exchanger

Relation between the total pressure coefficient and the flow coefficient in the form of curves: $\psi_t = f(\varphi)$ - for the cross flow fan working separately, it means that the air is discharged straight to the atmosphere so static pressure at the outlet is assumed to be zero – and $\psi_t^* = f(\varphi)$ as an element of a unit containing a heat exchanger, measured at the two rotational speeds: $n = 15$ s^{-1} and $n = 20$ s^{-1} – are shown in Fig. 3.
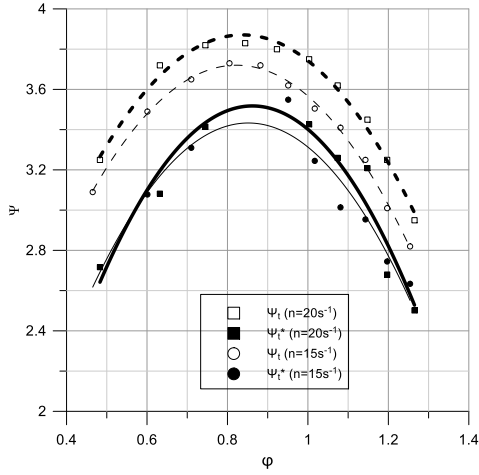
Fig. 3. Changes of the total pressure coefficient for the cross flow fan working separately ψ_t and as an element of a unit ψ_t^* at different rotational speeds: $n = 20$ s^{-1} and $n = 15$ s^{-1}
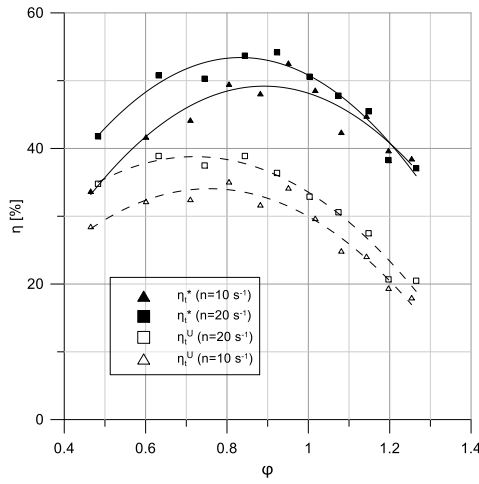
Fig. 4. Total efficiency vs. flow coefficient at rotational speed $n = 20$ s^{-1} and $n = 10$ s^{-1}

The experimental results have confirmed two expected phenomena: one that the higher values of the total pressure coefficient were obtained at higher rotational speed and the second that the lower values of the total pressure coefficient were obtained for the cross

flow fan working as an element of a unit ψ_t^* for both rotational speeds. The difference of the total pressure coefficient varying in the range between 8% and 10% should be treated as the consequence of the heat exchanger resistance.

Total efficiency of the cross flow fan working as an element of a unit η^* and efficiency of the unit η^u (dotted lines) in function of the flow coefficient for two rotational speeds: $n = 20 \text{ s}^{-1}$ and $n = 10 \text{ s}^{-1}$ is shown in Fig.4. Reduction of total efficiency of the unit in comparison with efficiency of the cross flow fan in unit from 7% to 18% may be treated as a heat exchanger "negative efficiency" located at the outlet part of the cross flow fan in considered range of φ.

Curves of dynamic pressure obtained for varied volumetric flow rate $\dot{V}$ at three rotational speeds: $n = 10 \text{ s}^{-1}$, 15 s^{-1} and 20 s^{-1} for the cross flow fan working as the element of a unit p_d^* and for the unit p_d^u are presented in Fig. 5.
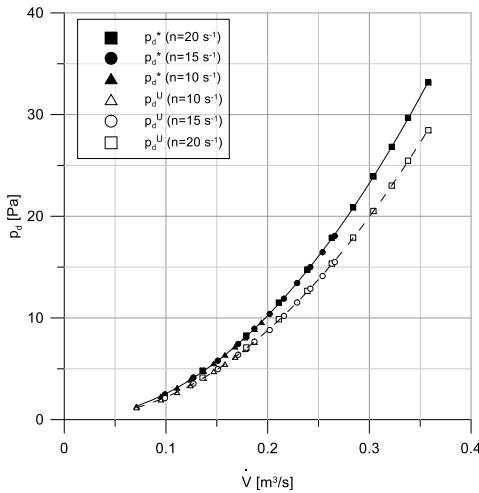
Fig. 5. Dynamic pressure versus volumetric flow rate for different rotational speeds

These results can be approximated by following functions, respectively:

$$p_d^* = 266.80 \cdot \dot{V}^2 - 3.28 \cdot \dot{V} + 0.22 \tag{1}$$

$$p_d^u = 230.39 \cdot \dot{V}^2 - 3.49 \cdot \dot{V} + 0.26 \tag{2}$$

and using them gives a possibility to estimate a total pressure rise Δp_t for the arbitrary value of Δp_s,

$$\Delta p_t^* = \Delta p_s^* + p_d^* \quad \text{and} \quad \Delta p_t^u = \Delta p_s^u + p_d^u \tag{3}$$

independently of the rotational speed of the cross flow fan impeller in determined range of the volumetric flow rate.

3. A quantitative effect of the heat exchanger as a discharge resistance

The heat exchanger has been mounted at the outlet part of the cross flow fan and connected with it by a short rectangular duct used to adapt the cross sections of these two elements. Measurements of pressure allow estimating the difference in values of static and total pressure for each element and for the whole unit. Some selected results are presented in the form of characteristics indicating the influence of the heat exchanger as a discharge resistance in the air flow as well as an effect of variable temperature of medium flowing inside the heat exchanger pipes on aerodynamic performances. Some selected experimental results of measurements presented in [6] have been used for the considerations and calculations in this part of publication.

3.1. An influence of impeller rotational speed on aerodynamic characteristics of the heat exchanger

Static pressure drop on a heat exchanger Δp_s^h was estimated as difference between averaged static pressure measured at the cross section for the unit and for the cross flow fan as an element of the unit (Fig. 2). The curves $\Delta p_s^h = f(\dot{V})$ obtained at different rotational speeds indicate a significant influence of cross flow fan acting. The aerodynamic drag of the heat exchanger increases with the increase of the air velocity but the curve runs differ from typical second degree curves with more intensive tendency at a higher rotational speed. Superposition of cross flow fan performances and resistance curves of the heat exchanger create characteristics shown in Fig. 6 changing their runs in dependence of the air velocity.
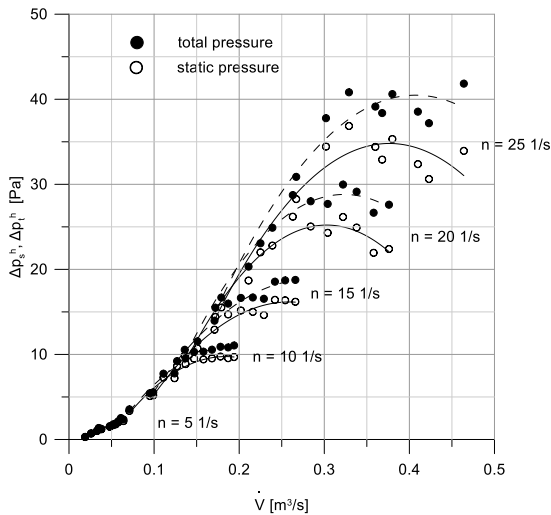
Fig. 6. Flow characteristics of heat exchanger $\Delta p_s^h = f(\dot{V})$ and $\Delta p_t^h = f(\dot{V})$ for different rotational speed

At lower values of volumetric flow rate ($\dot{V} < 0.125$ m³/s) the influence of dynamic pressure on the heat exchanger performance is not visible so for different rotational speeds at studied range the results are similar and the curves run identically.

3.2. An influence of medium temperature on aerodynamic characteristics of the heat exchanger

In Fig. 7. selected flow characteristics of heat exchanger: $\Delta p_s^{\,h} = f(\dot{V})$ and $\Delta p_t^{\,h} = f(\dot{V})$ measured at three different temperatures of medium: 20°C, 35°C and 50°C at constant rotational speed $n = 15$ s⁻¹ are presented. It is worth to notice that in this case the influence of aerodynamic performances of cross flow fan on the heat exchanger characteristics is much more visible than the temperature effect in the determined range of volumetric flow rate.
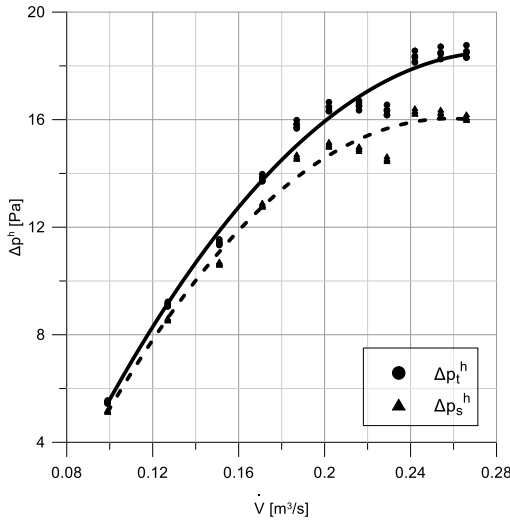
Fig. 7. Flow characteristics of the heat exchanger for various medium temperatures

The run of curves indicates a limited value of volumetric flow rate at which static and total pressure differences reach the highest values and then $\Delta p_t^{\,h}$ and $\Delta p_s^{\,h}$ decrease because of the stronger effect of the cross flow fan acting.

Dynamic pressure obtained as the difference between total pressure drop and static pressure drop measured for heat exchanger $\Delta p_{d\,(m)}^{\,h}$ (measured) was compared with dynamic pressures calculated as the difference between total and static pressures for a cross flow fan in the unit and the unit $\Delta p_{d\,(c)}^{\,h}$ (calculated) in the range of volumetric flow $\dot{V} = 0.08 \div 0.28$ m³/s for various medium temperatures (Fig. 8). Both calculated and measured results have been approximated using the following formula, respectively:

calculated: $\qquad p_{d\,(c)}^{\,h} = 33.041 \cdot \dot{V}^2 - 0.059 \cdot \dot{V} - 0.005$ \hfill (4)

measured: $\qquad p_{d\ (m)}^{\ h} = 34.451 \cdot \dot{V}^2 - 0.083 \cdot \dot{V} - 0.005$ (5)
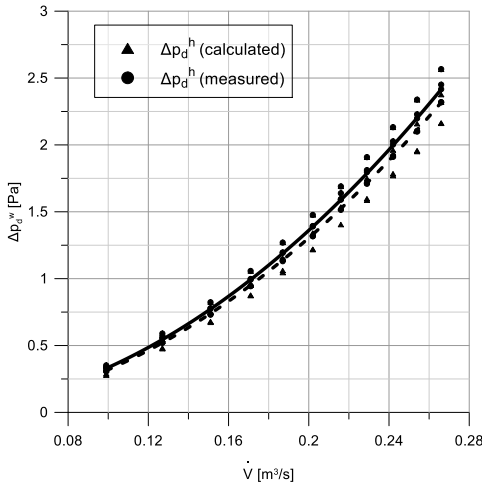
Fig. 8. Dynamic pressure vs. volumetric flow rate for different medium temperatures

Comparison of approximated results obtained from measurement and calculation show rather good agreement although calculated values lie below measured results. Differences between calculated and measured values of $\Delta p_d^{\ h}$ are in the range of 0.16 Pa, more visible at higher volumetric flow rate.

4. Quantitative evaluation of pressure loss

Analyzing the results of dynamic pressure obtained as a difference between total and static pressure at the cross section before (A_2) and behind (A_3) the heat exchanger evaluated from measurements for the unit and cross flow fan as well as calculated using a simplified formula [7]:

$$p_d^{\ h} = \frac{1}{2} \cdot \rho^2 \cdot V^2 \cdot \left[\frac{1}{\rho_3 \cdot A_3^{\ 2}} - \frac{1}{\rho_2 \cdot A_2^{\ 2}} \right] \qquad (6)$$

for medium temperatures: 20°C, 35°C , 40°C , 45°C and 50°C, some differences have been indicated. The ratio of dynamic pressure measured and calculated determined as "dimensionless coefficient of dynamic pressure" ξ_d plotted versus volumetric flow rate is shown in Fig. 9.

Independence of ξ_d from the medium temperature in the investigated range (20°C ÷ 50°C) and almost constant value of the ratio equal to 2.63 indicate the local dynamic pressure loss as an effect of the heat exchanger resistance.
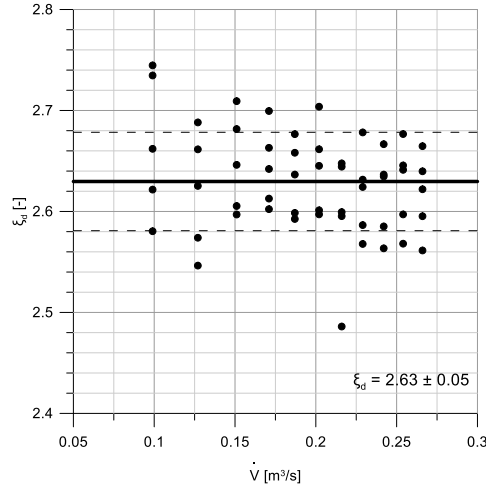
Fig. 9. Dimensionless coefficient ξ_d vs. volumetric flow rate for different medium temperatures

5. Conclusions

The runs of performance presented in this paper showed the different influence of rotational speed of the cross flow fan impeller as well as the temperature of working medium in the heat exchanger. The comparison of dimensionless curves $\psi = f(\varphi)$ obtained for the cross flow fan working alone and as an element of a unit incorporating heat exchanger indicated the effect of throttling . The similar effect has been seen comparing the efficiency $\eta = f(\varphi)$ obtained for the cross flow fan working as an element of a unit with the efficiency for the whole unit. The analysis allowed identifying an influence of cross flow fan rotational speed and temperature of working medium in a heat exchanger on its aerodynamic performances.

Nomenclature

A – area cross section, [m^2];
D_2 – outer diameter of impeller, [m];
L – length of impeller, [m];
u_2 – tangential velocity at outer diameter, [m s^{-1}];
n – rotational speed, [s^{-1}];
p – pressure, [Pa];
P – power, [W];
$\dot{V}$ – volumetric flow rate, [m^3 s^{-1}];
ξ_d – dimensionless coefficient of dynamic pressure;
ρ – density, [kg m^{-3}];

$$\eta = \frac{\Delta p \cdot \dot{V}}{P} \qquad \text{– efficiency;}$$

$$\varphi = \frac{\dot{V}}{D_2 \cdot L \cdot u_2} \qquad \text{– flow coefficient;}$$

$$\psi = \frac{2 \cdot \Delta p}{\rho \cdot u_2^2} \qquad \text{– pressure coefficient;}$$

Subscribes		Superscripts	
s	– static;	*	– cross flow fan;
t	– total;	h	– heat exchanger;
d	– dynamic;	u	– unit.

References

[1] Targosz B., Stacharska-Targosz J., Gołogórski J., *Wentylatorowy wymiennik ciepła z tworzyw sztucznych*, Technika Chłodnicza i Klimatyzacyjna, vol. 3, 1997, 129-135.

[2] Matsuki K., Shinobu Y., Takushima A., Tanaka S., *Experimental study of internal flow of a room air conditioner incorporating a cross flow fan,* ASHRAE Transactions, vol. 94, pt. 1, 1988, Dallas, TX.

[3] New Mei Yet, Raghavan V.R., Chin W.M., *Indoor Air Conditioning Unit Air Flow Performance Study – characterization of cross flow fan design*, vol. 58, 2012, 65-71 [www.journalteknologi.utm.my] eISSN 2180-3722I ISSN 0127-9696.

[4] Płachetko A., Stacharska-Targosz J., *Performance characteristics of fan heat exchanger incorporating a cross flow fan,* Materiały Konferencyjne SYMKOM'99, Łódź 1999.

[5] Stacharska-Targosz J., *Współpraca wentylatora poprzecznego z wymiennikiem ciepła w świetle badań wizualizacyjnych struktury przepływu oraz charakterystyk pracy badanych na stanowisku kanałowym* [in:] *Współczesne Technologie i Urządzenia Energetyczne*, Politechnika Krakowska, Kraków 2007.

[6] Stacharska-Targosz J., Wojtuń S., *Charakterystyki wentylatora poprzecznego w układzie z wymiennikiem ciepła*, Prace Naukowe Monografie Konferencje Z.13, Politechnika Śląska, Gliwice 2003, 165-172.

[7] Stacharska-Targosz J., Nering K., *Influence of Discharge Resistance on Internal Flow Structure and Performances of the Cross Flow Fan and the Unit Incorporating Heat Exchanger*, Technical Transactions, series Mechanics, vol. 112(7), 2015, 281-290.

DAMIAN SZUBARTOWSKI, ARTUR GANCZARSKI[*]

THE CONCEPT
OF A QUASI-MICROPOLAR FLUID MODEL

QUASI-MIKROPOLARNY MODEL CIECZY

Abstract

This paper presents a micropolar fluid model that direct applies Cosserat's continuum to hydrodynamics. The corresponding system of equations describing isotropic micropolar fluid is obtained by assuming lack of symmetry of the Cauchy stress tensor and taking into account the conservation of angular momentum. This turns out to be an extension of the Navier-Stokes fluid but containing turbulent effect built in.

Keywords: micropolar fluid, turbulent effect

Streszczenie

W artykule przedstawiono mikropolarny model cieczy stanowiący bezpośrednie zastosowanie kontinuum Cosseratów w hydromechanice. Zakładając brak symetrii tensora naprężenia Cauchy'ego oraz uwzględniając zasadę zachowania momentu pędu otrzymano układ równań opisujący izotropową ciecz mikropolarną. Układ równań jest uogólnieniem równań Naviera-Stokesa poprzez uwzględnienie efektu turbulentnego.

Słowa kluczowe: ciecz mikropolarna, efekt turbulentny

[*] MSc. Damian Szubartowski, Prof. PhD. DSc. Eng. Artur Ganczarski, Institute of Applied Mechanics, Faculty of Mechanical Engineering, Cracow University of Technology.

1. Introduction

Over one hundred years ago, the Cosserat brothers published fundamental work containing a new version of continuum mechanics [8]. This was based on the idea of considering rotational degrees of freedom of material particles to be independent variables and corresponding couple stresses. This material model was later named the Cosserat or micropolar continuum. The basic ideas of this approach were first presented in [7].

The general nonlinear theory of the micropolar continuum was developed by Truesdell [44, 45]. The problem of finite deformation was considered by Grioli [19, 20], Toupin [43], Green & Rivlin [18], Eringen & Kafadar [14, 24], Stojanovic [39, 40, 41], Besdo [5] and Reissner [33, 34, 35]. The linear Cosserat theory is presented in the original papers, by inter alia Günther [21], Aero & Kuvshinskii [3, 4], Toupin [42], Mindlin & Tiersten [28], Koiter [25], Palmov [32], Eringen [15, 16], Schaefer [38], and Ieşan [23].

In the case of micropolar fluids, the review of achievements starts with pioneering papers by Aero et al. [2] and Eringen [17] as well as monographs by Migoun & Prokhorenko [27], Łukaszewicz [26], Eremeyev & Zubov [9], the micropolar continuum is applied to model magnetic liquids, polymer suspension, liquid crystals, and other types of fluids with a microstructure. In particular, Rosensweig uses magnetic fluids [36], named also ferrofluids, developing the micropolar hydromechanics where a magnetic field induces voluminous couples. Compared to micropolar elasticity, micropolar hydrodynamics is a more extensive part of mechanics with well-established experimentally constitutive equations. Some generalizations of the viscous micropolar constitutive model are presented by Eremeyev & Zubov [10, 47] and also Eringen [11, 12, 13].

The Cosserat brothers considered a simplified version of the micropolar continuum called quasi micropolar theory. This is based on the assumption that the rotation of local particles is equal to the average rotation of displacement field. The quasi micropolar continuum is well developed and comprises several general theorems, methods of integration and solutions of fundamental problems, see Hamel [22], Koiter [25], Mindlin and Tiersten [28], Muki & Sternberg [29], Bogy & Sternberg [6], Sawin [37].

2. Micropolar fluid model

Classical hydromechanics is based on an idealised model of a continuum in which the transmission of transitions between both sides of a surface element is only described by the Cauchy stress $t_i = \sigma_{ji} n_j$. This approach leads to symmetrical states of stress and strain which properly describe majority of solid and fluid materials. However, essential differences between the model and experimental evidence arise in the case of high stress gradients, vibrations excited by high frequencies, granular media and polymers. The above discrepancies between the theory of symmetric continuum and experimental data were the subject of investigations by Voigt [46] who first introduced additional transmission by a couple traction $m_i = \mu_{ji} n_j$. Such an assumption leads to the existence of the couple stress tensor μ_{ij} as well as a lack of symmetry of Cauchy's stress tensor σ_{ij}. The general theory of non-symmetrical continuum was developed by the Cosserat brothers [8]. According to their concept, the kinematics of the continuum point is described by the displacement vector u_i

and the micropolar rotation vector φ_i. Since the present section deals with the micropolar fluid model let us adapt Cosserat's formalism to our purpose as was done by Ostoja-Starzewski [31]. First of all, both vectors u_i and φ_i are replaced by their respective time rates $v_i = \dot{u}_i$ and $\omega_i = \dot{\varphi}_i$. Additionally, the microinertia tensor of angular momentum per unit mass J_{ij} is introduced. The system of balance equations is as follows:

the conservation of mass

$$\frac{D\rho}{Dt} + \rho v_{i,i} = 0 \tag{1}$$

the balance of linear momentum

$$\rho\frac{Dv_i}{Dt} = \sigma_{ji,j} + \rho X_i \tag{2}$$

the balance of angular momentum

$$\rho\frac{D(J_{ij}\omega_j)}{Dt} = \mu_{ji,j} + \rho Y_i + \in_{ijk}\sigma_{jk} \tag{3}$$

In the case of an isotropic micropolar fluid, $J_{ij} = J\delta_{ij}$, where J is the microinertia of a continuum fluid particle. The above assumption comprises the isotropy of the geometric shape of fluid particles and has nothing to do with the isotropy of constitutive equations − these will be discussed separately.

Taking advantage of kinematic equations

$$\dot{\gamma}_{ji} = v_{i,j} - \in_{kji}\omega_k$$
$$\dot{\kappa}_{ji} = \omega_{i,j} \tag{4}$$

one can perform constitutive equations of the linear micropolar, isotropic and centrosymmetric fluid

$$\sigma_{ji} = (\mu + \mu_r)\dot{\gamma}_{ji} + (\mu - \mu_r)\dot{\gamma}_{ij} + (-p + \lambda\dot{\gamma}_{k,k})\delta_{ij}$$
$$\mu_{ji} = (c_d + c_a)\dot{\kappa}_{ji} + (c_d - c_a)\dot{\kappa}_{ij} + c_0\dot{\kappa}_{k,k}\delta_{ij} \tag{5}$$

in the format proposed by Łukaszewicz [26]

$$\sigma_{ji} = (-p + \lambda v_{k,k})\delta_{ij} + \mu(v_{j,i} + v_{i,j}) + \mu_r(v_{i,j} - v_{j,i}) - 2\mu_r \in_{mij}\omega_m$$
$$\mu_{ji} = c_0\omega_{k,k}\delta_{ij} + c_d(\omega_{j,i} + \omega_{i,j}) + c_a(\omega_{i,j} - \omega_{j,i}) \tag{6}$$

It is worth noting here that the term centrosymmetry plays an analogous role to the term isotropy in case of classical continuum. Therefore, the governing equations (2-3) become

$$\rho\frac{Dv_i}{Dt} = \rho X_i - p_{,i} + (\lambda + \mu - \mu_r)v_{j,ji} + (\mu + \mu_r)v_{i,kk} + 2\mu_r \in_{ijk}\omega_{k,j}$$
$$\rho J\frac{D\omega_i}{Dt} = \rho Y_i + 2\mu_r(\in_{ijk}v_{j,k} - 2\omega_i) + (c_0 + c_d - c_a)\omega_{j,ji} + (c_d + c_a)\omega_{i,kk} \tag{7}$$

If there are no body forces and couples, the governing equations (1, 7) may be rewritten in absolute notation to the format

$$\frac{D\rho}{Dt} + \rho \, \text{div}\mathbf{v} = 0$$

$$\rho \, {}^{D\mathbf{v}}/_{Dt} = -\text{grad}p + (\mu + \mu_r)\nabla^2\mathbf{v} + (\lambda + \mu - \mu_r)\text{grad}(\text{div}\mathbf{v}) + 2\mu_r\text{rot}\boldsymbol{\omega} \qquad (8)$$

$$\rho J \, {}^{D\boldsymbol{\omega}}/_{Dt} = (c_d + c_a)\nabla^2\boldsymbol{\omega} + (c_0 + c_d - c_a)\text{grad}(\text{div}\boldsymbol{\omega}) + 2\mu_r\text{rot}\mathbf{v} - 4\mu_r\boldsymbol{\omega}$$

in which the viscosity coefficients assuring the positive definiteness of the entropy growth are

$$\begin{array}{ll} \mu \geqslant 0 & 3\lambda + 2\mu \geqslant 0 \\ c_d + c_a \geqslant 0 & 3c_0 + 2c_d \geqslant 0 \\ -(c_d + c_a) \leqslant c_d - c_a \leqslant (c_d + c_a) & \mu_r \geqslant 0 \end{array} \qquad (9)$$

According to Eq. (8), the motion of micropolar fluid can be treated as turbulent. However, when the micropolar effects tend to vanish, the fluid becomes classical Newtonian and in the special case of vanishing bulk viscosity $\lambda + 2/3\mu \rightarrow 0$ it simplifies to a Navier-Stokes fluid.

3. Quasi-micropolar fluid model

Apart from the general micropolar theory, the Cosserat brothers also considered a simplified theory, according to which, couple inertia terms vanish $D\boldsymbol{\omega}/Dt = 0$ in Eq. (8$_3$) and the rotation of a local particle is equal to the average rotation of the displacement field, see Nowacki [30]. It is assumed that Eq. (4$_1$) reduces to

$$\dot{\boldsymbol{\gamma}}^A = \frac{1}{2}\text{rot} \, \mathbf{v} - \boldsymbol{\omega} = 0 \qquad (10)$$

nevertheless, the transmission of tractions and couple transitions through an arbitrary surface is done by stress tensor $\boldsymbol{\sigma}$ and couple stress tensor $\boldsymbol{\mu}$, and obviously, both tensors are still unsymmetrical.

Introducing $\boldsymbol{\omega}$ calculated from Eq. (10) into Eqs (8$_{2-3}$) we obtain

$$\rho \, {}^{D\mathbf{v}}/_{Dt} = -\text{grad}p + \mathcal{L}(\mathbf{v}) - 2\mu_r\text{rot}\dot{\boldsymbol{\gamma}}^A$$

$$(c_d + c_a)\nabla^2\dot{\boldsymbol{\gamma}}^A + (c_0 + c_d - c_a)\text{grad div}\dot{\boldsymbol{\gamma}}^A + 4\mu_r\dot{\boldsymbol{\gamma}}^A - \frac{1}{2}(c_d + c_a)\nabla^2\text{rot}\mathbf{v} = 0 \qquad (11)$$

in which the differential operator

$$\mathcal{L}(..) = (\mu + \mu_r)\nabla^2(..) + (\lambda + \mu - \mu_r)\text{grad div}(..) + \mu_r\text{rot rot}(..) \qquad (12)$$

may be simplified to the format

$$\mathcal{L}(..) = \lambda\nabla^2(..) + (\lambda + \mu)\text{grad div}(..) \qquad (13)$$

The above reduction yields of known relation $\nabla^2(..) - \text{grad div}(..) + \text{rot rot}(..) = 0$.
   Unsymmetrical stress tensor defined as

$$\boldsymbol{\sigma}^A = 2\mu_r \dot{\boldsymbol{\gamma}}^A \tag{14}$$

serves for the reduction of $\dot{\boldsymbol{\gamma}}^A$ in Eq. (11) yielding

$$\rho \, {}^{D\mathbf{v}}\!/_{Dt} = -\text{grad}p + \mathcal{L}(\mathbf{v}) - \text{rot}\boldsymbol{\sigma}^A$$
$$\boldsymbol{\sigma}^A = -\frac{1}{4}(c_d + c_a)\nabla^2 \text{rot}\mathbf{v} \tag{15}$$

Finally, applying differential operator (13) and introducing (15_2) into Eq. (15_1) we find

$$\frac{D\rho}{Dt} + \rho\,\text{div}\mathbf{v} = 0$$
$$\rho \, {}^{D\mathbf{v}}\!/_{Dt} = -\text{grad}p + \mu\nabla^2\mathbf{v} + (\lambda + \mu)\text{grad div } \mathbf{v} - \frac{1}{4}(c_d + c_a)\nabla^2\text{rot rot } \mathbf{v} \tag{16}$$

In the case of vanishing bulk viscosity $\lambda + 2/3\mu \rightarrow 0$, we get the system of equations

$$\frac{D\rho}{Dt} + \rho\,\text{div}\mathbf{v} = 0$$
$$\rho(^{\partial\mathbf{v}}\!/_{\partial t} + \mathbf{v}\cdot\nabla\mathbf{v}) = -\text{grad}p + \mu\left(\nabla^2\mathbf{v} + \frac{1}{3}\text{grad div } \mathbf{v}\right) - \underline{(c_d + c_a)\nabla^2\text{rot rot } \mathbf{v}} \tag{17}$$

which is the generalisation of the Navier-Stokes equations by the underlined term. Eq. (17_2) include not only the conventional coefficient of dynamic viscosity μ but also the sum of two micropolar viscosity coefficients $c_d + c_a$. All above coefficients of viscosity are constants according to the assumption of isotropy and linearity of constitutive equations (5) or (6). It is also worth to noting that the underlined term can be treated as a specific integral of the Navier-Stokes equations. Moreover, since according to Eq. (17_2) the turbulent effect is activated from the very beginning, we suggest that it be preceded by a specific continuous switch function dependent on Reynold's number

$$f(Re) = \frac{Re - Re_{min}}{Re_{max} - Re_{min}} \tag{18}$$

as is shown in Fig. 1. Reynold's number includes only the conventional coefficient of
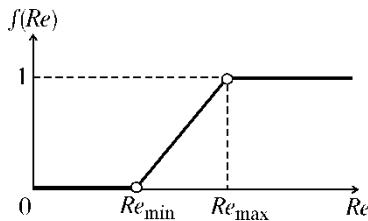
Fig. 1. Switch function $f(Re)$ preceding turbulent effect term in Eqs (17)

dynamic viscosity μ, hence the sum of two micropolar viscosity coefficients $c_d + c_a$ serves as the length scale.

Example of application of the above quasi-micropolar fluid model will be a subject of separate paper.

N o m e n c l a t u r e

c_0, c_d, c_a	– micropolar viscosity coefficients
D/Dt	– absolute differential with respect to time
J_{ij}	– microinertia tensor of a fluid particle
n_i	– outer normal unit vector
m_i	– couple traction vector
p	– pressure
Re	– Reynold's number
t	– time
t_i	– traction vector
$u_i, \boldsymbol{u}$	– displacement vector
$\mathrm{v}_i, \mathbf{v}$	– time differential of displacement vector
ω_i	– time differential of microrotation vector
X_i, Y_i	– body force per unit mass and body torque per unit mass
$\partial/\partial t$ or · over a symbol	– partial differential with respect to time
δ_{ij}	– Kronecker's symbol
$\in_{ijk}$	– Levi-Civita's symbol
$\dot{\gamma}_{ij}, \dot{\kappa}_{ij}$	– strain rate tensor and couple strain rate tensor
$\dot{\boldsymbol{\gamma}}^A$	– unsymmetrical part of strain rate tensor
λ, μ	– conventional viscosity coefficients
μ_r	– dynamic microrotation viscosity
ρ	– mass density
σ_{ij}, μ_{ij}	– Cauchy's stress tensor and couple stress tensor
$\boldsymbol{\sigma}^A$	– unsymmetrical part of Cauchy's stress tensor
$\varphi_i, \boldsymbol{\varphi}$	– micropolar rotation vector
$\omega_i, \boldsymbol{\omega}$	– time differential of micropolar rotation vector

R e f e r e n c e s

[1] Altenbach H., Eremeyev V.A., *Generalized Continua – from the Theory to Engineering Applications*, CISM Int. Centre for Mech. Sci. 541, 2013.

[2] Areo E.L., Bulygin A.N., Kuvshinskii E.V., *Asymmetric hydromechanics*, J. Appl. Math. Mech., 29(2), 1965, 333-346.

[3] Areo E.L., Kuvshinskii E.V., *Continuum theory of asymmetric elasticity. Equilibrium of an isotropic body* (in Russian), Fizika Tverdogo Tela, 6, 1964, 2689-2699.

[4] Areo E.L., Kuvshinskii E.V., *Fundamental equations of the theory of elastic media with rotationally interacting particles*, Sov. Phys. Solid State, 2(7), 1961, 1272-1281.

[5] Besdo D., *Ein Beitrag zur nichtlinearen Theorie des Cosserat-Kontinuums*, Acta Mechanica, 20(1-2), 1974, 105-131.

[6] Bogy D.B., Sternberg E., *The effect of couple-stresses on the corner singularity due to an asymmetric shear loading*, Int. J. solid Structures, 4(2), 1968.

[7] Cosserat E., Cosserat F., *Sur la théorie de l'elasticité*, Ann. Toulouse, 10, 1896, 1-116.

[8] Cosserat E., Cosserat F., *Théorie des corps déformables*, Hermann, Paris 1909.

[9] Eremeyev V.A., Zubov L.M., *Principles of Viscoelastic Micropolar Fluid Mechanics* (in Russian), SSC of RASci Publishers, Rostov on Don 2009.

[10] Eremeyev V.A., Zubov L.M., *The theory of elastic and viscoelastic micropolar liquids*, J. Appl. Math. Mech., 63(5), 1999, 755-767.

[11] Eringen A.C., *A unified continuum theory of electrodynamics of liquid crystals*, Int. J. Eng. Sci., 35(12-13), 1997, 1137-1157.

[12] Eringen A.C., *A unified continuum theory of electrodynamics of polymeric liquid crystals*, Int. J. Eng. Sci., 38(9-10), 2000, 959-987.

[13] Eringen A.C., *A unified continuum theory of liquid crystals*, ARI Int. J. Phys. Eng. Sci., 73-84(2), 1997, 369-374.

[14] Eringen A.C., Kafadar C.B., *Polar field theories*, in Continuum Physics, vol. IV, ed. Eringen A.C., Academic Press, New York, 1-75, 1976.

[15] Eringen A.C., *Linear theory of micropolar elasticity*, J. Math. Mech., 15(6), 1966, 909-923.

[16] Eringen A.C., *Linear theory of micropolar viscoelasticity*, Int. J. Eng. Sci., 5(2), 1967, 191-204.

[17] Eringen A.C., *Theory of micropolar fluids*, J. Math. Mech., 16(1), 1966, 1-18.

[18] Green A.E., Rivlin R.S., *Multipolar continuum mechanics*, Arch. Ration. Mech. Anal., 17(2), 1964, 113-147.

[19] Grioli G., *Contributo per una formulazione di tipo integrale della meccanica dei continui di Cosserat*, Annali di Matematica Pura ed Applicata, 111(1), 1976, 389-417.

[20] Grioli G., *Elasticita asimmetria*, Annali di Matematica Pura ed Applicata, 50(1), 1960, 389-417.

[21] Günther W., *Zur Statik und Kinematik des Cosseratschen Kontinuums*, Abhandlungen der Braunschweigschen Wissenschaftlischen Gesellschaft, Göttingen, 10, 1958, 196-213.

[22] Hammel G., *Elementare Mechanik*, Leipzig, Berlin 1912.

[23] Ieşan D., *On the linear theory of micropolar elasticity*, Int. J. Eng. Sci., 7(12), 1969, 1213-1220.

[24] Kafadar C.B., Eringen A.C., *Micropolar media – I. The classical theory*, Int. J. Eng. Sci., 9(3), 1964, 271-305.

[25] Koiter W.T., *Couple-stresses in the theory of elasticity*, Pt I-II, Proc. Koninkl. Neterland. Akad. Wetensh., B67, 1964, 17-44.

[26] Łukaszewicz G., *MicropolarFluids: Theory and Applications*, Birkhäuser, Basel 1999.

[27] Migoun N.P., Prokhorenko P.P., *Hydrodynamics and Heat Transfer in Gradient Flows of Microstructured Fluids* (in Russian), Nauka i Technika, Minsk 1984.

[28] Mindlin R.D., Tiersten H.F., *Effects of couple-stresses in linear elasticity*, Arch. Ration. Mech. Anal., 11, 1962, 415-448.

[29] Muki R., Sternberg E., *The influence of couple-stresses on singular stress concentrations in elastic solids*, ZAMP, 16(5), 1965.

[30] Nowacki W., *Theory of non-symmetric elasticity*, IPPT PAN, PWN, Warsaw 1981.

[31] Ostoja-Starzewski M., *Second law violations, continuum mechanics, and permeability*, Continuum Mech. Thermodyn. DOI 10.1007/s00161-015-0451-4, 2015.

[32] Pal'mov V.A., *Fundamental equations of the theory of asymmetric elasticity*, J. Appl. Mech. Math., 28(3), 1964, 496-505.

[33] Reissner E., *A further note on the equations of finite-strain force and moment stress elasticity*. ZAMP, 38, 1987, 665-673.

[34] Reissner E., *Note on the equations of finite-strain force and moment stress elasticity*, Stud. Appl. Math., 54, 1975, 1-8.

[35] Reissner E., *On kinematics and statics of finite-strain force and moment stress elasticity*, Stud. Appl. Math., 52, 1973, 93-101.

[36] Resensweig R.E., *Magnetic fluids*, Ann. Rev. Fluid Mech., 19, 1987, 437-461.

[37] Sawin G.N., *Stress distributions around holes* (in Russian), Naukova Dumka, Kiev 1968.

[38] Schaefer H., *Das Cosserat-Kontinuum*, ZAMM, 47(8), 1967, 485-498.

[39] Stojanovic R., *Mechanics of Polar Continua: Theory and Applications*, CISM Courses and Lectures, vol. 2, Springer Wien 1969.

[40] Stojanovic R., *Nonlinear micropolar elasticity*, in Micropolar Elasticity, vol. 151, ed. Nowacki W. and Olszak W., Springer Wien, 1974, 73-103.

[41] Stojanovic R., *Recent Developments in the Theory of Polar Continua*, CISM Courses and Lectures, vol. 27, Springer Wien 1969.

[42] Toupin R.A., *Elastic materials with couple-stress*, Arch. Ratin. Mech. Anal., 11, 1962, 385-414.

[43] Toupin R.A., *Theories of elasticity with couple-stress*, Arch. Ration. Mech. Anal., 17, 1964, 85-112.

[44] Truesdell C., Noll W., *The nonlinear field theories of mechanics*, in Handbook der Physik, vol. III/3, ed. Flügge S., Springer, Berlin 1987.

[45] Truesdell C., Toupin R., *The classical field theories*, in Handbook der Physik, vol. III/1, ed. Flügge S., Springer, Berlin 1960.

[46] Voigt W., *Theoretishe Studien über die Elastizitätsverhältnisse der Kristalle*, Abh. Ges. Wiss. Göttingen, Bd. 34, 1887.

[47] Zubov L.M., Eremeyev V.A., *Equations of elastic and viscoelastic micropolar fluid*, Doklady Phys., 14(2), 1996, 598-601.

DAWID TALER[*], KAROL KACZMARSKI[**]

A NUMERICAL MODEL
OF TRANSIENT PIPELINE OPERATION

NUMERYCZNY MODEL
NIEUSTALONEJ PRACY RUROCIĄGU

A b s t r a c t

The aim of this study is to develop a numerical model of a steam pipeline. The energy conservation equations for the pipeline wall and steam are solved using the finite volume method (FVM). The transient temperature of the pipeline wall, steam temperature and thermal stresses can be calculated using the model developed in the paper.

Keywords: pipeline heating, transient temperature, numerical model, thermal stresses

S t r e s z c z e n i e

Celem artykułu jest opracowanie modelu numerycznego rurociągu parowego. Równania zachowania energii dla ścianki rurociągu i pary są rozwiązywane przy użyciu metody objętości skończonych (MOS). Nieustalona temperatura ścianki rurociągu, temperatura pary oraz naprężenia cieplne mogą być obliczone za pomocą modelu przedstawionego w artykule.

Słowa kluczowe: nagrzewanie rurociągu, temperatura nieustalona, model numeryczny, naprężenia cieplne

* PhD. DSc. Eng. Dawid Taler, Prof. CUT, Institute of Thermal Engineering and Air Protection, Faculty of Environmental Engineering, Cracow University of Technology.
** MSc. Eng. Karol Kaczmarski, Institute of Thermal Power Engineering, Faculty of Mechanical Engineering, Cracow University of Technology.

1. Introduction

High-temperature steam pipelines in steam boilers are used to transport superheated steam from the boiler to the turbine. During start-ups and shutdowns of the power units, as well as during load changes, high thermal stresses can occur in the pipeline wall and in pipeline fittings. Particularly high stresses occur in T-pipes and Y-pipes. Additionally, thick-walled sections with complex shapes such as valves and gate valves are exposed to large thermal loads. Both high thermal stresses and time-variable thermal stresses may lead to the premature damage of pipelines in the form of cracks. Knowledge of the range of stresses in critical components allows conducting the startup of the boiler in a way that provides a safe and long life of the boiler and turbine. Issues relating to the direct and inverse calculation and monitoring of thermal stresses in cylindrical components are the subjects of current research [1, 2]. In this paper, transient temperature and thermal stress distributions in a pipeline connecting the boiler and turbine will be determine. The finite volume method (FVM) is used to determine the transient temperature of the steam and pipeline wall. Thermal stresses are also calculated.

2. Mathematical formulation

A scheme of the pipeline linking the boiler with a turbine in a power unit with a capacity of 120MW is depicted in Fig. 1.

The governing equations for the steam are:

- mass conservation equations

$$\frac{\partial \rho}{\partial t} = -\frac{1}{A} \cdot \frac{\partial \dot{m}}{\partial z} \tag{1}$$

- momentum conservation equations

$$\frac{\partial \dot{m}}{\partial z} = -\frac{\partial}{\partial z}\left(\frac{\dot{m}^2}{\rho \cdot A}\right) - A \cdot \left(\frac{\partial p}{\partial z} + \rho \cdot g \cdot sin\varphi - \frac{\xi}{d_{in}} \cdot \frac{\dot{m}|\dot{m}|}{2 \cdot \rho \cdot A^2}\right) \tag{2}$$

- energy conservation equations

$$\rho \cdot c_p \left(\frac{\partial T}{\partial t} + \frac{\dot{m}}{\rho \cdot A}\frac{\partial T}{\partial z}\right) = \beta \cdot T\left(\frac{\partial p}{\partial t} + \frac{\dot{m}}{\rho \cdot A}\frac{\partial p}{\partial z}\right) + \frac{\xi}{d_{in}}\frac{|\dot{m}^3|}{2 \cdot \rho^2 \cdot A^3} - \frac{\alpha(T - T_w)}{A} +$$
$$+ \frac{1}{A}\frac{\partial}{\partial z}\left(A \cdot \lambda \frac{\partial T}{\partial z}\right) \tag{3}$$
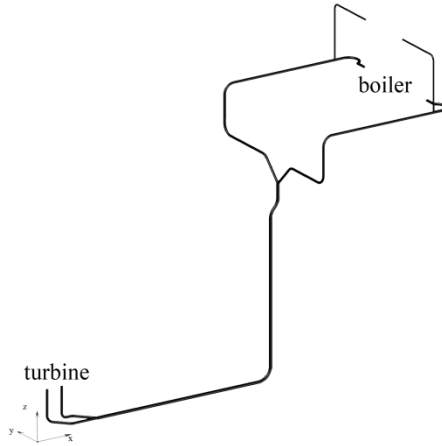
Fig. 1. The pipeline connecting the boiler and turbine

The transient heat conduction equation for the pipeline wall is

$$\rho_w \cdot c_{pw} \frac{\partial T_w}{\partial t} = \nabla \cdot \left[\lambda_w(T_w)\nabla T_w\right] \tag{4}$$

The derivative $\partial\rho/\partial t$ in Eq. (1) was assumed to be equal zero since the changes in pressure along the length of the pipeline are small and consequently the steam density can be assumed constant. The assumption $\partial\rho/\partial t = 0$ in Eq. (1) implies that mass flow rate $\dot{m}$ is constant over the tube length, i.e.

$$\dot{m} = const \tag{5}$$

The velocity of the steam in each cross-section of the pipeline can be calculated from the formula

$$w = \frac{4 \cdot \dot{m}}{\pi \cdot \rho \cdot d_{in}^2} \tag{6}$$

Considering that $\partial\dot{m}/\partial t = 0$, the momentum conservation equation (2) reduces to

$$\frac{dp}{dz} = -\rho \cdot w \frac{dw}{dz} - \rho \cdot g \cdot sin\varphi - \frac{\xi}{d_{in}} \frac{\rho \cdot w \cdot |w|}{2} \tag{7}$$

Using Eq. (7), the steam pressure can be determined along the path flow.

Neglecting the thermal expansion of the steam ($\beta = 0$), the heat generation due to friction and the axial thermal conduction in the steam, the energy conservation equation (3) for the steam simplifies to the form

$$\rho \cdot c_p \cdot \left(\frac{\partial T}{\partial t} + \frac{\dot{m}}{\rho \cdot A} \cdot \frac{\partial T}{\partial z} \right) = - \frac{\alpha \cdot (T - T_w) \cdot U_{in}}{A} \tag{8}$$

The heat conduction equation (4) in the cylindrical coordinate system is

$$\rho_w \cdot c_{pw} \frac{\partial T_w}{\partial t} = \frac{1}{r} \cdot \frac{\partial}{\partial r} \left[r \cdot \lambda_w (T_w) \frac{\partial T_w}{\partial r} \right] + \frac{\partial}{\partial z} \left[\lambda_w (T_w) \frac{\partial T_w}{\partial z} \right] \tag{9}$$

The system of partial differential equations (8, 9) is subject to the following initial and boundary conditions:

$$T \big|_{t=0} = T_0 \tag{10}$$

$$T_w \big|_{t=0} = T_{w,0} \tag{11}$$

$$T \big|_{x=0} = f(t) \tag{12}$$

$$\lambda_w \frac{\partial T}{\partial r} \bigg|_{r=r_{in}} = \alpha (T - T_w) \tag{13}$$

$$\lambda_w \frac{\partial T}{\partial r} \bigg|_{r=r_{out}} = 0 \tag{14}$$

$$\lambda_w \frac{\partial T_w}{\partial z} \bigg|_{z=0} = 0 \tag{15}$$

$$\lambda_w \frac{\partial T_w}{\partial z} \bigg|_{z=L} = 0 \tag{16}$$

In addition to the conditions (10 ÷ 16), the pressure and mass flow rate of the steam are known at the inlet of the pipeline.

The initial-boundary value problem (8 ÷ 16) was solved using the finite volume method (FVM) [3, 4].

First, the computational domain, i.e. the wall and the area occupied by the steam, was divided into finite volumes (Fig. 2).
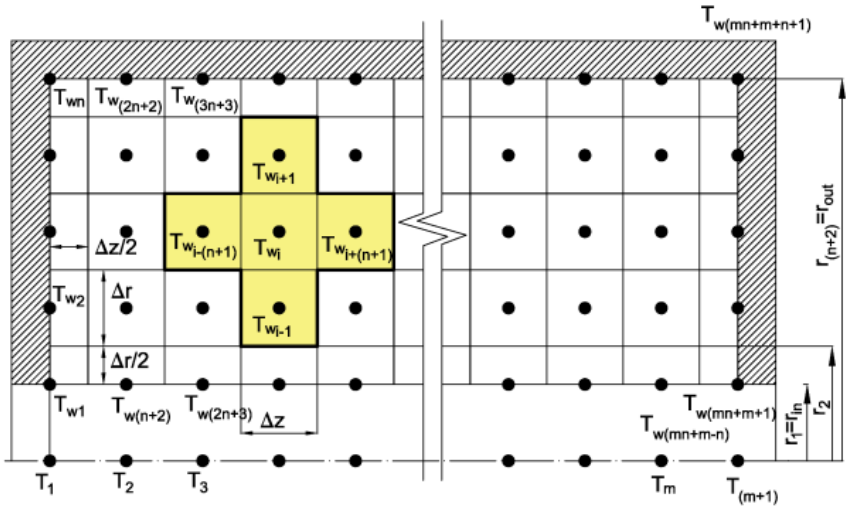
Fig. 2. Division of the computational domain into finite volumes

Energy balance equations were formed for each control volume lying both in the wall and the steam.

For example, the energy balance equation for node *i* is set for the control volume located in the computational area of the wall (Fig. 3).
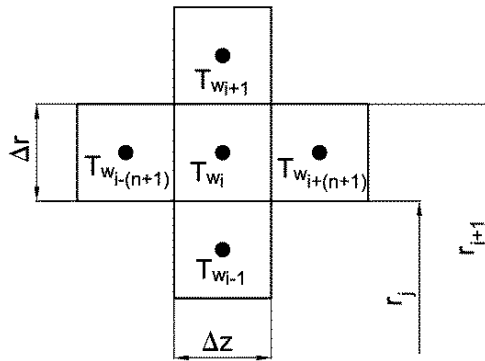
Fig. 3. Wall temperature at the node *i* and adjacent nodes *i-1, i+1, i-n-1, i+n+1*

The transformation of Eq.(9) gives

$$\frac{dT_{w_i}}{dt} = \frac{a(T_{w_i})}{\lambda_w(T_{w_i})} \left[\frac{r_j}{\Delta r} \frac{\lambda_w(T_{w_i}) + \lambda_w(T_{w_{i-1}})}{r_{j+1}^2 - r_j^2} \left(T_{w_{i-1}} - T_{w_i}\right) + \frac{r_{j+1}}{\Delta r} \frac{\lambda_w(T_{w_{i+1}}) + \lambda_w(T_{w_{i-1}})}{r_{j+1}^2 - r_j^2} \left(T_{w_{i-1}} - T_{w_i}\right) + \right.$$
$$\left. + \frac{\lambda_w(T_{w_{i+n+1}}) + \lambda_w(T_{w_{i-1}})}{2(\Delta z)^2} \left(T_{w_{i+n+1}} - T_{w_i}\right) + \frac{\lambda_w(T_{w_{i-n-1}}) + \lambda_w(T_{w_i})}{2(\Delta z)^2} \left(T_{w_{i-n-1}} - T_{w_i}\right) \right] \quad (17)$$

In a similar manner, the heat balance equation for the i-th control volume located in the region occupied by steam can be set

$$\frac{dT_{i+1}}{dt} = -\frac{\dot{m}}{\rho(T_i)A} \frac{T_{i+1} - T_i}{\Delta z} - \frac{\alpha(T_i)U_w}{A \cdot \rho(T_i) \cdot c_p(T_i)} \left[\frac{T_{i+1} + T_i}{2} - \frac{T_{w_{i(n+1)=1}} + T_{w_{(i-1)\cdot(n+1)+1}}}{2} \right] \quad i = 1,...,m \quad (18)$$

The heat transfer coefficient α on the inner surface of the pipeline was determined using Gnielinski's correlation [5]

$$Nu = \frac{(\xi/8) \cdot (Re - 1000) \cdot Pr}{1 + 12.7 \cdot (\xi/8)^{\frac{1}{2}} \cdot \left(Pr^{\frac{2}{3}} - 1\right)} \left[1 + \left(\frac{d_{in}}{L}\right)^{\frac{2}{3}} \right] \quad (19)$$

where the friction factor ξ is given by the Colebrook correlation

$$\xi = \left[1.8 \cdot \log(Re) - 1.51\right]^{-2} \quad (20)$$

The Reynolds number, Prandtl number, and Nusselt number are defined as

$$Re = \frac{\rho \cdot w \cdot d_{in}}{\mu}, \quad Pr = \frac{c_p \cdot \mu}{\lambda}, \quad Nu = \frac{\alpha \cdot d_{in}}{\lambda} \quad (21)$$

After the formulation of all balance equations for the wall and steam, a system of ordinary differential equations for node temperatures is obtained. The number of equations for the nodes lying in the wall area is $(m + 1)(n + 1)$, while for the steam, it is $(m + 1)$.

The system of ordinary differential equations was solved by the Runge-Kutta method of the fourth order.

To ensure the stability of determining the wall and steam temperature the Fourier stability condition for the wall and Courant-Friedrichs-Levy condition for the steam should be satisfied. The smallest allowable time step Δt_{max} results from the Courant-Friedrichs-Levy condition [6]

$$\frac{w_i \cdot \Delta t}{\Delta z} \leq 1, \quad i = 1,...,m+1 \quad (22)$$

Thermal stresses can be determined after calculating the transient temperature distribution in the wall.

Considering that the axial component of the temperature gradient $\partial T_w / \partial z$ is very small, only the radial temperature drop in the wall of the pipeline is taken into account. Assuming that the ends of the pipeline are free to lengthen, the thermal stress components are given by the following formulas [7]:

$$\sigma_r = \frac{E \cdot \beta_T}{2 \cdot (1-\nu)} \cdot \left(1 - \frac{r_{in}^2}{r^2}\right) \cdot \left[\overline{T}(t) - \overline{T}(r,t)\right] \tag{23}$$

$$\sigma_\varphi = \frac{E \cdot \beta_T}{2 \cdot (1-\nu)} \cdot \left[\left(1 - \frac{r_{in}^2}{r_2}\right) \cdot \overline{T}(t) + \left(1 - \frac{r_{in}^2}{r_2}\right) \cdot \overline{T}(r,t) - 2 \cdot T(r,t)\right] \tag{24}$$

$$\sigma_z = \frac{E \cdot \beta_T}{1-\nu} \cdot \left[\overline{T}(t) - T(r,t)\right] \tag{25}$$

where the mean wall temperature $T(t)$

$$\overline{T}(t) = \frac{2}{r_{out}^2 - r_{in}^2} \int_{r_{in}}^{r_{out}} r \cdot T \, dr \approx \frac{2 \cdot \Delta r}{r_{out}^2 - r_{in}^2} \left[r_2 \frac{T_1 + T_2}{2} + r_{n+1} \frac{T_n + T_{n+1}}{2} + \sum_{i=2}^{n-1} \frac{r_i + r_{i+1}}{2} T_i\right] \tag{26}$$

$$\overline{T}(r,t) = \overline{T}(r_i,t) = \frac{2}{r^2 - r_{in}^2} \int_{r_{in}}^{r} r \cdot T \, dr \approx \frac{2 \cdot \Delta r}{r_i^2 - r_{in}^2} \left[r_2 \frac{T_1 + T_2}{2} + \sum_{j=2}^{i} \frac{r_j + r_{j+1}}{2} T_j\right] \tag{27}$$

where

$$r_2 = r_1 + \frac{\Delta r}{2}$$

$$r_i = r_2 + (i-2) \cdot \Delta r, \quad i = 3,..., n+1 \tag{28}$$

$$r_{n+2} = r_{n+1} + \frac{\Delta r}{2}$$

Radial stresses σ_r are equal to zero on the inner and outer pipeline surfaces – circumferential σ_φ and axial stresses σ_z are equal on these surfaces.

3. Results

The paper presents the results of calculations concerning the pipeline connecting the boiler OP-380 with a steam turbine.

The steam pipeline is made of low-alloy steel 13HMF (C-0.18%, Mn-0.40%, Si-0.35%, P_{max}-0.040%, S_{max}-0.040%, Cu_{max}-0.25%, Cr-0.60%, Ni_{max}-0.30%, Mo-0.65%, Al_{max}-0.020%). The main dimensions are: outer diameter $d_{out} = 0.324$ m, wall thickness

238

$b = 0.04$ m, and length $L = 45$ m. The physical properties of steel are a function temperature:

$$\lambda = 48.495 + 0.0012 \cdot T - 6.46 \cdot 10^{-5} \cdot T^2 + 4.175 \cdot 10^{-8} \cdot T^3 \tag{29}$$

$$a = 1.341 \cdot 10^{-5} - 3.452 \cdot 10^{-9} \cdot T - 3.193 \cdot 10^{-11} \cdot T + 2.853 \cdot 10^{-14} \cdot T^3 \tag{30}$$

where the thermal conductivity λ is in W/(m·K), the thermal diffusivity a is in m²/s, and the temperature T is in °C.

The temperature of the wall in the radial direction is computed in five evenly-spaced nodes ($n = 4$). The number of nodes in the axial direction is $m + 1 = 21$. The calculation of the transient temperature of the fluid and pipeline wall was carried out for a different number of finite volumes across the thickness of pipe wall.

Inspection of the results shown in Fig. 4 illustrates that even at four finite volumes, i.e. for the five nodes evenly distributed over the wall thickness, satisfactory accuracy of the calculations is obtained.

Almost identical results are obtained for the division of the pipe wall into nine (10 nodes) or nineteen finite volumes (20 nodes) as were obtained for the division into four finite volumes (5 nodes) Fig. 4.

The temperature of the wall in the radial direction is computed in five evenly-spaced nodes ($n = 4$). The number of nodes in the axial direction is $m + 1 = 21$.
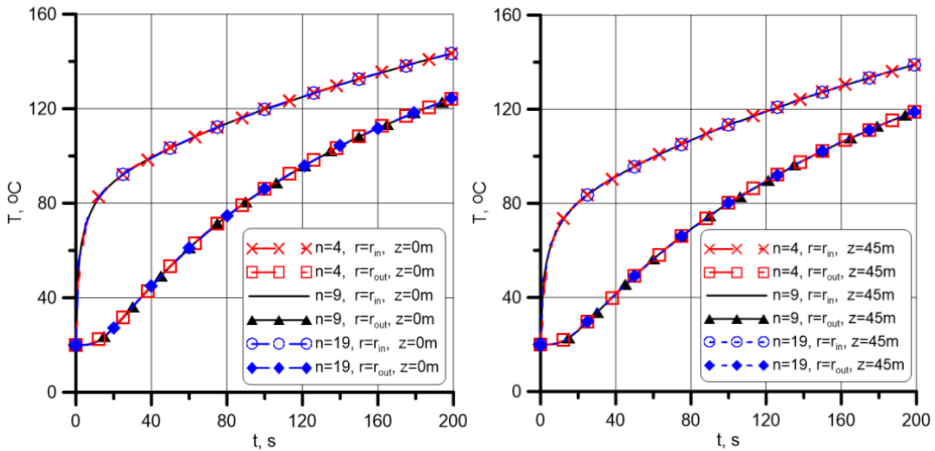
Fig. 4. The temperature of the inner and outer surface of the pipeline at the inlet $z = 0$ m (a) and outlet $z = 45$ m (b), as a function of time t for various numbers of control volumes n across the thickness of the pipeline wall

The pressure is $p = 13.9$ MPa. The mass flow rate of the steam is $\dot{m} = 105.55$ kg/s. The initial temperature of the pipeline and steam is $Tw_0 = 20$°C. At time $t > 0$, the temperature of the steam pipeline inlet increases abruptly to a constant temperature of $T_0 = 540$°C.

Selected modelling results are shown in Figures $5 \div 9$. The steam temperature as a function of time at nodes no. 2 ($z = 2.25$ m), no.10 ($z = 20.25$ m), and no. 20 ($z = 42.75$ m) are displayed in Fig. 5.

The analysis of the results shown in Fig. 5 shows that after about 600 seconds, steam temperature reaches a steady state.
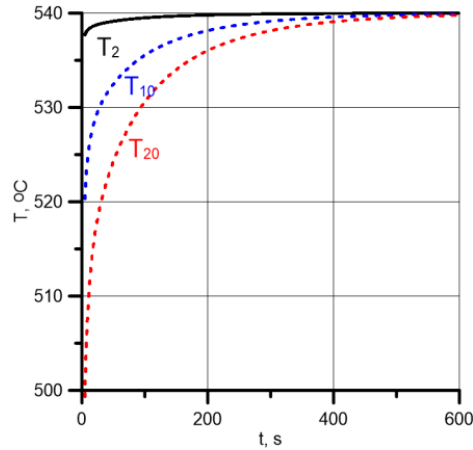
Fig. 5. Steam temperature as a function of time at nodes no. 2 ($z = 2.25$ m), no. 10 ($z = 20.25$ m), and no. 20 ($z = 42.75$ m)

Fig. 6 illustrates steam temperature changes over the length of the pipeline at time points 10s, 60s, 240s, and 600s.
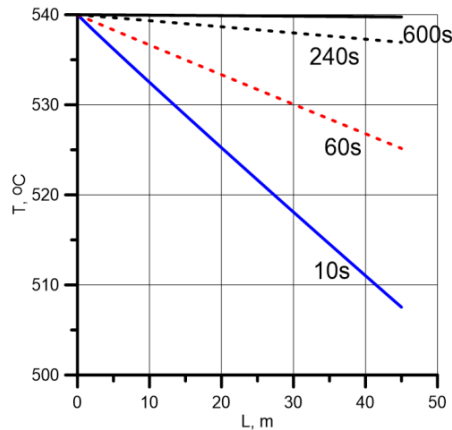
Fig. 6. Steam temperature changes over the length of the pipeline at time points 10 s , 60 s, 240 s, and 600 s

Fig. 7 depicts the pipeline wall temperature in two different cross-sections as a function of time. The wall temperature is shown in five uniformly spaced nodes. Nodes 11 and 101

are located on the inner surface while nodes 15 and 105 lie on the outer surface of the pipeline.

At the beginning of the heating process, the temperature differences over the thickness of the wall are large but rapidly decrease over time (Fig. 7).

Circumferential stresses on the inner and outer surface of the pipeline as a function of time are presented in Fig. 8.
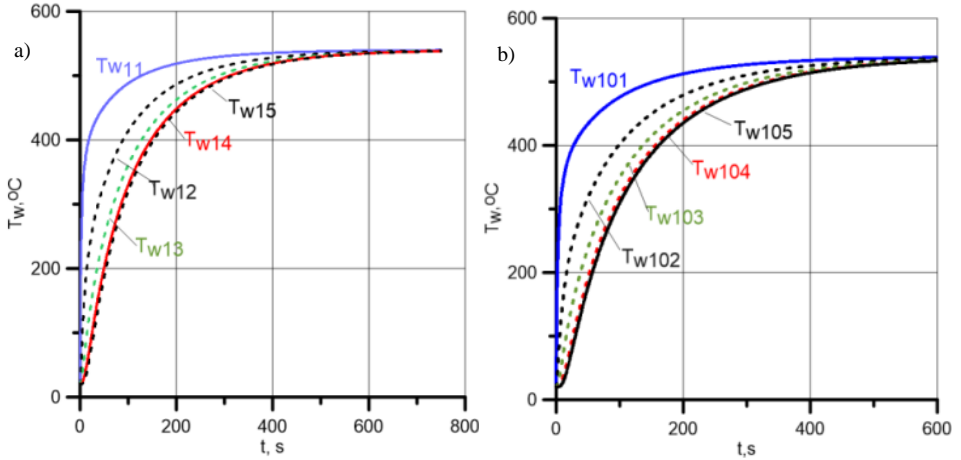
Fig. 7. Wall temperature in tree cross-sections as a function of time a) $z = 2.25$ m, b) $z = 42.75$ m

The analysis of the results presented in Fig. 8 shows that the inner surface is exposed to high compressive stresses while on the outer surface, substantially lower tensile stresses occur.

High thermal stresses in the pipeline are caused by a high jump of 520 K in steam temperature at time $t = 0$.
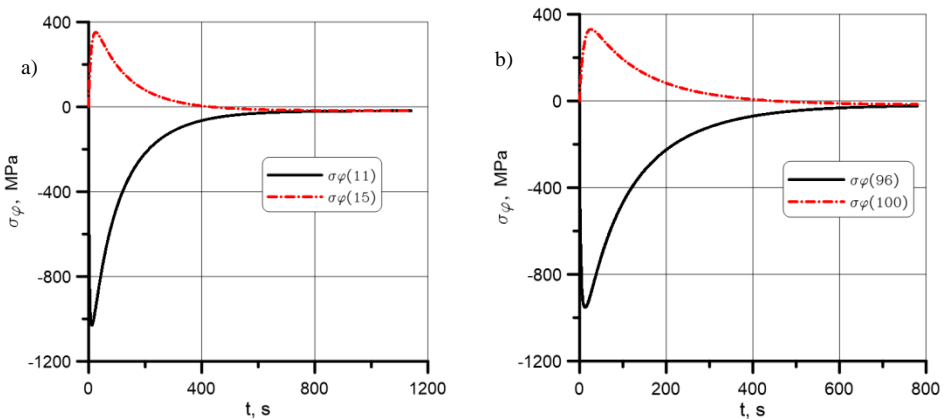
Fig. 8. Circumferential thermal stress on the inner (nodes 11 and 96) and outer (nodes 15 and 100) surfaces of the pipeline as a function of time; a) $z = 2.25$ m, b) $z = 42.75$ m

The largest absolute value of stress occurs at the beginning of heating and tends to zero over time Fig. 8.

4. Summary

The mathematical model of the steam pipeline heating developed in the paper allows determining the temperature of the steam and the pipeline wall as a function of position and time. It is possible to determine transient thermal stresses caused by the temperature difference across the wall thickness using the developed model. Examples of calculations of the steam temperature, wall temperature and circumferential thermal stresses on the inner and outer surface of the pipeline have been presented. The calculation tests performed in the paper show that the developed mathematical model can be used to simulate the actual pipeline heating or cooling in a power plant.

Nomenclature

a	– thermal diffusivity a $= \lambda/(c\,\rho)$, m^2/s
b	– wall thickness, m
A	– cross-section area, m^2
c_p	– specific heat capacity, J/(kg·K)
d_{in}	– inner diameter, m
d_{out}	– outer diameter, m
E	– modulus of elasticity (Young's modulus), Pa
f	– fluid temperature at the inlet of the pipeline, °C
g	– gravity acceleration, m/s^2
L	– length of the pipeline, m
$(m+1)$	– number of nodes in the longitudinal direction
$\dot{m}$	– fluid mass flow rate, kg/s
$(n+1)$	– number of nodes in radial direction
Nu	– Nusselt number
p	– absolute pressure, Pa
Pr	– Prandtl number
r	– radius, m
r_{in}	– inner radius, m
r_{out}	– outer radius, m
Re	– Reynolds number
T	– temperature, °C or K
t	– time, s
$\bar{T}(t)$	– mean temperature on the wall thickness, °C or K
$\bar{T}(r,t)$	– mean temperature of the wall between r_{in} and r, °C or K
U_{in}	– inner perimeter of the tube, m
w	– fluid velocity, m/s

242

Greek symbols

α – heat transfer coefficient, $W/(m^2 \cdot K)$
β – volumetric thermal expansion coefficient, 1/K
β_T – linear thermal expansion coefficient, 1/K
Δr – radial step, m
Δt – time step, s
Δz – axial step, m
λ – thermal conductivity, $W/(m \cdot K)$
μ – dynamic viscosity, $Pa \cdot s$
ν – Poisson's ration
ξ – friction fraction
ρ – density, kg/m^3
σ_r – radial stress component, Pa
σ_φ – circumferential stress component, Pa
σ_z – axial stress component, Pa
φ – inclination angle of the pipeline with respect to the horizontal plane

Subscripts

i – node number
in – inner surface
out – outer surface
w – wall

R e f e r e n c e s

[1] Taler J., Zima W, Jaremkiewicz M., *Simple method for monitoring transient thermal stresses in pipelines*, Journal of Thermal Stresses, 39(4), 2016, 386-397.

[2] Dzierwa P., Taler D., Taler J., *Optimum heating of cylindrical pressure vessels,* Forsch Ingenieurwes*,* 80, 2016, DOI 10.1007/s10010-016-0196-7.

[3] Taler J., Duda P., *Solving Direct and Inverse Heat Conduction Problems*, Springer, Berlin-Heidelberg 2006.

[4] Taler D., *Dynamics of tube heat exchangers*, Dissertation and monographs 193, Publishing House of AGH, Cracow 2009.

[5] Gnieliński V., *New Equation for Heat and Mass Transfer in Turbulent Pipe and channel flow*, Int. Chem. Engng. 16, 1976, 359-368.

[6] Pletcher R.H., Tannehill J.C., Anderson D., *Computational Fluid Mechanics and Heat Transfer*, Third edition, CRC Press, Boca Raton 2013.

[8] Hetnarski R.B., Noda N. Tanigawa Y., *Thermal Stresses*, Second Edition Solution Manual, Taylor & Francis Inc, Boca Raton 2002.

ROBERT WILHELM, ERIK ESCHE, GÜNTER WOZNY, JENS-UWE REPKE[*]
ZION GUETTA, HOLGER THIELERT[**]

DEVELOPMENT OF A MOBILE PILOT PLANT FOR THE EVALUATION OF NOVEL SCRUBBING LIQUIDS FOR THE ABSORPTION OF CO_2 FROM INDUSTRIAL GASES

MOBILNA INSTALACJA PILOTAŻOWA DO OCENY NOWEGO PŁYNU DO ABSOPRPCJI CO_2 Z PRZEMYSŁOWYCH GAZÓW ODLOTOWYCH

A b s t r a c t

Most available scrubbing liquids suffer from either high heating duties for the regeneration or vulnerability towards gas components. In order to increase the efficiency of the absorption process a novel scrubbing liquid has been developed by thyssenkrupp Industrial Solutions AG. For verifying relevance and feasibility of long-term operation of the new fluid assumptions for installation were created – conceptual design and detailed simulation of the process without detailed thermodynamic information.

Keywords: CO_2 separation, process engineering, modular construction

S t r e s z c z e n i e

Na większość dostępnych cieczy absorpcyjnych oddziaływają wysoka temperatura i są one wrażliwe na składniki gazów odlotowych. W celu zwiększenia wydajności procesu absorpcji firma thyssenkrupp Industrial Solutions AG przedstawiła nowy płyn do skruberów. Dla weryfikacji przydatności i możliwości długoterminowej eksploatacji nowego płynu przedstawiono założenia dla instalacji – projekt koncepcyjny oraz szczegółową symulację procesu bez szczegółowych informacji termodynamicznych.

Słowa kluczowe: wydzielanie CO_2, projektowanie procesowe, konstrukcja modułowa

[*] MSc. Robert Wilhelm, DSc. Eng. Erik Esche, Prof. PhD. DSc. Eng. Günter Wozny, Prof. PhD. DSc. Eng. Jens-Uwe Repke, Process Dynamics and Operations Group, Faculty of Process Sciences, Technical University of Berlin.

[**] DSc. Eng. Guetta, DSc. Eng. Holger Thielert, thyssenkrupp Industrial Solutions AG.

1. Introduction

The importance of the removal of carbon dioxide (CO_2) from various industrial gases, such as coke oven gas, is of great scientific and industrial interest [1]. A common method for the removal of CO_2 is the application of reactive scrubbing fluids in an absorption process. Chemical absorption is advantageous for the application of gases with low partial pressures and a high required selectivity regarding the absorption of CO_2.

For this purpose, a novel scrubbing liquid has been developed by *thyssenkrupp Industrial solutions AG* in order to improve the process efficiency. Therefore, an application for the separation of CO_2 is discussed in this contribution to evaluate the applicability and the long-term robustness of the novel scrubbing liquid under industrial conditions.

The objective of the work is the operation of the pilot plant industrial conditions at a steel mill in Duisburg, Germany. In order to gain experience for the subsequent scale-up, a flexible, modular, and transportable pilot plant is designed and built at *Process Dynamics and Operations Group* at *Technische Universität Berlin* [4]. The pilot-plant itself mainly consists of the absorption section and desorption for the regeneration of the amine solution. Proceeding and following these, pre- and posterior treatment columns are installed to maintain sustainable operational conditions despite fluctuations in the gas feed.

The main goal of the operation of the plant and experiments is the evaluation of the novel scrubbing liquid under industrial conditions and the determination of viable operation conditions. Therefore, the minimal heat required for desorption is determined for each operating point and the scrubbing liquid is analysed in terms of selectivity, longevity, and applicability.

1.1. Proposed Workflow for the Plant Engineering

Towards the scaled up industrial application, experimental data is required to examine the removal of carbon dioxide from industrial gases and to investigate a conceptual design for a faster process development. For this purpose, the pilot plant is designed to gain information about the operability and the process itself to compensate for the lack of operational experience [2]. For this reason, workflow for the plant engineering of a pilot plant is given in this contribution.

2. Research and Process Concept

The objective of the plant is the evaluation of the scrubbing liquid under industrial conditions and the optimisation of the operation of the pilot plant to develop an efficient process concept, independent of the various industrial production sites. Due to the variety of possible applications, the plant needs to be designed with regard to mobility and consideration for a modular construction that offers increased flexibility.

The basic engineering of a pilot plant to examine the novel scrubbing liquids without operational experience or limited thermodynamic knowledge can be attempted by using a comparable medium. In this contribution, monoethanolamine (MEA) is used as a scrubbing liquid and considered as a typical representative for the separation of CO_2 [5]. Coke oven

gas from a steel mill is considered as the feed. In the following table, the possible compositions of the feed gas are shown.

Composition of the feed gas with pressure and temperature

	N_2	H_2	O_2	CO	CH_4	CO_2	NH_3	H_2S	p [bar]	T [°C]
Range [Vol.-%]	5-49	1-4	0-1	10-65	0-1	0-25	0-1	0-1	1-1.4	30-150

Regarding the compositions of the gases, a flexible operation of the process is required, such as a protection against corrosive or acidifying components. The operational pressure ranges from 1 to 1.4 bar in the absorption section, whereas in the desorption section, the pressure is increased to reduce the evaporation of water and amine at the required temperature for desorption (see Fig. 1). In the following section, the aforementioned plant design is detailed.

3. Plant Design
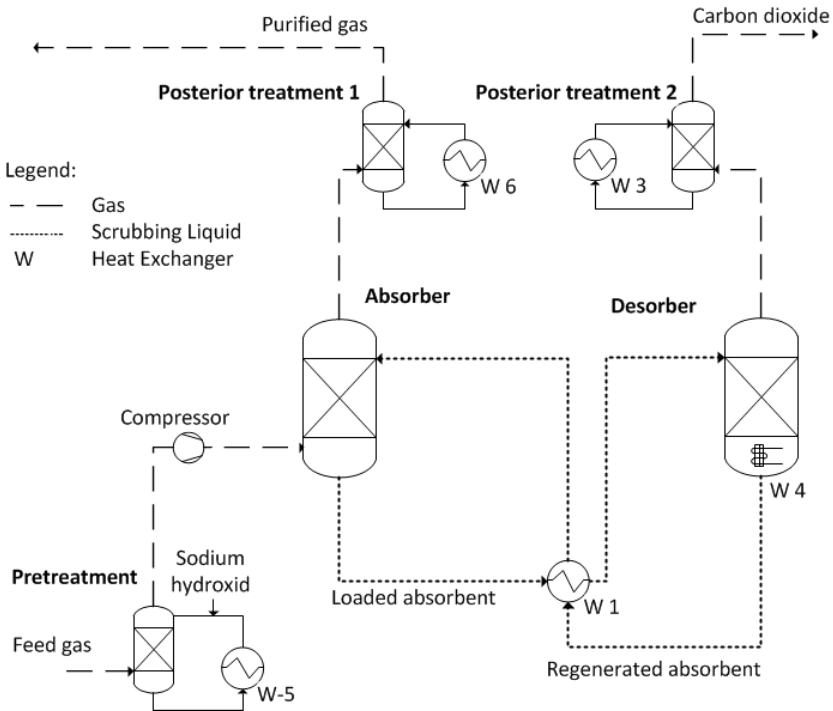
Fig. 1 Simplified flow diagram for the separation of CO_2

Based on the process concept a simplified flow diagram for the separation of CO_2 is shown in Fig. 1. The feed gas enters the plant in the pre-treatment column at almost ambient pressure, where cooling takes place and impurities or corrosive components, such as H_2S, are removed by using sodium hydroxide. The suction and transportation of the gases is realised by using a compressor. Upon entering the absorption section, carbon dioxide is separated from the gas and chemically dissolved in the scrubbing liquid as carbonate and carbamate ions. The gas leaving the absorber may contain smaller amounts of absorbent. Therefore, posterior treatment columns are installed in order to reduce the quantity of the absorbent and decrease the temperature of the purified gas. The loaded scrubbing liquid is pumped to the desorber, wherein, the regeneration of the scrubbing liquid takes place by electrical heating. The carbon dioxide is emitted to the gaseous phase and leaves the process through the second posterior treatment column. In turn, the regenerated liquid is reused and pumped to the absorber, thus closing the scrubbing liquid cycle.

3.1. Process Simulations and Assumptions

After the conceptual design of the process, a preliminary estimation of the operation conditions and design parameters with further investigations is needed. For this purpose, the process is modelled and simulated in Aspen Plus®. The rigorous simulation is required for the following sizing of the equipment and the estimation of the number of theoretical stages for both the absorption and desorption columns.

Fixed specifications for the estimation of the packing height is the separation of 90 Vol.-% of carbon dioxide. This is set by a *design spec* within the simulation. In order to keep the flexibility of the pilot plant, three different gas loads factors are considered, which are characterised by the F factor and three different gases with varying CO_2 concentrations. For the different values of the F factor, the operation points needed to be determined. Under the restriction of the separation of 90 n/n % of CO_2, the operation point is set by the minimal required electrical heating. The minimal required heating value is defined by the following equation:

$$q_{spez} = \frac{Q_{Desorber}}{m_{CO2,seperated}} \qquad (1)$$

where

      q_{spez} – specific amount of heating for the current operation conditions,
      $Q_{Desorber}$ – required amount of heating in the desorber,
      $m_{seperated}$ – mass flow of separated carbon dioxide in the scrubbing liquid.

The results for the operation points of the pilot plant are shown in the following table:

**Operation conditions of the pilot plant for three gas load factors with following composition:
22.7 Vol.-% CO$_2$, 24.6 Vol.-% CO, 4 Vol.-% H$_2$, 48.6 Vol.-% N$_2$**

F factor [Pa$^{0.5}$]	Q$_{Desorber}$ [kW]	q$_{spez}$ [MJ/kg$_{CO2}$]
0.5	5.36	3.37
1.0	11.47	3.61
1.2	14.06	3.72

Changes of the gas load have an influence not only on the absorber, but also on the loading of the scrubbing liquid. An increasing gas load requires an elevated liquid flow of scrubbing fluid and additional electrical heating [5]. Fig. 2 represents an operation point with its conditions for an F factor of 1 Pa$^{0.5}$.
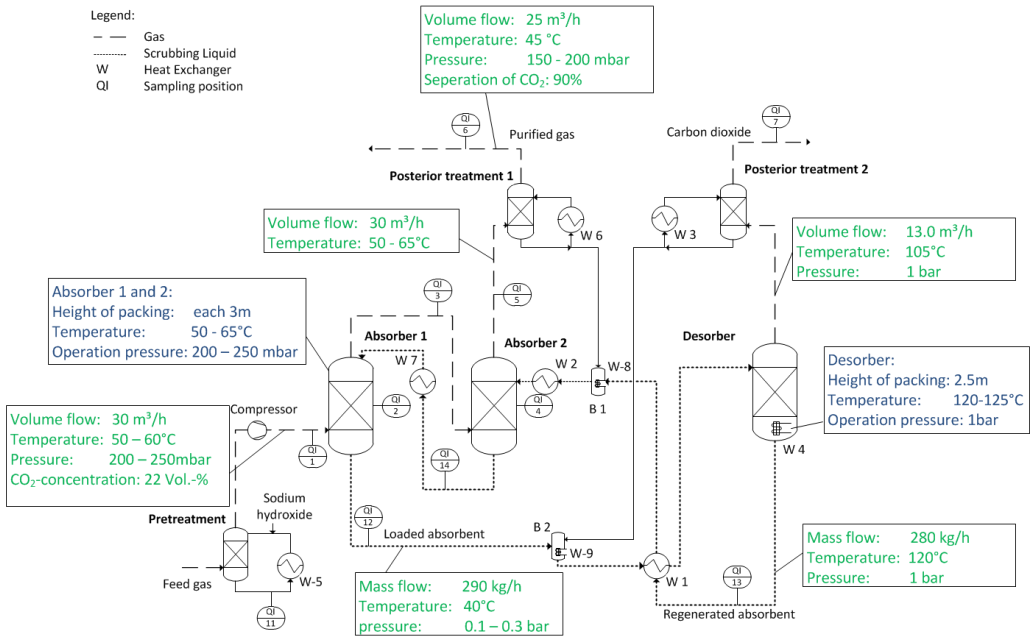
Fig. 2. Operation conditions for a gas load factor F of 1 Pa$^{0.5}$

3.2. Technical specifications and equipment planning

Based on the process simulation the equipment is sized and the technical specifications are determined [3].

Structured packings are employed for the columns with a total height of 6m packing for the absorption and 2.5m for the desorption. The additional columns for the pre- and posterior treatment contain 1m of structured packing each. With the height of the packing in the columns, the technical drawings of the apparatuses are drafted. For safe operation of the plant, strict safety regulations are required. Therefore, the whole pilot plant is planned,

constructed, and operated under European explosion protection ATEX/II2G. For safety reasons, a *HAZOP* analysis is conducted and the results are transferred to the process concept. The next step is the design of a three-dimensional (3D) model, which is necessary for the piping and the positioning of the apparatus in the condensed space of the mobile modular pilot plant.

Fig. 3 shows a 3D model of the whole pilot plant within the steel framework. This highlights the main challenge for the design of the plant, namely, the limited space. Each module has a height of 2.8 m, is 5.3 m wide and 2.3 m deep. The total height including the handrail on the upper level is 6.7m. Within the framework, which consists of two separate modules, apparatus need to be affixed. In addition to the pre-treatment columns, the two post-treatment columns, the two absorption columns, and the desorption column, the plant contains a compressor, ten pumps, and two liquid tanks. To handle this challenge, a comprehensive 3D model is developed in AVEVA PDMS® to ensure access for maintenance and operation. With the sole exception of piping for the pressurised air, the 3D model contains the piping for all utilities, gas, and liquid streams. The positioning of the gas pipes is of especially great importance due to their comparatively large diameter.

The pipes reaching out of the steel frame are the gas inlet and outlet. In addition, cable trays are positioned at the top of each module for supplying electricity and controlling all devices.

A basin below the lower module is installed to catch liquids in case of leaks or emergencies. Components, such as pumps and electrical heaters are placed at the bottom to facilitate maintenance work.
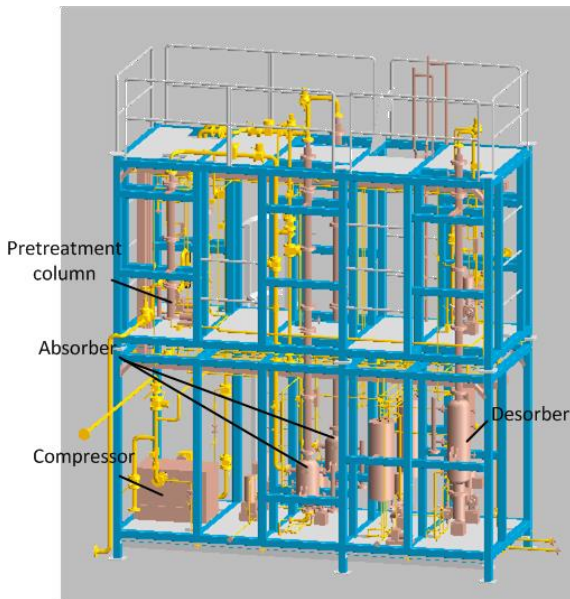
Fig. 3 3D model of the plant with apparatuses and the complete piping

Fig. 4 shows two photographs of the current state of construction work at TU Berlin. Due to the considerable height of the pilot plant, both the lower and the upper modules are separated and worked on side by side.

Fig. 4 Photos of the lower module (left) and of the upper module (right)

3.2 Process automation and analytics

The plant is automated using ABB's Freelance 700F process control systems. More than 30 temperature, 13 pressure, 8 level, and 13 flow indicators provide the required information for the process control. In addition, control sequences are implemented for the start-up, shut-down, emergency shut-down, and inertisation procedures.

As mentioned before, the main goal is the separation of CO_2 from the feed gas. Hence, samplings are intended to measure the CO_2 concentration within the gas stream by an infrared photometer of ABB (*Multiwave Model 3502*). This device enables online measurements at different positions. The positions are shown in Fig. 2. In total, seven positions are intendent for accurate measuring. To keep the coefficient of absorption under surveillance, positions QI1, QI3, and QI5 are of great importance and are equipped with automated valves. In addition, manual sampling locations are positioned in the liquid pipes for the analysis of the scrubbing fluid in order to measure the load of carbon dioxide within the fluid.

4. Conclusion and Outlook

This contribution tackles the challenge of overcoming the step between lab experiments and the first industrial application. Therefore, a modular and mobile pilot plant is constructed to gain experience in the separation of CO_2 from industrial gases. Besides evaluating the novel scrubbing liquid without detailed thermodynamic knowledge or operation experience, the possibilities of a faster process development are investigated.

For basic engineering, it is necessary to clarify the operating conditions and to provide a conceptual design. Following the process simulations and the sizing of equipment, a detailed 3D model is required which puts a larger emphasis on safe operation and maintenance of the plant.

The goal of this work is to evaluate aspects such as the long-term robustness and the applicability, and to prove the industrial viability of the scrubbing liquid under real conditions. For this reason, the continuous operation of the process for more than 500 hours is planned. Furthermore, a more complex and detailed analysis of the liquid and gas phase is intended in order to increase the availability of the process.

A b b r e v i a t i o n s

ATEX   – European directives on equipment and work in explosive atmospheres,
CO_2 – carbon dioxide,
MEA   – monoethanolamine,
n/n   – mole per mole.

R e f e r e n c e s

[1] Bock C., *Gaswäsche – Industrielle CO₂-Abtrennung: Miniplant zur schnellen Evaluation von Waschmitteln,* CITplus, vol. 25, 2014.
[2] Stünkel S., *Simultaneous Synthesis of the Downstream Process and the Reactor Concept for the Oxidative Coupling of Methane (OCM),* 10th International Symposium on Process Systems Engineering, PSE 2009.
[3] Esche E., *Innovative Product and Process Development with Mobile and Modular Mini-plant Technologies,* Technical Transactions, series Mechanics, vol. 1, 2012.
[4] Müller M., *Innovative Produkt- und Prozessentwicklung mittels mobiler und modularer Mini-plant Technik*, Jahrestreffen der Fachgemeinschaft Prozess-, Apparate- und Anlagentechnik, Fulda 2011.
[5] Shen K.P., *Solubility of Carbon Dioxide in Aqueous Mixtures of Monoethanolamine with Methyldiethanolamine*, Chem. Eng., vol. 37, 1992, 96-100.

CONTENTS

252

TREŚĆ

254